Distribution Agreement

In presenting this thesis or dissertation as a partial fulfillment of the requirements for an advanced degree from Emory University, I hereby grant to Emory University and its agents the non-exclusive license to archive, make accessible, and display my thesis or dissertation in whole or in part in all forms of media, now or hereafter known, including display on the world wide web. I understand that I may select some access restrictions as part of the online submission of this thesis or dissertation. I retain all ownership rights to the copyright of the thesis or dissertation. I also retain the right to use in future works (such as articles or books) all or part of this thesis or dissertation.

Signature:

_____ _____

Elliot N. Glass Date

Charge Separation in Polyoxometalate-Based Systems for Solar Energy Production

By

Elliot N. Glass
Doctor of Philosophy

Chemistry

_____
Craig L. Hill, Ph.D.
Advisor

_____
Tianquan Lian, Ph.D.
Committee Member

_____
Christopher C. Scarborough, Ph.D.
Committee Member

Accepted:

_____
Lisa A. Tedesco, Ph.D.
Dean of the James T. Laney School of Graduate Studies

_____
Date

Charge Separation in Polyoxometalate-Based Systems for Solar Energy Production

By

Elliot N. Glass
Bachelor of Science, Purdue University, 2008
Bachelor of Science, Florida State University, 2011

Advisor: Craig L. Hill, Ph.D.

An abstract of
a dissertation submitted to the Faculty of the
James T. Laney School of Graduate Studies of Emory University
in partial fulfillment of the requirements for the degree of
Doctor of Philosophy
in Chemistry
2016

Abstract

Charge Separation in Polyoxometalate-Based Systems for Solar Energy Production

By

Elliot N. Glass

The desire for green, renewable energy has driven many areas of science in recent years. In chemistry, one popular vision for sustainable energy utilizes sunlight to split water molecules into hydrogen and oxygen gas. When used as a fuel, these gases release energy that can be used to power our civilization, with water as the only waste product. To realize this vision, cost-effective and robust materials are being sought to improve upon current approaches. This includes molecular catalysts to promote water oxidation (yielding oxygen) and proton reduction (yielding hydrogen), and robust materials capable of absorbing sunlight to generate a charge separated state, providing the driving force for both catalytic reactions. The research described herein focuses on the latter problem, exploring the underlying photophysical properties of chromophoric polyoxometalates (POMs) as photosensitizers for solar energy production.

The first part of this work investigates the photophysical properties of Keggin POM chromophores by principally utilizing ultrafast spectroscopic techniques. While the excited state lifetimes of most POMs are too short to facilitate catalytic reactions, $[Co^{II}W_{12}O_{40}]^{6-}$ was found to have a far-longer lived excited state generated through a metal-to-polyoxometalate charge transfer (MPCT) transition (Chapter 2). This extended lifetime was ascribed to a transient structural change and charge localization within the POM. In Chapter 3, the influence of structural modifications of this POM on the excited state lifetime were investigated by substituting transition metals into the structure to yield the series $[Co^{II}(M^xOH_y)W_{11}O_{39}]^{(12-x-y)-}$ (M^xOH_y = $V^{IV}O$, $Cr^{III}(OH_2)$, $Mn^{II}(OH_2)$, $Fe^{III}(OH_2)$, $Co^{II}(OH_2)$, $Ni^{II}(OH_2)$, $Cu^{II}(OH_2)$, $Zn^{II}(OH_2)$). Transition metal substitution maintains and modulates the original MPCT transition, but decreases the excited state lifetime. These complexes serve as useful models for advancing the development of robust photosensitizers, though their photophysical properties limit their direct application in a light-driven chemical system.

Chapter 4 describes the synthesis, structure, and excited state dynamics of three Sn-containing POMs. A charge transfer transition in one complex is attributed to a unique interaction between Sb and Sn ions in the structure. In Chapter 5, additional POM chromophores are investigated by ultrafast spectroscopy, exhibiting short-lived excited states that limit their applications as effect chromophores for solar energy applications.

Charge Separation in Polyoxometalate-Based Systems for Solar Energy Production

By

Elliot N. Glass
Bachelor of Science, Purdue University, 2008
Bachelor of Science, Florida State University, 2011

Advisor: Craig L. Hill, Ph.D.

A dissertation submitted to the Faculty of the
James T. Laney School of Graduate Studies of Emory University
in partial fulfillment of the requirements for the degree of
Doctor of Philosophy
in Chemistry
2016

Acknowledgments

Earning a doctorate is an opportunity afforded to few, and I am grateful to be counted among them. Reaching this point requires significant work, perseverance, and patience, through which one inevitably must overcome occasional feelings of doubt and hopelessness. While these burdens ultimately weigh down just one, the aid of many lightens the load. This accomplishment would have been more difficult, if not impossible, without the support of a few individuals in particular, and many others left unmentioned.

My dissertation committee, and in particular my advisor, Dr. Craig L. Hill, will have a lasting and formative impact on my scientific career. Dr. Hill provided me the opportunity to pursue this research, and lent valuable scientific and professional guidance along the way. Prior to meeting him, I had no idea polyoxometalates existed; now I see polyhedra everywhere. Dr. Tianquan “Tim” Lian was a sage advisor who gave me the chance to collaborate with his group and use his expensive laser equipment, without which most of this work could not have happened. Dr. Christopher C. Scarborough lent a valuable (and comparatively youthful) voice to my committee, and offered useful discussions and professional guidance.

Of all the collaborative efforts with which I have taken part, two researchers stand apart as valuable contributors to my success. Dr. John Fielden, with whom my most important works were published, provided tireless expertise and guidance in multiple experimental aspects of my work. Dr. Djamaladdin “Jamal” G. Musaev, provided computational support for several papers, and his scientific guidance and generous support were greatly appreciated.

Those with whom one spends most of their time with on a daily basis in graduate school are fellow graduate students. Beyond merely people of similar inclination stuck in the same boat, they become cherished colleagues and friends. In particular, more senior graduate students play a critical role in showing new students how to perform research in a new setting and set the standard with which you measure your accomplishments. I count myself lucky to have known four graduate students who guided me as I was first starting my graduate career. Dr. Zhuangqun "Teddy" Huang was a valuable graduate student in the Lian lab who guided me in my early ultrafast laser experiments. Dr. Guibo Zhu offered me the opportunity to contribute to her research early in my career, leading to two early published works, and provided kind guidance in early experimental aspects of polyoxometalate chemistry. Dr. Chongchao "Charlie" Zhao offered me the opportunity to study several of his complexes using ultrafast spectroscopy, leading to two other published works. His creative synthetic chemistry and diligence largely define what I consider to be a model graduate researcher. Finally, Dr. James "Jim" Vickers was a valued colleague and friend who showed me many of the finer aspects of polyoxometalate synthesis, crystallization, and characterization. Of all the graduate students I met while at Emory, Jim stands out, not just for his unique style, but as the first contact I made in the Hill group during recruitment in early 2011, the first member who greeted me when I started in June 2011, and the doctoral graduate who immediately preceded my own successful defense.

Table of Contents

List of Figures

Chapter 1

Chapter 2

Chapter 3

Chapter 4

Chapter 5

List of Tables

Chapter 2

Chapter 3

Chapter 5

List of Symbols and Abbreviations

α, β, γ	interaxial angles between unit cell vectors (X-ray crystallography)
Å	angstrom (10^{-10} meters)
°	degrees
°C	degrees Celsius
ε	molar absorptivity or extinction coefficient
λ	wavelength
λ_{max}	wavelength at maximum molar absorptivity
μ	micro (10^{-6})
μ	total linear absorption coefficient (X-ray crystallography)
μJ	microjoule (10^{-6} Joule)
μm	micrometer (10^{-6} meter)
$\tilde{\nu}$	wavenumber
ρ_{calc}	calculated density (X-ray crystallography)
τ	exponential decay constant
θ_{max}	maximum angle of data collected (X-ray crystallography)
a, b, c	unit cell axis length (X-ray crystallography)
a.u.	arbitrary unit
A_0	modified chlorophyll electron acceptor
A_1	phylloquinone
ADP	adenosine diphosphate
AM1.5	Air Mass 1.5
ASTM	American Society for Testing and Materials

ATP	adenosine triphosphate
bpy	2,2'-bipyridine
calcd.	calculated
cm	centimeter (10^{-2} meter)
cm^{-1}	reciprocal centimeter (wavenumber)
CT	charge transfer
Cyt b_6f	cytochrome b_6f complex
DFT	density functional theory
DMF	dimethylformamide
$eÅ^{-3}$	residual electron density (X-ray crystallography)
e^-	electron
eV	electronvolt
F^2	square of the amplitude, F (X-ray crystallography)
FD	ferredoxin
FNR	ferredoxin NADP+ reductase
fs	femtosecond (10^{-15} second)
FT-IR	Fourier transform infrared spectroscopy
FW	formula weight
fwhm	full width at half maximum
F_x	iron-sulfur clusters (one of three, F_X, F_A, and F_B)
g	gram
GS	ground state
HOMO	highest occupied molecular orbital
IR	infrared

IC	internal conversion
ISC	intersystem crossing
IVCT	intervalence charge transfer (electronic transition)
K	Kelvin
kcal	kilocalorie (10^3 calories)
k_{cat}	rate constant for a catalytic process
k_{et}	rate constant for intermolecular electron transfer
k_f	fluorescence rate constant
kHz	kilohertz (10^3 Hertz)
k_{isc}	rate constant for intersystem crossing
k_{nr}	nonradiative decay rate constant
k_{obs}	observed rate constant
k_p	phosphorescence rate constant
k_{pd}	rate constant for a photodissociative mechanism
k_r	radiative decay rate constant
k_{rc}	rate constant for charge recombination
LC	ligand-centered (electronic transition)
LED	light-emitting diode
LUMO	lowest unoccupied molecular orbital
M	molarity
m	medium (IR)
m^2	square meter
MC	metal-centered (electronic transition)
MeCN	acetonitrile, CH_3CN

mJ	millijoule (10^{-3} Joule)
mL	milliliter (10^{-3} liter)
mm	millimeter (10^{-3} meter)
mM	millimolar (10^{-3} molar)
mm^3	cubic millimeter (10^{-9} cubic meter)
MMCT	metal-to-metal charge transfer (electronic transition)
mmol	millimole (10^{-3} mole)
mV	millivolt (10^{-3} volt)
mol	mole
MLCT	metal-to-ligand charge transfer (electronic transition)
MPCT	metal-to-polyoxometalate charge transfer (electronic transition)
mW	milliwatt (10^{-3} watt)
$NADP^+$	nicotinamide adenine dinucleotide phosphate (oxidized form)
NADPH	nicotinamide adenine dinucleotide phosphate (reduced form)
NHE	normal hydrogen electrode
NIR	near infrared
nm	nanometer (10^{-9} meter)
norm.	normalized
ns	nanosecond (10^{-9} second)
OEC	oxygen evolving complex, the Mn_4CaO_5 cluster in Photosystem II
ORTEP	Oak Ridge Thermal Ellipsoid Plot
osc. str.	oscillator strength
P680	chlorophyll *a* pigment in Photosystem II
P700	chlorophyll *a* pigment in Photosystem I

PC	plastocyanine
PCET	proton-coupled electron transfer
PCM	polarizable continuum model
PES	polyethersulfone
pH	potential of hydrogen, a measure of the acidity/alkalinity of a solution
Pheo	pheophytin
POM	polyoxometalate
PRC	proton reduction catalyst
PQ_x	plastoquinone (one of two, PQ_A and PQ_B)
ps	picosecond (10^{-12} second)
PW	petawatt (10^{15} watt)
R_1	structure confidence factor (X-ray crystallography)
R_{int}	merging error (X-ray crystallography)
s	strong (IR)
S	electronic multiplicity
sh	shoulder (IR, UV-Vis)
SHE	standard hydrogen electrode
T	temperature
TA	transient absorption
TBA	tetrabutylammonium, $(C_4H_9)_4N^+$
TD-DFT	time-dependent density functional theory
TGA	thermogravimetric analysis
TMSP	transition metal substituted polyoxometalate
TW	terawatt (10^{12} watt)

UV	ultraviolet
V	volt, electric potential
V	volume of the unit cell (X-ray crystallography)
Vis	visible
vs	very strong (IR)
vw	very weak (IR)
w	weak (IR)
WOC	water oxidation catalyst
wR_2	residual confidence factor (X-ray crystallography)
Y_Z	tyrosine radical proximal to the OEC
Z	number of molecules per unit cell (X-ray crystallography)

Charge Separation in Polyoxometalate-Based Systems for Solar Energy Production

Chapter 1

Polyoxometalates in Solar Energy Research

1.1 Fundamental Challenges in Solar Energy Production

Humans have been harnessing energy since before recorded history, acquiring a control of fire that allowed early humans to push back the shadows of the night and generate warmth. As societies developed, the ability to control and manipulate the environment to suit their needs became a critical factor in the rise and fall of nations. The impact humans have on our planet, from an individual to national level, can be correlated with the capacity to use the energy resources at our disposal. Over time, improvements in technology have afforded the ability to use energy resources beyond those of pure human and animal effort (e.g. primitive agriculture), leading to the development of machinery exploiting, among others, coal, oil, and nuclear energy.

On a macroeconomic level, an increased ability to use energy is correlated with improved productivity, societal affluence, and technological achievement.[1,2] Historically, a region's per capita income loosely parallels its per capita consumption of energy.[3-5] Since countries have a vested interest in improving the lives of their citizens, and a higher per capita income is associated with prosperity, it is only natural that energy consumption should increase over time with normal economic growth. Developed, industrialized countries are relatively wealthy compared to developing countries, and consequently have a higher energy consumption. For example, comparing the United States to India, the ratio of total primary energy supply per capita is 11.2, and the ratio of electricity consumption per capita is 16.6.[6]

Global energy demand is projected to increase dramatically during the 21st century, driven by population growth and rising standards of living.[7,8] Global energy consumption over the last fifteen years has increased by >2% annually and is expected to

continue for the foreseeable future, requiring a doubling of energy production capacity within 35 years or less.[9] Currently, greater than 80% of global energy production is derived from the combustion of fossil fuels, a finite resource that is also a valuable chemical feedstock.[6] The continued burning of fossil fuels for energy has also contributed to significant environmental degradation and global climate change.[10] The development of sustainable, renewable, and economically viable means of energy production will require the capture and exploitation of energy in new ways to meet the demands of a growing world.

Energy derived from the sun is the most practical and available resource for sustained, renewable energy.[8] The average amount of solar electromagnetic radiation that strikes the Earth is 1361 W/m^2,[11] which, when multiplied by the cross-sectional area of the Earth, equates to 1.73×10^{17} W (173 PW). Of this radiation, 73.8% penetrates the atmosphere and irradiates the Earth's surface at wavelengths spread across the UV, visible, and NIR (Figure 1.1).[12] For comparison, the average global total energy consumption in 2012 was 1.75×10^{13} W (17 TW), 0.0138% of the solar radiation that reaches the Earth's surface.[4] While plants take advantage of this resource, and most other energy sources are ultimately derived from solar (the exception being nuclear energy), the vast majority of solar radiation is untapped and available for use, if we can develop an appropriate means of exploiting it.

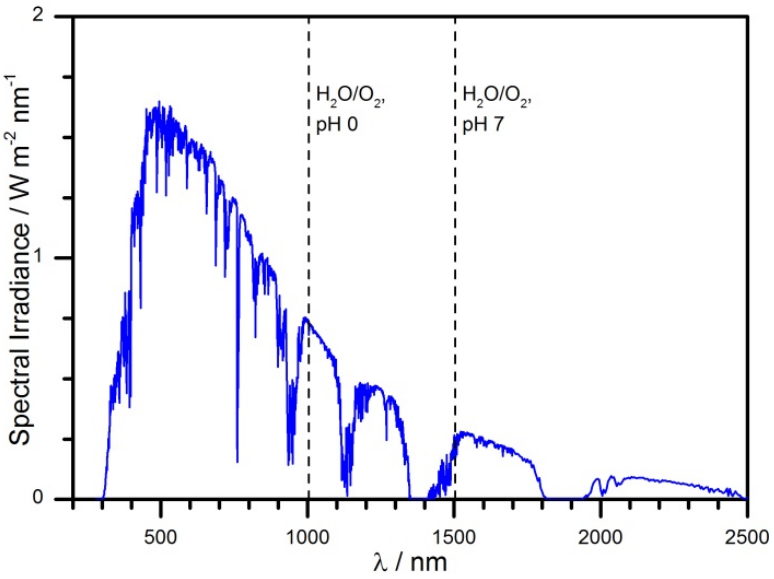

Figure 1.1. The spectrum of total solar radiation incident upon the Earth at sea level, under standard average conditions for the lower 48 states of the United States, as defined by the American Society for Testing and Materials (ASTM) Terrestrial Reference Spectra (ASTM G-173).[12] The standard spectrum corresponds to Air Mass 1.5 (AM1.5). Vertical lines correspond to the theoretical maximum wavelength of light capable of oxidizing water at pH 0 and pH 7, assuming no overpotential.

The surge of interest in renewable energy over the last decade has led to a considerable growth in solar cell (photovoltaic) deployment. Solar cell deployment combined with improvements in technology have led to double digit growth since 2000, though the installed capacity, <1% of global electricity generation, is still dwarfed by other energy sources.[9] However, the variability of solar energy, the poor efficiency of electrical storage, and the need for higher energy density sources remains an issue.[7,8] One solution to this problem is to convert solar energy directly into chemical bonds.[13,14] In particular, solar-driven water splitting ($H_2O + h\nu \rightarrow H_2 + ½\ O_2$) is a carbon-neutral

method of storing energy in H_2, a single bond with the highest energy density per unit mass. Alternatively, energy can be stored in a carbon-based substrate to form liquid fuels and chemical feedstocks, obviating the need for fossil fuels altogether.[15-18] In general, this process seeks to mimic photosynthesis, and has been referred to as solar fuels or artificial photosynthesis.[19-24]

The overall process for water splitting can be represented by two half-reactions, with their respective standard reduction potentials relative to NHE:

$$\text{Oxidation: } 2\ H_2O_{(l)} \rightarrow O_{2(g)} + 4\ H^+_{(aq)} + 4\ e^- \qquad E° = 1.23\ V \qquad (1.1)$$

$$\text{Reduction: } 4\ H^+_{(aq)} + 4\ e^- \rightarrow 2\ H_{2(g)} \qquad E° = 0.00\ V \qquad (1.2)$$

$$\text{Overall: } 2\ H_2O_{(l)} \rightarrow 2\ H_{2(g)} + O_{2(g)} \qquad \Delta G° = +475\ \text{kJ/mol} \qquad (1.3)$$

In equation 1.1, two molecules of water are oxidized, releasing oxygen gas, four protons, and four electrons. The protons and electrons are combined in equation 1.2, yielding hydrogen gas. Of the two reactions, water oxidation is the most difficult, as it involves four electrons, a highly oxidizing potential, large overpotentials, and necessitates a proton-coupled electron transfer (PCET) process to be feasible. Proton reduction is easier, only involving two electrons, but must also go through a PCET mechanism to avoid a prohibitively high activation barrier. The overall reaction, equation 1.3, is endothermic and endergonic. Catalysts are necessary to reduce the activation barriers on both half-reactions and achieve acceptable reaction rates.[22,25,26]

From a purely thermodynamic perspective, the energy required to drive equation 1.1, 1.23 V at pH 0, is carried in any photon of solar energy of wavelength 1008 nm or shorter (any photon to the left of the first vertical line in Figure 1.1). Because protons are

involved in the half-reaction, equation 1.1 is pH-dependent, and at higher pH values the thermodynamic barrier decreases further, to 0.82 V at pH 7 (1512 nm), and 0.40 V at pH 14 (3100 nm). As a result, most of the solar radiation spectrum could be used to drive equation 1.1, if it was fully reversible and a negligible reaction rate was acceptable. Neither of these conditions are true, so a greater amount of energy is necessary than expected thermodynamically. This extra energy, an overpotential, is a manifestation of multiple factors, including the activation energy of a reaction. Consequently, water oxidation reactions typically suffer from large overpotentials. The first demonstrated photoelectrochemical cell for water splitting observed activity using a TiO_2 semiconductor irradiated at <415 nm (>3.0 eV).[27]

Improving the efficiency of solar fuel devices is critical to realizing a cost-effective replacement for fossil fuels, but the challenge is daunting, as evidenced by the fact that nearly fifty years of research in the area have not yielded a viable product. An ideal system must be capable of: 1) absorbing a maximal portion of the solar spectrum; 2) efficiently utilizing the absorbed energy by minimizing charge recombination; 3) rapidly oxidizing water; 4) rapidly evolving hydrogen gas; 5) maintaining high activity for a sustained period of time (i.e. years); and 6) being cheap and mass-producible. These needs will require the combined efforts of scientists and engineers aiming to optimize all aspects of these complicated systems. There is no lack of inspiration, however, as natural systems offer multiple examples from which to draw insight.

1.2 Photosynthesis as a Guide

Photosynthesis sustains most of the life on Earth by storing solar energy in chemical bonds. In this process, carbon dioxide and water are converted into carbohydrates and oxygen:

$$nCO_2 + nH_2O \rightarrow (CH_2O)_n + nO_2 \qquad (1.4)$$

By comparing equation 1.4 with equation 1.3, one can see that water oxidation is a critical component of photosynthesis. The solar energy absorbed in photosynthesis drives the oxidation of water to yield protons and oxygen gas, and the protons are stored in carbohydrates as higher energy products. Nature also provides examples of hydrogen evolution in the hydrogenase class of enzymes. Observing what allows natural systems to perform these reactions, and elucidating their relative strengths and weaknesses, may provide the means to build biomimetic systems that incorporate the functions of biological systems into technological devices.

The biological solution to water oxidation involves many components, but can be summarized as absorbing light from the sun and channeling the captured energy through a series of coupled energetically favorable events to form higher energy products. This process is described in the Z-scheme energy diagram illustrated in Figure 1.2, showing the sequence of energy/electron flow. Two light absorption processes drive the chemical reactions in the entire system, those of the pigments P680 and P700 and their associated antennae within specialized light-harvesting complexes. When a photon is absorbed by the complexes, the absorbed energy is transferred to the reaction center (P680 or P700) via a Förster resonance energy transfer mechanism. The absorbed energy induces an

excited state, $P680^*$ or $P700^*$, and the photoexcited electrons are rapidly transferred to nearby electron acceptors, Pheo and A_0, respectively.

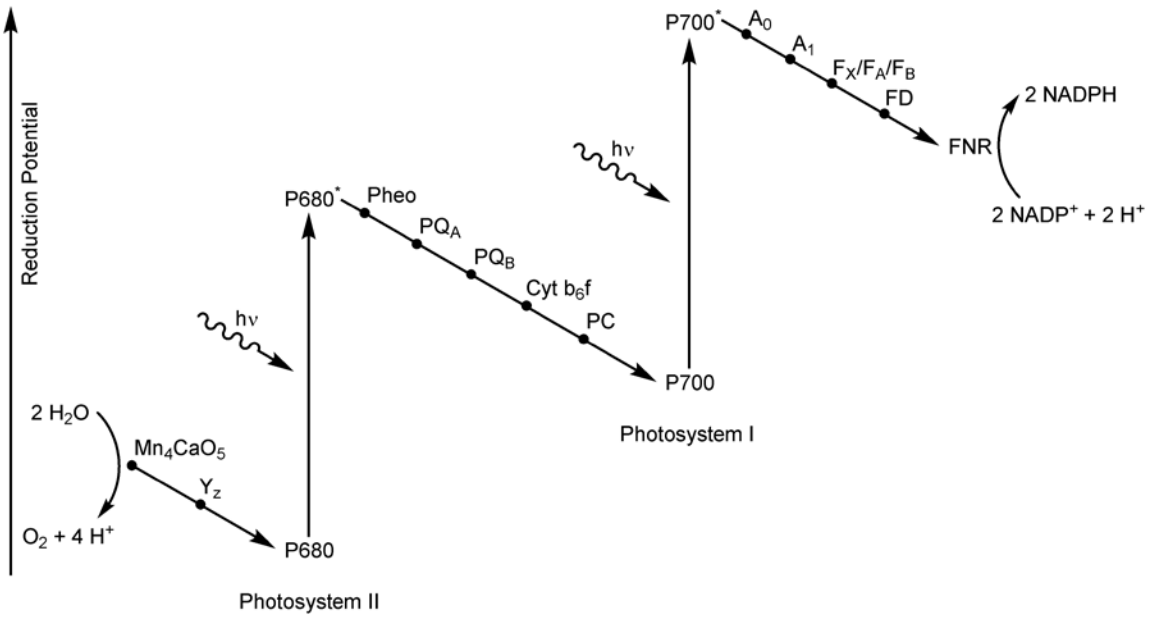

Figure 1.2. The Z-scheme energy diagram for plant photosynthesis. Notation: Mn_4CaO_5, the oxygen evolving complex (OEC); Y_Z, tyrosine residue proximal to the OEC; P680, chlorophyll *a* pigment in Photosystem II; Pheo, pheophytin; PQ_x, plastoquinone; Cyt b_6f, cytochrome b_6f complex; PC, plastocyanine; P700, chlorophyll *a* pigment in Photosystem I; A_0, modified chlorophyll electron acceptor; A_1, phylloquinone; F_x, iron-sulfur clusters; FD, ferredoxin; FNR, ferredoxin $NADP^+$ reductase.

$P680^*$ is a strong reducing agent, and the photoexcited electron proceeds through a series of electron transfer events, losing a small amount of energy at each step. This energy loss, coupled with spatial separation from P680, reduces the probability of charge recombination, facilitating energy transfer down the electron transport chain. The electron that originated at P680 is passed along a series of weaker reducing agents,

generating a chemiosmotic potential that is used to phosphorylate adenosine diphosphate (ADP) to adenosine triphosphate (ATP), a ubiquitous biological energy storage molecule. The electron ultimately reduces $P700^+$ to P700, regenerating the pigment.

The photoexcited electron in $P700^*$ transiently generates an exceptional reducing agent (*ca.* -1.4 V vs. SHE), the strongest known in biology, and initiates a second electron transport chain similar to the one previously described. The electron passes through several intermediates before reaching ferredoxin $NADP^+$ reductase, which catalyzes the two-electron, one-proton reduction of nicotinamide adenine dinucleotide phosphate from $NADP^+$ to NADPH. The photosynthetic organism uses NADPH in the Calvin cycle as a high energy molecule to synthesize carbohydrates.

The ultimate source for the electrons in the Z-scheme is water, which is oxidized at the oxygen evolving complex (OEC), a Mn_4CaO_5 cluster situated energetically uphill from P680.[28-30] Oxidation of $P680^*$ to $P680^+$ (*vide supra*) generates the strongest biological oxidizing agent (*ca.* +1.3 V vs. SHE).[31] $P680^+$ recovers an electron by oxidizing a tyrosine residue proximal to the OEC. The OEC is oxidized four times by successive charge separation events, catalyzing the oxidation of two water molecules to one oxygen molecule at a rate of 100-400 s^{-1}.[22,32] However, the OEC and Photosystem II as a whole is susceptible to photodamage, with a quantum yield of photoinhibition on the order of 10^{-7}.[33-34] As a result, photosynthesis at a single site has an average lifetime of less than an hour before it is rendered inoperable.

The overall process of photosynthesis serves as a biological analogue for the water splitting reaction desired for solar fuel utilization, accomplished by coupling a functional unit to absorb light and promote charge separation to catalysts that oxidize

water and store hydrogen. Eight photons are absorbed and converted into the equivalent energy yield of 10 ATP, a photon-to-ATP energy efficiency of *ca.* 32%, but a solar-to-sugar efficiency of up to *ca*. 9%.[35,36] The need for plant organisms to grow ultimately decreases the global photosynthesis energy efficiency to *ca.* 1%.[37] In making the leap from biological inspiration to a practical solar fuel device, three opportunities for improvement can be identified. First, the energy efficiency can be improved by maximizing the photon-to-fuel energy efficiency and minimizing unnecessary anabolic reactions. Second, the enormous complexity of the light-absorbing apparatus can be simplified, ideally taking the form of a monolithic semiconductor component equivalent to a photovoltaic cell. Third, the long term stability of the OEC to photoinhibition is a critical limitation that must be improved, because a technological device must realistically survive for billions of turnovers to be economically viable.

A prototypical model of this yet-unrealized device has three major components, each analogous to the natural photosynthetic system, as illustrated in Figure 1.3. A photosensitizer absorbs light from the sun, generating a photoexcited electron and a virtual hole. The electron and hole are efficiently separated to allow for their independent utilization, with the electron being used in a proton reduction catalyst (PRC) to evolve hydrogen gas, and the hole being used to oxidize water at a water oxidation catalyst (WOC). To minimize the inefficiencies and photoinhibition observed in other systems, the rates of each component must be not only maximized, but also matched to each other, and the interfaces between the components optimized. The considerable challenges inherent in this task are best illustrated by investigating the role of the photosensitizer.

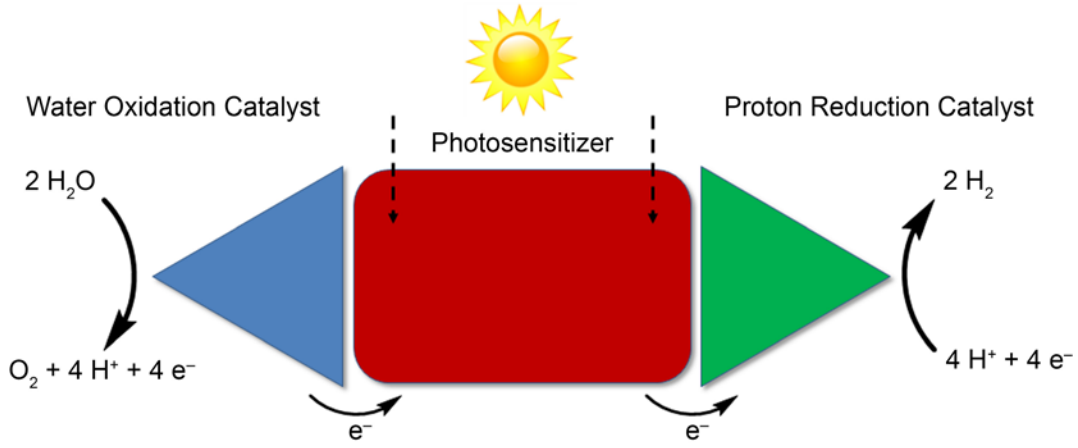

Figure 1.3. A general scheme for triadic solar fuel production. Arrows indicate the flow of energy, electrons, and the catalytic pathways in the system.

1.3 Photosensitizers in Solar Fuel Production

As the critical and central component of a solar fuel device, the photosensitizer has attracted considerable interest from researchers.[20,38] Owing to the exceptional properties of its excited state (*vide infra)*, the ruthenium(II) tris-2,2'-bipyridyl cation, $[Ru(bpy)_3]^{2+}$ (**1.1**), is consistently one of the most extensively studied compounds in the literature.[39] The combination of chemical stability, redox properties, and excited state photochemistry also makes **1.1** a suitable prototypical photosensitizer for solar fuel production.[40-44] As will be demonstrated, the photochemistry of this transition metal complex is reminiscent of the light-absorbing pigments in photosynthesis, and, properly designed and integrated, can serve a similar function.

The unique properties of **1.1** are owed to its molecular and electronic structure (Figure 1.4). Ru^{II} is low-spin d^6 and in a D_3 symmetry (though using O_h symmetry yields qualitatively similar results), coordinated to three bidentate 2,2'-bipyridine (bpy) ligands. Electronic transitions between orbitals largely on the Ru atom lead to metal-centered

(MC) states, while electronic transitions localized in the bpy ligands ($\pi \rightarrow \pi^*$) lead to ligand-centered (LC) states. More interesting are the metal-to-ligand charge transfer (MLCT) transitions between low-lying metal orbitals and bpy ($d \rightarrow \pi^*$). These transitions involve the spatial transfer of electronic charge and are strongly absorbing. The ^{1}MLCT transition at 452 nm in **1.1** is also energetically in the visible spectrum, absorbing a significant amount of energetically favorable energy for solar energy conversion.

Photoexcitation of **1.1** within the ^{1}MLCT transition generates a singlet excited state, which rapidly and efficiently undergoes intersystem crossing (ISC) due to the heavy atom effect to yield the excited triplet state, $[Ru(bpy)_3]^{2+*}$ (**1.1***).[45-47] The resulting ^{3}MLCT state is actually three closely spaced, thermally equilibrated orbitals,[48-51] with a fourth ^{3}MLCT state observed at higher energy.[52] Many of the remarkable properties of **1.1** are the result of the ^{3}MLCT state, which exhibits a long excited state lifetime (τ = 650 ns in water) due to the spin-forbidden transition to the singlet ground state, occurring through phosphorescence centered at 620 nm. Thus, **1.1*** is a molecular analogue of P680 and the electron transport chain in Photosystem II, separating the photoexcited electron from its virtual hole to promote redox chemistry.

The ^{3}MLCT state of **1.1*** has the transient molecular formula $[Ru^{III}(bpy)_2bpy^-]^{2+}$, and exhibits both oxidizing (from photogenerated Ru^{III}, E° = 1.26 V vs. NHE) and reducing (from the photoexcited electron on bpy, E° = -0.84 V vs. NHE) properties greater than the ground state.[43,53,54] These two properties allow **1.1*** to both promote water oxidation by removal of an electron from a WOC to regenerate Ru^{II}, and promote proton reduction by providing the photoexcited electron on bpy^- to a PRC. These processes are illustrated in Figure 1.5, where the desirable forward processes (blue lines)

move electrons from water, through the WOC to **1.1**, undergo photoexcitation to **1.1***, and are transferred to the PRC to generate hydrogen gas.

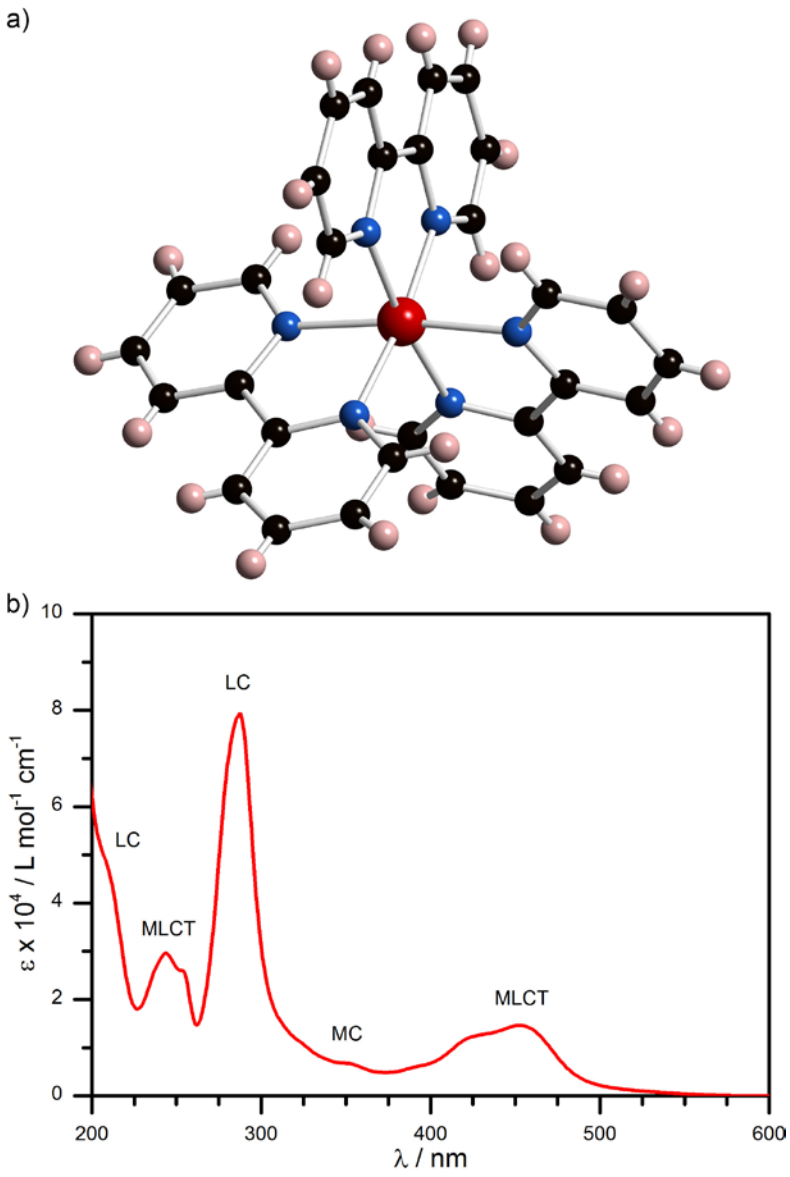

Figure 1.4. The a) molecular structure and b) electronic absorption spectrum of **1.1** in water. The primary electronic transitions are labelled. Color scheme: Ru, red; N, blue; C, black; H, beige.

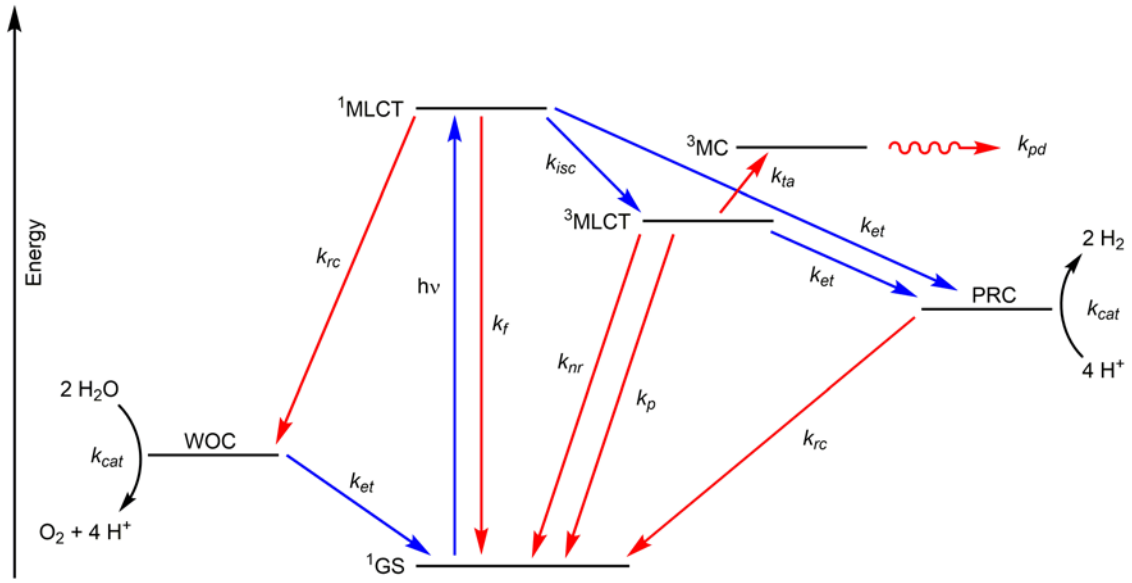

Figure 1.5. Photophysical and photochemical processes in a prototypical photosensitizer for solar fuel production, using **1.1** as a model. Desirable forward processes (blue arrows) must compete with undesirable processes (red arrows) to maximize the efficiency of water oxidation and proton reduction catalysis.

Implicit within Figure 1.5, maximizing the efficiency of a solar fuel device requires that the desirable processes outcompete all undesirable processes, namely recombination, deactivation, and decomposition processes (red lines). Briefly, the photoexcited electron in **1.1** can undergo recombination with the WOC (k_{rc}), nullifying a light absorption event. The same electron could undergo radiative (k_f or k_p) or nonradiative decay (k_{nr}) to the ground state. Likewise, if the ground state Ru^{II} is not regenerated fast enough by the WOC, recombination can occur from the PRC to **1.1** (k_{rc}). In each case, appropriate molecular and system design aim to minimize the rate constants of competitive processes while maximizing the favorable ones.

While **1.1** is widely considered a model photosensitizer, decades of research have been devoted to improving its properties further and correcting its few but notable deficiencies. The MLCT transition of **1.1** absorbs a relatively narrow slice of the solar radiation spectrum capable of promoting water oxidation (Figure 1.6). Substantial research efforts have been made to expand the spectral reach of this class of complexes.[55-58] Of even greater paramount importance is the long-term stability of the photosensitizer, and while **1.1** is generally considered substitutionally inert, the quantum yield of **1.1** *disappearance* in aqueous solution is 10^{-5}-10^{-3}.[40] This disappearance is attributed to thermal activation (k_{ta}) of the ^{3}MC excited state composed of orbitals that are anti-bonding with respect to the Ru-N bonds, leading to photodissociation.[59] The probability of accessing the ^{3}MC state can be minimized by increasing the rate at which the ^{3}MLCT state is quenched (k_{et}), further demonstrating the value of a fast catalyst. Similarly, if the WOC is too slow, the high potential of Ru^{III} will activate the bpy ligands toward nucleophilic addition of hydroxide to a bpy carbon.[60] This leads to repeated and irreversible oxidative damage to the organic ligands of the photosensitizer and photoinhibition, similar to Photosystem II. One potential solution to this problem is to design complexes, both catalysts and photosensitizers, that avoid the use of organic ligands, entirely.

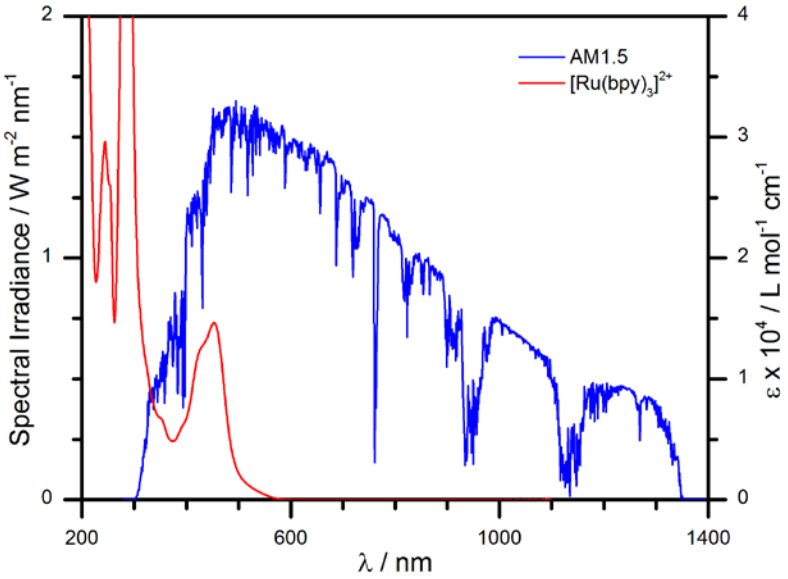

Figure 1.6. Comparison of the solar radiation spectrum at sea level (AM1.5) and the electronic absorption spectrum of **1.1** in water.

1.4 Overview of Polyoxometalate Chemistry

Polyoxometalates (POMs) are a broad and diverse class of discrete transition metal oxoanion clusters.[61-64] These clusters are intermediate species between mononuclear metallic oxides and polymeric (bulk) metal oxides, formed by aggregation and condensation of metal ions in an aqueous environment. Many metal ions dissolve in aqueous solution, and their typical behavior upon acidification results in the precipitation of insoluble neutral oxides or hydroxides. Prior to this point, however, equilibria exist in which monomeric species spontaneously aggregate through condensation reactions:

$$7\,[WO_4]^{2-}_{(aq)} + 8\,H^{+}_{(aq)} \rightarrow [W_7O_{24}]^{6-}_{(aq)} + 4\,H_2O_{(l)} \qquad (1.5)$$

A POM consisting of a single metallic element is called an isopolymetalate or isopolyanion. The condensation reaction can also occur in the presence of another soluble species, in which case the latter, called a heteroatom, is incorporated into a heteropolyoxometalate, or heteropolyanion:

$$12\ [WO_4]^{2-}_{(aq)} + H_3PO_{4(aq)} + 21\ H^+_{(aq)} \rightarrow [PW_{12}O_{40}]^{3-}_{(aq)} + 12\ H_2O_{(l)} \qquad (1.6)$$

An enormous variety of POMs can be formed as a result of the properties the metallic and nonmetallic elements of which they are composed. POMs are notable for the general absence of carbon in their structures, a strong contrast to the ubiquity of organic structures otherwise. In the broadest sense, POMs are found in two regions of the periodic table, the early transition metals and a number of p-block metalloids. However, the chemical properties of these two regions differ, and while the latter group tends to form open structures susceptible to oligomerization, the former forms closed clusters bounded by weakly nucleophilic oxygens. As a result, there are five principal metal elements that compose the majority of POMs structures, termed addenda atoms, shown in Figure 1.7.

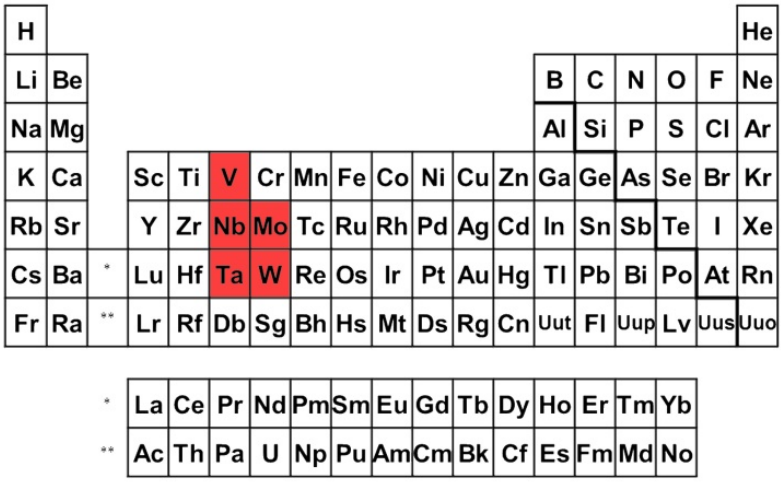

Figure 1.7. The principal metal elements, highlighted in red, that form most discrete polyoxometalate complexes.

While the diversity of POMs is vast, there are a number of properties common to most structures. The addenda atoms of POMs are typically in their highest oxidation states (d^0; e.g. W^{VI}, Mo^{VI}, V^{V}). The addenda atoms tend to aggregate as polyhedra, favoring octahedral coordination. Heteroatoms may exist in several geometries depending on the structure, such as tetrahedral, square pyramidal, or octahedral. The diversity of structures possible in POMs is largely a function of their ability to include heteroatoms and other elements that substitute for one or more addenda atoms. POMs have been characterized with more than 25 different heteroatoms, and most of the elements in the periodic table can be substituted for addenda atoms in their structures (Figure 1.8).

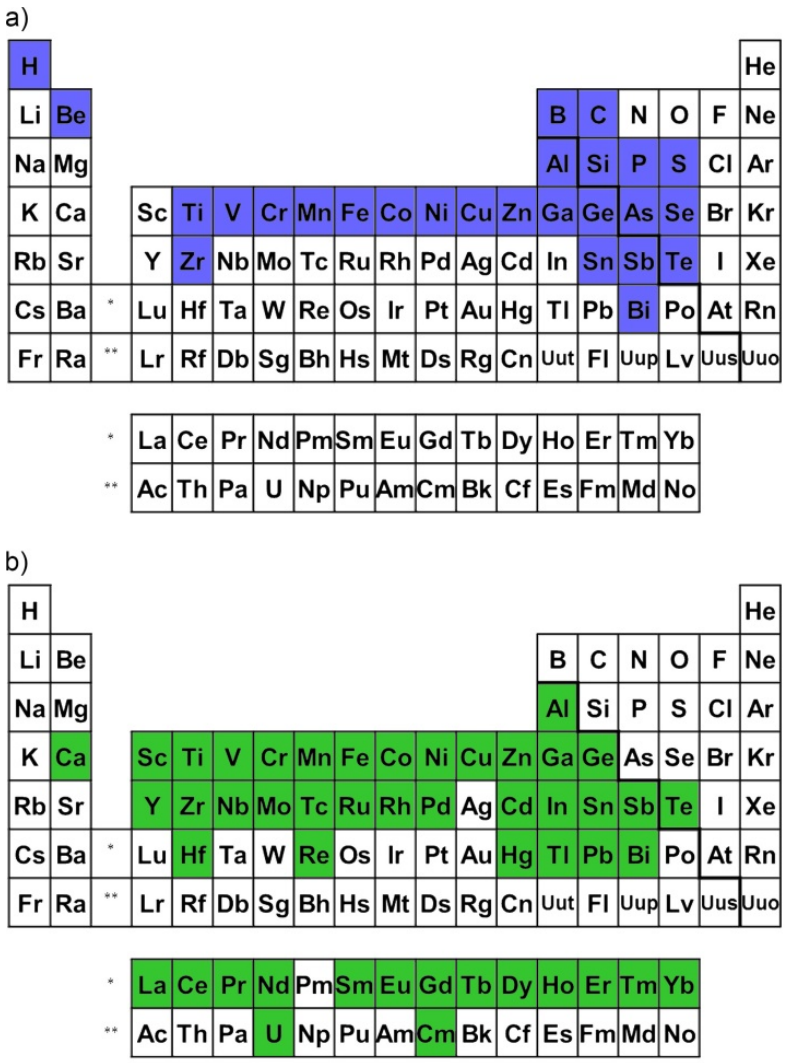

Figure 1.8. The known elements of the periodic table that have been found in polyoxometalate complexes as: a) heteroatoms, highlighted in blue, structurally significant atoms around which oxometallic groups condense; b) substituted metals, highlighted in green, that replace an addenda metal.

Synthesis of POMs is most frequently and conveniently performed in an aqueous mixture of the addenda oxoanion and heteroatom. Careful control of the reaction conditions allows for the predominance of one species over others in the equilibrium,

affording appreciable yields. Several factors influence this, chief among them the stoichiometric ratio of constituents, concentration, temperature, pH, solvent conditions, reaction time, and the nature of any counterions present. POMs can be precipitated or crystallized from solution by the addition of appropriate alkali metal countercations (e.g. Na^+, K^+, Rb^+, Cs^+); the introduction of alkylammonium cations or other organic ions affords solubility in a number of organic solvents.

The discovery of POMs is credited to Berzelius in 1826, but only a handful of compounds were known until the 20th century.[65] The invention of more advanced analytical and synthetic techniques, and in particular X-ray crystallography, allowed for the unambiguous determination of POM molecular structures. Given the large number of atoms often present in a given POM, and a three-dimensional structure that defies conventional naming conventions, many structures are given names attributed to the discoverer of the structural class (e.g. Keggin,[66,67] Wells-Dawson,[68] Lindqvist,[69] Weakley,[70] Preyssler[71,72]; see Figure 1.9 for a few examples). The routine use of X-ray diffraction methods in chemical research has led to the explosive growth of new POM compounds in the last few decades, with well over ten thousand compounds known to date. As a class of compounds between the extremes of mononuclear metal ions and bulk metal oxides/semiconductors, POMs have contributed to many fields, including analytical methods, catalysis, energy storage and conversion, magnetism, and medicine.[73,74]

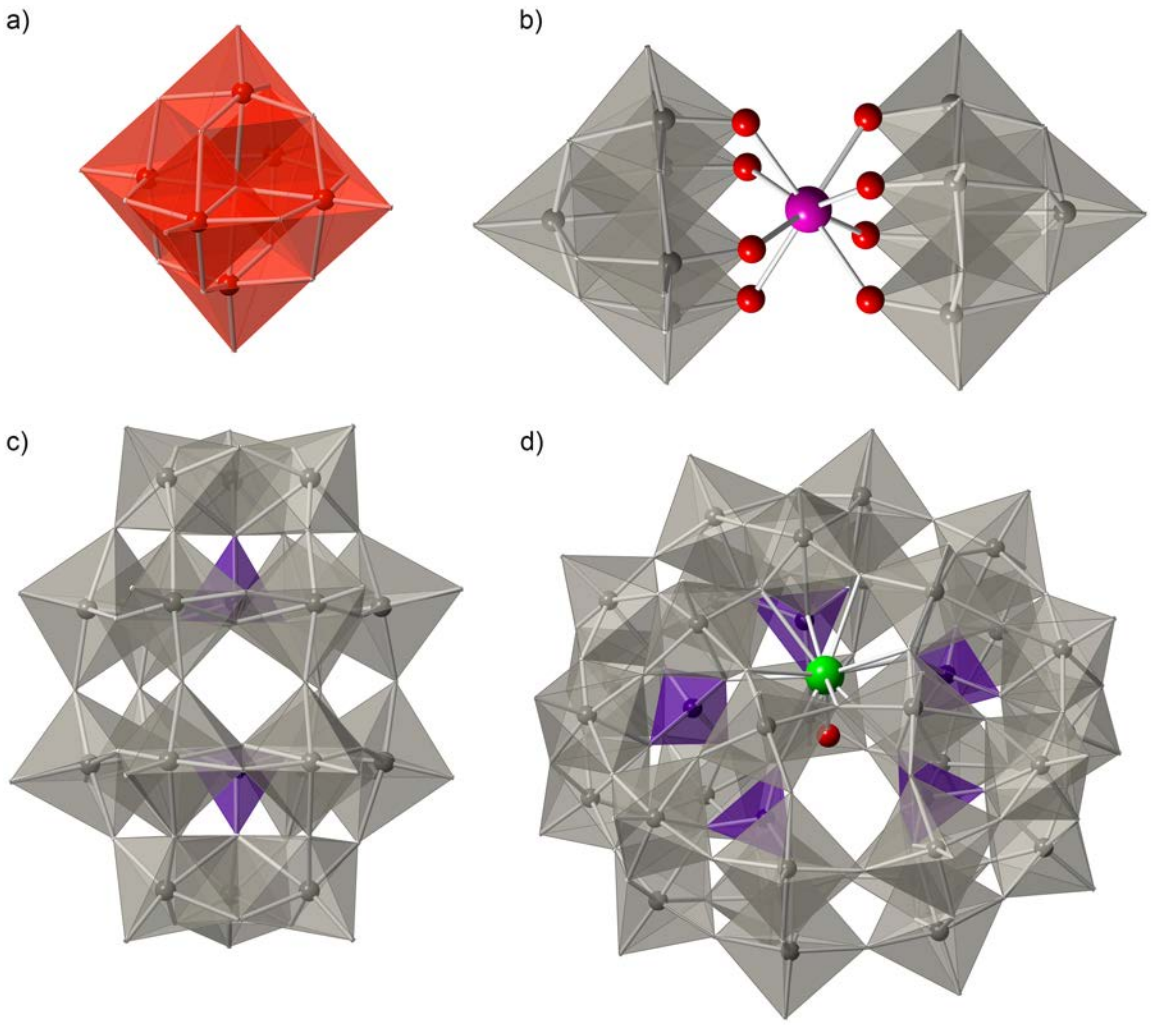

Figure 1.9. Four representative examples of polyoxometalate structures in mixed polyhedral notation: a) the Lindqvist anion, $[V_6O_{19}]^{8-}$; b) the Weakley-Yamase structure, $[Eu(W_5O_{18})_2]^{9-}$; c) the Wells-Dawson anion, $[P_2W_{18}O_{62}]^{6-}$; d) the Preyssler anion, $[U(H_2O)P_5W_{30}O_{110}]^{11-}$. Color scheme: W, grey; V, dark red; P, purple; Eu, magenta; U, green; O, red.

The breadth of the polyoxometalate field makes it difficult to render a full review of their structures and properties. Instead, the structure and some key properties of one representative POM, the Keggin anion, will be discussed. Keggin-type POMs have the

general formula $[XM_{12}O_{40}]^{n-}$, where X is the heteroatom and M is Mo or W. The Keggin structure can have a number of heteroatoms, but by far the most common are those where X = P^{V}, Si^{IV}, and Ge^{IV}. The structure of a representative Keggin, $[SiW_{12}O_{40}]^{4-}$ (**1.2**), is represented in Figure 1.10, in both the traditional ball-and-stick notation and the more common polyhedral notation. The structure has overall T_d symmetry, and is composed of a tetrahedrally coordinated heteratom encapsulated within twelve symmetrically-equivalent tungsten octahedra. The twelve tungsten atoms are arranged in four W_3O_{13} units, within which the tungsten octahedral are edge-sharing, while adjacent W_3O_{13} units are corner-sharing. Each tungsten atom is in a pseudo-octahedral local symmetry, with five single bonds to oxygen atoms and one doubly-bound terminal oxygen.

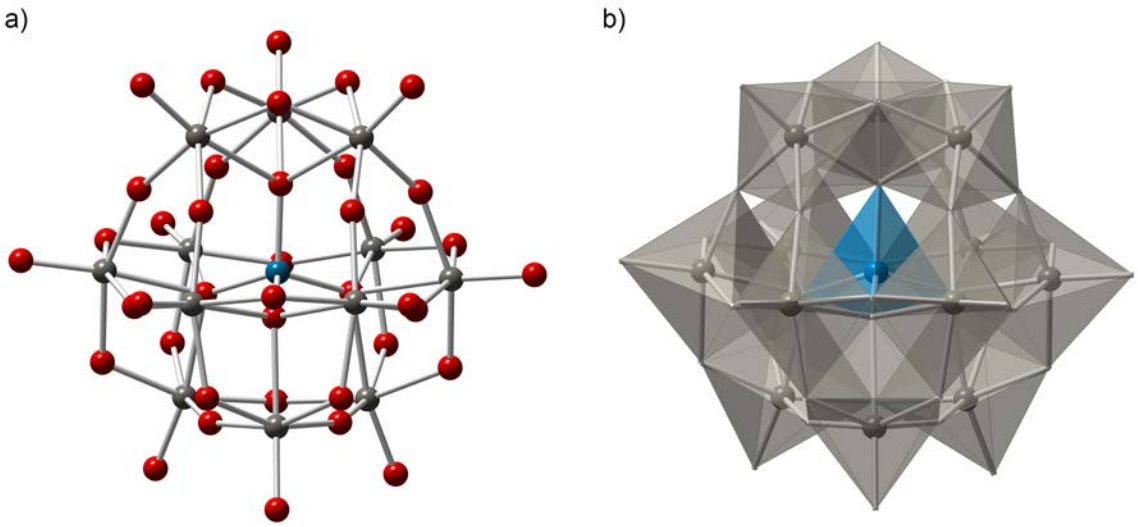

Figure 1.10. A representative example of the Keggin POM structure, $[SiW_{12}O_{40}]^{4-}$ (**1.2**), in ball-and-stick (left) and polyhedral notation (right). Color scheme: W, grey; Si, cyan; O, red.

The structure of **1.2** as described is one of five geometric isomers of the Keggin structure, denoted the α-isomer, or $[\alpha\text{-}SiW_{12}O_{40}]^{4-}$. Another geometric isomer, the β-isomer, is identical with the exception of one W_3O_{13} unit, which is rotated 60° relative to the rest of the structure. Additional isomers (γ, δ, and ε) are conceptually formed by rotating the remaining three W_3O_{13} units by 60°.[75] The α-isomer is exclusively the thermodynamically most stable isomer of the Keggin structure, with successive isomers being more difficult to isolate. Each isomer has unique structural, spectroscopic, and catalytic properties, and a number of papers have been published attempting to delineate them in a systematic fashion.[76-88] Because the α-isomer is the most stable, and in many cases, the only isolable isomer, further discussion will assume this isomer unless otherwise noted.

In aqueous solution, **1.2** is stable below pH 4.5.[89] As the pH of the solution increases, however, hydrolysis reactions take place, slowly reversing the original formation by condensation. The first species to be obtained from this reaction is that of $[SiW_{11}O_{39}]^{8-}$, a Keggin structure in which one $[W{=}O]^{4+}$ unit has been removed. This removal leaves a gap in the structure, exposing five oxygen atoms, and is referred to as a lacunary structure, with the parent structure called a plenary structure. Further increases in pH yield the trivacant species $[SiW_9O_{34}]^{9-}$, followed by complete decomposition to the simple monometallic oxoanions. Starting from $[SiW_9O_{34}]^{9-}$, acidification of the solution yields the reverse process, eventually reforming **1.2**.

The ability for POMs to form lacunary structures greatly expands the range of possible compounds. The five exposed oxygen atoms in $[SiW_{11}O_{39}]^{8-}$ are strongly basic, making them the starting point for further condensation reactions.[64] These oxygen atoms

will bind to many metal cations, effectively turning the POM into a large, inorganic pentadentate or tetradentate ligand. POMs where a transition metal has replaced a tungsten-oxo group are called transition metal-substituted polyoxometalates (TMSPs). The binding modes, bond strength, and other properties of TMSPs are analogous to metalloporphyrins, and have been frequently studied to that effect.[90-101] Unlike porphyrins, however, POMs are stable against oxidative decomposition, an advantage in catalytic processes.[102] Figure 1.11 illustrates the structure and metal binding of a lacunary POM to form a TMSP species.

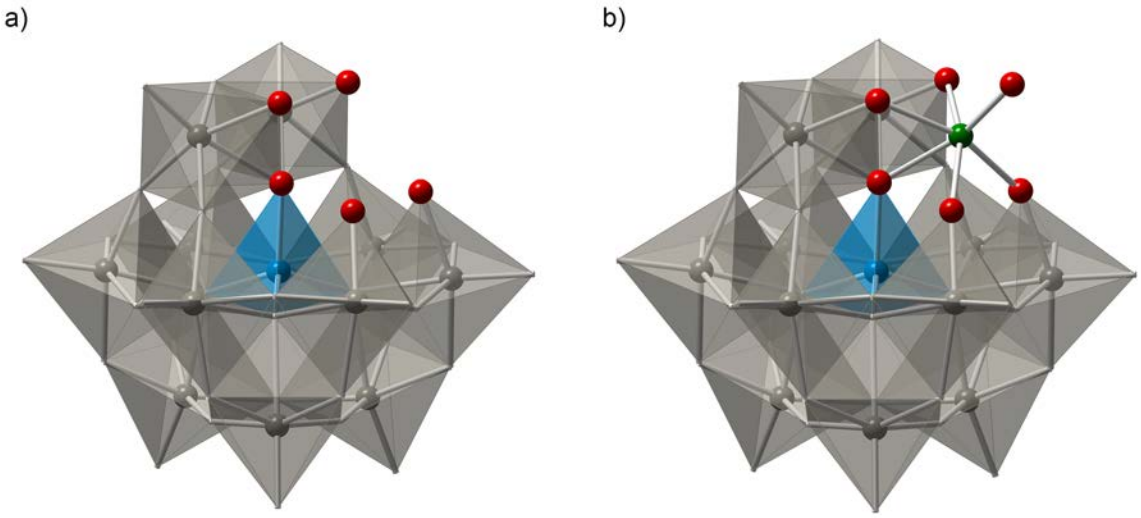

Figure 1.11. Representative examples of a lacunary Keggin POM structure, $[SiW_{11}O_{39}]^{8-}$, and a TMSP, $[SiNi(H_2O)W_{11}O_{39}]^{6-}$, in mixed polyhedral notation. The oxygen atoms exposed in the lacunary structure and bound to a metal cation in the TMSP are visible. Color scheme: W, grey; Si, cyan; Ni, green; O, red.

The physical and chemical properties of POMs have been extensively studied, and in the context of solar fuel production, the light-absorbing, photochemical, and photophysical properties are worth noting.[103-106] Because many POMs are composed of transition metals in their highest oxidation states, the electronic structure of these POMs is relatively simple. For example, **1.2** contains only Si^{IV} (d^0), W^{VI} (d^0), and oxygen, resulting in low-lying filled oxygen orbitals (the HOMO), and empty metal orbitals at higher energy (the LUMO). As a result, the electronic absorption spectrum of **1.2** (Figure 1.12b) is dominated by two intense LMCT ($O_{2p} \rightarrow W_{5d}$) transitions in the UV region. In the absence of d-electron containing metals, POMs are white (colorless in solution) or pale-yellow if the LMCT bands tail significantly into the visible region. When lower oxidation state metals are present, the POMs exhibit color due to d-d bands, and lower energy charge transfer bands that are either LMCT, metal-to-metal charge transfer (MMCT), or intervalence charge transfer (IVCT) in character may contribute to the visible absorption spectrum.

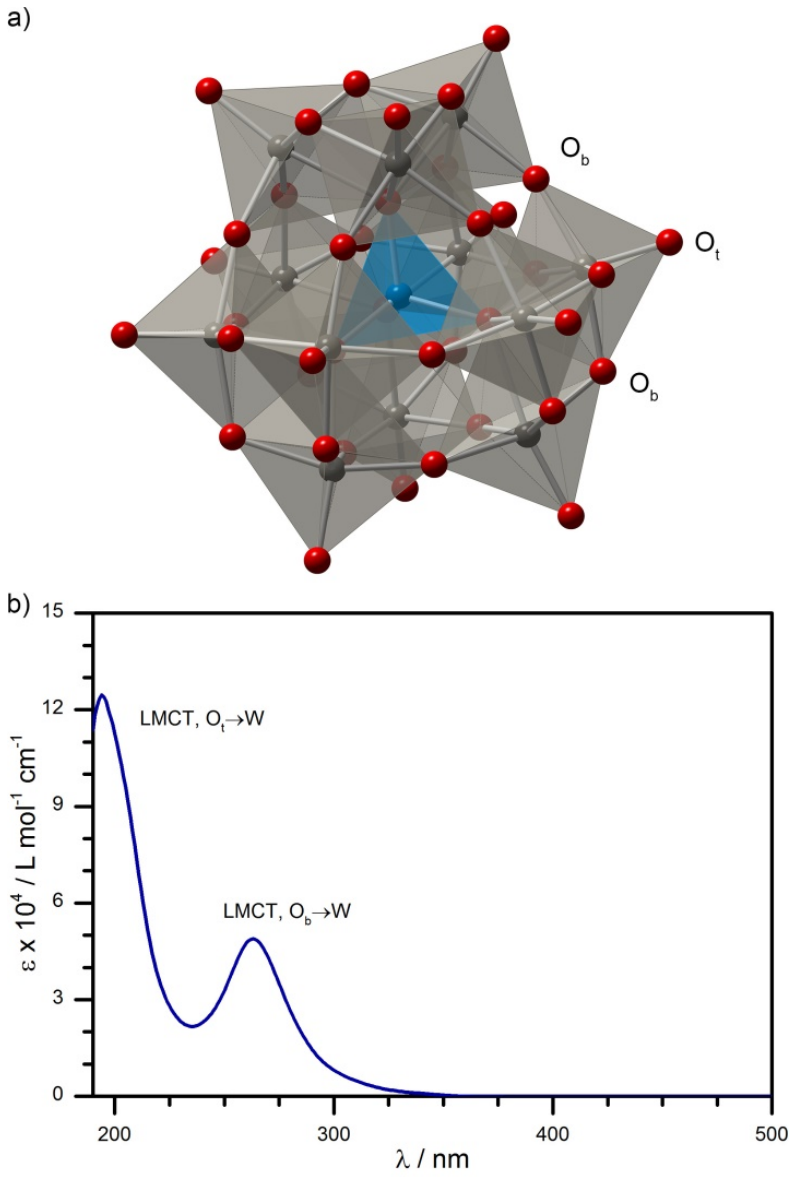

Figure 1.12. The molecular structure (top) and electronic absorption spectrum of **1.2** in water (bottom). The electronic transitions are labelled, with the corresponding oxygen atoms noted in the molecular structure. Color scheme: W, grey; Si, cyan; O, red.

The photochemistry of POMs, typically in the UV, has been studied since 1916,[107] and has been extensively reviewed in the literature.[108-110] Upon photoexcitation of the LMCT bands, an electron is promoted from the oxygen-centered HOMO to the tungsten-centered LUMO.[111] The excited states typically exhibit oxygen-centered radical character and readily oxidize organic substrates. The resulting POM species contains an electron that is delocalized across equivalent metal-centered orbitals, resulting in intense IVCT ($W^{V} \rightarrow W^{VI}$) bands in the visible and NIR.[112-114] These states are broadly classified as "heteropoly blues" in polyoxotungstates and "heteropoly browns" in polyoxomolybdates based on their intense color. The same states can be generated and studied electrochemically.[115-119] Much like the prototypical photosensitizer $[Ru(bpy)_3]^{2+}$ (**1.1**), there is an active interest in developing the means of exploiting the excited states of POMs for their catalytic and light-absorbing properties.

1.5 Applications of Polyoxometalates in Solar Fuels Production

The pursuit of efficient catalysts and photosensitizers for a viable solar fuel device has driven researchers to develop many creative approaches over the course of several decades. Since the first demonstration of photoelectrochemical water oxidation on TiO_2 in 1972, a number of heterogeneous metal oxide systems have been developed.[120-123] Similarly, the initial report of a homogeneous ruthenium-based WOC in 1982, the "blue dimer,"[124] led to a large amount of interest in homogeneous water oxidation systems.[22,125-128] Both approaches have their merits. As a class that blurs the lines between molecular and bulk systems, POMs combine some of the advantages of both approaches.

General interest in the catalytic properties of POMs grew substantially in 2008, when the first all-inorganic POM WOC, $[\{Ru^{IV}_4O_4(OH)_2(H_2O)_4\}(\gamma\text{-}SiW_{10}O_{36})_2]^{10-}$, containing a tetraruthenium core reminiscent of the OEC, was reported.[129,130] Subsequent reports elaborated on the mechanism of water oxidation, and demonstrated homogeneous light-driven water oxidation activity using $[Ru(bpy)_3]^{2+}$ as a photosensitizer.[131-134] Reports of other POM WOCs containing iridium and ruthenium quickly followed.[135,136] Significant improvements in catalytic activity and quantum yield were achieved when $[Co_4(H_2O)_2(PW_9O_{34})_2]^{10-}$, a POM WOC composed of more abundant cobalt atoms, was reported.[137,138] Further advances in the field have come quickly, expanding the range of transition metals,[139] applications, [140-143] and water oxidation activity,[144] details of which have been recently reviewed.[145,146] On the opposite side of the solar fuel production scheme, POMs have also been investigated for their catalytic activity towards proton reduction.[147-150] With this flurry of research activity, POMs have been used as components in two of the three components of a solar fuels device.

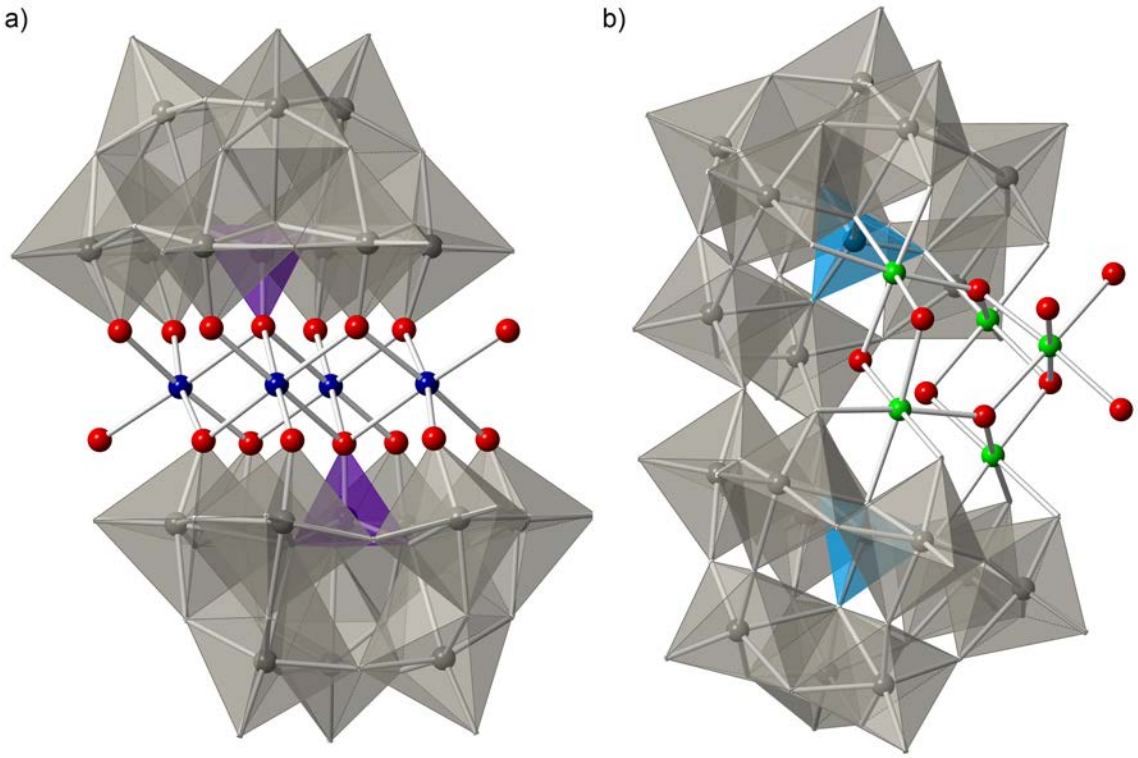

Figure 1.13. Two polyoxometalate water oxidation catalysts in mixed polyhedral notation: a) $[Co_4(H_2O)_2(PW_9O_{34})_2]^{10-}$, and b) $[Ni_5(OH)_6(OH_2)_3(Si_2W_{18}O_{66})]^{12-}$. Color scheme: W, grey; P, purple; Si, cyan; Co, blue; Ni, green; O, red.

In a research setting, most homogeneous light-driven water oxidation is driven by $[Ru(bpy)_3]^{2+}$ as a photosensitizer, a well-studied system.[151-153] The ^{3}MLCT excited state is quenched by a sacrificial electron acceptor, such as $S_2O_8^{2-}$, which generates $[Ru(bpy)_3]^{3+}$ and $SO_4^{\bullet-}$ (a sulfate radical). The sulfate radical generates a second molecule of $[Ru(bpy)_3]^{3+}$, building up four hole equivalents with which the WOC oxidizes water. The rate of oxygen evolution can be measured in several ways, such as by gas chromatography (Figure 1.14). It is worth noting that this system contains three powerful oxidants ($SO_4^{\bullet-}$, E° = 2.7 V vs. NHE; $S_2O_8^{2-}$, E° = 2.1 V vs. NHE; $[Ru(bpy)_3]^{3+,}$ E° = 1.26 V vs. NHE)[53,54,154] in the presence of organic ligands, leaving them susceptible to

oxidative photoinhibition. The need for photosensitizers resistant to these oxidative conditions encourages the expansion of POM chemistry into this challenging area.

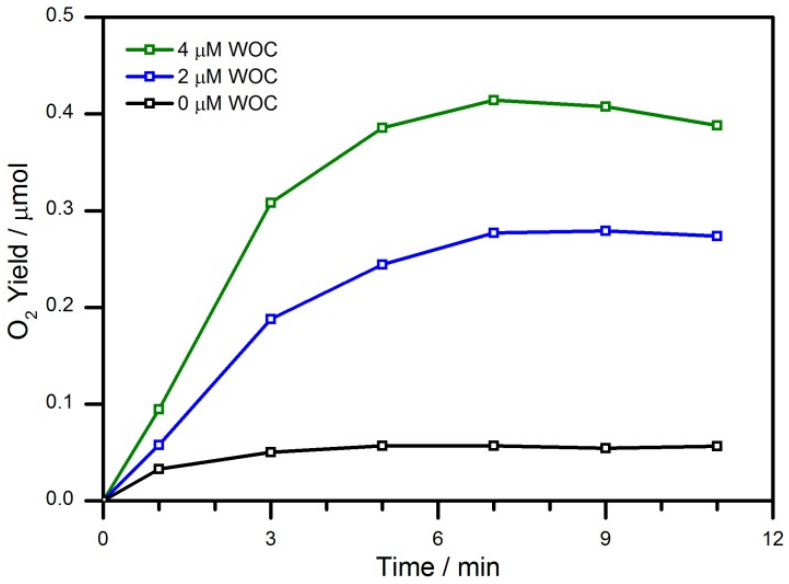

Figure 1.14. Kinetics of light-driven catalytic oxygen evolution from water oxidation by $[Ni_5(OH)_6(OH_2)_3(Si_2W_{18}O_{66})]^{12-}$, at 4 μM (green), 2 μM (blue), and 0 μM (black, control). Conditions: 455 nm LED light (17 mW, beam diameter ~0.5 cm), 1.0 mM $[Ru(bpy)_3]Cl_2$, 5.0 mM $Na_2S_2O_8$, 80 mM sodium borate buffer (pH 8.0), total volume 2.0 mL. Oxygen detected by gas chromatographic analysis of the cuvette headspace.

To this end, efforts to develop photosensitizers absent of organic ligands have led to the investigation of heterogeneous bimetallic assemblies that exploit metal-to-metal charge transfer (MMCT) excited states. These novel systems exhibit absorption bands in the visible region, and have demonstrated the ability to facilitate multielectron catalytic reactions.[155-168] In a similar fashion, POMs have been utilized for this purpose as well, by anchoring Keggin POMs and Ce^{III} ions on a mesoporous silica surface.[169,170] The

resulting heterogeneous assemblies exhibit electronic transitions ($Ce^{III} \rightarrow W^{VI}$) in the visible region and excited states characterized by an oxidized metal and a reduced polytungstate ("heteropoly blues," *vide supra*).

Molecular POM analogues of bimetallic heterogeneous assemblies have been recently investigated as potential visible light photosensitizers. The first POM-based chromophore of this class, $[P_4W_{35}O_{124}\{Re(CO)_3\}_2]^{16-}$ (Figure 1.15a), was found to have a very short excited state lifetime of only 1.4 ps ($k_{obs} \sim 7\times10^{11}$ s^{-1}) following photoexcitation.[171] This short lifetime, the consequence of high rates of undesirable recombination and nonradiative photophysical processes, make it difficult for the bimolecular electron transfer reactions necessary for catalytic reactions to effectively compete (Figure 1.5). The photocatalytic activity of another POM chromophore, $[\{Ce(H_2O)\}_2\{Ce(CH_3CN)\}_2(\mu_4\text{-}O)(\gamma\text{-}SiW_{10}O_{36})_2]^{6-}$ (Figure 1.15b) towards oxidative dehydrogenation and hydrogen evolution has been recently reported, though no detailed investigations of its photophysical properties have been made to date.[172,173] A better understanding of the fundamental photophysical properties of POMs will permit the rational development of stable photosensitizers for solar fuel production.

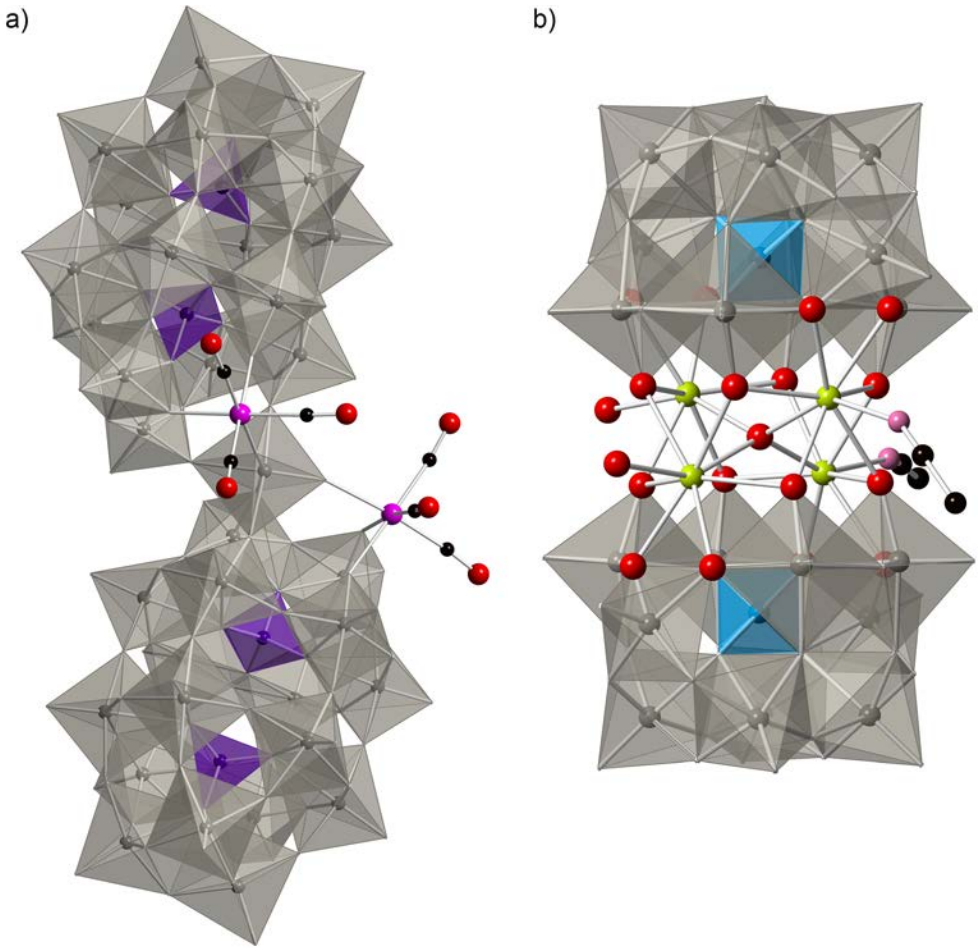

Figure 1.15. Two representative polyoxometalates studied as potential photocatalysts, in mixed ball-and-stick/polyhedral notation: a) $[P_4W_{35}O_{124}\{Re(CO)_3\}_2]^{16-}$, and b) $[\{Ce(H_2O)\}_2\{Ce(CH_3CN)\}_2(\mu_4\text{-}O)(\gamma\text{-}SiW_{10}O_{36})_2]^{6-}$. Color scheme: W, grey; P, purple; Si, cyan; Re, magenta; Ce, yellow; C, black; N, pink; O, red.

1.6 Goal of This Work and Outline

The central motivation of this work is to identify the underlying photophysical properties of visible-light absorbing POM complexes, in an effort to extend their excited state lifetimes in a rational manner. To accomplish this, target compounds were synthesized and their properties investigated using a variety of experimental techniques, including ultrafast pump-probe transient absorption spectroscopy. Computational results were used to support the conclusions obtained through experimental techniques.

In Chapter 2, the electronic structure and excited state dynamics of four cobalt-containing Keggin POMs is reported. A rational investigation of the coordination geometry and oxidation state of these POMs identifies one complex, $[Co^{II}W_{12}O_{40}]^{6-}$, with a longer-lived excited state generated through an MPCT transition. The long-lived excited state ascribed to a transient structural change and charge localization within the POM. In Chapter 3, an eight-complex series of TMSPs, $[Co^{II}(M^{x}OH_{y})W_{11}O_{39}]^{(12-x-y)-}$ ($M^{x}OH_{y}$ = $V^{IV}O$, $Cr^{III}(OH_2)$, $Mn^{II}(OH_2)$, $Fe^{III}(OH_2)$, $Co^{II}(OH_2)$, $Ni^{II}(OH_2)$, $Cu^{II}(OH_2)$, $Zn^{II}(OH_2)$), is synthesized to study the influence of substituted transition metals on their electronic properties and excited state lifetimes. Substitution within these complexes modulates their light absorption properties, but decreases their excited state lifetimes.

In Chapter 4, the synthesis, structure, and excited state dynamics of three tin-containing POMs are described. A charge transfer transition in one of the reported complexes is attributed to an interaction between antimony and tin ions in the structure.

In Chapter 5, the structure and photodynamics of two POM chromophores are investigated. These complexes are representative of the types of visible light-absorbing POMs reported previously in the literature and exhibit short-lived excited states.

1.7 References

(1) Ehrlich, P. R.; Holdren, J. P. *Science* **1971**, *171*, 1212.

(2) O'Neill, B. C.; MacKellar, F. L.; Lutz, W. In *The End of World Population Growth in the 21st Century: New Challenges for Human Capital Formation and Sustainable Development*; Lutz, W., Sanderson, W. C., Scherbov, S., Eds.; Earthscan: London, UK, 2004, p 283.

(3) *World Development Indicators*, The World Bank, 2015.

(4) *International Energy Statistics*, U.S. Energy Information Administration, 2012.

(5) *International Financial Statistics*, International Monetary Fund, 2011.

(6) *Key World Energy Statistics*, International Energy Agency, 2015.

(7) Cook, T. R.; Dogutan, D. K.; Reece, S. Y.; Surendranath, Y.; Teets, T. S.; Nocera, D. G. *Chem. Rev.* **2010**, *110*, 6474.

(8) Lewis, N. S.; Nocera, D. G. *Proc. Natl. Acad. Sci.* **2006**, *103(43)*, 15729.

(9) *BP Statistical Review of World Energy: June 2015*, British Petroleum, 2015.

(10) *IPCC, 2014: Climate Change 2014: Synthesis Report. Contribution of Working Groups I, II and III to the Fifth Assessment Report of the Intergovernmental Panel on Climate Change*; Intergovernmental Panel on Climate Change: Geneva, Switzerland, 2014.

(11) Kopp, G.; Lean, J. L. *Geophys. Res. Lett.* **2011**, *38*.

(12) ASTM G173-03(2012), Standard Tables for Reference Solar Spectral Irradiances: Direct Normal and Hemispherical on 37° Tilted Surface, ASTM International, West Conshohocken, PA, 2012, www.astm.org.

(13) McCusker, J. K. *Science* **2001**, *293*, 1599.

(14) Heyduk, A. F.; Nocera, D. G. *Science* **2001**, *293*, 1639.

(15) Benson, E. E.; Kubiak, C. P.; Sathrum, A. J.; Smieja, J. M. *Chem. Soc. Rev.* **2009**, *38*, 89.

(16) Costentin, C.; Robert, M.; Saveant, J.-M. *Chem. Soc. Rev.* **2013**, *42*, 2423.

(17) Finn, C.; Schnittger, S.; Yellowlees, L. J.; Love, J. B. *Chem. Commun.* **2012**, *48*, 1392.

(18) Oh, Y.; Hu, X. *Chem. Soc. Rev.* **2013**, *42*, 2253.

(19) Ciamician, G. *Science* **1912**, *36*, 385.

(20) Grätzel, M. *Nature* **2001**, *414*, 338.

(21) Meyer, T. *Acc. Chem. Res.* **1989**, *22*, 163.

(22) Rüttinger, W.; Dismukes, G. C. *Chem. Rev.* **1997**, *97*, 1.

(23) Gust, D.; Moore, T. A.; Moore, A. L. *Acc. Chem. Res.* **2009**, *42*, 1890.

(24) Barber, J. *Chem. Soc. Rev.* **2009**, *38*, 185.

(25) Duan, L.; Bozoglian, F.; Mandal, S.; Stewart, B.; Privalov, T.; Llobet, A.; Sun, L. *Nat. Chem.* **2012**, *4*, 418.

(26) Kalisman, P.; Nakibli, Y.; Amirav, L. *Nano Lett.* **2016**, *16*, 1776.

(27) Fujishima, A.; Honda, K. *Nature* **1972**, *238*, 37.

(28) Umena, Y.; Kawakami, K.; Shen, J.-R.; Kamiya, N. *Nature* **2011**, *473*, 55.

(29) Pushkar, Y.; Yano, J.; Sauer, K.; Boussac, A.; Yachandra, V. K. *Proc. Natl. Acad. Sci.* **2008**, *105*, 1879.

(30) Ferreira, K. N.; Iverson, T. M.; Maghlaoui, K.; Barber, J.; Iwata, S. *Science* **2004**, *303*, 1831.

(31) Rappaport, F.; Guergova-Kuras, M.; Nixon, P. J.; Diner, B. A.; Lavergne, J. *Biochemistry* **2002**, *41*, 8518.

(32) Dismukes, G. C.; Brimblecombe, R.; Felton, G. A. N.; Pryadun, R. S.; Sheats, J. E.; Spiccia, L.; Swiegers, G. F. *Acc. Chem. Res.* **2009**, *42*, 1935.

(33) Tyystjärvi, E. *Coord. Chem. Rev.* **2008**, *252*, 361.

(34) Ohnishi, N.; Allakhverdiev, S. I.; Takahashi, S.; Higashi, S.; Watanabe, M.; Nishiyama, Y.; Murata, N. *Biochemistry* **2005**, *44*, 8494.

(35) Hall, D. O.; Rao, K. *Photosynthesis*; Cambridge University Press: New York, NY, 1999.

(36) *Renewable biological systems for alternative sustainable energy production (FAO Agricultural Services Bulletin - 128)*; Food and Agriculture Organization of the United Nations: Osaka University, Osaka, Japan, 1997.

(37) Pisciotta, J. M.; Zou, Y.; Baskakov, I. V. *PLoS One* **2010**, *5*, e10821.

(38) Hagfeldt, A.; Boschloo, G.; Sun, L.; Kloo, L.; Pettersson, H. *Chem. Rev.* **2010**, *110*, 6595.

(39) Watts, R. J. *J. Chem. Educ.* **1983**, *60*, 834.

(40) Juris, A.; Balzani, V.; Barigelletti, F.; Campagna, S.; Belser, P.; von Zelewsky, A. *Coord. Chem. Rev.* **1988**, *84*, 85.

(41) Treadway, J. A.; Loeb, B.; Lopez, R.; Anderson, P. A.; Keene, F. R.; Meyer, T. J. *Inorg. Chem.* **1996**, *35*, 2242.

(42) Balzani, V.; Juris, A.; Venturi, M.; Campagna, S.; Serroni, S. *Chem. Rev.* **1996**, *96*, 759.

(43) Kalyanasundaram, K. *Coord. Chem. Rev.* **1982**, *46*, 159.

(44) Kutal, C. *J. Chem. Educ.* **1983**, *60*, 882.

(45) Demas, J. N.; Taylor, D. G. *Inorg. Chem.* **1979**, *18*, 3177.

(46) Damrauer, N. H.; Cerullo, G.; Yeh, A.; Boussie, T. R.; Shank, C. V.; McCusker, J. K. *Science* **1997**, *275*, 54.

(47) Yeh, A. T.; Shank, C. V.; McCusker, J. K. *Science* **2000**, *289*, 935.

(48) Hager, G. D.; Watts, R. J.; Crosby, G. A. *J. Am. Chem. Soc.* **1975**, *97*, 7037.

(49) Hager, G. D.; Crosby, G. A. *J. Am. Chem. Soc.* **1975**, *97*, 7031.

(50) Crosby, G. A.; Hipps, K. W.; Elfring, W. H. *J. Am. Chem. Soc.* **1974**, *96*, 629.

(51) Crosby, G. A.; Demas, J. N. *J. Am. Chem. Soc.* **1971**, *93*, 2841.

(52) Lumpkin, R. S.; Kober, E. M.; Worl, L. A.; Murtaza, Z.; Meyer, T. J. *J. Phys. Chem.* **1990**, *94*, 239.

(53) Creutz, C.; Sutin, N. *Inorg. Chem.* **1976**, *15*, 496.

(54) Bock, C. R.; Connor, J. A.; Gutierrez, A. R.; Meyer, T. J.; Whitten, D. G.; Sullivan, B. P.; Nagle, J. K. *J. Am. Chem. Soc.* **1979**, *101*, 4815.

(55) Li, G.; Ray, L.; Glass, E. N.; Kovnir, K.; Khoroshutin, A.; Gorelsky, S. I.; Shatruk, M. *Inorg. Chem.* **2012**, *51*, 1614.

(56) Li, G.; Bomben, P. G.; Robson, K. C. D.; Gorelsky, S. I.; Berlinguette, C. P.; Shatruk, M. *Chem. Commun.* **2012**, *48*, 8790.

(57) Li, G.; Hu, K.; Yi, C.; Knappenberger, K. L.; Meyer, G. J.; Gorelsky, S. I.; Shatruk, M. *J. Phys. Chem. C* **2013**, *117*, 17399.

(58) Li, G.; Hu, K.; Robson, K. C. D.; Gorelsky, S. I.; Meyer, G. J.; Berlinguette, C. P.; Shatruk, M. *Chem. Eur. J.* **2015**, *21*, 2173.

(59) Salassa, L.; Garino, C.; Salassa, G.; Gobetto, R.; Nervi, C. *J. Am. Chem. Soc.* **2008**, *130*, 9590.

(60) Ghosh, P. K.; Brunschwig, B. S.; Chou, M.; Creutz, C.; Sutin, N. *J. Am. Chem. Soc.* **1984**, *106*, 4772.

(61) Pope, M. T. *Heteropoly and Isopoly Oxometalates*; Springer-Verlag: Berlin, 1983.

(62) *Polyoxometalates: From Platonic Solids to Anti-retroviral Activity*; Pope, M. T.; Müller, A., Eds.; Kluwer Academic Publishers: Dordrecht, Netherlands, 1993.

(63) *Polyoxometalate Chemistry From Topology via Self-Assembly to Applications*; Pope, M. T.; Müller, A., Eds.; Kluwer Academic Publishers: Dordrecht, 2001.

(64) Borrás-Almenar, J. J.; Coronado, E.; Müller, A.; Pope, M. T. *Polyoxometalate Molecular Science. Proceedings of the NATO Advanced Study Institute, Tenerife, Spain from 25 August to 4 September 2001*; Kluwer Academic Publishers: Dordrecht, 2003; Vol. 98.

(65) Berzelius, J. J. *Poggendorfs Ann. Phys. Chem.* **1826**, *6*, 369.

(66) Keggin, J. F. *Nature* **1933**, *131*, 908.

(67) Keggin, J. F. *Proc. R. Soc. Lond. A* **1934**, *144*, 75.

(68) Dawson, B. *Acta Crystallogr., Sect. B: Struct. Sci.* **1953**, *6*, 113.

(69) Lindqvist, I. *Acta Crystallogr.* **1952**, *5*, 667.

(70) Weakley, T. J. R.; Evans, H. T., Jr.; Showell, J. S.; Tourné, G. F.; Tourné, C. M. *J. Chem. Soc., Chem. Commun.* **1973**, *4*, 139.

(71) Creaser, I.; Heckel, M. C.; Neitz, R. J.; Pope, M. T. *Inorg. Chem.* **1993**, *32*, 1573.

(72) Kim, K.-C.; Pope, M. T.; Gama, G. J.; Dickman, M. H. *J. Am. Chem. Soc.* **1999**, *121*, 11164.

(73) Katsoulis, D. E. *Chem. Rev.* **1998**, *98*, 359.

(74) Hill, C. L. *Chem. Rev.* **1998**, *98*, 1.

(75) Baker, L. C. W.; Figgis, J. S. *J. Am. Chem. Soc.* **1970**, *92*, 3794.

(76) Wang, S. H.; Jansen, S. A. *Chem. Mater.* **1994**, *6*, 2130.

(77) Thouvenot, R.; Fournier, M.; Franck, R.; Rocchiccioli-Deltcheff, C. *Inorg. Chem.* **1984**, *23*, 598.

(78) Matsumoto, K. Y.; Kobayashi, A.; Sasaki, Y. *Bull. Chem. Soc. Jpn.* **1975**, *48*, 3146.

(79) Kobayashi, A.; Sasaki, Y. *Bull. Chem. Soc. Jpn.* **1975**, *48*, 885.

(80) Pope, M. T.; O'Donnell, S. E.; Prados, R. A. *J. Chem. Soc., Chem. Commun.* **1975**, 22.

(81) Weinstock, I. A.; Cowan, J. J.; Barbuzzi, E. M. G.; Zeng, H.; Hill, C. L. *J. Am. Chem. Soc.* **1999**, *121*, 4608.

(82) Yamamura, K.; Sasaki, Y. *J. Chem. Soc., Chem. Commun.* **1973**, *18*, 648.

(83) Cowan, J. J.; Bailey, A. J.; Heintz, R. A.; Do, B. T.; Hardcastle, K. I.; Hill, C. L.; Weinstock, I. A. *Inorg. Chem.* **2001**, *40*, 6666.

(84) López, X.; Maestre, J. M.; Bo, C.; Poblet, J.-M. *J. Am. Chem. Soc.* **2001**, *123*, 9571.

(85) Neiwert, W. A.; Cowan, J. J.; Hardcastle, K. I.; Hill, C. L.; Weinstock, I. A. *Inorg. Chem.* **2002**, *41*, 6950.

(86) López, X.; Bo, C.; Poblet, J.-M. *Inorg. Chem.* **2003**, *42*, 2634.

(87) Sundaram, K. M.; Neiwert, W. A.; Hill, C. L.; Weinstock, I. A. *Inorg. Chem.* **2006**, *45*, 958.

(88) Zhang, F.-Q.; Zhang, X.-M.; Wu, H.-S.; Jiao, H. *J. Phys. Chem. A* **2007**, *111*, 159.

(89) Tézé, A.; Hervé, G. In *Inorg. Synth.*; Ginsberg, A. P., Ed.; John Wiley and Sons: New York, 1990; Vol. 27, p 85.

(90) Khenkin, A. M.; Kumar, D.; Shaik, S.; Neumann, R. *J. Am. Chem. Soc.* **2006**, *128*, 15451.

(91) Visser, S. P. d.; Kumar, D.; Neumann, R.; Shaik, S. *Angew. Chem. Int. Ed.* **2004**, *43*, 5661.

(92) Khenkin, A. M.; Hill, C. L. *J. Am. Chem. Soc.* **1993**, *115*, 8178.

(93) Ellis, S.; Kozhevnikov, I. V. *J. Mol. Catal. A: Chem.* **2002**, *187*, 227.

(94) Qu, L. Y.; Ma, R. H.; Chen, Y. G.; Chen, Y.; Liu, C. T. *J. Therm. Anal.* **1995**, *45*, 275.

(95) Randall, W. J.; Weakley, T. J. R.; Finke, R. G. *Inorg. Chem.* **1993**, *32*, 1068.

(96) Lyon, D. K.; Miller, W. K.; Novet, T.; Domaille, P. J.; Evitt, E.; Johnson, D. C.; Finke, R. G. *J. Am. Chem. Soc.* **1991**, *113*, 7209.

(97) Mansuy, D.; Bartoli, J.-F.; Battioni, P.; Lyon, D. K.; Finke, R. G. *J. Am. Chem. Soc.* **1991**, *113*, 7222.

(98) Katsoulis, D. E.; Pope, M. T. *J. Chem. Soc., Chem. Commun.* **1986**, *15*, 1186.

(99) Harmalker, S. P.; Pope, M. T. *J. Inorg. Biochem.* **1986**, *28*, 85.

(100) Hill, C. L. In *Activation and Functionalization of Alkanes*; Hill, C. L., Ed.; Wiley: New York, 1989, p 243.

(101) Hill, C. L.; Brown, R. B., Jr. *J. Am. Chem. Soc.* **1986**, *108*, 536.

(102) Neumann, R.; Dahan, M. *Nature* **1997**, *388*, 353.

(103) Pope, M. T. In *Comprehensive Coordination Chemistry*; Wilkinson, G., Gillard, R. D., Eds.; Pergamon: New York, 1987, p 1023.

(104) Cronin, L. In *Comprehensive Coordination Chemistry II: From the Molecular to the Nanoscale: Synthesis, Structure, and Properties*; McCleverty, J. A., Meyer, T. J., Eds.; Elsevier: Amsterdam, 2004; Vol. 7, p 1.

(105) Hill, C. L. In *Comprehensive Coordination Chemistry-II: From Biology to Nanotechnology*; Wedd, A. G., Ed.; Elsevier Ltd.: Oxford, UK, 2004; Vol. 4, p 679.

(106) Pope, M. T. In *Comprehensive Coordination Chemistry II: From Biology to Nanotechnology*; Wedd, A. G., Ed.; Elsevier Ltd.: Oxford, UK, 2004; Vol. 4, p 635.

(107) Rindl, M. *S. Afr. J. Sci.* **1916**, *11*, 362.

(108) Yamase, T. *Chem. Rev.* **1998**, *98*, 307.

(109) Papaconstantinou, E. *Chem. Soc. Rev.* **1989**, *18*, 1.

(110) Hill, C. L.; Prosser-McCartha, C. M. In *Photosensitization and Photocatalysis Using Inorganic and Organometallic Compounds*; Kalyanasundaram, K., Grätzel, M., Eds.; Kluwer Academic Publishers: Dordrecht, 1993; Vol. 14, p 307.

(111) Duncan, D. C.; Netzel; L., T.; Hill, C. L. *Inorg. Chem.* **1995**, *34*, 4640.

(112) Prados, R. A.; Meiklejohn, P. T.; Pope, M. T. *J. Am. Chem. Soc.* **1974**, *96*, 1261.

(113) Altenau, J.; Pope, M. T.; Prados, R. A.; So, H. *Inorg. Chem.* **1975**, *14*, 417.

(114) Pope, M. T. *Inorg. Chem.* **1972**, *11*, 1973.

(115) Pope, M. T.; Varga, G. M. *Inorg. Chem.* **1966**, *5*, 1249.

(116) Pope, M. T.; Papaconstantinou, E. *Inorg. Chem.* **1967**, *6*, 1147.

(117) Papaconstantinou, E.; Pope, M. T. *Inorg. Chem.* **1967**, *6*, 1152.

(118) Varga, G. M.; Papaconstantinou, E.; Pope, M. T. *Inorg. Chem.* **1970**, *9*, 662.

(119) Papaconstantinou, E.; Pope, M. T. *Inorg. Chem.* **1970**, *9*, 667.

(120) Kanan, M. W.; Nocera, D. G. *Science* **2008**, *321*, 1072.

(121) Kanan, M. W.; Surendranath, Y.; Nocera, D. G. *Chem. Soc. Rev.* **2009**, *38*, 109.

(122) Youngblood, W. J.; Lee, S.-H. A.; Maeda, K.; Mallouk, T. E. *Acc. Chem. Res.* **2009**, *42*, 1966.

(123) Youngblood, W. J.; Lee, S.-H. A.; Kobayashi, Y.; Hernandez-Pagan, E. A.; Hoertz, P. G.; Moore, T. A.; Moore, A. L.; Gust, D.; Mallouk, T. E. *J. Am. Chem. Soc.* **2009**, *131*, 926.

(124) Gersten, S. W.; Samuels, G. J.; Meyer, T. J. *J. Am. Chem. Soc.* **1982**, *104*, 4029.

(125) Concepcion, J. J.; Jurss, J. W.; Brennaman, M. K.; Hoertz, P. G.; Patrocinio, A. O. T.; Iha, N. Y. M.; Templeton, J. L.; Meyer, T. J. *Acc. Chem. Res.* **2009**, *42*, 1954.

(126) Yagi, M.; Kaneko, M. *Chem. Rev.* **2001**, *101*, 21.

(127) Sala, X.; Romero, I.; Rodríguez, M.; Escriche, L.; Llobet, A. *Angew. Chem. Int. Ed.* **2009**, *48*, 2842.

(128) Hurst, J. K. *Coord. Chem. Rev.* **2005**, *249*, 313.

(129) Geletii, Y. V.; Botar, B.; Kögerler, P.; Hillesheim, D. A.; Musaev, D. G.; Hill, C. L. *Angew. Chem. Int. Ed.* **2008**, *47*, 3896.

(130) Sartorel, A.; Carraro, M.; Scorrano, G.; Zorzi, R. D.; Geremia, S.; McDaniel, N. D.; Bernhard, S.; Bonchio, M. *J. Am. Chem. Soc.* **2008**, *130*, 5006.

(131) Sartorel, A.; Miro, P.; Salvadori, E.; Romain, S.; Carraro, M.; Scorrano, G.; Valentin, M. D.; Llobet, A.; Bo, C.; Bonchio, M. *J. Am. Chem. Soc.* **2009**, *131*, 16051.

(132) Geletii, Y. V.; Besson, C.; Hou, Y.; Yin, Q.; Musaev, D. G.; Quinonero, D.; Cao, R.; Hardcastle, K. I.; Proust, A.; Kögerler, P.; Hill, C. L. *J. Am. Chem. Soc.* **2009**, *131*, 17360.

(133) Geletii, Y. V.; Huang, Z.; Hou, Y.; Musaev, D. G.; Lian, T.; Hill, C. L. *J. Am. Chem. Soc.* **2009**, *131*, 7522.

(134) Kuznetsov, A. E.; Geletii, Y. V.; Hill, C. L.; Morokuma, K.; Musaev, D. G. *J. Am. Chem. Soc.* **2009**, *131*, 6844.

(135) Cao, R.; Ma, H.; Geletii, Y. V.; Hardcastle, K. I.; Hill, C. L. *Inorg. Chem.* **2009**, *48*, 5596.

(136) Besson, C.; Huang, Z.; Geletii, Y. V.; Lense, S.; Hardcastle, K. I.; Musaev, D. G.; Lian, T.; Proust, A.; Hill, C. L. *Chem. Commun.* **2010**, 2784.

(137) Yin, Q.; Tan, J. M.; Besson, C.; Geletii, Y. V.; Musaev, D. G.; Kuznetsov, A. E.; Luo, Z.; Hardcastle, K. I.; Hill, C. L. *Science* **2010**, *328*, 342.

(138) Huang, Z.; Luo, Z.; Geletii, Y. V.; Vickers, J.; Yin, Q.; Wu, D.; Hou, Y.; Ding, Y.; Song, J.; Musaev, D. G.; Hill, C. L.; Lian, T. *J. Am. Chem. Soc.* **2011**, *133*, 2068.

(139) Zhu, G.; Glass, E. N.; Zhao, C.; Lv, H.; Vickers, J. W.; Geletii, Y. V.; Musaev, D. G.; Song, J.; Hill, C. L. *Dalton Trans.* **2012**, *41*, 13043.

(140) Toma, F. M.; Sartorel, A.; Iurlo, M.; Carraro, M.; Parisse, P.; Maccato, C.; Rapino, S.; Gonzalez, B. R.; Amenitsch, H.; Ros, T. D.; Casalis, L.; Goldoni, A.;

Marcaccio, M.; Scorrano, G.; Scoles, G.; Paolucci, F.; Prato, M.; Bonchio, M. *Nat. Chem.* **2010**, *2*, 826.

(141) Steinmiller, E. M. P.; Choi, K.-S. *Proc. Natl. Acad. Sci.* **2009**, *106*, 20633.

(142) Goberna-Ferrón, S.; Vigara, L.; Soriano-López, J.; Galán-Mascarós, J. R. *Inorg. Chem.* **2012**, *51*, 11707.

(143) Soriano-López, J.; Goberna-Ferrón, S.; Vigara, L.; Carbó, J. J.; Poblet, J. M.; Galán-Mascarós, J. R. *Inorg. Chem.* **2013**, *52*, 4753.

(144) Lv, H.; Song, J.; Geletii, Y. V.; Vickers, J. W.; Sumliner, J. M.; Musaev, D. G.; Kögerler, P.; Zhuk, P. F.; Bacsa, J.; Zhu, G.; Hill, C. L. *J. Am. Chem. Soc.* **2014**, *136*, 9268.

(145) Lv, H.; Geletii, Y. V.; Zhao, C.; Vickers, J. W.; Zhu, G.; Luo, Z.; Song, J.; Lian, T.; Musaev, D. G.; Hill, C. L. *Chem. Soc. Rev.* **2012**, *41*, 7572.

(146) Sartorel, A.; Bonchio, M.; Campagna, S.; Scandola, F. *Chem. Soc. Rev.* **2013**, *42*, 2262.

(147) Lv, H.; Song, J.; Zhu, H.; Geletii, Y. V.; Bacsa, J.; Zhao, C.; Lian, T.; Musaev, D. G.; Hill, C. L. *J. Catal.* **2013**, *307*, 48.

(148) Lv, H.; Guo, W.; Wu, K.; Chen, Z.; Bacsa, J.; Musaev, D. G.; Geletii, Y. V.; Lauinger, S. M.; Lian, T.; Hill, C. L. *J. Am. Chem. Soc.* **2014**, *136*, 14015.

(149) Lv, H.; Chi, Y.; Leusen, J. v.; Kögerler, P.; Chen, Z.; Bacsa, J.; Guo, W.; Lian, T.; Hill, C. L. *Chem. Eur. J.* **2015**, *21*, 17363

(150) Guo, W.; Lv, H.; Bacsa, J.; Gao, Y.; Lee, J. S.; Hill, C. L. *Inorg. Chem.* **2016**, *55*, 461.

(151) Shafirovich, V. Y.; Khannanov, N. K.; Strelets, V. V. *Nouveau J. de Chim.* **1980**, *4*, 81.

(152) Harriman, A.; Porter, G.; Walters, P. *J. Chem. Soc., Faraday Trans. 2* **1981**, *77*, 2373.

(153) White, H. S.; Becker, W. G.; Bard, A. J. *J. Phys. Chem.* **1984**, *88*, 1840.

(154) Block, P. A.; Brown, R. A.; Robinson, D. In *Proceedings of the Fourth International Conference on Remediation of Chlorinated and Recalcitrant Compounds*; Battelle Press: Monterey, CA, 2004.

(155) Lin, W.; Han, H.; Frei, H. *J. Phys. Chem. B* **2004**, *108*, 18269.

(156) Lin, W.; Frei, H. *J. Am. Chem. Soc.* **2005**, *127*, 1610.

(157) Lin, W.; Frei, H. *J. Phys. Chem. B* **2005**, *109*, 4929.

(158) Lin, W.; Frei, H. *C. R. Chimie.* **2006**, *9*, 207.

(159) Nakamura, R.; Frei, H. *J. Am. Chem. Soc.* **2006**, *128*, 10668.

(160) Han, H.; Frei, H. *Microporous Mesoporous Mater.* **2007**, *103*, 265.

(161) Nakamura, R.; Okamoto, A.; Osawa, H.; Irie, H.; Hashimoto, K. *J. Am. Chem. Soc.* **2007**, *129*, 9596.

(162) Han, H.; Frei, H. *J. Phys. Chem. C* **2008**, *112*, 8391.

(163) Han, H.; Frei, H. *J. Phys. Chem. C* **2008**, *112*, 16156.

(164) Weare, W. W.; Pushkar, Y.; Yachandra, V. K.; Frei, H. *J. Am. Chem. Soc* **2008**, *130*, 13555.

(165) Jiao, F.; Frei, H. *Angew. Chem. Int. Ed.* **2009**, *48*, 1841.

(166) Wu, X.; Weare, W. W.; Frei, H. *Dalton Trans.* **2009**, 10114.

(167) Cuk, T.; Weare, W. W.; Frei, H. *J. Phys. Chem. C* **2010**, *114*, 9167.

(168) Soo, H. S.; Macnaughtan, M. L.; Weare, W. W.; Yano, J.; Frei, H. *J. Phys. Chem. C* **2011**, *115*, 24893.

(169) Takashima, T.; Nakamura, R.; Hashimoto, K. *J. Phys. Chem. C* **2009**, *113*, 17247.

(170) Takashima, T.; Yamaguchi, A.; Hashimoto, K.; Nakamura, R. *Chem. Commun.* **2012**, *48*, 2964.

(171) Zhao, C.; Huang, Z.; Rodríguez-Córdoba, W.; Kambara, C. S.; O'Halloran, K. P.; Hardcastle, K. I.; Musaev, D. G.; Lian, T.; Hill, C. L. *J. Am. Chem. Soc.* **2011**, *133*, 20134.

(172) Suzuki, K.; Tang, F.; Kikukawa, Y.; Yamaguchi, K.; Mizuno, N. *Angew. Chem. Int. Ed.* **2014**, *53*, 5356.

(173) Suzuki, K.; Tang, F.; Kikukawa, Y.; Yamaguchi, K.; Mizuno, N. *Chem. Lett.* **2014**, *43*, 1429.

Charge Separation in Polyoxometalate-Based Systems for Solar Energy Production

Chapter 2

Influence of Heterometal Location on Charge Transfer Lifetimes in Keggin Polyoxometalate Chromophores

with John Fielden, Alexey L. Kaledin, Djamaladdin G. Musaev, Tianquan Lian, and Craig L. Hill

Published partially in: Glass, E. N.; Fielden, J.; Kaledin, A. L.; Musaev, D. G.; Lian, T.; Hill, C. L. "Extending Metal-to-Polyoxometalate Charge Transfer Lifetimes: The Effect of Heterometal Location", *Chemistry – A European Journal*, **2014**, *20(15)*, 4297-4307.

2.1 Abstract

In an effort to develop robust molecular sensitizers for solar fuel production, we examine the electronic structure and photodynamics of transition-metal-substituted polyoxometalates (POMs), a novel class of compound in this context. Experimental and computational techniques including femtosecond (fs) transient absorption spectroscopy have been used to study the cobalt-containing Keggin POMs, $[Co^{II}W_{12}O_{40}]^{6-}$ (**2.1a, $Co^{II}W_{12}$**), $[Co^{III}W_{12}O_{40}]^{5-}$ (**2.2a, $Co^{III}W_{12}$**), $[SiCo^{II}(H_2O)W_{11}O_{39}]^{6-}$ (**2.3a, $SiCo^{II}$**), and $[SiCo^{III}(H_2O)W_{11}O_{39}]^{5-}$ (**2.4a, $SiCo^{III}$**), finding the longest lived charge transfer excited state so far observed in a POM and elucidating the electronic structures and excited state dynamics of these compounds at an unprecedented level. All species exhibit a bi-exponential decay in which early dynamic processes with time constants in the fs domain yield longer lived excited states which decay with time constants in the ps to ns domain. The initially formed states of **2.1a** and **2.3a** are considered to result from metal-to-polyoxometalate charge transfer (MPCT) from Co^{II} to W, while the longer-lived excited state of **2.1a** is tentatively assigned to a localized intermediate MPCT state. The excited state formed by the tetrahedral cobalt(II) centered heteropolyanion (**2.1a**) is far longer-lived (τ = 420 ps in H_2O; τ = 1700 ps in MeCN) than that of **2.3a** (τ = 1.3 ps), where the single Co^{II} atom is located in a pseudo-octahedral addendum site. Short-lived states are observed for the two Co^{III} containing heteropolyanions **2.2a** (τ = 4.4 ps) and **2.4a** (τ = 6.3 ps) and assigned solely to $O \rightarrow Co^{III}$ charge transfer. The dramatically extended lifetime for **2.1a** *vs* **2.3a** is ascribed to a structural change permitted by the coordinatively flexible central site, weak orbital overlap of the central Co with the polytungstate framework, and

putative transient valence trapping of the excited electron on a single W atom, a phenomenon not noted previously in POMs.

2.2 Introduction

Chromophores based on oxo-bridged heterobimetallic groups (M-O-M′; M = Zr^{IV}, Ti^{IV}; M′ = Cu^{I}, Ce^{III}, Sn^{II}) supported on mesoporous substrates have recently shown themselves to be promising alternatives to metal oxide semiconductors, and organic/metallo-organic chromophores in photocatalytic solar fuel production.[1-8] In these materials, visible absorption results from photoinduced formation of long lived metal-to-metal charge transfer (MMCT) excited states that can be coupled with multi-electron transfer catalysts. Thus, such MMCT chromophores have the potential to side-step the problems of oxidative degradation of metallo-organic materials such as $[Ru(bpy)_3]^{2+}$,[9] and the challenge of engineering metal oxides with the appropriate combination of band gap, electron/hole diffusion length, recombination rate and conduction band edge potential.[10-15] Even so, surface-supported species are more difficult to characterize, optimize and interface with catalysts than molecular chromophores.

Inspired by these heterobimetallic MMCT assemblies, we recently embarked upon the study of transition metal substituted polyoxometalates (POMs) as *molecular* inorganic MMCT (or MPCT, metal-to-polyoxometalate charge transfer) chromophores. POMs have not yet been systematically explored as tunable electron-accepting chromophores,[16,17] but are excellent candidates because of their stability (oxidative and thermal) and ability to accommodate multiple heterometals. Previous reports from our group have found that Re^{I} carbonyls supported by lacunary Wells-Dawson anions and

Krebs dimers show extended visible absorption due to Re^{I}-to-POM charge transfer, but the excited state lifetimes of these species (<2 ps) are too short to be attractive for application in solar devices.[18,19] Here, we study the electronic structure and excited state dynamics of a representative family of transition-metal-substituted POMs, the cobalt-containing Keggin derivatives: $[Co^{II}W_{12}O_{40}]^{6-}$ (**2.1a, $Co^{II}W_{12}$**), $[Co^{III}W_{12}O_{40}]^{5-}$ (**2.2a, $Co^{III}W_{12}$**), $[SiCo^{II}(H_2O)W_{11}O_{39}]^{6-}$ (**2.3a, $SiCo^{II}$**) and $[SiCo^{III}(H_2O)W_{11}O_{39}]^{5-}$ (**2.4a, $SiCo^{III}$**).[20-30] This systematic approach facilitates the in-depth elucidation of POM excited state properties as a function of the coordination site and oxidation state of the transition-metal electron donor. The dramatically longer lived (τ = 420 ps in H_2O; τ = 1700 ps in MeCN) excited state of **2.1a** is consistent with the ability of the central Co site to undergo structural distortions, poorer orbital overlap between this site and the reduced tungstate framework, and a possible valence-trapped intermediate.

2.3 Experimental

2.3.1 Materials and Instrumentation

All materials were purchased as ACS analytical or reagent grade and used as received, and syntheses were carried out in the ambient atmosphere. $K_5H[Co^{II}W_{12}O_{40}]\bullet 15H_2O$ (**2.1, $Co^{II}W_{12}$**),[20,21,23] $K_5[Co^{III}W_{12}O_{40}]\bullet 20H_2O$ (**2.2, $Co^{III}W_{12}$**),[20,21,23] $K_6[SiCo^{II}(H_2O)W_{11}O_{39}]\bullet 10H_2O$ (**2.3, $SiCo^{II}$**),[31] and $Cs_5[SiCo^{III}(H_2O)W_{11}O_{39}]\bullet 3H_2O$ (**2.4, $SiCo^{III}$**)[32] were prepared based on published procedures (improved synthetic procedures for **2.1** and **2.2** are detailed below). Salt metathesis to prepare $(C_{16}H_{36}N)_4H_2[Co^{II}W_{12}O_{40}]$ (**2.1-TBA, $Co^{II}W_{12}$-TBA**) was based on known procedures.[33,34] The identities and purities of **2.1-2.4** were confirmed by infrared

and UV-visible spectroscopy, thermogravimetric analysis, and X-ray diffraction. Infrared spectra (2% by weight in KBr) were recorded on a Thermo Nicolet 6700 FT-IR spectrometer. Static electronic absorption spectra were acquired using an Agilent 8453 spectrophotometer equipped with a diode-array detector and Agilent 89090A cell temperature controller unit. Near infrared (NIR) spectra were acquired using a Shimadzu UV-3600 UV-Vis-NIR spectrophotometer. Thermogravimetric data were collected on ISI TGA 1000 and Perkin Elmer STA 6000 instruments. X-ray diffraction data were acquired using a Bruker APEX II diffractometer with an Oxford Cryostream. Cyclic voltammograms were recorded on a BAS CV-50W electrochemical analyzer equipped with a glassy-carbon working electrode, a platinum wire auxiliary electrode and an Ag/AgCl (3 M NaCl) BAS reference electrode, using sodium sulfate (0.250 M, pH 2) or lithium acetate (0.250 M, pH 5) as buffer/electrolyte. All redox potentials are reported relative to this reference electrode (~+202 mV nominal difference between NHE and the BAS electrode). Elemental analyses (C, H, N) were performed by Atlantic Microlab Inc. (Norcross, Georgia). Two-electron reduced spectra of **2.1** and **2.3** were prepared by bulk electrolysis of 0.5 mM **2.1** and **2.3** in equivalent conditions to transient measurements, at -0.49 V and -1.0 V vs. Ag/AgCl, respectively. A glassy carbon mesh electrode was used as the working electrode. Static electronic absorption spectra were recorded of the reduced species immediately following electrolysis. The one-electron reduced spectra were approximated by scaling the two-electron reduced spectra by a one-half factor, consistent with the nature of heteropoly blue absorptions in Keggin POMs.[35]

2.3.2 Syntheses

$K_5H[Co^{II}W_{12}O_{40}]\bullet 15H_2O$ (2.1, $Co^{II}W_{12}$). The synthesis was adapted from published methods.[20,21,23] Sodium tungstate dihydrate (19.8 g, 60 mmol) was dissolved with stirring in 40 mL of deionized water. The pH was adjusted to 7.0 using glacial acetic acid. A solution of cobalt(II) acetate tetrahydrate was prepared (2.5 g, 10 mmol) by addition to 12 mL deionized water, with the pH adjusted to ~7 by the addition of a few drops of glacial acetic acid. Both solutions were heated with stirring until near boiling and the cobalt(II) acetate solution was added to the sodium tungstate solution slowly with stirring, yielding a dark green solution. The mixture was boiled for 20 minutes and filtered hot. A saturated solution of potassium acetate adjusted to pH 7.0 by the addition of glacial acetic acid was prepared while the filtrate was reheated. The potassium acetate solution was added slowly to the filtrate with stirring, precipitating a green solid. The resulting mixture was allowed to cool to room temperature and filtered, rinsing the solid twice with the filtrate. The solid was redissolved in 40 mL 2M H_2SO_4 with stirring and gentle heating for 15 minutes, yielding a dark blue solution. Insoluble material was removed by filtration. The solution volume was reduced by half through gentle heating, then allowed to develop crystals via slow evaporation. The dark blue crystals collected from the mother liquor were further purified by passing a concentrated solution through Dowex 50WX8 ion-exchange resin conditioned in the K^+ cycle to remove a large excess of latent cobalt cations. The eluent was evaporated to dryness using a rotary evaporator. The amorphous solid was dissolved in minimal 1M HCl and allowed to develop crystals of **2.1** via slow evaporation. FTIR (2% KBr pellet), $\tilde{\nu}$, cm^{-1}: 943 (s), 889 (s), 871 (sh), 739 (s), 692 (sh), 580 (w), 449 (m). UV-Vis (H_2O), λ_{max}, nm (ε, L mol^{-1} cm^{-1}): 625 (223).

$(C_{16}H_{36}N)_4H_2[Co^{II}W_{12}O_{40}]$ (2.1-TBA, $Co^{II}W_{12}$-TBA). From a 10.0 gram sample of **2.1** dissolved in minimal 2M H_2SO_4, the heteropoly acid, $H_6[Co^{II}W_{12}O_{40}]$ was prepared by the addition of concentrated H_2SO_4 and extraction with diethyl ether, using the etherate method.[33] Cation metathesis was accomplished by addition of a stoichiometric equivalent of $(C_{16}H_{36}N)Br$ dissolved in MeCN.[34] A solution of $(C_{16}H_{36}N)Br$ **(**2.17 g, 6.7 mmol) in 25 mL MeCN was added dropwise to a concentrated aqueous solution of the heteropoly acid with vigorous stirring, yielding the dark blue MeCN-soluble **2.1-TBA**. The solid was crashed out by addition of excess deionized water, then recovered by filtration. Repeated dissolution in MeCN and precipitation with water yielded pure **2.1-TBA** as a dark blue powder, which yields dark blue crystals by slow evaporation from MeCN. FTIR (2% KBr pellet), $\tilde{\nu}$, cm^{-1}: 3442 (w), 3200 (w), 2961 (s), 2935 (s), 2873 (s), 1630 (w), 1484 (s), 1381 (s), 945 (vs), 877 (vs), 759 (vs), 731 (sh), 688 (sh), 559 (w), 445 (m). UV-Vis (H_2O), λ_{max}, nm (ε, L mol^{-1} cm^{-1}): 628 (205). Elemental analysis: calcd. (found) for $C_{64}H_{146}N_4Co_1W_{12}O_{40}$, %: C, 19.83 (20.06); H, 3.80 (3.89); N, 1.45 (1.56). TGA (Figure 2.1) shows a mass loss of 26.3% between 300 and 420 °C (calcd. 25.1% for TBA_4H_2**2.1**).

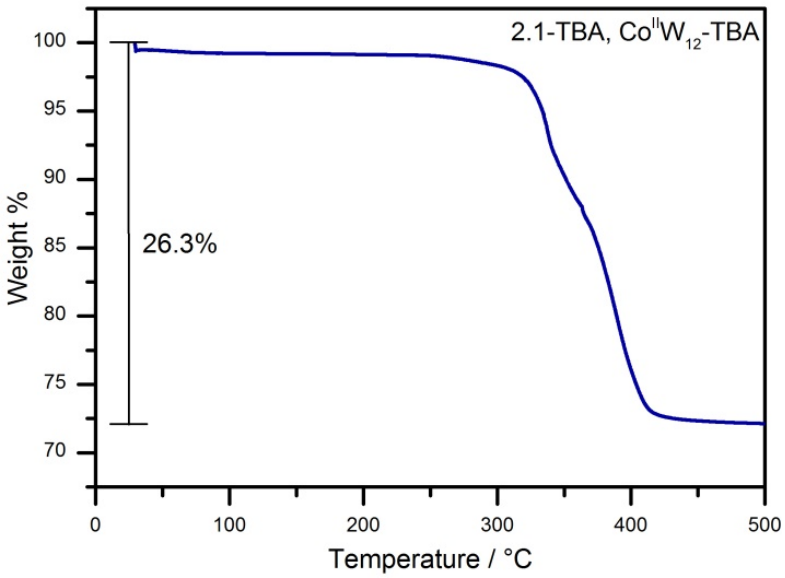

Figure 2.1. Thermogravimetric analysis of **2.1-TBA**. The annotated total weight loss is attributed to decomposition of the tetrabutylammonium cation.

$K_5[Co^{III}W_{12}O_{40}]\cdot 20H_2O$ (2.2, $Co^{III}W_{12}$). The synthesis was adapted from published methods.[20,21,23] Sodium tungstate dihydrate (19.8 g, 60 mmol) was dissolved with stirring in 40 mL of deionized water. The pH was adjusted to 7.0 using glacial acetic acid. A solution of cobalt(II) acetate tetrahydrate was prepared (2.5 g, 10 mmol) by addition to 12 mL deionized water, the pH being adjusted to ~7 by the addition of a few drops of glacial acetic acid. Both solutions were heated with stirring until near boiling and the cobalt(II) acetate solution was added to the sodium tungstate solution slowly with stirring, yielding a dark green solution. The mixture was boiled for 20 minutes and filtered hot. A saturated solution of potassium acetate adjusted to pH 7.0 by the addition of glacial acetic acid was prepared while the filtrate was reheated. The potassium acetate solution was added slowly to the filtrate with stirring, precipitating a green solid. The resulting mixture was allowed to cool to room temperature and filtered,

rinsing the solid twice with the filtrate. The solid was redissolved in 40 mL 2M H_2SO_4 with stirring and gentle heating for 15 minutes, yielding a dark blue solution. Insoluble material was removed by filtration. The filtrate was reheated to boiling and potassium persulfate (10 g, 37 mmol) was added in small portions until the color change from blue to yellow was complete. The solution was cooled in ice and the yellow needle crystals were collected by filtration. The product was further purified by passing a concentrated solution through Dowex 50WX8 ion-exchange resin conditioned in the K^+ cycle. The eluent was evaporated to dryness using a rotary evaporator. The yellow solid was dissolved in minimal deionized water, heated to boiling, and a small amount of potassium persulfate was added to ensure complete oxidation. Yellow needle crystals of **2.2** were obtained via slow evaporation and recrystallized twice from hot water. FTIR (2% KBr pellet), $\tilde{\nu}$, cm^{-1}: 954 (s), 896 (sh), 876 (s), 757 (vs), 498 (w), 440 (m). UV-Vis (H_2O), λ_{max}, nm (ε, L mol^{-1} cm^{-1}): 390 (1270).

2.3.3 Single Crystal X-ray Structural Determination

Compounds **2.1** and **2.2** were crystallized from water, compound **2.1** requiring almost complete evaporation of the solvent due to its high aqueous solubility. Suitable single crystals were selected under ambient conditions, mounted on a cryoloop using Paratone-N oil, and placed under the cryostream at 173 K. Crystal evaluation and collection of X-ray diffraction intensity data were performed using a Bruker Apex II CCD diffractometer ($Mo_{K\alpha}$, λ = 0.71073 Å), and data reduction was carried out using the Bruker *APEXII* program suite.[36] Correction for incident and diffracted beam absorption effects were applied using numerical methods.[37] Compound **2.1** crystallized in the space

group $P3_221$ and compound **2.2** in $P6_222$ as determined by systematic absences in the intensity data, intensity statistics and the successful solution and refinement of the structure. Structure solution and refinement was carried out using the Bruker SHELXTL software package.[38] The structures were solved by direct methods and refined against F^2 by the full matrix least-square technique. All non-H atoms were refined anisotropically, H atoms were not located or refined. Crystal data, data collection parameters and refinement statistics are summarized in Table 2.1. ORTEP representations of the cluster anions **2.1a** and **2.2a** are given in Figure 2.2. X-ray analysis was not performed on **2.3** and **2.4** due to positional disorder in the polytungstate framework, a common problem in Keggin POMs, which limits the amount of information that can be obtained regarding the pseudo-octahedral Co addendum site.

Table 2.1. Crystal data, collection parameters and refinement statistics for **2.1** and **2.2**

	2.1	**2.2**
Empirical formula	$CoH_{29}K_5O_{54}W_{12}$	$CoH_{32}K_5O_{56}W_{12}$
FW / g mol^{-1}	3353.86	3388.89
T / K	173(2)	173(2)
λ / Å	0.71073	0.71073
Crystal system	Hexagonal	hexagonal
Space group	$P3_221$	$P6_222$
***a* / Å**	18.997(1)	18.980(3)
***b* / Å**	18.997(1)	18.980(3)
***c* / Å**	12.479(1)	12.524(3)
***α* / °**	90	90
***β* / °**	90	90
***γ* / °**	120	120
***V* / Å^3**	3900.1(5)	3907(1)
Z	3	3
***ρcalc* / g cm^{-3}**	4.284	4.321
***μ* / mm^{-1}**	27.248	27.203
Crystal size / mm	0.39 × 0.39 × 0.36	0.40 × 0.27 × 0.16
No. reflections (unique)	44212 (6874)	61027 (2818)
R_{int}	0.1093	0.0884
θ_{max}	29.00	26.91
Completeness to θ_{max}	99.3%	99.5%
Data / restraints / parameters	6874 / 3 / 306	2818 / 6 / 169
Goodness-of-fit on F^2	1.064	1.094
Residuals: R_1; wR_2	0.0506; 0.1355	0.0207; 0.0514
Final difference peak and hole / eÅ^{-3}	1.188, -1.710	0.888, -0.814
ICSD numbers	427379	427380

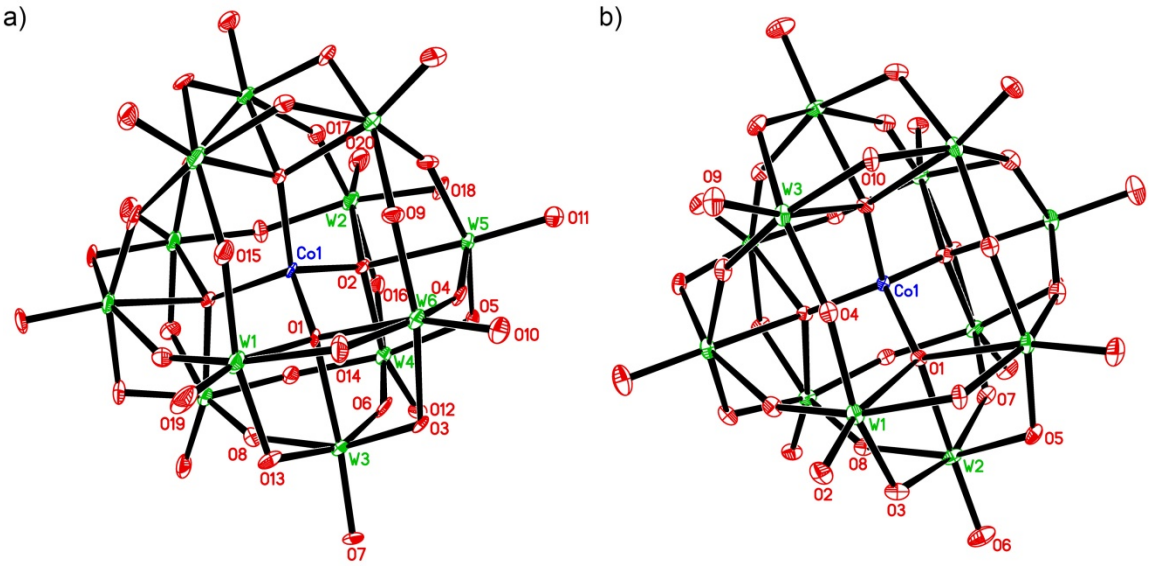

Figure 2.2. ORTEP representations of the cluster anions a) **2.1a** and b) **2.2a**, thermal ellipsoids are drawn at the 30% probability level. Color scheme: Co, blue; O, red; W, green.

2.3.4 Femtosecond Visible Transient Absorption Measurements

The femtosecond (0.1 ps – 1.2 ns) transient absorption (TA) spectrometer used in this study was based on a regeneratively amplified Ti:sapphire laser system (Coherent Legend, 800 nm, 150 fs, 3 mJ/pulse, 1 kHz repetition rate) and the Helios spectrometer (Ultrafast Systems, LLC). The fundamental output from the regenerative amplifier was split in two with a 10% beam splitter, the majority being directed to generate the pump pulse and the reflected remainder used to generate the probe pulse. Pump pulses at 400 nm were generated by frequency-doubling of the fundamental pulse in a β-barium borate (BBO) crystal. The energy of the pump pulse was controlled by a variable neutral-density filter wheel. The pump pulse passed through a computer-controlled optical delay line and a chopper prior to passing through the sample. The visible probe was generated

by attenuating and focusing ~10 μJ of the 800 nm pulse into a 2 mm thick sapphire window to produce a white light continuum from 400 nm to 800 nm. After collimation with an off-axis parabolic mirror, the white light was split into equal signal and reference beams. The reference beam was used to normalize the laser intensity fluctuation. The signal beam was collimated and focused on the sample coincident with the pump pulse beam using Al parabolic mirrors. The beam waists at the sample were 300 and 150 μm for the pump and probe beam, respectively. Both the signal (after passing through the sample) and reference beams were focused into a CMOS array detector and detected at a frequency of 1 kHz, from which transient spectra and kinetics were recorded with Helios (Ultrafast Systems) software.

Samples were measured in a 1 mm path length quartz cuvette to minimize the transient solvent response. The solvent effect in neat buffered solvent was recorded immediately following each sample measurement. During the data collection the samples were constantly stirred by a magnetic stirrer to minimize localized thermal effects. No evidence of sample degradation was seen based on comparisons of electronic absorption spectra before and after TA experiments. All samples were filtered with a Whatman 0.2 μm PES syringe filter prior to measurement. Detailed analysis of the transient spectra, temporal chirp correction, and quantitative kinetic analysis was performed using Ultrafast Systems Surface Xplorer Pro software. Global fit analysis via singular value decomposition was performed on all transient spectra. Both single wavelength kinetics and the principal kinetic components were fit to a multiexponential decay function convoluted with the Gaussian instrument response function (fwhm: ~150 fs).

2.3.5 Computational Studies

Geometries of the anions $[Co^{II}W_{12}O_{40}]^{6-}$ (**2.1a**), $[Co^{III}W_{12}O_{40}]^{5-}$ (**2.2a**), $[SiCo^{II}(H_2O)O_{39}W_{11}]^{6-}$ (**2.3a**) and $[SiCo^{III}(H_2O)O_{39}W_{11}]^{5-}$ (**2.4a**) were optimized at their several lower-lying electronic states, in the gas phase with no geometry constraints. Vibrational analyses were performed to ensure that all converged structures are true minima. In these calculations we used the spin-unrestricted DFT method (the hybrid M06L functional)[39] in conjunction with the D95V[40] basis sets for O, and the lanl2dz basis with the associated Hay-Wadt ECPs[41] for the W and Co atoms, which below will be referred to as "UM06L/lanl2dz". The basis set for Si was augmented by single polarization d-function (ζ=0.55). Electronic spectra and electric dipole transition moments for ground-to-excited state transitions were calculated at the optimized geometries of the ground states of the corresponding compounds using the time-dependent (TD)[42] DFT, i.e. TD-UM06L/lanl2dz approach. Solvent effects were applied as single point calculations on top of the gas phase structures and approximated by the polarizable continuum model (PCM)[43] employing the UFF[44] radii for all atoms. All calculations were carried out with the Gaussian 09 software package.[45]

2.4 Results and Discussion

2.4.1 Calculated Ground State Geometries and Electronic Structures

Our study comprises four cobalt-containing POMs - the cobalt-centered Keggin anions $[Co^{II}W_{12}O_{40}]^{6-}$ (**2.1a**) and $[Co^{III}W_{12}O_{40}]^{5-}$ (**2.2a**), and the cobalt *substituted* counterparts, $[SiCo^{II}(H_2O)W_{11}O_{39}]^{6-}$ (**2.3a**) and $[SiCo^{III}(H_2O)W_{11}O_{39}]^{5-}$ (**2.4a**), in which a Co atom replaces one of the W addendum atoms. This allows study of the effects of

transition metal location and oxidation state on the nature and lifetime of the MPCT excited state. Compounds **2.1a** and **2.2a** have been well-studied since they were first synthesized by Baker and McCutcheon in 1956;[20] however, investigations of the photodynamics of simple transition-metal containing POMs are entirely lacking.

As Keggin anions, all four clusters have super-tetrahedral structures, with a tetrahedral heteroatom (Co or Si) at the center (Figure 2.3). Their experimentally determined and calculated metal-oxygen bond lengths are summarized in Table 2.2. Crystallographic information is only included for anions **2.1a** and **2.2a**, because positional disorder prevents extraction of meaningful information on the Co atoms of **2.3a** and **2.4a**. Note that while several previous studies have addressed the crystal structures of **2.1a** and **2.2a**,[25,26,46] the pentapotassium salt of **2.1a** used in this study, $K_5H[Co^{II}W_{12}O_{40}]\bullet 15H_2O$ (**2.1**), is crystallographically characterized for the first time.

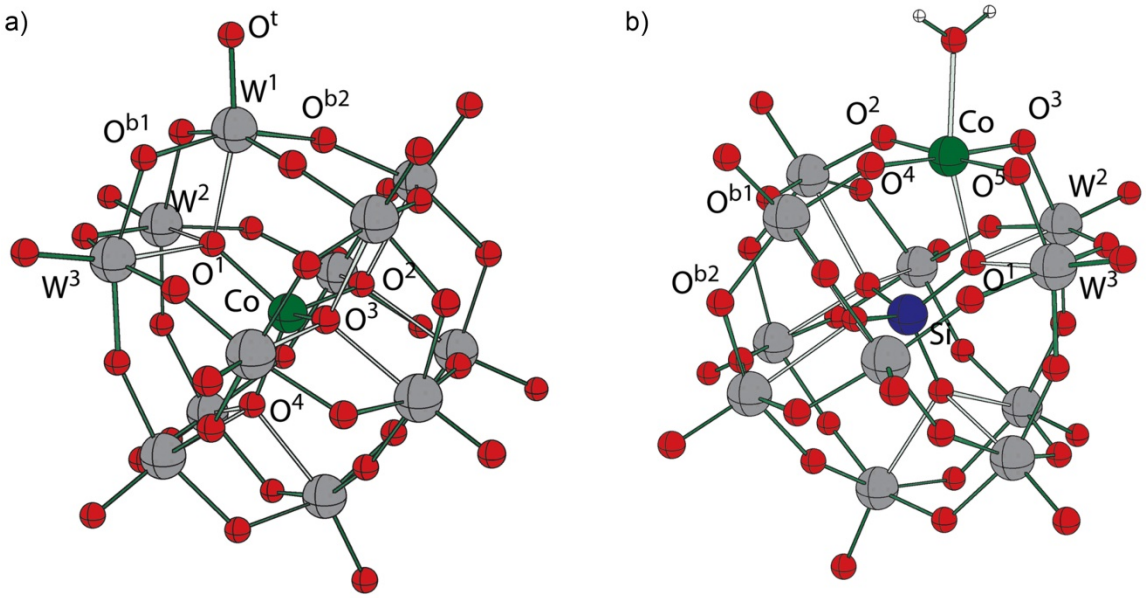

Figure 2.3. Calculated geometrical representations of the cluster anions a) **2.1a**/**2.2a** and b) **2.3a**/**2.4a**, with atomic labels corresponding to distances tabulated in Table 2.2. Color scheme: W, gray; O, red; Co, green; Si, blue.

Table 2.2. Experimental (crystallographic) and calculated bond lengths (Å) in the cluster anions **2.1a**, **2.2a**, **2.3a** and **2.4a**. Where appropriate, crystallographically determined distances have been averaged.

Parameter	**Experimental**		**Computational**			
	2.1a	**2.2a**	**2.1a**	**2.2a**	**2.3a**	**2.4a**
Co-O^1	1.900(12)	1.805(5)	1.92	1.83	2.08	2.11
Co-O^2			---	---	2.06	1.88
Co-O^3			---	---	2.08	1.88
Co-O^4			---	---	1.99	1.88
Co-O^5			---	---	2.00	1.88
Co/W^1-O^1	2.137(11)	2.202(5)	2.20	2.25	2.08	2.11
W^2-O^1	2.159(12)	2.216(5)	2.20	2.25	2.39	2.36
W^3-O^1	2.165(12)	2.262(5)	2.20	2.30	2.42	2.36
Co-W	3.491(3)	3.512(1)	3.55	3.57	---	---

Our crystal structures of cobalt-centered **2.1a** and **2.2a** are consistent with the literature, in showing Co-O bond lengths that are indicative of the Co oxidation state.[32,33,48] Thus Co^{II}-O^1 in **1a** is significantly longer than Co^{III}-O^1 in **2.2a** (1.900(12) vs. 1.805(5) Å), an observation well reproduced by our computed geometries for their S=3/2 (**2.1a**) and S=2 (**2.2a**) ground electronic states. Other computed and crystallographically determined bond distances for **2.1a** and **2.2a** are also in good agreement, the small differences being within expectations for crystallographic and gas phase calculated structures. The calculated ground state spins are also consistent both with previous studies,[22,27,28] and with expectations for tetrahedral d^7 and d^6 ions based on crystal field theory. Thus, the electronic configuration of the ground state of **2.3a** is $\{\ldots[17e(O)]^4[18e(Co)]^4[33t_2(Co)]^3[19e(W)]^0\ldots\}$, where 17e(O) are doubly occupied orbitals of the W-O-W bridging O-center, 18e are doubly occupied d-orbitals of the Co-center, $33t_2$ the singly occupied d-orbitals of Co-center, and 19e is an unoccupied orbital of the W-centers. Oxidation of **2.1a** to **2.2a** results in removal of one electron from the doubly occupied 18e orbital of the Co-center, and a small Jahn-Teller distortion that reduces the total symmetry of the anion from T_d (for **2.1a**) to D_{2d} (for **2.2a**). The resulting ground electron configuration for **2.2a** is $\{\ldots[a_1(Co)]^2[b_1(Co)]^1[b_2(Co)]^1[e(Co)]^2[a_1(W)]^0[b_1(W)]^0\ldots\}$. It is worth noting that the $1e^-$ reduction of **2.2a** yields **2.1a**, but not a heteropoly blue species, which is also consistent with previous findings.[24]

The calculated structures of **2.3a** and **2.4a**, with addendum Co sites, also show shortening of the Co-O bonds upon oxidation (Co-O^2 to Co-O^5), with the exception of the bond to the internal oxygen O^1 of the SiO_4 unit. The calculated ground spin state of **2.3a**

is a quartet, S=3/2, as would be expected for a high spin, octahedral d^7 ion, and calculations find that the Co-center has almost 2.75 unpaired electrons. The doubly occupied MOs of **2.3a** are Co-O bonding orbitals, and the singly occupied MOs are Co-d orbitals. In this case, frontier orbital analysis indicates that oxidation of **2.3a** to **2.4a** results in loss of one electron from the doubly occupied (CoO) orbital. As a result, the Co^{III} center in **2.4a** bears 1.75 unpaired electrons, essentially giving a triplet (S=1) ground state. However, it should be noted that the calculated energetic separation between this triplet state, and the expected diamagnetic (S=0) state is very close (*ca.* 0.6 kcal/mol). As the triplet wavefunction is cleaner and more accurate than the open-shell singlet wavefunction, computationally the UV-visible spectra are assigned starting from the triplet state.

2.4.2 UV-Visible Spectroscopic and Electrochemical Studies

Comparison of the UV-visible absorption spectra of **2.1** to **2.4**, in combination with the results of our calculations and electrochemical experiments, allows a comprehensive assignment of the electronic transitions of these compounds. This includes the MPCT transitions excited in the transient experiments.

The UV-visible absorption spectra of compounds **2.1** and **2.4** (350 to 750 nm) are displayed in Figure 2.4a. At shorter wavelengths (<300 nm), all four compounds show strong UV absorptions arising from the $O_{2p} \rightarrow W_{5d}$ charge transfer (CT) transitions common to all polyoxotungstates. However, compared to transition metal-free POMs such as $[SiW_{12}O_{40}]^{4-}$ and $[PW_{12}O_{40}]^{3-}$, the absorption spectra of **2.1** to **2.4** tail more significantly into the visible and show additional features arising from the cobalt d-

orbitals. For cobalt-centered anions **2.1a** and **2.2a**, the main observations are a broad transition at 625 nm in **2.1** that is absent in **2.2**, and a strong peak at 389 nm in **2.2** in place of a much weaker shoulder in **2.1**. Our DFT calculations (Figures 2.5 and 2.6) agree with previous work,[21,22,27,30] indicating that the feature at 625 nm (calculated ~650 nm) is associated with the $^4A_2 \rightarrow {}^4T_1$ d-d transition of the tetrahedral Co^{II} ion in **2.1a** while the peak at 390 nm (calculated range ~375-450 nm for **2.2a**) arises from the O→Co CT transitions which are present in Co^{III}-based **2.2a** because the Co *e* orbital is partially occupied. The spectra of anions **2.3a** and **2.4a**, with a pseudo-octahedral addendum Co site, are significantly different. Compound **2.3** shows a d-d transition centered at 546 nm that resembles that of $[Co^{II}(H_2O)_6]^{2+}$, although the broken octahedral symmetry causes the extinction coefficient to be substantially higher. The broad $^1A_1 \rightarrow {}^1T_1$ d-d transition for **2.4** is centered at 692 nm, while the peak at 453 nm is ascribed to a $^1A_1 \rightarrow {}^1T_2$ d-d transition.[32] Calculated absorption spectra for anions **2.3a** and **2.4a** (Figures 2.7 and 2.8) reproduce the dipole allowed Co d-d transitions seen at longer wavelengths in both spectra. Calculations for **2.4a** also indicate that the transition at approximately 450 nm has Co d-d character along with a strong O→W signature. The short wavelength regimes of both anions are dominated by μ_2-O→W and μ_2-O→CoO transitions, with the majority being non-charge-transfer in nature.

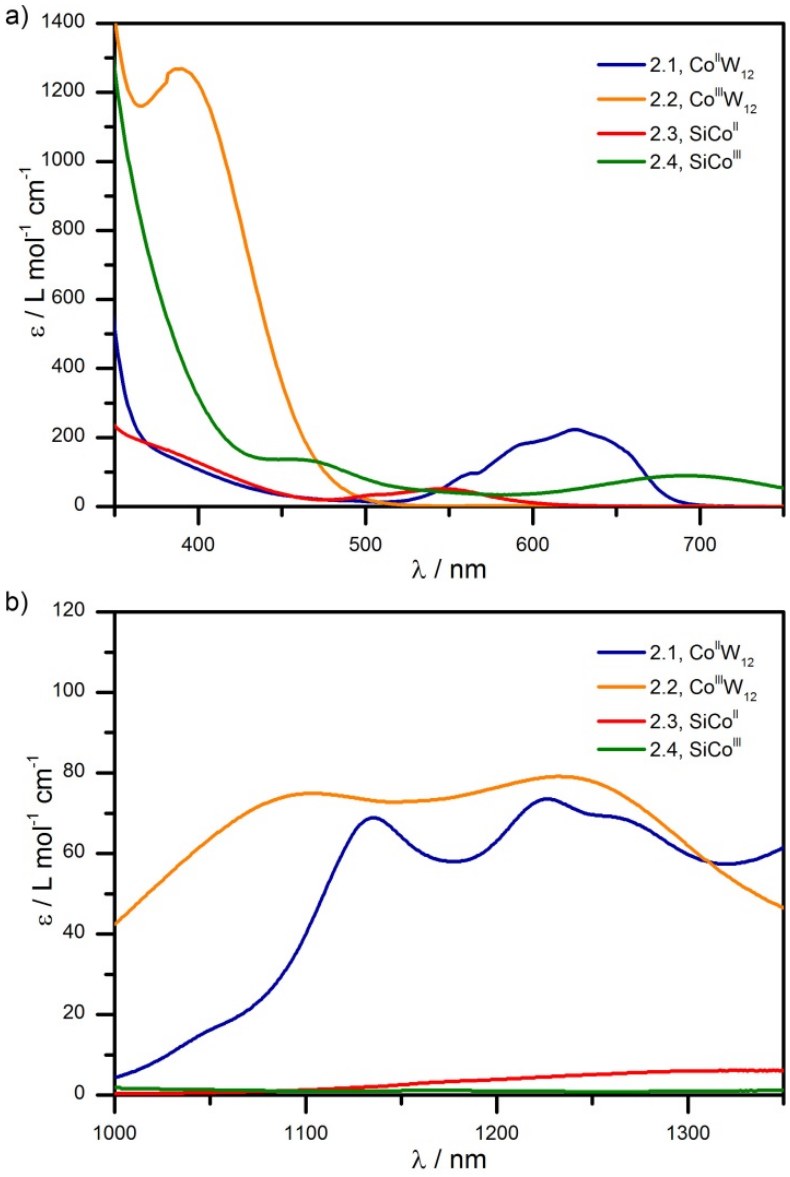

Figure 2.4. Electronic absorption spectra of **2.1**-**2.4** in water in a) the visible spectrum and b) the near infrared spectrum.

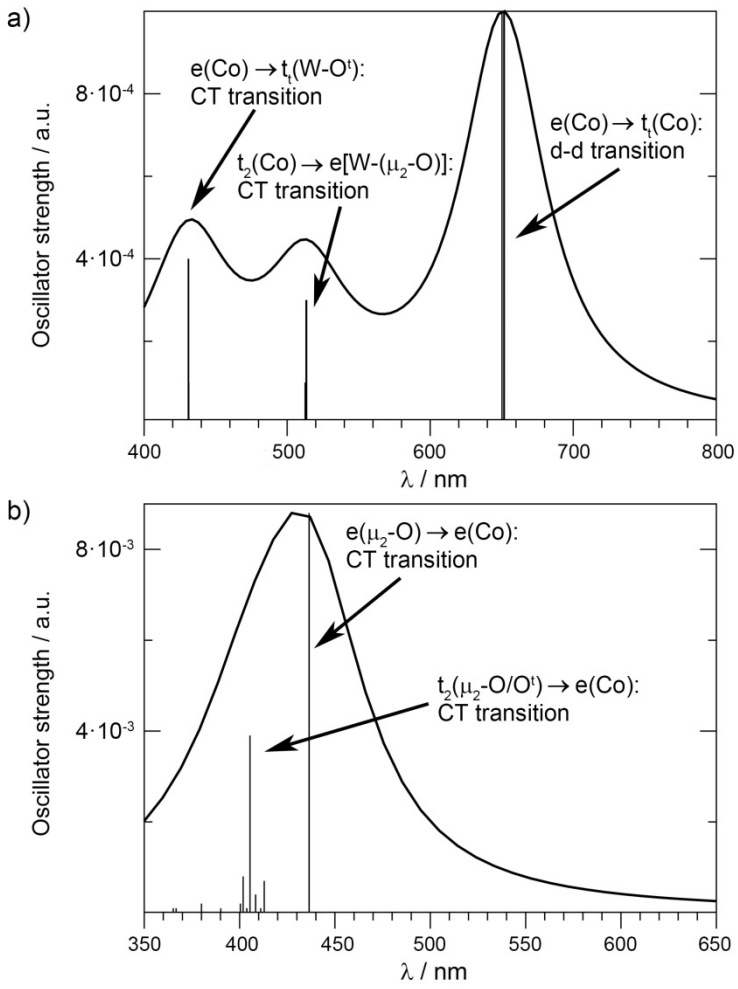

Figure 2.5. The calculated UV-visible spectrum of a) quartet **2.1a** and b) quintet **2.2a**. The lines in the main feature are marked by their dominant electronic transitions. See Figure 2.6 for definitions of the presented frontier orbitals.

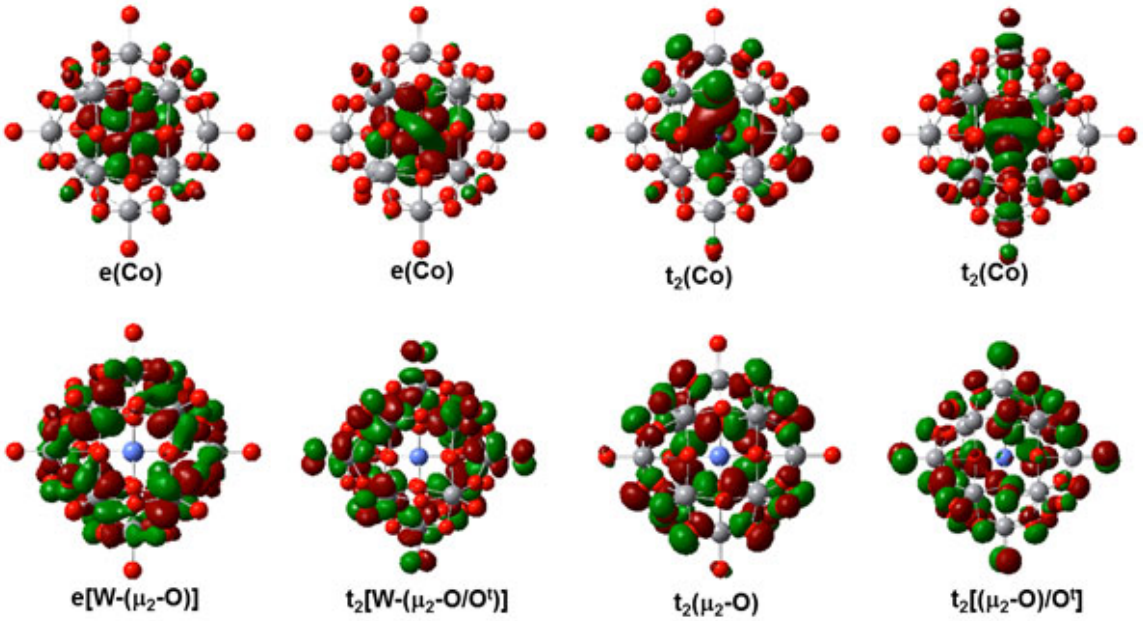

Figure 2.6. Important molecular orbitals for $[Co^{II}W_{12}O_{40}]^{6-}$ (**2.1a**) and $[Co^{III}W_{12}O_{40}]^{5-}$ (**2.2a**) cluster anions.

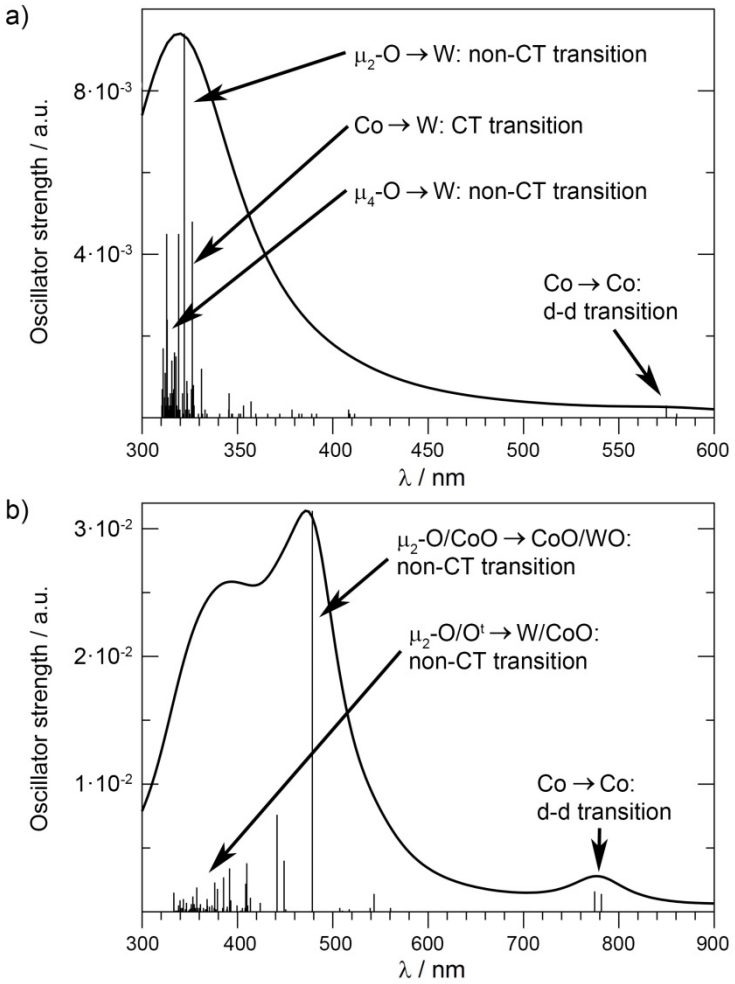

Figure 2.7. The calculated UV-visible spectrum of a) quartet **2.3a** and b) triplet **2.4a**. The lines in the main feature are marked by their dominant electronic transitions. See Figure 2.8 for definitions of the presented frontier orbitals.

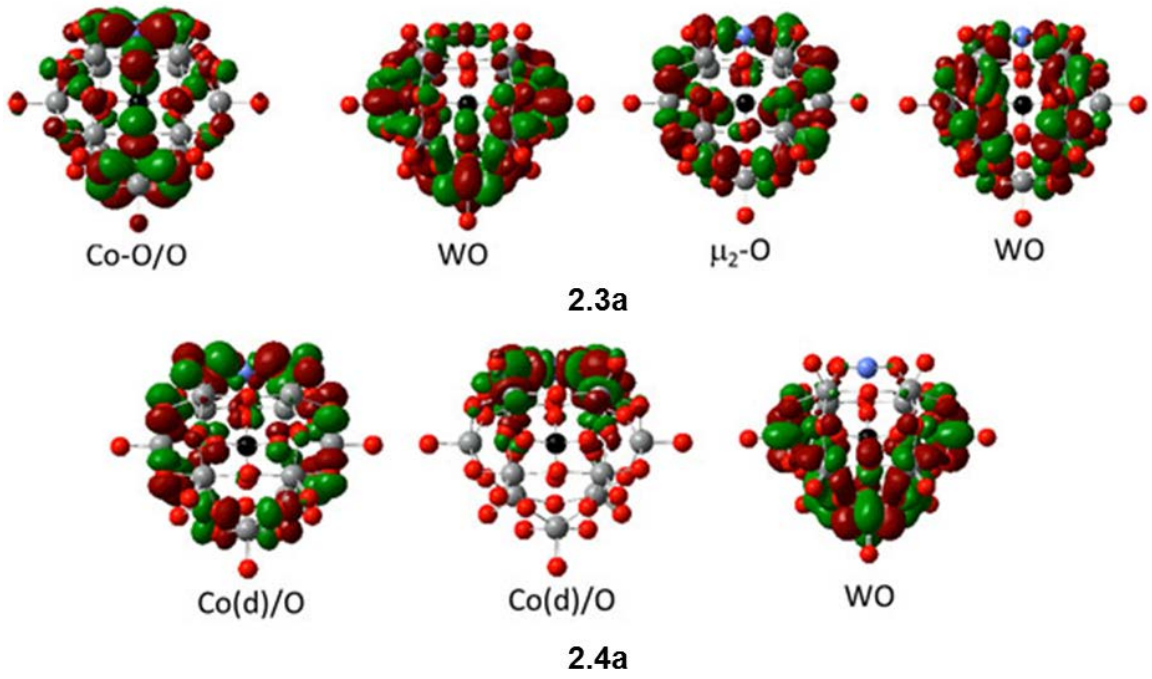

Figure 2.8. Important molecular orbitals for quartet anions $[SiCo^{II}(H_2O)W_{11}O_{39}]^{6-}$ (**2.3a**, first line) and triplet $[SiCo^{III}(H_2O)W_{11}O_{39}]^{5-}$ (**2.4a,** second line) cluster anions.

In anions containing Co^{II}, it is expected that Co→W CT transitions should be observed. For **2.1a**, electrochemically determined potentials for the $Co^{2+/3+}$ couple and first polytungstate reduction (Figure 2.9a) allow estimation of an energy difference of 1.29 eV (961 nm) between the highest energy Co^{II}-based orbitals and the polytungstate LUMO. The same analysis cannot be performed on **2.3a** (Figure 2.9b), because the tungstate redox process cannot be cleanly observed at pH values in which the anion is stable. Based on the more oxidizing position of the $Co^{2+/3+}$ couple in **2.3a**, however, it is expected that the same transition would occur at higher energy compared to **2.1a.** Indeed, several overlapping absorption peaks are observed between 1000 and 1400 nm (Figure 2.4b), which have been attributed to ligand-field and charge-transfer transitions.[27]

Detailed computational analysis of the lower-lying excited states of **2.1a** also finds e(Co)→t_2(W) CT character in three dipole forbidden transitions at ~1200 nm, although this is dominated by e(Co)→t_2(Co), i.e., non-CT Co d-d transitions (see Table 2.3). Combining the electrochemically estimated HOMO – LUMO gap with the 1.98 eV (625 nm) *e* to t_2 d-orbital splitting allows prediction of higher energy Co→W transitions at *ca*. 3.25 eV (380 nm), which have not been previously identified.[27,30] This is supported by our calculations, which for **2.1a** predict e(Co_{Td})→e(W) and t_2(Co_{Td})→e(W) CT transitions at ~430 and 510 nm respectively. These transitions are observed in the form of a gentle rise in absorption between 420 and 380 nm, which may coincide with O→Co transitions. In the case of pseudo-octahedral Co^{II}-based **2.3a**, examination of the excited state wavefunctions reveals a group of CT-like Co→W excitations in **2.3a** near 320 nm which are obscured by O→Co and O→W processes. It therefore seems likely (and is experimentally demonstrated below) that excitation of either **2.1a** or **2.3a** at around 400 nm will cause transfer of an electron from Co to the polyoxotungstate framework, allowing study of the influence of the metal coordination site on excited state behavior.

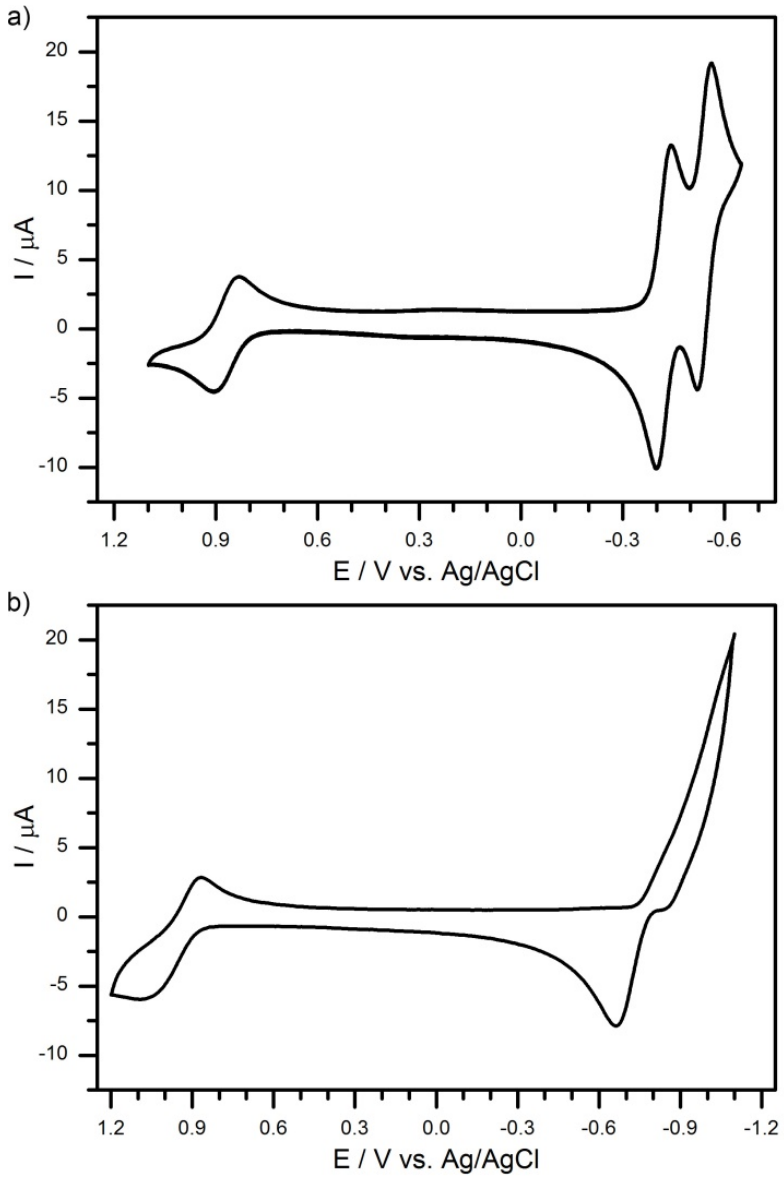

Figure 2.9. Cyclic voltammograms of a) 0.50 mM **2.2** in 0.250 M sodium sulfate buffer, pH 2, and b) 1.10 mM **2.3** in 0.250 M lithium acetate buffer, pH 5, both at a 50 mV/s scan rate.

Table 2.3. Excited states of the cluster anion **2.1a** computed at the TD-DFT level of theory in water

State	λ / nm	Osc. Str. / a.u.	Leading Configurations
1^4T	1215	0.0000	$\{e_{CoO} \rightarrow t_{CoO}\} + \{e_{CoO} \rightarrow t_{Co...W}\}$
1^4E	672	0.0000	$\{e_{CoO} \rightarrow e_{CoO}\} + \{e_{CoO} \rightarrow e_{WO}\}$
2^4E	670	0.0000	$\{e_{CoO} \rightarrow e_{CoO}\} + \{e_{CoO} \rightarrow e_{WO}\}$
2^4T	652	0.0010	$\{e_{CoO} \rightarrow t_{CoO}\}$
3^4T	565	0.0000	$\{e_{CoO} \rightarrow t_{WO}\}$
4^4T	563	0.0000	$\{e_{CoO} \rightarrow t_{WO}\}$
5^4T	513	0.0003	$\{t_{CoO} \rightarrow e_{WO}\}$
6^4T	512	0.0001	$\{t_{CoO} \rightarrow e_{WO}\}$
3^4E	454	0.0000	$\{t_{CoO} \rightarrow t_{WO}\}$
7^4T	448	0.0000	$\{t_{CoO} \rightarrow t_{WO}\}$
1^4A	443	0.0000	$\{t_{CoO} \rightarrow t_{WO}\}$
8^4T	442	0.0000	$\{t_{CoO} \rightarrow t_{WO}\}$
9^4T	431	0.0004	$\{e_{CoO} \rightarrow t_{WO}\}$
10^4T	430	0.0004	$\{e_{CoO} \rightarrow t_{WO}\}$
2^4A	429	0.0000	$\{e_{CoO} \rightarrow e_{WO}\}$
4^4E	428	0.0000	$\{e_{CoO} \rightarrow a_{WO}\}$
5^4E	425	0.0000	$\{e_{CoO} \rightarrow e_{WO}\}$

2.4.3 Transient Absorption Spectra and Kinetics

Transient absorption spectra and kinetics of aqueous **2.1** at selected time delays after 400 nm excitation are shown in Figure 2.10. Immediately following excitation, **2.1** produces broad, intense absorption features that rapidly decay within 5 ps. The initial excited state of **2.1** decays with a time constant of τ_1 = 730 ± 40 fs, after which the overall shape of the difference spectrum does not change until full ground state recovery takes place. This second excited state species is much longer lived, with a transient spectrum showing a ground state bleach centered at 625 nm and absorption bands at <500 nm and >700 nm. Clear isosbestic points are observed at 550 nm and 675 nm, with single-exponential nonradiative decay dynamics, indicating decay of a single species to

the ground state. The lifetime of this species, τ_2 = 420 ± 30 ps, is far in excess of those measured for any transition-metal substituted polyoxometalate thus far.[18,19,47]

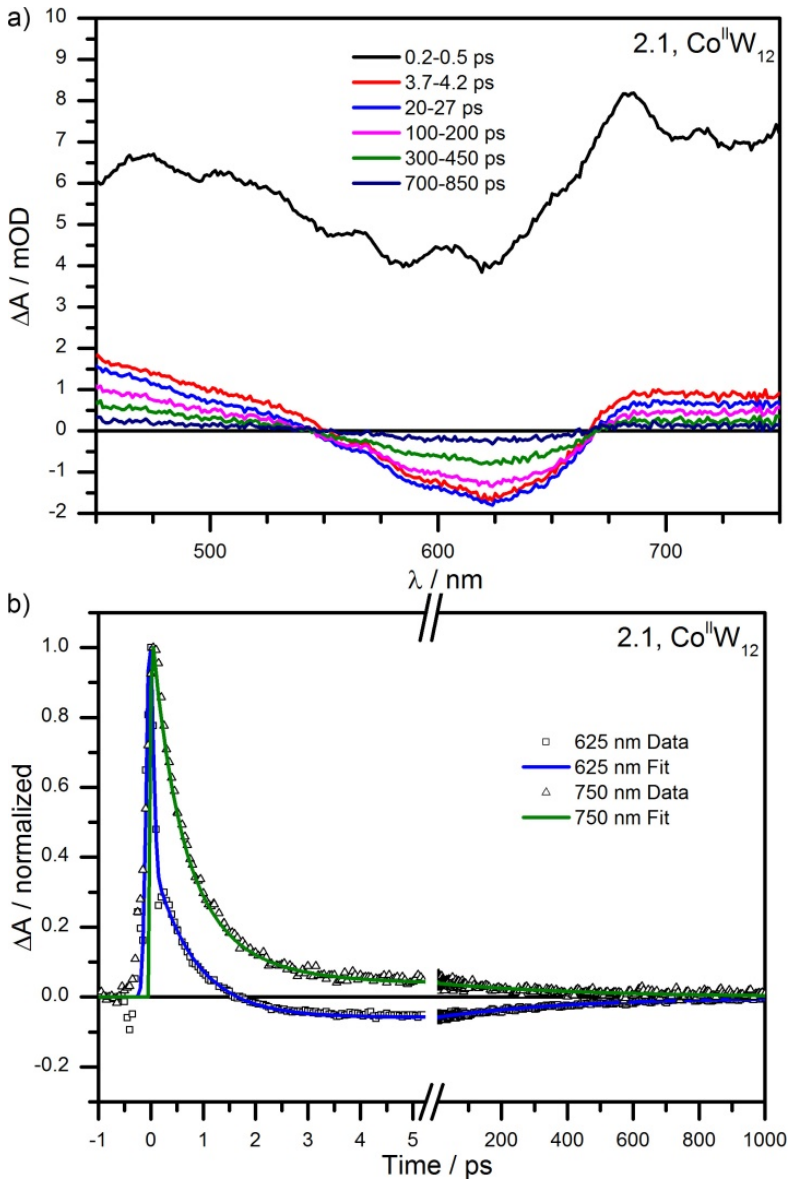

Figure 2.10. a) Transient absorption spectra and b) kinetics of **2.1** after excitation by an ultrafast pump pulse at 400 nm, measured in 0.250 M sodium sulfate buffer, pH 2. Spectral traces are the average of multiple measurements within the noted time windows. Empirical measurements and multiexponential fits to the kinetics at representative wavelengths are shown normalized to their respective peak fit values.

The excited state spectral features of **2.1** bear a strong resemblance to the inverted static ground state absorption spectra and $1e^-$ reduced forms of **2.1** (Figure 2.11). The simulated excited state spectrum for **2.1** (Figure 2.11, blue line) was calculated by taking the $1e^-$ reduced spectrum of **2.1**, adding the spectrum for the oxidized species **2.2**, and subtracting the ground state spectrum of **2.1** twice. The ground state spectrum of **2.1** was subtracted twice to remove the d-d band contribution from the $1e^-$ reduced species as well as the ground state bleach, as expected in a simulated difference spectrum. The initial short-lived species τ_1 resembles a $1e^-$ heteropoly blue, but with lower intensity than the simulated difference spectrum, presumably because the very short lifetime means that substantial decay has already occurred. Thus this strongly absorbing initial state is assigned as a metal-to-polyoxometalate CT (MPCT) excited state, which decays rapidly to a longer-lived intermediate state before ground state recovery. The long-lived excited state, τ_2, exhibits a bleach at 625 nm that matches the ground state $^4A_2 \rightarrow {}^4T_1$ d-d transitions, and the broad absorption at >700 nm resembles the heteropoly blue species formed by one-electron reduction of **2.1**.[48] The ground state bleach of the Co^{II} d-d band reveals that an electron is photoexcited from the tetrahedral Co^{II} center to the vacant tungstate W orbitals, and the intensity of this feature declines only very slightly between τ_1 and τ_2. However, the intensity of the heteropoly blue spectral features in τ_2 are a fraction of those expected in a true $1e^-$ heteropoly blue, having features with extinction coefficients of only ~100 L mol^{-1} cm^{-1}. Regardless, placing an electron-rich metal at the *center*, rather than in the addendum of a POM anion appears to result in a dramatically extended (by two orders of magnitude) MPCT excited state lifetime.[18,19]

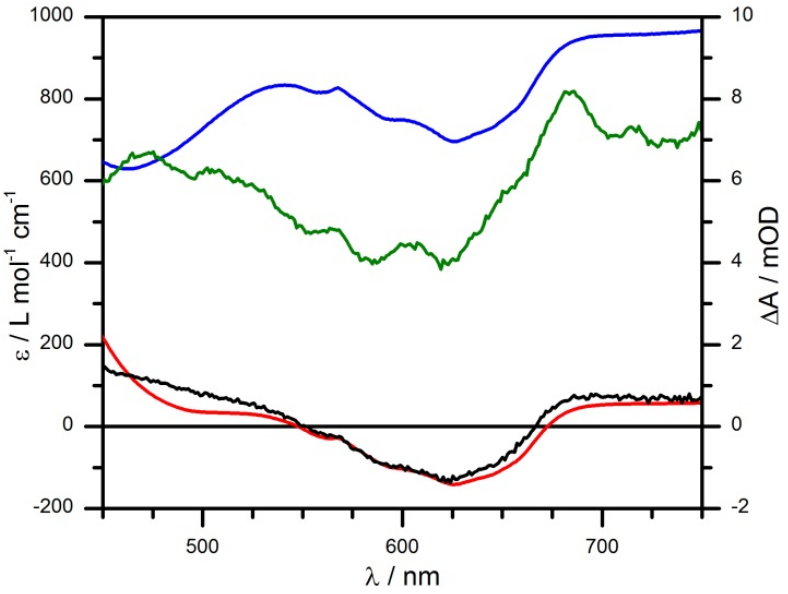

Figure 2.11. Comparison of the transient difference spectra of **2.1** and the simulated difference spectra of the excited states calculated from static ground state spectra of **2.1**, **2.2** and reduced **2.1**. The simulated heteropoly blue species (blue line) is compared to the spectra from 0.2-0.5 ps after excitation, representative of τ_1 (green line). A simulated excited state (red line) with a smaller ($1/12^{th}$) heteropoly blue contribution is compared to the transient spectra from 3.7-4.2 ps, representative of τ_2 (black line).

Both excited state spectra for **2.1** share similar features, though the ground state bleach is clearer for the longer lived process τ_2. The spectra show unexpected absorptions <500 nm which can be explained by red-shifting and intensification of the $O \rightarrow Co_e$ transition observed in **2.2**, due to formation of a Co^{III} center surrounded by a more strongly electron donating *reduced* tungstate framework. The transient spectrum for τ_2 closely resembles a simulated difference spectrum in which a smaller contribution from the heteropoly blue is assumed. The second simulated excited state spectrum for **2.1** (Figure 2.11, red line) was calculated by subtracting the ground state spectrum of **2.1**

from that of the oxidized species **2.2**, then adding a $1/12^{th}$ scaled spectrum of the $1e^-$ reduced species from which **2.1** was previously subtracted. This assumes 100% formation of Co^{III} from Co^{II} during photoexcitation, scaled to a heteropoly blue contribution that closely resembles the observed transient measurement. Reduced frameworks contain delocalized electrons which yield mixed valence heteropoly blues as the result of multiple tungsten atoms being structurally equivalent. The low intensity of the absorptions in τ_2 may suggest that the electron is localized on one or a few of the tungstates instead of being delocalized across the entire framework. Consequently, this proposal implies that a transient structural change occurs that breaks the symmetry of the framework (*vide infra*).

The hypothesis that the weak heteropoly blue contribution to τ_2 is the result of localized charge should be contrasted with the alternative of a low quantum yield process, whereby only ~8% of the photoexcited electrons from τ_1 would form τ_2 and the remainder would collapse back to the ground state via internal conversion. If this were the case, however, one would expect to see a commensurate decrease in the contributions from Co^{III} and the Co^{II} ground state bleach. Instead, a simulated excited state spectrum very close to τ_2 is produced by combining full contributions from spectra of **2.1** and **2.2** and $1/12^{th}$ that of a $1e^-$ reduced heteropoly blue. This suggests that the heteropoly blue spectral signature observed in τ_2 is weaker than expected because less of the tungsten framework is involved, not because electrons have returned to the Co atom.

Salt metathesis of **2.1** to **2.1-TBA** was performed to measure the excited state lifetimes in an organic solvent. The electronic absorption spectrum of **2.1-TBA** in MeCN (Figure 2.12) is nearly identical to that of **2.1** in water. The slight shift of the Co_{Td} d-d band, with λ_{max} shifting to 628 nm, is consistent with a central heteroatom that is largely

isolated from the polytungstate framework and the solvent, showing minimal solvatochromism.[21,35,46,49] The excited state dynamics of **2.1-TBA** show similar biphasic decay kinetics (Figure 2.13), with the initial excited state decaying with a time constant of $\tau_1 = 810 \pm 30$ fs. Remarkably, the long-lived excited state component is extended by a factor of four, having a time constant of $\tau_2 = 1700 \pm 140$ ps. This appreciable solvent dependence supports the notion of charge localization in the long-lived excited state. If the initial MPCT excited state is delocalized, a dipole moment does not exist in the molecule due to symmetry. As a result, the initial excited state shows minimal solvent dependence in going to a less polar solvent (730 fs in water vs. 810 fs in MeCN). On the other hand, the solvent dependence of τ_2 suggests the presence of a charge transfer dipole moment, only possible if the electron residing on the polytungstate framework is localized to some degree.[50,51] This is reminiscent of the charge localization that occurs in $[Ru(bpy)_3]^{2+}$ on the ultrafast time scale.[52,53] The nanosecond lifetime of τ_2 in MeCN is consistent with the energy-gap law for nonradiative decay in intramolecular charge transfer excited states. Hydrogen bonding in water can also contribute to the shorter lifetime of τ_2 in water, as protic media can contribute to nonradiative decay pathways due to favorable interaction with charge transfer states.[54]

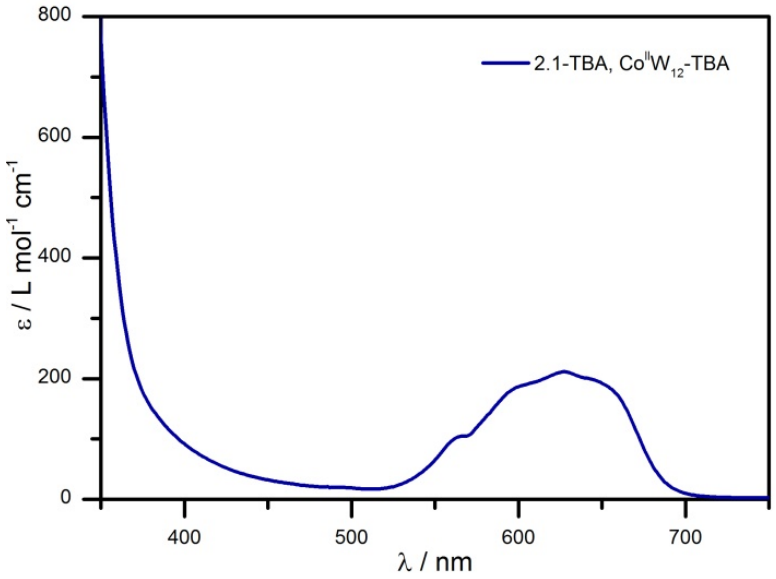

Figure 2.12. Visible electronic absorption spectra of **2.1-TBA** in MeCN.

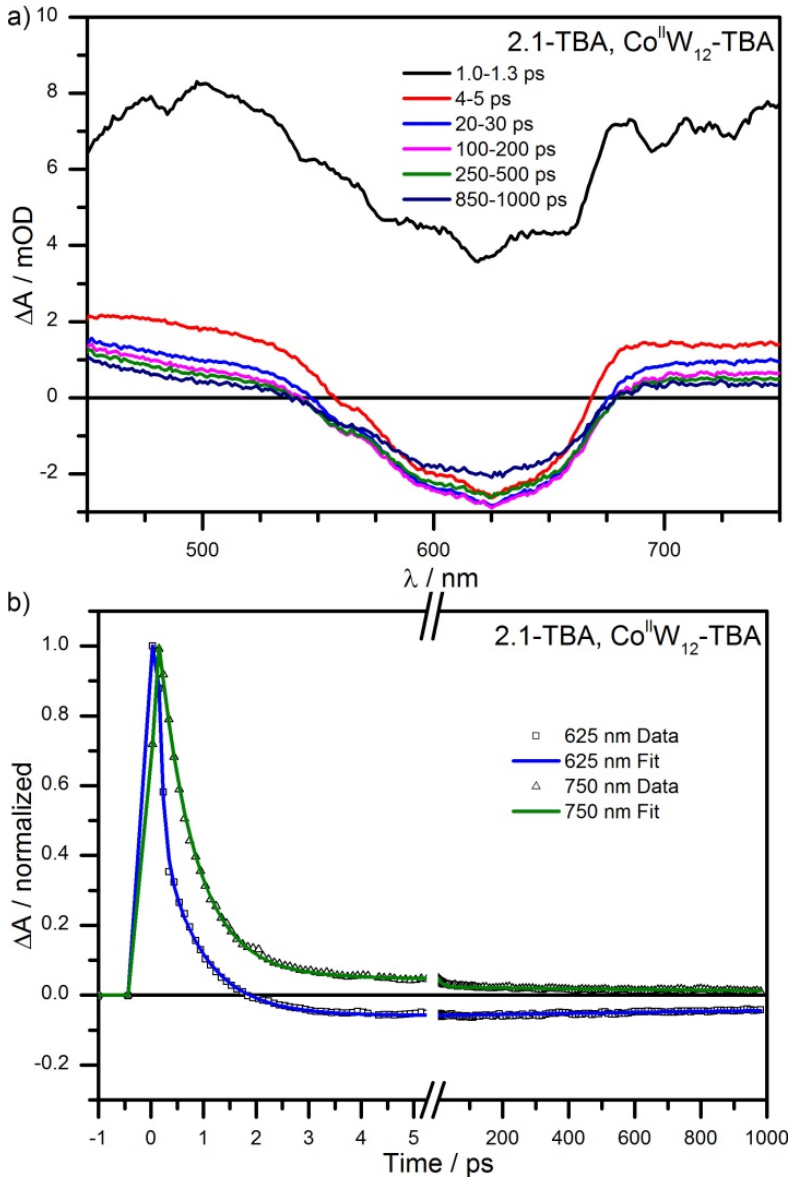

Figure 2.13. a) Transient absorption spectra and b) kinetics of **2.1-TBA** measured in MeCN after excitation by an ultrafast pump pulse at 400 nm. Spectral traces are the average of multiple measurements within the noted time windows. Empirical measurements and multiexponential fits to the kinetics at representative wavelengths are shown normalized to their respective peak fit values.

To confirm that the location and oxidation state of cobalt are important to generation of the long-lived excited state, we studied the excited-state dynamics of **2.2** to **2.4**. In **2.2** (the oxidized analogue of **2.1**), biphasic decay kinetics are also observed (Figure 2.14), but with complete decay to the ground state within around 20 ps (τ_1 = 220 ± 50 fs; τ_2 = 4.4 ± 0.6 ps). This provides further evidence that electron transfer from Co^{II} to the polytungstate ligand is responsible for the long-lived excited state in **2.1**. Excitation of **2.2** at 400 nm should only involve the $O \rightarrow Co_e$ transition, as lowering of the Co_{Td} Co_e orbitals due to Jahn-Teller distortion[24,26,28,29] increases the energy of the $Co \rightarrow W$ charge transfer transition, while lowering the energy of $O \rightarrow Co$ charge transfer. The resulting excited state consisting of a hole on an oxygen atom adjacent to a distorted Co^{II} should recombine rapidly. Involvement of $Co \rightarrow W$ processes is unlikely as it would generate very high energy states containing Co^{IV} and reduced tungstate. Electrochemical generation of $[Co^{IV}W_{12}O_{40}]^{4-}$ to provide a spectroscopic handle for Co^{IV} in these systems has not been possible.

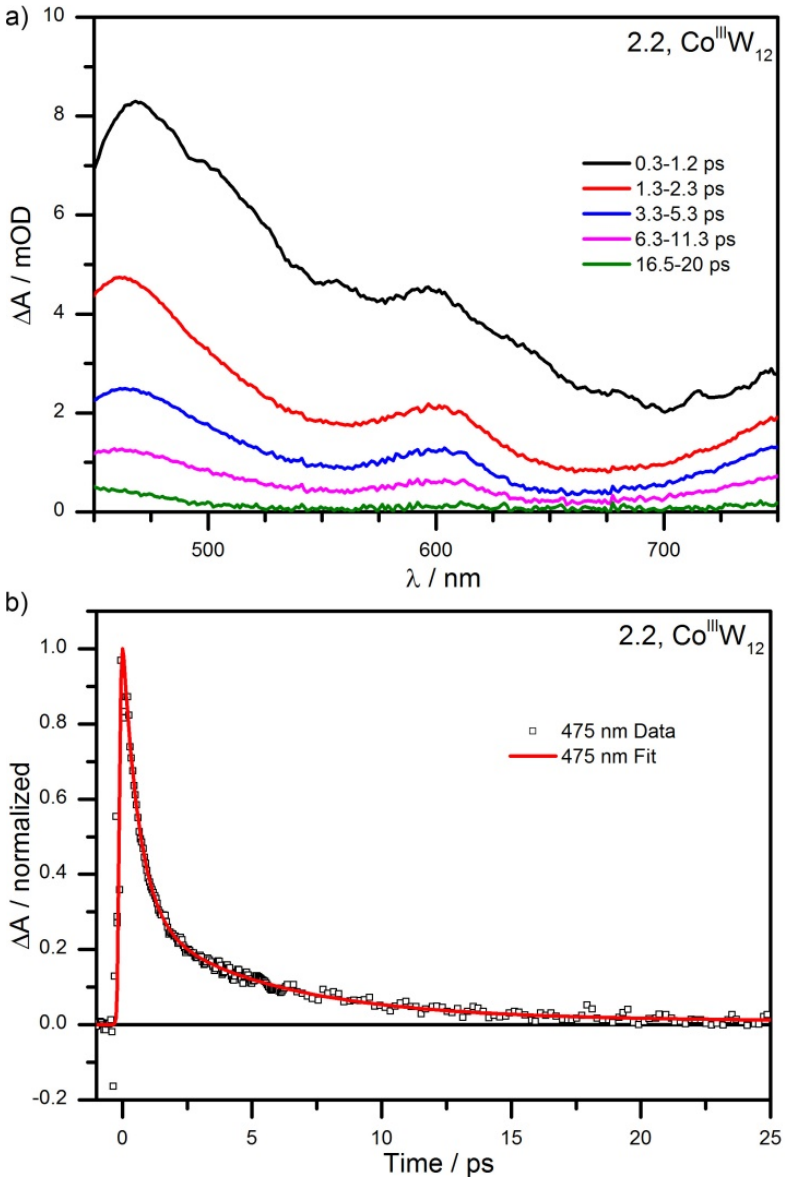

Figure 2.14. a) Transient absorption spectra and b) kinetics of **2.2** after excitation by an ultrafast pump pulse at 400 nm, measured in 0.250 M sodium sulfate buffer, pH 2. Spectral traces are the average of multiple measurements within the noted time windows. Empirical measurements and multiexponential fits to the kinetics at representative wavelengths are shown normalized to their respective peak fit values.

In anion **2.3a**, the Co^{II} is moved to a pseudo-octahedral addendum site, with a Si heteroatom. In this case, $Co_{Oh}^{II} \rightarrow W$ charge transfer may occur. Transient spectral features (Figure 2.15) suggest that it does, through formation of a bleach at 546 nm corresponding to the Co_{Oh}^{II} d-d bands and a broad absorption at >600 nm consistent with reduction of the polytungstate. An additional new absorption is seen at 440 nm. Similar to **2.1a**, the initially formed MPCT state rapidly decays (τ_1 = 570 ± 40 fs) to a less intense state featuring similar features bracketing the Co_{Oh}^{II} d-d bleach (Figure 2.16). The first simulated excited state spectrum for **2.3** was calculated the same way as for **2.1**. The second excited state spectrum was most closely approximated by subtracting the ground state spectrum of **2.3** from that of the oxidized species **2.4**, with no heteropoly blue contribution. However, the features of the second excited state decay much more quickly than in **2.1a** (within 5 ps), although the weakness of the 546 nm feature has prevented accurate fitting and extraction of time constants for decay (τ_2 = 1.3 ± 3.8 ps). To complete the series, the ultrafast dynamics of **2.4** (the oxidized analogue of **2.3**, Figure 2.17) exhibit a short-lived biphasic excited state (τ_1 = 400 ± 150 fs; τ_2 = 6.3 ± 0.6 ps), where a single broad absorption at 470 nm rapidly decays to the baseline within 30 ps. In this case, the primary excited transition should be O→Co/W mixed orbitals. Overall, these results strongly suggest that the long-lived excited state in **2.1** is linked to location of a Co^{II} heterometal in the central, tetrahedral site of the anion **2.1a**.

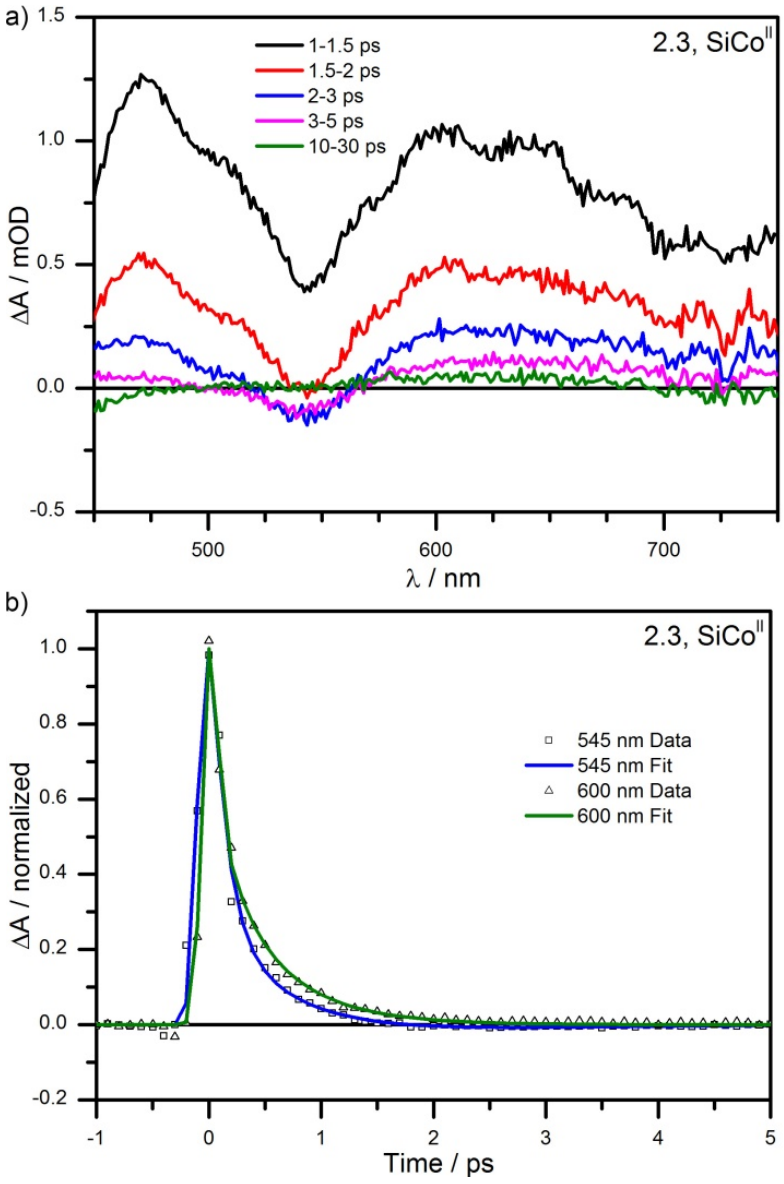

Figure 2.15. a) Transient absorption spectra and b) kinetics of **2.3** after excitation by an ultrafast pump pulse at 400 nm, measured in 0.250 M lithium acetate buffer, pH 5. Spectral traces are the average of multiple measurements within the noted time windows. Empirical measurements and multiexponential fits to the kinetics at representative wavelengths are shown normalized to their respective peak fit values.

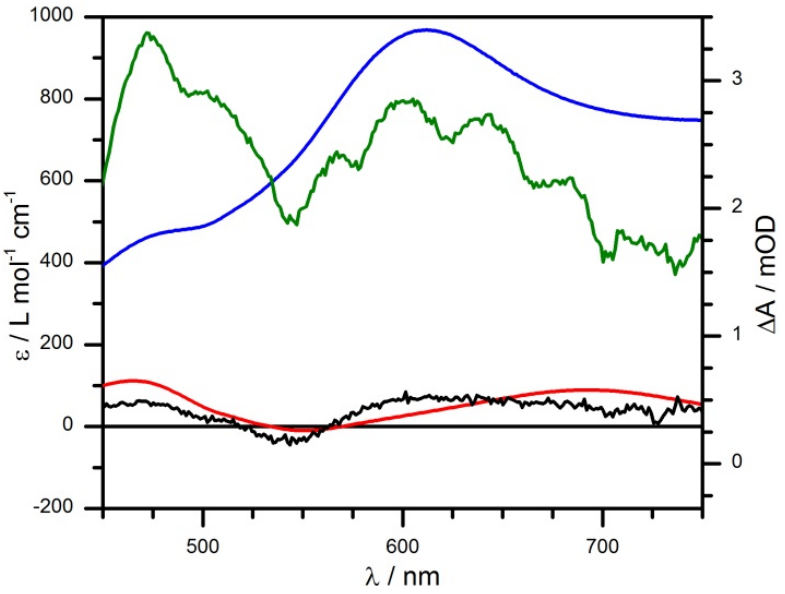

Figure 2.16. Comparison of the transient spectra of **2.3** and the simulated difference spectra of the excited states calculated from static ground state spectra of **2.3**, **2.4** and reduced **2.3**. The simulated heteropoly blue species (blue line) is compared to the spectra from 0.5-1.0 ps after excitation, representative of τ_1 (green line). A simulated excited state (red line) is compared to the transient spectra from 2.0-3.0 ps, representative of τ_2 (black line).

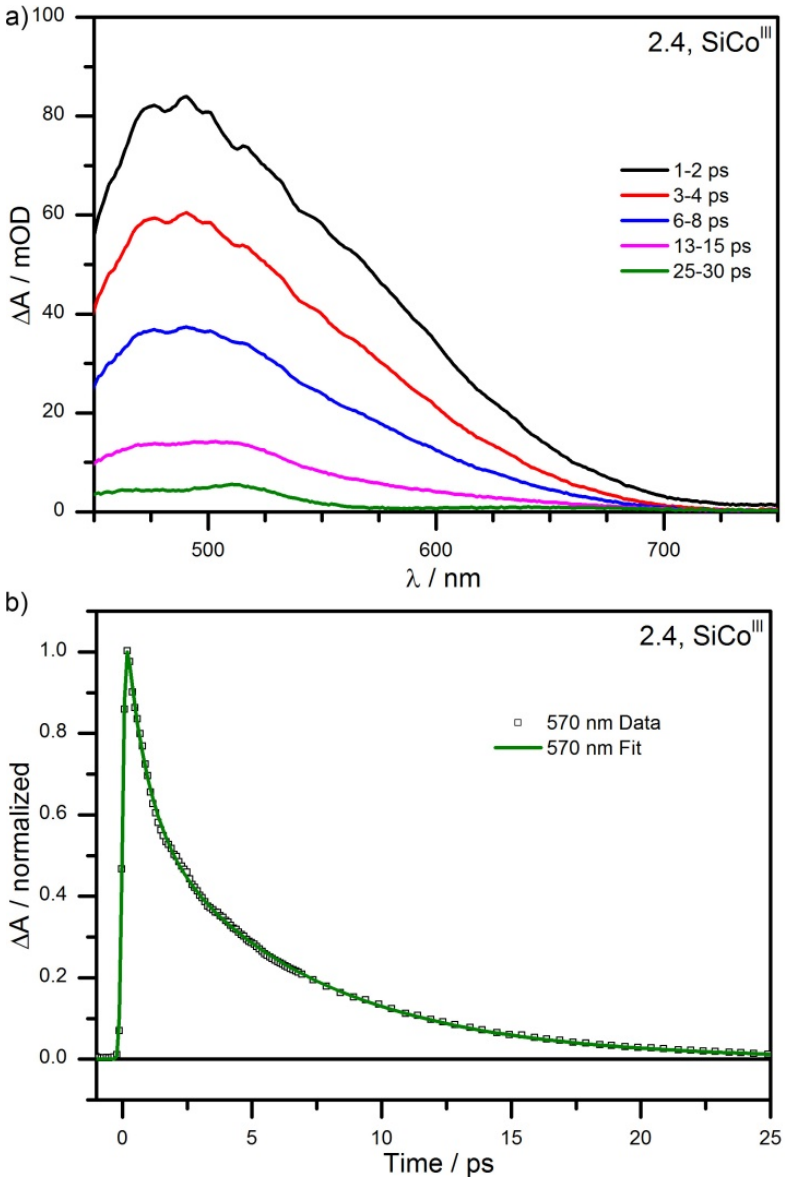

Figure 2.17. a) Transient absorption spectra and b) kinetics of **2.4** after excitation by an ultrafast pump pulse at 400 nm, measured in 0.250 M lithium acetate buffer, pH 5. Spectral traces are the average of multiple measurements within the noted time windows. Empirical measurements and multiexponential fits to the kinetics at representative wavelengths are shown normalized to their respective peak fit values.

Briefly, we also note here that early time data (0.3 to 5 ps) for all four anions indicates broad, intense absorptions peaking between 400 and 500 nm. Interpretation of this data is difficult due to the combination of dynamic processes associated with the initial excited state and the temporal resolution of the instrument (~150 fs), but their observation in all four anions suggests they are related to concurrent internal conversion and vibrational relaxation within the polytungstate framework (Tables 2.4 and 2.5). For **2.1** and **2.3**, these processes complete within 5 ps to yield secondary excited states. Different transitions are involved in **2.2** and **2.4**, and the second excited state lifetime is likely the result of thermalization.

Table 2.4. Multi-exponential lifetimes of transient absorption spectra

Compound	**Lifetimes**	
	τ_1 / fs	τ_2 / ps
$[Co^{II}W_{12}O_{40}]^{6-}$ (**2.1**)	730 ± 40	420 ± 30
2.1-TBA in MeCN	810 ± 30	1700 ± 140
$[Co^{III}W_{12}O_{40}]^{5-}$ (**2.2**)	220 ± 50	4.4 ± 0.6
$[SiCo^{II}(H_2O)W_{11}O_{39}]^{6-}$ (**2.3**)[a]	570 ± 40	1.3 ± 3.8
$[SiCo^{III}(H_2O)W_{11}O_{39}]^{5-}$ (**2.4**)	400 ± 150	6.3 ± 0.6

[a] Lifetime determined by single wavelength kinetics at 546 nm only

Table 2.5. Multi-exponential fit parameters of transient absorption decay spectra at selected wavelengths

Compound	**Wavelength**	**Lifetimes**		**Norm. Coefficients**	
	λ / nm	τ_1 / fs	τ_2 / ps	A_1	A_2
$[Co^{II}W_{12}O_{40}]^{6-}$ (**2.1**)	475	710 ± 50	340 ± 50	0.89	0.11
	625	700 ± 40	430 ± 30	0.86	-0.14
	700	710 ± 40	400 ± 90	0.94	0.06
	750	790 ± 50	480 ± 100	0.94	0.06
$[Co^{III}W_{12}O_{40}]^{5-}$	475	380 ± 90	5.2 ± 0.6	0.66	0.34
(**2.2**)	600	150 ± 40	4.3 ± 0.5	0.80	0.20
	750	180 ± 60	7.1 ± 0.5	0.63	0.37
$[SiCo^{II}(H_2O)W_{11}$	475	580 ± 50	-	1.00	0.00
$O_{39}]^{6-}$ (**2.3**)	545	260 ± 60	6.0 ± 20	0.99	-0.01
	546	570 ± 40	1.3 ± 3.8	0.99	-0.01
	600	630 ± 60	-	1.00	0.00
$[SiCo^{III}(H_2O)W_{11}$	470	230 ± 30	5.9 ± 0.1	0.44	0.56
$O_{39}]^{5-}$ (**2.4**)	490	350 ± 130	5.8 ± 0.2	0.21	0.79
	570	980 ± 80	6.6 ± 0.2	0.44	0.56

2.4.4 Origin of the Long-Lived Excited State in Anion 2.1a

Given the enormous difference in the excited state lifetimes of Co_{Td}^{II}-centered **2.1a** and Co_{Oh}^{II}-substituted **2.3a**, it appears that the coordination environment of Co must have an important influence on the nature of the excited state. In other words, a substantial barrier to ultrafast recombination must exist in **2.1a** that does not exist in **2.3a**.

Structural barriers to ground state recovery resulting from distorted excited state geometries are important in the photophysics of transition metal complexes. For example, substantial structural changes occurring on the ultrafast timescale have been reported for tetrahedral copper complexes,[55,56] and structural distortions have been invoked as an explanation for the surprisingly long excited state lifetimes measured for silica supported MMCT heterodimers.[6] Therefore, it is worth noting that the central heteroatom site of

the $[X^{n+}W_{12}O_{40}]^{(8-n)-}$ Keggin anion shows considerable coordinative flexibility, with a brief survey of crystal structures indicating a range of central X-O distances from *ca*. 1.53 to 1.93 Å.[26] This is because the preferences of the heteroatom X can be compensated by changes in the length of the relatively weak bond from W to the internal oxygen.[28] In the case of $[Co^{II}W_{12}O_{40}]^{6-}$ (**2.1a**) and $[Co^{III}W_{12}O_{40}]^{5-}$ (**2.2a**) a shortening of Co-O bond lengths of approximately 0.1 Å is observed upon moving from Co^{II} to Co^{III}, accompanied by a small Jahn-Teller distortion and reduction in symmetry. The addendum coordination site is less flexible: the rather few positional disorder-free structures available for $[X^{n+}Z^{m+}(L)W_{11}O_{39}]^{(12-n-m)-}$ anions show relatively little variation in their average equatorial Z-O distances (*ca*. 1.94 to 2.01 Å).[57-65] Bond distances for Co_{Oh}^{II}-O (around 2.09 Å in $[Co(H_2O)_6]^{2+}$)[66] are therefore likely to be compressed to around 2 Å in **2.3a**, and may not contract much further upon transient oxidation to Co^{III} ($[Co(H_2O)_6]^{3+}$ has Co-O distances of around 1.98 Å).[67] There is also less reorganization energy for Jahn-Teller distortion between octahedral Co^{II} and Co^{III} than for their tetrahedral $Co^{II/III}$ counterparts. The shorter lifetime of the excited state of **2.3** could also be influenced by the presence of a labile aqua ligand, which may contribute additional vibrational relaxation pathways via hydrogen bonding and solute-solvent interactions.[68-70]

The degree of Jahn-Teller distortion during photo-excitation of **2.1** can be qualitatively evaluated by considering the reorganization energy, calculated by direct measurement of the self-exchange rates for the outer sphere electron transfer between **2.1a** and **2.2a**.[71] A range of 23 to 85 kcal mol^{-1} (1.0 to 3.7 eV) has been calculated for the *total* reorganization energy of the **2.1a**/**2.2a** system.[49,72-75] The inner sphere reorganization energy, corresponding to the energy barrier for interconversion of the

$[Co^{II}O_4]^{6-}/[Co^{III}O_4]^{5-}$ tetrahedron, was measured as 11.05 kcal mol^{-1} (0.48 eV).[71] This large reorganization energy could easily account for the long excited-state lifetime of **2.1a** by decreasing the rate of back-electron transfer between the polytungstate framework and Co^{III}. In the case of **2.3a**, such a significant reorganization barrier is unlikely. Furthermore, the orbital overlap between the central Co^{II} and the polytungstate framework is known to be poor, as multiple studies have established the electronic isolation of the central atom in **2.1a**.[21,35,46,49] Consequently, the electronic coupling term will be lower for the tetrahedral central atom compared to that of the pseudo-octahedral addendum site. This will also contribute to a slower back-electron transfer rate, although it also lowers the oscillator strength of the initial transition (hence its weakness).

It is clear from the transient absorption data that the initially formed MPCT state of **2.1a** rapidly decays to a second excited state with similar, though less intense, spectral features. The dynamic Jahn-Teller distortion in moving from Co^{II} to Co^{III} reduces the local symmetry of the tetrahedral $[Co^{II}O_4]^{6-}$ heteroatom. Concurrently, the reduced polytungstate framework, normally composed of twelve structurally equivalent tungstates, is perturbed by the irregular $[Co^{III}O_4]^{5-}$ tetrahedron. The heteropoly blue MPCT state subsequently collapses from a 12-fold delocalization to a 3-fold (delocalized across a single triad cap) or singly-reduced tungstate. Such a transient valence trap (illustrated in Figure 2.18) would explain the spectral features of the long-lived excited state of **2.1a**, with the long lifetime attributed to a localized electron impeded from returning to the ground state by a significant reorganization energy barrier. Valence trapping has been observed in other heteropoly blue complexes at low temperatures and in vanadium-substituted POMs,[76,77] though this is the first time this has been proposed in

the photophysical mechanism of a POM.

Intersystem crossing is a final factor that may contribute to the excited state lifetime of **2.1a**. The initially formed Franck-Condon state following excitation is ^{4}MPCT, with four singly occupied Co orbitals, and is not energetically favorable. Intersystem crossing (ISC) should therefore occur to yield a ^{6}MPCT state. This most likely occurs within the same time scale as the dynamic Jahn-Teller distortion of the transient Co^{III} e.g. within the 5 ps it takes for the early dynamic process, τ_1, to complete, suggesting an intersystem crossing rate constant in excess of 10^{12} s^{-1}. Such fast rates for ISC have been previously demonstrated in $[Ru(bpy)_3]^{2+}$,[56] a low-spin Fe^{II} complex,[78] and Au^I naphthalene compounds,[79] among others. However, it is important to note that ISC would also be expected to apply to MPCT excited states generated from octahedral Co^{II}, so this factor alone cannot account for the difference in excited state lifetimes.

In the context of molecular sensitizers for solar fuel production, **2.1a** has the longest lived charge transfer excited state observed in a POM to date by more than two orders of magnitude.[18,19] While still short compared to many organic and metal-organic photosensitizers, this extended lifetime is potentially chemically interceptable considering the femtosecond electron injection kinetics known for dye-sensitized metal oxides.[78,80-83] Furthermore, **2.1a** leverages the known thermal and oxidative stability of POMs by being exceptionally stable in solution and under irradiation. No evidence of structural decomposition is observed by electronic absorption spectroscopy after prolonged irradiation at 400 nm, and solutions of **2.1** kept in aqueous buffer (pH 2-5), water, or MeCN for several months show no change in their absorption spectrum.

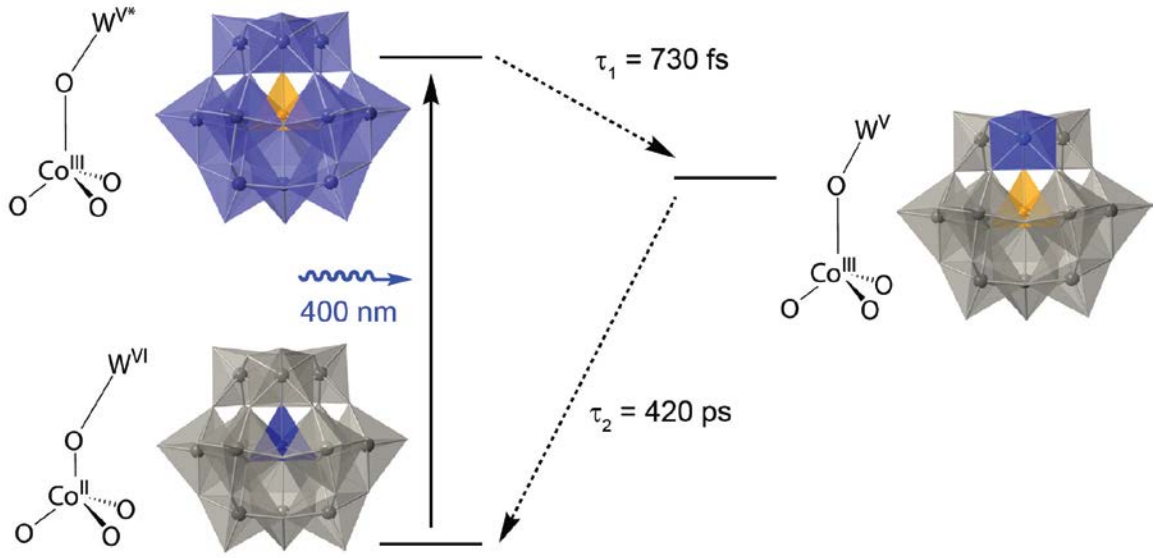

Figure 2.18. Proposed excited state decay pathway for **2.1a** illustrating the transient valence trap suggested by the long-lived excited state τ_2. W^{V*} indicates a fully delocalized heteropoly blue state. Stick diagrams of the core tetrahedron illustrate distortion of the heteroatom environment; polyhedral representations of the complete POM indicate the position of the photoexcited electron (blue shading).

2.5 Conclusion

The polyoxometalate anions $[Co^{II}W_{12}O_{40}]^{6-}$ (**2.1a**) and $[SiCo^{II}(H_2O)W_{11}O_{39}]^{6-}$ (**2.3a**) both have MPCT excited states which are accessible with visible excitation. In the case of **2.1a**, this state decays to a second excited state which is far longer-lived (at 420 ps in H_2O, 1700 ps in MeCN) than for any other polyoxometalate studied thus far. The lifetime of the MPCT excited state of **2.1a** can be rationalized through geometric distortions - both shortening of Co-O bond distances and Jahn-Teller distortion - induced by the change in oxidation state at the Co center, and permitted by the more flexible central coordination site. This insight may help design new systems which combine the

stronger visible extinction coefficients of our previous rhenium carbonyl systems, with longer lifetimes which might allow exploitation these chromophores in solar energy applications where their oxidative, photochemical and thermal stability is advantageous.

2.6 References

(1) Lin, W.; Frei, H. *J. Am. Chem. Soc.* **2005**, *127*, 1610.

(2) Lin, W.; Frei, H. *J. Phys. Chem. B* **2005**, *109*, 4929.

(3) Han, H.; Frei, H. *J. Phys. Chem. C* **2008**, *112*, 16156.

(4) Han, H.; Frei, H. *J. Phys. Chem. C* **2008**, *112*, 8391.

(5) Wu, X.; Weare, W. W.; Frei, H. *Dalton Trans.* **2009**, 10114.

(6) Cuk, T.; Weare, W. W.; Frei, H. *J. Phys. Chem. C* **2010**, *114*, 9167.

(7) Takashima, T.; Yamaguchi, A.; Hashimoto, K.; Nakamura, R. *Chem. Commun.* **2012**, *48*, 2964.

(8) Takashima, T.; Nakamura, R.; Hashimoto, K. *J. Phys. Chem. C* **2009**, *113*, 17247.

(9) Ghosh, P. K.; Brunschwig, B. S.; Chou, M.; Creutz, C.; Sutin, N. *J. Am. Chem. Soc.* **1984**, *106*, 4772.

(10) Moshofsky, B.; Mokari, T. *Chem. Mater.* **2012**, *25*, 1384.

(11) Zhu, L. F.; She, J. C.; Luo, J. Y.; Deng, S. Z.; Chen, J.; Xu, N. S. *J. Phys. Chem. C* **2010**, *114*, 15504.

(12) Mor, G. K.; Prakasam, H. E.; Varghese, O. K.; Shankar, K.; Grimes, C. A. *Nano Lett.* **2007**, *7*, 2356.

(13) Klahr, B. M.; Martinson, A. B. F.; Hamann, T. W. *Langmuir* **2010**, *27*, 461.

(14) Han, S.; Li, J.; Chen, X.; Huang, Y.; Liu, C.; Yang, Y.; Li, W. *Int. J. Hydrogen Energy* **2012**, *37*, 16810.

(15) Lee, W. J.; Shinde, P. S.; Go, G. H.; Ramasamy, E. *Int. J. Hydrogen Energy* **2011**, *36*, 5262.

(16) Hill, C. L. *Chem. Rev.* **1998**, *98*, 1.

(17) Borrás-Almenar, J. J.; Coronado, E.; Müller, A.; Pope, M. T. *Polyoxometalate Molecular Science. Proceedings of the NATO Advanced Study Institute, Tenerife, Spain from 25 August to 4 September 2001*; Kluwer Academic Publishers: Dordrecht, 2003; Vol. 98.

(18) Zhao, C.; Huang, Z.; Rodríguez-Córdoba, W.; Kambara, C. S.; O'Halloran, K. P.; Hardcastle, K. I.; Musaev, D. G.; Lian, T.; Hill, C. L. *J. Am. Chem. Soc.* **2011**, *133*, 20134.

(19) Zhao, C.; Kambara, C. S.; Yang, Y.; Kaledin, A. L.; Musaev, D. G.; Lian, T.; Hill, C. L. *Inorg. Chem.* **2013**, *52*, 671.

(20) Baker, L. C. W.; McCutcheon, T. P. *J. Am. Chem. Soc.* **1956**, *78*, 4503.

(21) Simmons, V. E. Ph.D. dissertation, Boston University, 1953.

(22) Baker, L. C. W.; Baker, V. E. S.; Wasfi, S. H.; Candela, G. A.; Kahn, A. H. *J. Chem. Phys.* **1972**, *56*, 4917.

(23) Nolan, A. L.; Burns, R. C.; Lawrance, G. A. *J. Chem. Soc., Dalton Trans.* **1998**, 3041.

(24) Acerete, R.; Casañ-Pastor, N.; Bas-Serra, J.; Baker, L. C. W. *J. Am. Chem. Soc.* **1989**, *111*, 6049.

(25) Muncaster, G.; Sankar, G.; Catlow, C. R. A.; Thomas, J. M.; Coles, S. J.; Hursthouse, M. *Chem. Mater*. **2000**, 16.

(26) Nolan, A. L.; Allen, C. C.; Burns, R. C.; Craig, D. C.; Lawrance, G. A. *Aust. J. Chem.* **2000**, *53*, 59.

(27) Maestre, J. M.; López, X.; Bo, C.; Daul, C.; Poblet, J.-M. *Inorg. Chem.* **2002**, *41*, 1883.

(28) Maestre, J. M.; López, X.; Bo, C.; Poblet, J.-M.; Casañ-Pastor, N. *J. Am. Chem. Soc.* **2001**, *123*, 3749.

(29) Zhang, F.-Q.; Zhang, X.-M.; Wu, H.-S.; Jiao, H. *J. Phys. Chem. A* **2007**, *111*, 159.

(30) Kojima, K.; Matsuda, J. *Bull. Chem. Soc. Jpn.* **1985**, *58*, 821.

(31) Müller, A.; Dloczik, L.; Diemann, E.; Pope, M. T. *Inorg. Chim. Acta* **1997**, *257*, 231.

(32) Weakley, T. J. R.; Malik, S. A. *J. Inorg. Nucl. Chem.* **1967**, *29*, 2935.

(33) Mair, J. A. *J. Chem. Soc.* **1950**, *1950*, 2364.

(34) Lyon, D. K.; Miller, W. K.; Novet, T.; Domaille, P. J.; Evitt, E.; Johnson, D. C.; Finke, R. G. *J. Am. Chem. Soc.* **1991**, *113*, 7209.

(35) Varga, G. M.; Papaconstantinou, E.; Pope, M. T. *Inorg. Chem.* **1970**, *9*, 662.

(36) APEXII (Version 2.0-1), SAINT (Version 7.23 A) and SADABS (Version 2004/1), Bruker AXS, Inc., Madison, WI, USA, 2005.

(37) Coppens, P.; Leiserowitz, L.; Rabinovich, D. *Acta Crystallogr.* **1965**, *18*, 1035.

(38) SHELXTL (v 6.1), Bruker AXS, Inc., Madison, WI, USA, 2000.

(39) Zhao, Y.; Truhlar, D. G. *J. Chem. Phys.* **2006**, *125*, 194101.

(40) Dunning Jr., T. H.; Hay, P. J. *Modern Theoretical Chemistry* Plenum, New York, 1976; Vol. 3.

(41) Hay, P. J.; Wadt, W. R. *J. Chem. Phys.* **1985**, *82*, 270.

(42) Furche, F.; Ahlrichs, R. *J. Chem. Phys.* **2002**, *117*, 7433.

(43) Tomasi, J.; Mennucci, B.; Cammi, R. *Chem. Rev.* **2005**, *105*, 2999.

(44) Rappe, A. K.; Casewit, C. J.; Colwell, K. S.; Goddard, W. A.; Skiff, W. M. *J. Am. Chem. Soc.* **1992**, *114*, 10024.

(45) Frisch, M. J.; Trucks, G. W.; Schlegel, H. B.; Scuseria, G. E.; Robb, M. A.; Cheeseman, J. R.; Scalmani, G.; Barone, V.; Mennucci, B.; Petersson, G. A.; Nakatsuji, H.; Caricato, M.; Li, X.; Hratchian, H. P.; Izmaylov, A. F.; Bloino, J.; Zheng, G.; Sonnenberg, J. L.; Hada, M.; Ehara, M.; Toyota, K.; Fukuda, R.; Hasegawa, J.; Ishida, M.; Nakajima, T.; Honda, Y.; Kitao, O.; Nakai, H.; Vreven, T.; J. A. Montgomery, J.; Peralta, J. E.; Ogliaro, F.; Bearpark, M.; Heyd, J. J.; Brothers, E.; Kudin, K. N.; Staroverov, V. N.; Kobayashi, R.; Normand, J.; Raghavachari, K.; Rendell, A.; Burant, J. C.; Iyengar, S. S.; Tomasi, J.; Cossi, M.; N. Rega, J. M. M.; Klene, M.; Knox, J. E.; Cross, J. B.; Bakken, V.; Adamo, C.; Jaramillo, J.; Gomperts, R.; Stratmann, R. E.; Yazyev, O.; Austin, A. J.; Cammi, R.; Pomelli, C.; Ochterski, J. W.; Martin, R. L.; K. Morokuma, V. G. Z.; Voth, G. A.; Salvador, P.; Dannenberg, J. J.; Dapprich, S.; Daniels, A. D.; Ö. Farkas, J. B. F.; Ortiz, J. V.; Cioslowski, J.; Fox, D. J. *Gaussian 09*, Revision C.01; Gaussian, Inc.: Wallingford, CT, 2009.

(46) Casan-Pastor, N.; Gomez-Romero, P.; Jameson, G. B.; Baker, L. C. W. *J. Am. Chem. Soc.* **1991**, *113*, 5658.

(47) Huang, Z. Ph.D. dissertation, Emory University, 2011.

(48) Pope, M. T.; Varga, G. M. *Inorg. Chem.* **1966**, *5*, 1249.

(49) Weinstock, I. A. *Chem. Rev.* **1998**, *98*, 113.

(50) Caspar, J. V.; Meyer, T. J. *J. Am. Chem. Soc.* **1983**, *105*, 5583.

(51) Kober, E. M.; Sullivan, B. P.; Meyer, T. J. *Inorg. Chem.* **1984**, *23*, 2098.

(52) Campagna, S.; Puntoriero, F.; Nastasi, F.; Bergamini, G.; Balzani, V. In *Photochemistry and Photophysics of Coordination Compounds I*; Balzani, V., Campagna, S., Eds.; Springer Berlin Heidelberg: 2007; Vol. 280, p 117.

(53) Yeh, A. T.; Shank, C. V.; McCusker, J. K. *Science* **2000**, *289*, 935.

(54) Pavlovich, V. S. *ChemPhysChem* **2012**, *13*, 4081.

(55) Iwamura, M.; Takeuchi, S.; Tahara, T. *J. Am. Chem. Soc.* **2007**, *129*, 5248.

(56) Bhasikuttan, A. C.; Suzuki, M.; Nakashima, S.; Okada, T. *J. Am. Chem. Soc.* **2002**, *124*, 8398.

(57) Li, B.; Zheng, S.-T.; Yang, G.-Y. *Chin. J. Struct. Chem.* **2009**, *28*, 531.

(58) Li, D.-J.; Zheng, S.-T.; Yang, G.-Y. *Chin. J. Struct. Chem.* **2009**, *28*, 655.

(59) Zhao, J.-W.; Zhang, J.; Zheng, S.-T.; Yang, G.-Y. *Chin. J. Struct. Chem.* **2008**, *27*, 933.

(60) Li, M.-X.; Wang, K.-H.; Niu, J.-Y. *Chin. J. Struct. Chem.* **2008**, *27*, 340.

(61) Lisnard, L.; Dolbecq, A.; Mialane, P.; Marrot, J.; Sécheresse, F. *Inorg. Chim. Acta* **2004**, *357*, 845.

(62) Pichon, C.; Dolbecq, A.; Mialane, P.; Marrot, J.; Rivière, E.; Goral, M.; Zynek, M.; McCormac, T.; Borshch, S. A.; Zueva, E.; Sécheresse, F. *Chem. Eur. J.* **2008**, *14*, 3189.

(63) Radkov, E. V.; Beer, R. H. *Inorg. Chim. Acta* **2000**, *297*, 191.

(64) Sadakane, M.; Tsukuma, D.; Dickman, M. H.; Bassil, B.; Kortz, U.; Higashijima, M.; Ueda, W. *Dalton Trans.* **2006**, *0*, 4271.

(65) Reinoso, S.; Vitoria, P.; Lezama, L.; Luque, A.; Gutiérrez-Zorrilla, J. M. *Inorg. Chem.* **2003**, *42*, 3709.

(66) Zhang, W.; Chen, Y.-T. *Acta Crystallogr., Sect. E: Struct. Rep. Online* **2009**, *65*, m1548.

(67) Stein, I.; Ruschewitz, U. *Z. Naturforsch., B: Chem. Sci.* **2011**, *66*, 471.

(68) Bhaumik, M. L.; Nugent, L. J. *J. Chem. Phys.* **1965**, *43*, 1680.

(69) Hehlen, M. P.; Riesen, H.; Guedel, H. U. *Inorg. Chem.* **1991**, *30*, 2273.

(70) Dong, H.; Wheeler, R. A. *Chem. Phys. Lett.* **2005**, *413*, 176.

(71) Rasmussen, P. G.; Brubaker, J., Carl H. *Inorg. Chem.* **1964**, *3*, 977.

(72) Eberson, L. *J. Am. Chem. Soc.* **1983**, *105*, 3192.

(73) Amjad, Z.; Brodovitch, J.-C.; McAuley, A. *Can. J. Chem.* **1977**, *55*, 3581.

(74) Eberson, L. *New J. Chem.* **1992**, *16*, 151.

(75) Kozhevnikov, L. V.; Kholdeeva, O. A. *Izv. Akad. Nauk SSSR, Ser. Khim.* **1987**, 528.

(76) Altenau, J.; Pope, M. T.; Prados, R. A.; So, H. *Inorg. Chem.* **1975**, *14*, 417.

(77) Prados, R. A.; Meiklejohn, P. T.; Pope, M. T. *J. Am. Chem. Soc.* **1974**, *96*, 1261.

(78) Monat, J. E.; McCusker, J. K. *J. Am. Chem. Soc.* **2000**, *122*, 4092.

(79) Vogt, R. A.; Gray, T. G.; Crespo-Hernández, C. E. *J. Am. Chem. Soc.* **2012**, *134*, 14808.

(80) Ghosh, H. N.; Asbury, J. B.; Lian, T. *J. Phys. Chem. B* **1998**, *102*, 6482.

(81) Ghosh, H. N.; Asbury, J. B.; Weng, Y.; Lian, T. *J. Phys. Chem. B* **1998**, *102*, 10208.

(82) Ferrere, S.; Gregg, B. A. *J. Am. Chem. Soc.* **1998**, *120*, 843.

(83) Kuciauskas, D.; Monat, J. E.; Villahermosa, R.; Gray, H. B.; Lewis, N. S.; McCusker, J. K. *J. Phys. Chem. B* **2002**, *106*, 9347.

Charge Separation in Polyoxometalate-Based Systems for Solar Energy Production

Chapter 3

Transition Metal Substitution Effects on Charge Transfer Lifetimes in Keggin Polyoxometalates

with John Fielden, Zhuangqun Huang, Xu Xiang, Djamaladdin G. Musaev, Tianquan Lian, and Craig L. Hill

Published partially in: Glass, E. N.; Fielden, J.; Huang, Z.; Xiang, X.; Musaev, D. G.; Lian, T.; Hill, C. L. "Transition Metal Substitution Effects on Metal-to-Polyoxometalate Charge Transfer", *Inorganic Chemistry*, **2016**, accepted pending minor revisions.

3.1 Abstract

A series of heterobimetallic transition metal substituted polyoxometalates (TMSPs) have been synthesized based on the Co^{II}-centered ligand $[Co^{II}W_{11}O_{39}]^{10-}$. The eight complex series, $[Co^{II}(M^xOH_y)W_{11}O_{39}]^{(12-x-y)-}$ (M^xOH_y = $V^{IV}O$, $Cr^{III}(OH_2)$, $Mn^{II}(OH_2)$, $Fe^{III}(OH_2)$, $Co^{II}(OH_2)$, $Ni^{II}(OH_2)$, $Cu^{II}(OH_2)$, $Zn^{II}(OH_2)$), of which six are reported for the first time, was synthesized starting from $[Co^{III}W_{11}O_{39}]^{9-}$ and studied using spectroscopic, electrochemical, and computational techniques to evaluate the influence of substituted transition metals on the photodynamics of the metal-to-polyoxometalate charge transfer (MPCT) transition. The bimetallic complexes all show higher visible light absorption than the plenary $[Co^{II}W_{12}O_{40}]^{6-}$ and demonstrate the same MPCT transition as the plenary complex, but have shorter excited state lifetimes (sub-300 ps in aqueous media). The decreased lifetimes are rationalized on the basis of nonradiative relaxation due to coordinating aqua ligands, increased interaction with cations due to increased negative charge, and the energy gap law, with the strongest single factor appearing to be the charge on the anion. The most promising results are from the Cr- and Fe-substituted systems, which retain excited state lifetimes at least 50% of that of $[Co^{II}W_{12}O_{40}]^{6-}$ while more than tripling the absorbance at 400 nm.

3.2 Introduction

Molecular charge transfer (CT) chromophores are relevant to conversion of sunlight into electrical energy[1-3] or chemical fuels,[4-13] as photocatalysts for other chemical transformations,[14,15] and a wide range of photonic applications (e.g. non-linear optics,[16-18] photo- and electroluminescence,[19-21] sensing[22,23]). The vast majority of these

molecular CT systems are organic, or metal-organic in nature, and compared to solid state inorganic semiconductors they can offer advantages in cost, synthetic versatility for tailoring properties, and processability. However, they are typically more vulnerable to photo- and other degradation processes than semiconductors, particularly if used to drive demanding photo-redox chemistry such as light driven water oxidation.[24] Development of robust, molecular, all-inorganic CT chromophores is therefore a highly desirable goal, as these could combine the stability of solid-state materials with many of the advantages of molecular organic and metal-organic systems.

To this end, chromophores composed of heterobimetallic groups have recently attracted interest as possible replacements for organic/metal-organic photosensitizers in photocatalytic solar fuel production. In these materials, a donor and an acceptor transition metal are bound by an oxido group to form a chromophoric unit in which light absorption generates metal-to-metal charge transfer (MMCT) excited states and metal oxidation states conducive to catalysis.[25-35] These units have been shown to act as photocatalysts for multi-electron processes, including CO_2 reduction[25] and water oxidation.[27] MMCT chromophores thus represent a new class of materials that avoid some of the pitfalls of traditional organic photosensitizers and metal oxide semiconductors. However, the only molecular example so far is supported by organic ligands.[35]

We are investigating polyoxometalates (POMs), a broad class of molecular metal oxide structures, as the basis for molecular all-inorganic MMCT or metal-to-polyoxometalate (MPCT) chromophores. As molecular species, these complexes combine the advantages of molecular characterization and controlled synthesis with the robustness of all-inorganic metal oxide semiconductors and substrates. Previously, we

showed that coordination of Re carbonyls, or lone pair donors (Sn^{II}/Sb^{III}) to POMs resulted in strong visible MPCT-based absorptions, but excited state lifetimes were too short (2 to 66 ps) to be of use in solution photochemistry.[36-40] At the same time, our systematic investigation of a series of four cobalt-containing Keggin POMs, found one complex, cobalt-centered $[Co^{II}W_{12}O_{40}]^{6-}$, with a much longer intramolecular MPCT excited state lifetime (1.7 ns in MeCN, 420 ps in H_2O) but much weaker visible light absorption.[41] Analogous to other MMCT chromophores, photoexcitation of the MPCT transition in $[Co^{II}W_{12}O_{40}]^{6-}$ forms transient Co^{III} ($E° = ca.$ +1.1 V vs. NHE) and reduced polytungstate ($E° = ca.$ -0.3 vs. NHE) species with potentials suitable for various electron transfer reactions. Here, we report the rational synthesis of a series of heterobimetallic transition metal-substituted polyoxometalates (TMSPs) to systematically investigate the effect of 3d-transition metal substitution on the light absorption properties and excited state dynamics of the cobalt-centered Keggin system. A series of eight TMSP complexes $[Co^{II}(M^xOH_y)W_{11}O_{39}]^{(12-x-y)-}$ (M^xOH_y = $V^{IV}O$, $Cr^{III}(OH_2)$, $Mn^{II}(OH_2)$, $Fe^{III}(OH_2)$, $Co^{II}(OH_2)$, $Ni^{II}(OH_2)$, $Cu^{II}(OH_2)$, $Zn^{II}(OH_2)$), of which six (M^xOH_y = $Cr^{III}(OH_2)$, $Mn^{II}(OH_2)$, $Fe^{III}(OH_2)$, $Ni^{II}(OH_2)$, $Cu^{II}(OH_2)$, $Zn^{II}(OH_2)$) are reported for the first time, were compared to the parent complex using spectroscopic, electrochemical, and computational techniques. The results show that, while charge-transfer (CT) excited state lifetimes decrease significantly compared to $[Co^{II}W_{12}O_{40}]^{6-}$, visible light absorption increases across the entire series and the CT lifetimes (up to 270 ps to H_2O) are still longer than those of other molecular MPCT and lone-pair-to-POM CT systems.[36-40]

3.3 Experimental

3.3.1 General Methods and Materials

All reagents were purchased as ACS analytical or reagent grade and used as received. Syntheses were carried out in the ambient atmosphere. The identities and purities of all synthesized compounds were confirmed by infrared and UV-visible spectroscopy. Infrared spectra (2% by weight in KBr) were recorded on a Thermo Nicolet 6700 FT-IR spectrometer. Static electronic absorption spectra were acquired using an Agilent 8453 spectrophotometer equipped with a diode-array detector and Agilent 89090A cell temperature controller unit. Elemental analyses were performed by Galbraith Laboratories, Inc. (Knoxville, Tennessee). Thermogravimetric analyses (TGA) were acquired on a Perkin Elmer STA 6000 analyzer. Cyclic voltammograms were recorded on a Pine Research Instruments WaveDriver 20 bipotentiostat using a standard three-electrode setup equipped with a glassy-carbon working electrode, a platinum wire auxiliary electrode and an Ag/AgCl (1 M KCl) BAS reference electrode, using potassium acetate (0.500 M, pH 5) as the buffer/electrolyte. All redox potentials are reported relative to this reference electrode (~+235 mV nominal difference between NHE and the BAS electrode).

3.3.2 Syntheses

$K_5H[Co^{II}W_{12}O_{40}]\cdot 12H_2O$ (3.1, $Co^{II}W_{12}$). The synthesis was adapted from published methods.[41-44] Sodium tungstate dihydrate (19.8 g, 60 mmol) was dissolved with stirring in 40 mL of deionized water, after which the pH was adjusted to 7.0 using glacial acetic acid. A separate solution of cobalt(II) acetate tetrahydrate (2.5 g, 10 mmol) in 12

mL deionized water was prepared, with the pH adjusted to *ca.* 7 by the addition of a few drops of glacial acetic acid. Both solutions were heated with stirring until near boiling, and the cobalt(II) acetate solution was added to the sodium tungstate solution slowly, yielding a dark green solution. The mixture was boiled for 20 minutes and filtered hot. A 20 mL saturated solution of potassium acetate adjusted to pH 7.0 by the addition of glacial acetic acid was prepared while the filtrate was reheated. The potassium acetate solution was added slowly to the filtrate with stirring, precipitating a green solid. The resulting mixture was allowed to cool to room temperature and filtered, rinsing the solid twice with the filtrate. The solid was redissolved in 40 mL 2M sulfuric acid with stirring and gentle heating for 15 minutes, yielding a dark blue solution. Insoluble material was removed by filtration. The solution volume was reduced by half through gentle heating, then allowed to develop crystals via slow evaporation. The dark blue crystals collected from the mother liquor were further purified by passing a concentrated solution through Dowex 50WX8 ion-exchange resin conditioned in the K^+ cycle, removing a large excess of latent cobalt cations. The eluent was evaporated to dryness using a rotary evaporator, dissolved in minimal 1M HCl and allowed to develop crystals of **3.1** via slow evaporation. Yield: 3.82 g (22.3% based on W). FTIR (2% KBr pellet), $\tilde{\nu}$, cm^{-1}: 943 (s), 889 (s), 871 (sh), 739 (s), 692 (sh), 580 (w), 449 (m). UV-vis (H_2O), λ_{max}, nm (ε, L mol^{-1} cm^{-1}): 625 (223). Elemental analysis: calcd. (found) for $K_5Co_1W_{12}O_{52}H_{25}$, %: K, 5.89 (5.77); Co, 1.78 (1.69); W, 66.5 (62.9). TGA (Figure 3.1) shows a weight loss of 6.22% from 30-400 °C (calcd. 6.52% for 12 H_2O).

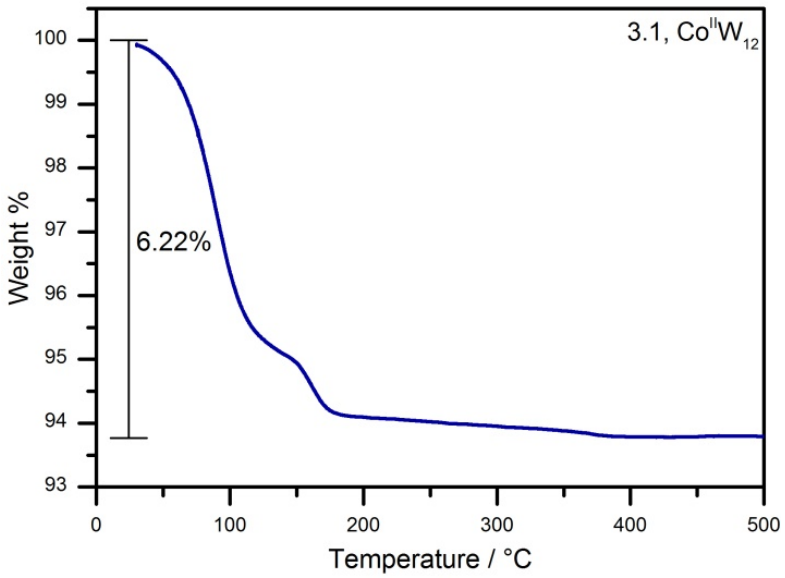

Figure 3.1. Thermogravimetric analysis of **3.1**. The annotated total weight loss is attributed to waters of hydration.

$K_5[Co^{III}W_{12}O_{40}]\bullet 16H_2O$ (3.2, $Co^{III}W_{12}$). The synthesis was adapted from published methods.[41-44] Sodium tungstate dihydrate (19.8 g, 60 mmol) was dissolved with stirring in 40 mL of deionized water, after which the pH was adjusted to 7.0 using glacial acetic acid. A separate solution of cobalt(II) acetate tetrahydrate (2.5 g, 10 mmol) in 12 mL deionized water was prepared, with the pH adjusted to *ca.* 7 by the addition of a few drops of glacial acetic acid. Both solutions were heated with stirring until near boiling, and the cobalt(II) acetate solution was added to the sodium tungstate solution slowly, yielding a dark green solution. The mixture was boiled for 20 minutes and filtered hot. A 20 mL saturated solution of potassium acetate adjusted to pH 7.0 by the addition of glacial acetic acid was prepared while the filtrate was reheated. The potassium acetate solution was added slowly to the filtrate with stirring, precipitating a green solid. The resulting mixture was allowed to cool to room temperature and filtered, rinsing the solid

twice with the filtrate. The solid was redissolved in 40 mL 2M sulfuric acid with stirring and gentle heating for 15 minutes, yielding a dark blue solution. Insoluble material was removed by filtration. The filtrate was reheated to boiling and potassium persulfate (1.5 g, 5.5 mmol) was added in portions until the color change from blue to yellow was complete. The volume of the solution was reduced by half with heating, then allowed to cool to room temperature. Yellow needle crystals developed overnight and were collected by filtration. The product was further purified by passing a concentrated solution through Dowex 50WX8 ion-exchange resin conditioned in the K^+ cycle. The eluent was evaporated to dryness using a rotary evaporator. The yellow solid was dissolved in minimal deionized water, heated to boiling, and a small amount of potassium persulfate was added to ensure complete oxidation. Yellow needle crystals of **3.2** were obtained via slow evaporation. Yield: 7.41 g (42.3% based on W). FTIR (2% KBr pellet), $\tilde{\nu}$, cm^{-1}: 954 (s), 893 (s), 878 (sh), 756 (vs), 500 (w), 442 (m). UV-vis (H_2O), λ_{max}, nm (ε, L mol^{-1} cm^{-1}): 390 (1270). Elemental analysis: calcd. (found) for $K_5Co_1W_{12}O_{56}H_{32}$, %: K, 5.77 (5.25); Co, 1.74 (1.75); W, 65.1 (62.0). TGA (Figure 3.2) shows a weight loss of 8.78% from 30-500 °C (calcd. 8.51% for 15 H_2O).

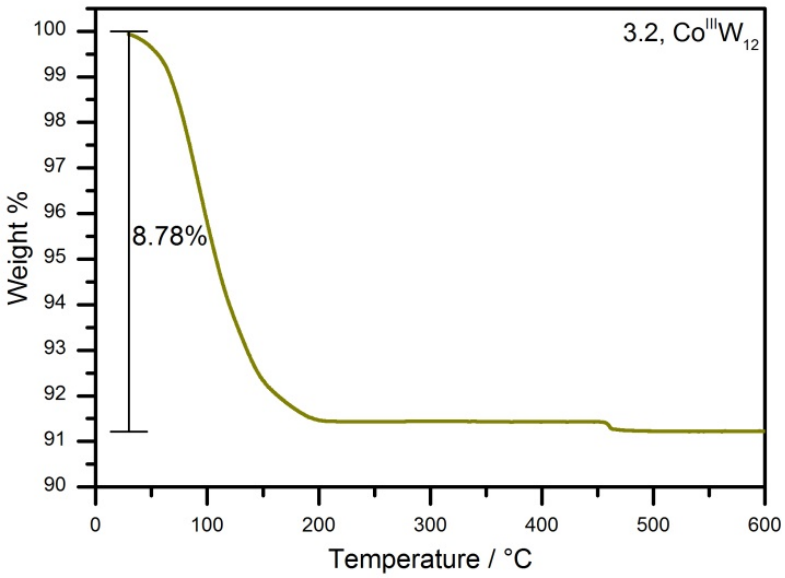

Figure 3.2. Thermogravimetric analysis of **3.2**. The annotated total weight loss is attributed to waters of hydration.

$K_9[Co^{III}W_{11}O_{39}]\bullet 13H_2O$ (3.3, $Co^{III}W_{11}$). The synthesis was adapted from published methods.[45] Crystalline $K_5[Co^{III}W_{12}O_{40}]\bullet 16H_2O$ (10.0 g, 2.9 mmol) was dissolved in 25 mL hot (80 °C) deionized water with stirring. Saturated potassium acetate (10 mL, ~1 mL/1g $Co^{III}W_{12}$ added) was added dropwise to the yellow-orange solution. The solution turned dark quickly upon addition, with a red precipitate forming after *ca.* 20% of the potassium acetate solution had been added. Precipitate continued to form throughout the addition process and the solution color changed to turquoise. The red precipitate was filtered hot on a medium glass frit and rinsed with 3 mL cold deionized water. After air drying overnight, the precipitate was dissolved in minimal boiling deionized water (>90 °C, ~6.7 mL/1 g crude product) and filtered hot with coarse filter paper. The dark red filtrate was cooled at 5 °C overnight to yield small cubic orange-red crystals of **3.3**, which were collected on a medium glass frit. Yield: 5.37 g (55.3%). FTIR

(2% KBr pellet), $\tilde{\nu}$, cm^{-1}: 941 (s), 867 (vs), 839 (sh), 778 (vs), 711 (s), 670 (m), 547 (sh), 517 (w), 495 (w), 470 (sh), 450 (m), 428 (m). UV-vis (H_2O), λ_{max}, nm (ε, L mol^{-1} cm^{-1}): 390 (1340, sh). Elemental analysis: calcd. (found) for $K_9Co_1W_{11}O_{57}H_{36}$, %: K, 10.69 (10.00); Co, 1.79 (1.74); W, 61.4 (60.0). TGA (Figure 3.3) shows a weight loss of 7.17% from 30-425 °C (calcd. 7.12% for 13 H_2O).

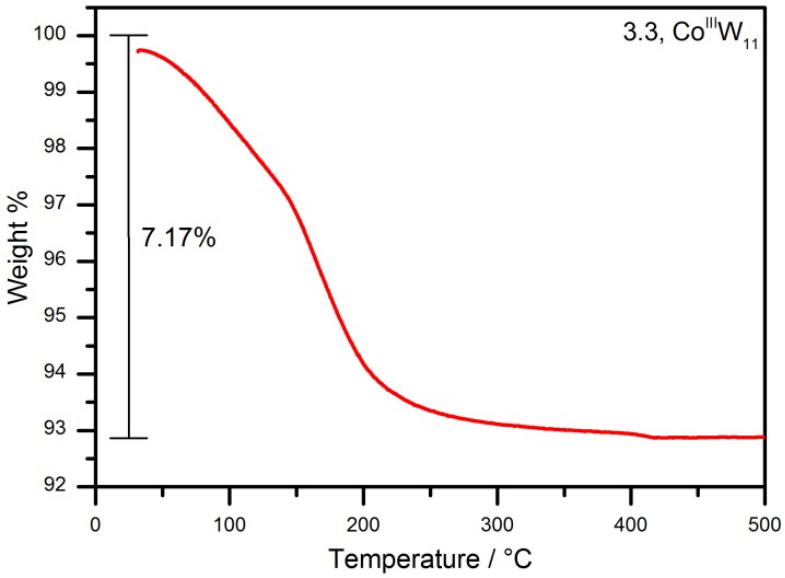

Figure 3.3. Thermogravimetric analysis of **3.3**. The annotated total weight loss is attributed to waters of hydration.

$K_8[Co^{II}(V^{IV}O)W_{11}O_{39}]\bullet 11H_2O$ (3.4, $Co^{II}V^{IV}$). The synthesis was adapted from published methods.[45] Vanadyl sulfate pentahydrate (0.16 g, 0.61 mmol) was dissolved in 40 mL potassium acetate buffer, pH 5, and heated to 60 °C. Crystalline $K_9[Co^{III}W_{11}O_{39}]\bullet 13H_2O$ (1.0 g, 0.30 mmol) was added in portions, and the solution turned dark grey-black. The solution was stirred and heated for one hour, filtered, potassium chloride (10 g, 0.13 mol) was added, and the solution was cooled at 5 °C

overnight to yield small black crystals. The crude product was collected by filtration, rinsed with 5 mL cold 2M potassium chloride solution, and redissolved in minimal hot deionized water. Black cubic crystals of **3.4** were obtained by slow evaporation. Yield: 0.802 g (80.4%). FTIR (2% KBr pellet), $\tilde{\nu}$, cm^{-1}: 941 (s), 879 (sh), 865 (s), 769 (vs), 715 (w), 648 (w), 532 (w), 440 (m). UV-vis (H_2O), λ_{max}, nm (ε, L mol^{-1} cm^{-1}): 445 (552), 557 (463), 593 (453). Elemental analysis: calcd. (found) for $K_8Co_1V_1W_{11}O_{51}H_{22}$, %: K, 9.53 (8.83); Co, 1.80 (1.73); V, 1.55 (1.49); W, 61.6 (60.0). TGA (Figure 3.4) shows a weight loss of 6.29% from 30-375 °C (calcd. 6.04% for 11 H_2O).

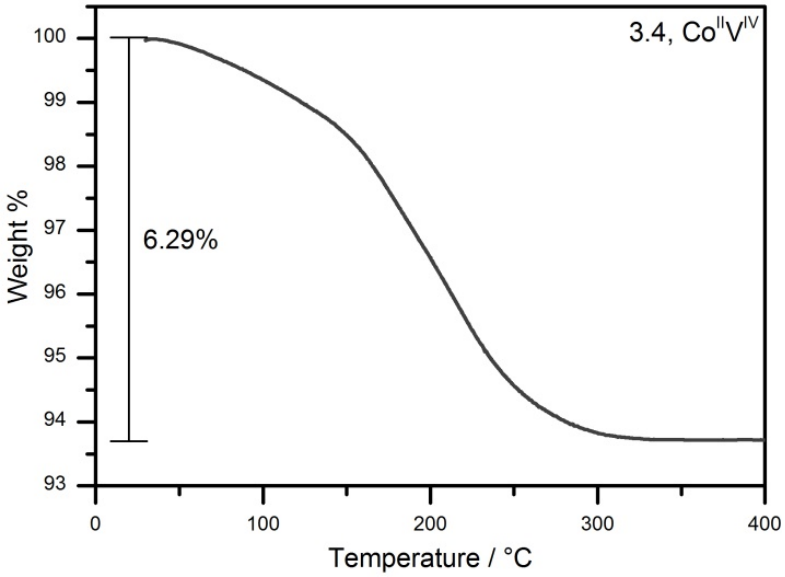

Figure 3.4. Thermogravimetric analysis of **3.4**. The annotated total weight loss is attributed to waters of hydration.

$K_7[Co^{II}Cr^{III}(H_2O)W_{11}O_{39}]\bullet 14H_2O$ (3.5, $Co^{II}Cr^{III}$). Chromium nitrate nonahydrate (140 mg, 0.35 mmol) was dissolved in 15 mL potassium acetate buffer, pH 5, and heated to 60 °C. Crystalline $K_9[Co^{III}W_{11}O_{39}]\bullet 13H_2O$ (1.0 g, 0.30 mmol) was added

in portions, and the solution turned dark forest green. The solution was stirred and heated for one hour, during which time sodium ascorbate (60 mg, 0.30 mmol) was added. The solution was filtered, potassium chloride (5.0 g, 67 mmol) was added, and the solution was cooled at 5 °C overnight to yield a green solid. The crude product was collected by filtration, rinsed with 5 mL cold 2M potassium chloride solution, and redissolved in minimal hot deionized water. Dark green crystals of **3.5** were obtained by slow evaporation. Yield: 0.194 g (19.3%). FTIR (2% KBr pellet), $\tilde{\nu}$, cm^{-1}: 945 (s), 884 (vs), 764 (vs), 722 (m), 689 (w), 568 (w), 532 (w), 456 (m). UV-vis (H_2O), λ_{max}, nm (ε, L mol^{-1} cm^{-1}): 624 (285). Elemental analysis: calcd. (found) for $K_7Co_1Cr_1W_{11}O_{54}H_{30}$, %: K, 8.29 (7.87); Co, 1.79 (1.73); Cr, 1.58 (1.61); W, 61.3 (60.6). TGA (Figure 3.5) shows a weight loss of 7.56% from 30-375 °C (calcd. 7.64% for 15 H_2O).

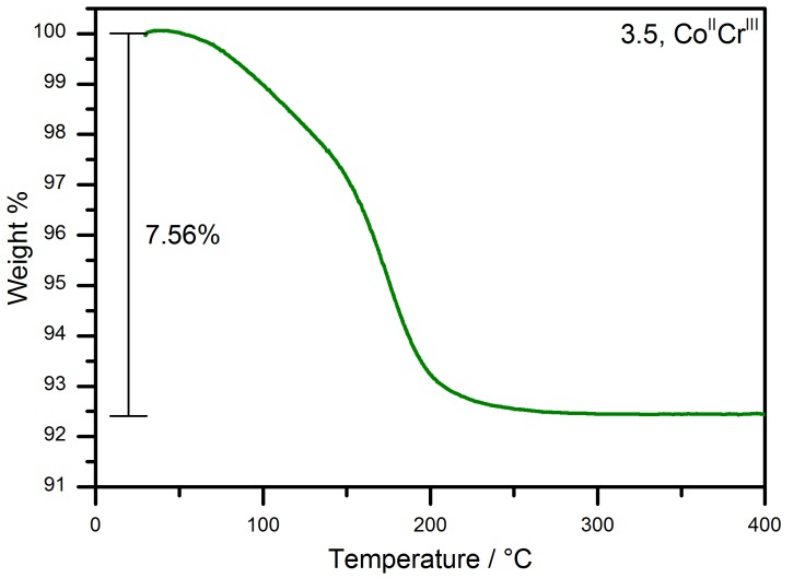

Figure 3.5. Thermogravimetric analysis of **3.5**. The annotated total weight loss is attributed to waters of hydration and bound aqua ligands.

$K_8[Co^{II}Mn^{II}(H_2O)W_{11}O_{39}]\bullet 13H_2O$ (3.6, $Co^{II}Mn^{II}$). Manganese(II) chloride tetrahydrate (69 mg, 0.35 mmol) was dissolved in 15 mL potassium acetate buffer, pH 5, and heated to 60 °C. Crystalline $K_9[Co^{III}W_{11}O_{39}]\bullet 13H_2O$ (1.0 g, 0.30 mmol) was added in portions, and the solution turned grey-black. The solution was stirred and heated for one hour, during which time sodium ascorbate (60 mg, 0.30 mmol) was added and the solution turned royal blue. The solution was filtered, potassium chloride (5.0 g, 67 mmol) was added, and the solution was cooled at 5 °C overnight to yield a blue solid. The crude product was collected by filtration, rinsed with 5 mL cold 2M potassium chloride solution, and redissolved in minimal hot deionized water. Blue-green crystals of **3.6** were obtained by slow evaporation. Yield: 0.507 g (50.2%). FTIR (2% KBr pellet), $\tilde{\nu}$, cm^{-1}: 933 (s), 917 (sh), 859 (vs), 789 (vs), 700 (m), 528 (w), 475 (sh), 435 (m). UV-vis (H_2O), λ_{max}, nm (ε, L mol^{-1} cm^{-1}): 601 (190). Elemental analysis: calcd. (found) for $K_8Co_1Mn_1W_{11}O_{53}H_{28}$, %: K, 9.41 (8.79); Co, 1.77 (1.86); Mn, 1.65 (1.42); W, 60.8 (60.4). TGA (Figure 3.6) shows a weight loss of 7.03% from 30-400 °C (calcd. 7.04% for 14 H_2O).

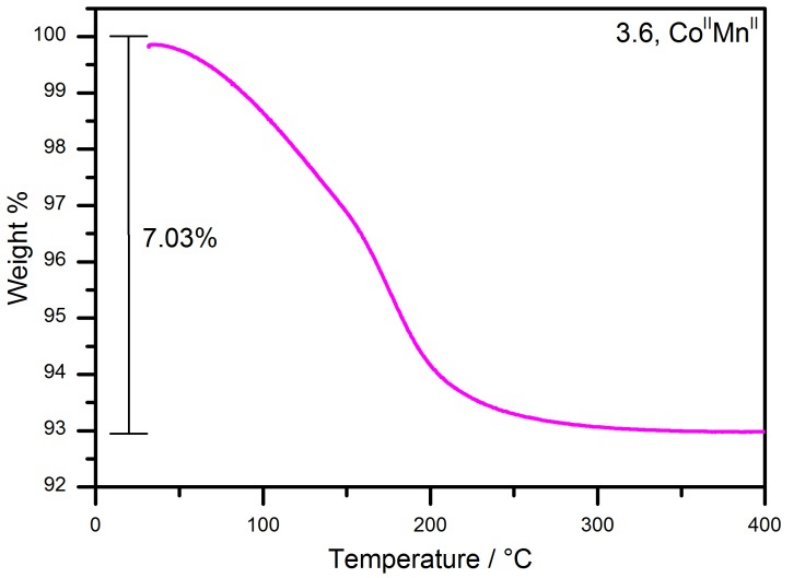

Figure 3.6. Thermogravimetric analysis of **3.6**. The annotated total weight loss is attributed to waters of hydration and bound aqua ligands.

$K_7[Co^{II}Fe^{III}(H_2O)W_{11}O_{39}]\cdot 13H_2O$ (3.7, $Co^{II}Fe^{III}$). Iron(II) sulfate heptahydrate (97 mg, 0.35 mmol) and crystalline $K_9[Co^{III}W_{11}O_{39}]\cdot 13H_2O$ (1.0 g, 0.30 mmol) were added to 15 mL potassium acetate buffer, pH 5, and stirred at room temperature. The solution gradually turned dark green as the solids dissolved. Once no further color change was observed, the solution was heated at 60 °C for one hour. The solution was filtered, potassium chloride (5.0 g, 67 mmol) was added, and the solution was cooled at 5 °C overnight to yield a green solid. The crude product was collected by filtration, rinsed with 5 mL cold 2M potassium chloride solution, and redissolved in minimal hot deionized water. Dark green crystals of **3.7** were obtained by slow evaporation. Yield: 0.780 g (78.1%). FTIR (2% KBr pellet), $\tilde{\nu}$, cm^{-1}: 942 (s), 879 (vs), 763 (vs), 709 (m), 534 (w), 436 (m). UV-vis (H_2O), λ_{max}, nm (ε, L mol^{-1} cm^{-1}): 477 (179), 623 (233). Elemental analysis: calcd. (found) for $K_7Co_1Fe_1W_{11}O_{53}H_{26}$, %: K, 8.33 (8.20); Co, 1.79 (1.72); Fe,

1.70 (1.75); W, 61.5 (58.7). TGA (Figure 3.7) shows a weight loss of 7.47% from 30-350 °C (calcd. 7.13% for 14 H_2O).

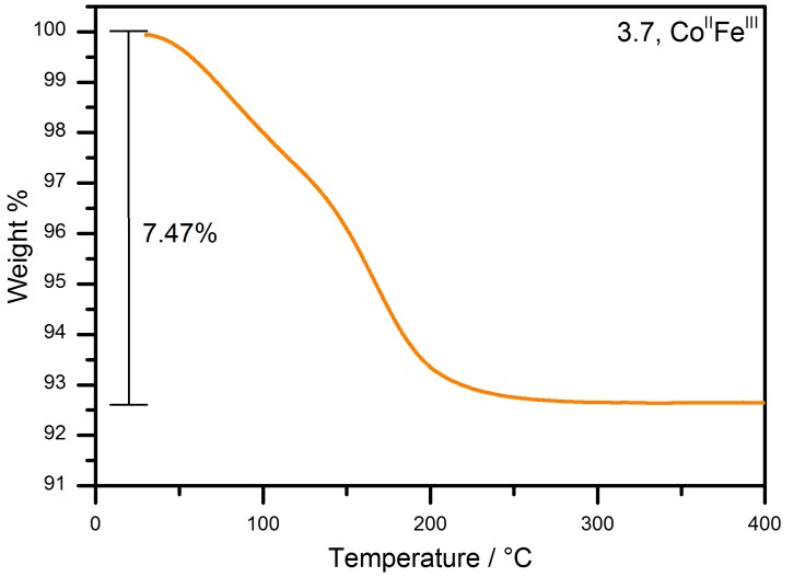

Figure 3.7. Thermogravimetric analysis of **3.7**. The annotated total weight loss is attributed to waters of hydration and bound aqua ligands.

$K_8[Co^{II}Co^{II}(H_2O)W_{11}O_{39}]\cdot 13H_2O$ (3.8, $Co^{II}Co^{II}$). This is an alternative synthetic route, using **$Co^{III}W_{11}$**, to published methods.[42,43] Cobalt(II) chloride hexahydrate (83 mg, 0.35 mmol) was dissolved in 15 mL potassium acetate buffer, pH 5, and heated to 60 °C. Crystalline $K_9[Co^{III}W_{11}O_{39}]\cdot 13H_2O$ (1.0 g, 0.30 mmol) was added in portions, and the solution turned dark red. The solution was stirred and heated for one hour, during which time sodium ascorbate (60 mg, 0.30 mmol) was added and the solution turned blue. The solution was filtered, potassium chloride (5.0 g, 67 mmol) was added, and the solution was cooled at 5 °C overnight to yield a blue solid. The crude product was collected by filtration, rinsed with 5 mL cold 2M potassium chloride

solution, and redissolved in minimal hot deionized water. Blue-green crystals of **3.8** were obtained by slow evaporation. Yield: 0.433 g (42.8%). FTIR (2% KBr pellet), $\tilde{\nu}$, cm^{-1}: 933 (s), 872 (vs), 756 (vs), 658 (w), 532 (w), 473 (sh), 444 (m). UV-vis (H_2O), λ_{max}, nm (ε, L mol^{-1} cm^{-1}): 598 (190). Elemental analysis: calcd. (found) for $K_8Co_2W_{11}O_{52}H_{26}$, %: K, 9.40 (8.92); Co, 3.54 (3.79); W, 60.7 (59.7). TGA (Figure 3.8) shows a weight loss of 7.10% from 30-350 °C (calcd. 7.03% for 14 H_2O).

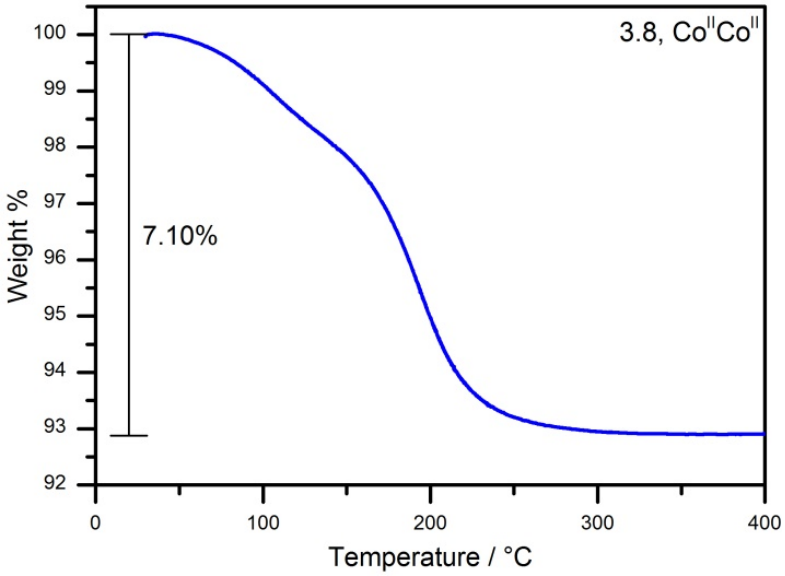

Figure 3.8. Thermogravimetric analysis of **3.8**. The annotated total weight loss is attributed to waters of hydration and bound aqua ligands.

$K_8[Co^{II}Ni^{II}(H_2O)W_{11}O_{39}]\bullet 13H_2O$ (3.9, $Co^{II}Ni^{II}$). Nickel(II) chloride hexahydrate (83 mg, 0.35 mmol) was dissolved in 25 mL potassium acetate buffer, pH 5, and heated to 60 °C. Crystalline $K_9[Co^{III}W_{11}O_{39}]\bullet 13H_2O$ (1.0 g, 0.30 mmol) was added in portions, and the solution turned dark brown. The solution was stirred and heated for one hour, during which time sodium ascorbate (60 mg, 0.30 mmol) was added and the

solution turned royal blue. The solution was filtered, potassium chloride (10 g, 0.13 mol) was added, and the solution was cooled at 5 °C overnight to yield a blue solid. The crude product was collected by filtration, rinsed with 5 mL cold 2M potassium chloride solution, and redissolved in minimal hot deionized water. Blue-green crystals of **3.9** were obtained by slow evaporation. Yield: 0.699 g (69.1%). FTIR (2% KBr pellet), $\tilde{\nu}$, cm^{-1}: 933 (s), 863 (s), 783 (vs), 708 (w), 667 (w), 534 (w), 451 (m), 424 (m). UV-vis (H_2O), λ_{max}, nm (ε, L mol^{-1} cm^{-1}): 624 (191). Elemental analysis: calcd. (found) for $K_8Co_1Ni_1W_{11}O_{53}H_{28}$, %: K, 9.40 (8.98); Co, 1.77 (2.05); Ni, 1.76 (1.64); W, 60.7 (58.6). TGA (Figure 3.9) shows a weight loss of 7.02% from 30-350 °C (calcd. 7.04% for 14 H_2O).

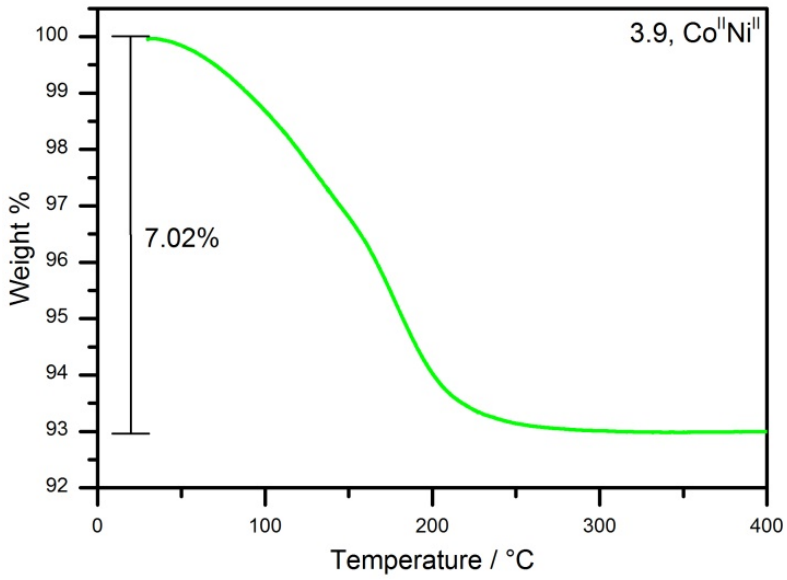

Figure 3.9. Thermogravimetric analysis of **3.9**. The annotated total weight loss is attributed to waters of hydration and bound aqua ligands.

$K_8[Co^{II}Cu^{II}(H_2O)W_{11}O_{39}]\cdot 14H_2O$ (3.10, $Co^{II}Cu^{II}$). The synthesis was adapted from the published method for the synthesis of $K_7[Co^{III}Cu^{II}(H_2O)W_{11}O_{39}]$.[46] Copper(II) chloride dihydrate (60 mg, 0.35 mmol) was dissolved in 15 mL potassium acetate buffer, pH 5, and heated to 60 °C. Crystalline $K_9[Co^{III}W_{11}O_{39}]\cdot 13H_2O$ (1.0 g, 0.30 mmol) was added in portions, and the solution turned dark red. The solution was stirred and heated for one hour, during which time sodium ascorbate (60 mg, 0.30 mmol) was added and the solution turned dark blue-green. The solution was filtered, potassium chloride (5.0 g, 67 mmol) was added, and the solution was cooled at 5 °C overnight to yield a blue solid. The crude product was collected by filtration, rinsed with 5 mL cold 2M potassium chloride solution, and redissolved in minimal hot deionized water. Dark blue-green crystals of **3.10** were obtained by slow evaporation. Yield: 0.211 g (20.7%). FTIR (2% KBr pellet), $\tilde{\nu}$, cm^{-1}:929 (s), 859 (s), 754 (vs), 696 (w), 660 (w), 444 (m), 421 (m). UV-vis (H_2O), λ_{max}, nm (ε, L mol^{-1} cm^{-1}): 600 (199). Elemental analysis: calcd. (found) for $K_8Co_1Cu_1W_{11}O_{54}H_{30}$, %: K, 9.33 (9.00); Co, 1.76 (2.13); Cu, 1.90 (1.64); W, 60.3 (59.3). TGA (Figure 3.10) shows a weight loss of 7.59% from 30-400 °C (calcd. 7.52% for 15 H_2O).

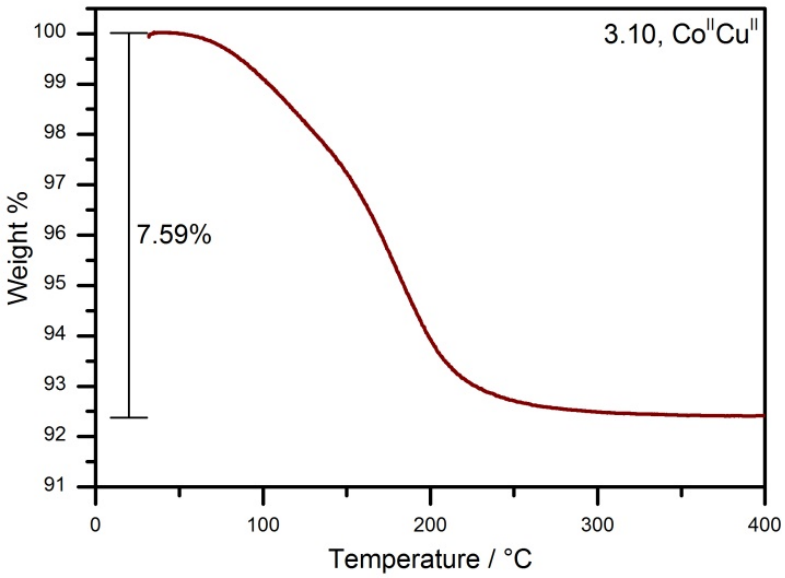

Figure 3.10. Thermogravimetric analysis of **3.10**. The annotated total weight loss is attributed to waters of hydration and bound aqua ligands.

$K_8[Co^{II}Zn^{II}(H_2O)W_{11}O_{39}]\bullet 14H_2O$ (3.11, $Co^{II}Zn^{II}$). Zinc chloride (48 mg, 0.35 mmol) was dissolved in 15 mL potassium acetate buffer, pH 5, and heated to 60 °C. Crystalline $K_9[Co^{III}W_{11}O_{39}]\bullet 13H_2O$ (1.0 g, 0.30 mmol) was added in portions, and the solution turned orange. The solution was stirred and heated for one hour, during which time sodium ascorbate (60 mg, 0.30 mmol) was added and the solution turned dark blue. The solution was filtered, potassium chloride (5.0 g, 67 mmol) was added, and the solution was cooled at 5 °C overnight to yield a blue solid. The crude product was collected by filtration, rinsed with 5 mL cold 2M potassium chloride solution, and redissolved in minimal hot deionized water. Blue crystals of **3.11** were obtained by slow evaporation. Yield: 0.666 g (65.4%). FTIR (2% KBr pellet), $\tilde{\nu}$, cm^{-1}:934 (s), 921 (sh), 858 (s), 789 (sh), 750 (vs), 704 (m), 535 (w), 442 (m). UV-vis (H_2O), λ_{max}, nm (ε, L mol^{-1} cm^{-1}): 600 (185). Elemental analysis: calcd. (found) for $K_8Co_1Zn_1W_{11}O_{54}H_{30}$, %: K,

9.33 (8.71); Co, 1.76 (1.92); Zn, 1.95 (1.79); W, 60.3 (58.3). TGA (Figure 3.11) shows a weight loss of 7.49% from 30-500 °C (calcd. 7.52% for 15 H_2O).

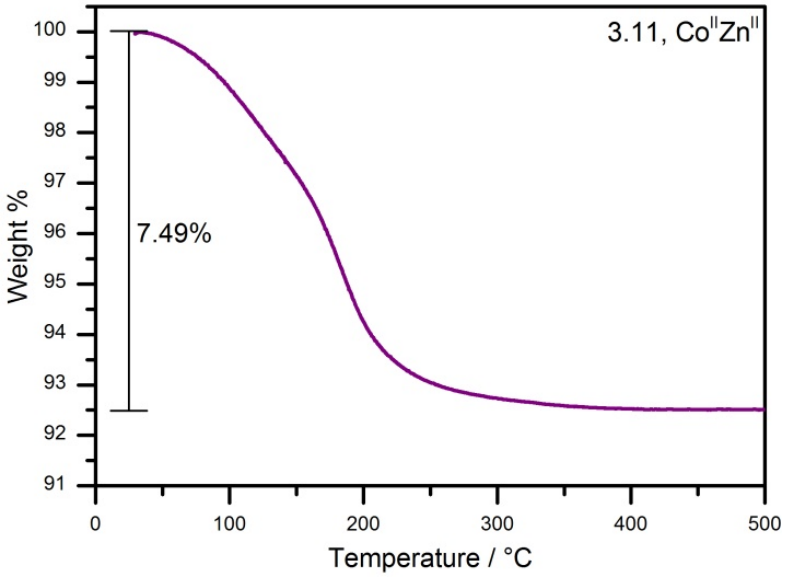

Figure 3.11. Thermogravimetric analysis of **3.11**. The annotated total weight loss is attributed to waters of hydration and bound aqua ligands.

3.3.3 Single Crystal X-ray Structural Determination

The dicobalt anion **3.8** was synthesized as X-ray diffraction quality crystals of the ammonium salt $[NH_4]_7[Co(H_2O)_6]_{0.5}[Co_2(H_2O)W_{11}O_{39}]$ following the method of Baker and McCutcheon.[42] Suitable single crystals were selected under ambient conditions, mounted on a cryoloop using Paratone-N oil, and placed under the cryostream at 173 K. Crystal evaluation and collection of X-ray diffraction intensity data were performed using a Bruker Apex II CCD diffractometer (Mo K_a, l = 0.71073 Å), and data reduction was carried out using the Bruker *APEXII* program suite.[47] Correction for incident and diffracted beam absorption effects were applied using numerical methods.[48] The compound crystallized in *Fm-3m* as determined by systematic absences in the intensity data, intensity statistics and the successful solution and refinement of the structure. Structure solution and refinement was carried out using the Bruker SHELXTL software package.[49] The structure was solved by direct methods and refined against F^2 by the full matrix least-squares technique. All non-H atoms were refined anisotropically, H atoms were not located or refined, and the addendum Co^{II} atom was 12-fold disordered (position modelled as 16.7% Co, 83.3% W). Crystal data, data collection parameters and refinement statistics are listed in Table 3.1, an ORTEP representation of **3.8** is provided in Figure 3.12, and bond lengths and angles are tabulated in Table 3.2.

Table 3.1. Crystal data, data collection parameters and refinement statistics for $[NH_4]_7[Co(H_2O)_6]_{0.5}[Co_2(H_2O)W_{11}O_{39}]$ (**3.8-NH$_4$**)

Empirical formula	$Co_{2.5}H_{68}N_7O_{59}W_{11}$
F_w **/ g mol^{-1}**	3280.29
T **/ K**	173(2)
λ **/ Å**	0.71073
Crystal system	cubic
Space group	*Fm-3m*
a **/ Å**	22.376(8)
b **/ Å**	22.376(8)
c **/ Å**	22.376(8)
α **/ °**	90
β **/ °**	90
γ **/ °**	90
V **/Å^3**	11203(7)
Z	8
ρ_{calc} **/ g cm^{-3}**	3.890
μ **/ mm^{-1}**	23.331
Crystal size / mm^3	0.16 × 0.14 × 0.10
No. reflections (unique)	57069 (918)
R_{int}	0.0557
θ_{max}	30.46
Completeness to θ_{max}	99.7%
Data / restraints / parameters	918 / 6 / 53
Goodness-of-fit on F^2	1.217
Residuals: R_1; wR_2	0.0231 (0.0616)
Final difference peak and hole / eÅ^{-3}	1.259, -2.524

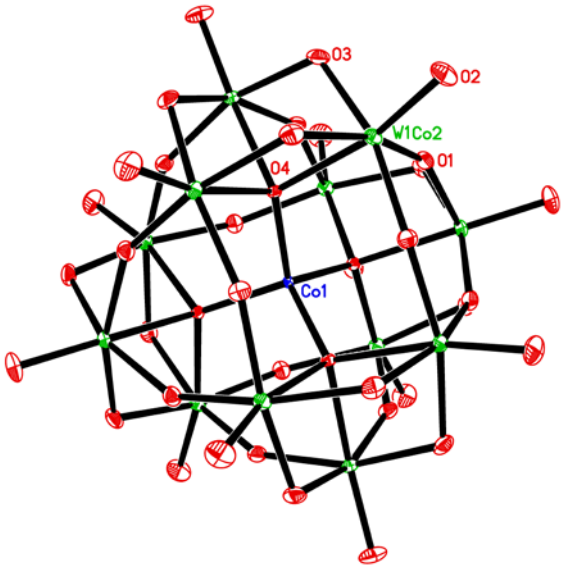

Figure 3.12. ORTEP representation of the **3.8** anion, $[Co^{II}Co^{II}(H_2O)W_{11}O_{39}]^{8-}$. Thermal ellipsoids are at the 30% probability level. Color scheme: W, green; O, red; Co, blue. H atoms were not located. W1Co2 is modelled as 16.7% Co, 83.3% W.

Table 3.2. Coordinate bond lengths (Å) and angles (°) in **3.8** by x-ray diffraction

Distances / Å		**Angles / °**	
Co1-O4	1.914(7)	O4-Co1-O4*	109.471(1)
W1/Co2-O1	1.923(2)	O1-W1/Co2-O1*	86.5(3)
W1/Co2-O2	1.753(5)	O1-W1/Co2-O2	100.6(2)
W1/Co2-O3	1.965(3)	O1-W1/Co2-O3	88.8(2)
W1/Co2-O4	2.147(4)	O1-W1/Co2-O3*	162.3(2)
		O1-W1/Co2-O4	88.3(2)
		O2-W1/Co2-O3	97.1(2)
		O2-W1/Co2-O4	167.7(3)
		O3-W1/Co2-O3*	90.6(3)
		O3-W1/Co2-O4	74.5(2)
		Co1-O4-W1/Co2	118.7(2)
		W1/Co2-O1-W1/Co2*	151.2(3)
		W1/Co2-O3-W1/Co2*	112.1(2)
		W1/Co2-O4-W1/Co2*	98.8(2)

***Signifies symmetry generated position

3.3.4 Transient Absorption Measurements

The femtosecond (0.1 ps – 1.2 ns) transient absorption (TA) spectrometer used in this study was based on a regeneratively amplified Ti:sapphire laser system (Coherent Legend, 800 nm, 150 fs, 3 mJ/pulse, 1 kHz repetition rate) and the Helios spectrometer (Ultrafast Systems, LLC). Details about the instrument setup can be found in the previous study.[41] Samples for transient analysis were filtered with a Whatman 0.2 μm PES syringe filter, measured in a 1 mm path length quartz cuvette to minimize the transient solvent response, constantly stirred by a magnetic stirrer during data collection to minimize localized thermal effects, and the solvent effect in neat buffered solvent was recorded immediately following each sample measurement. No evidence of sample degradation was seen based on comparisons of electronic absorption spectra before and after transient measurements. Detailed analysis of the transient spectra, temporal chirp correction, quantitative kinetic analysis, and global fit analysis via singular value decomposition was performed using Ultrafast Systems Surface Xplorer Pro The principal kinetic components were fit to a multiexponential decay function convoluted with the Gaussian instrument response function (fwhm: ~150 fs).

3.3.5 Computational Studies

Geometries of the anions $[Co^{II}(M^{x}OH_{y})W_{11}O_{39}]^{(12-x-y)-}$, [**CoM^{x}**], and their one-electron oxidized forms $[Co^{II}(M^{x}OH_{y})W_{11}O_{39}]^{(11-x-y)-}$, [**CoM^{x}**]$^{+}$, for $M^{x}OH_{y}$ = $V^{IV}O$, $Cr^{III}(OH_2)$, $Mn^{II}(OH_2)$, $Fe^{III}(OH_2)$, $Co^{II}(OH_2)$, $Ni^{II}(OH_2)$, $Cu^{II}(OH_2)$ and $Zn^{II}(OH_2)$, were optimized at their several lower-lying electronic states in the gas phase with no geometry constraints. Vibrational analyses were performed to ensure that all reported structures are

true minima. In these calculations we used the spin-unrestricted DFT method (the hybrid B3LYP functional)[50-52] in conjunction with the D95V[53,54] basis sets for O, and the lanl2dz basis set with the associated Hay-Wadt ECPs[55-57] for the W, V, Cr, Mn, Fe, Co, Ni, Cu and Zn atoms, which below will be referred to as "UB3LYP/lanl2dz". Previously,[41,58] we have shown that the DFT/lanl2dz approach describes both low-lying electronic states and geometries of the transition metal substituted polyoxometalate anions with reasonable accuracy. Therefore, here we discuss the DFT/lanl2dz calculated geometries and low-lying electronic states of the studied anions with confidence. Solvent effects were applied as single point calculations on top of the gas phase structures and approximated by the polarizable continuum model (PCM)[59] employing the UFF[58] radii for all atoms. All calculations were carried out with the Gaussian 09 software package.[60]

3.4 Results and Discussion

3.4.1 Synthesis

The synthetic strategy used to prepare the reported series of TMSP derivative complexes is an extension of work reported by Bas-Serra *et al* in isolating $[Co^{III}W_{11}O_{39}]^{9-}$.[45] Controlled increase of the pH by addition of potassium acetate to a solution containing the plenary complex $[Co^{III}W_{12}O_{40}]^{5-}$ (**3.2**) leads to the dissociation of a single tungsten oxo (W=O) unit from the polytungstate framework, converting the plenary complex to the monolacunary complex $[Co^{III}W_{11}O_{39}]^{9-}$ (**3.3**). The resulting lacunary POM serves as a pentadentate ligand, wherein the "pocket" consists of four proximal oxygen atoms (O^5, O^6, O^7 and O^8, in Figure 3.13) and a fifth oxygen atom (O^1) bound to the central heteroatom at the center of the complex. Binding of a transition

metal (M) within the pocket affords an oxido bound bimetallic complex, where the central tetrahedral heteroatom is indirectly bound to a transition metal with pseudo-octahedral local symmetry.

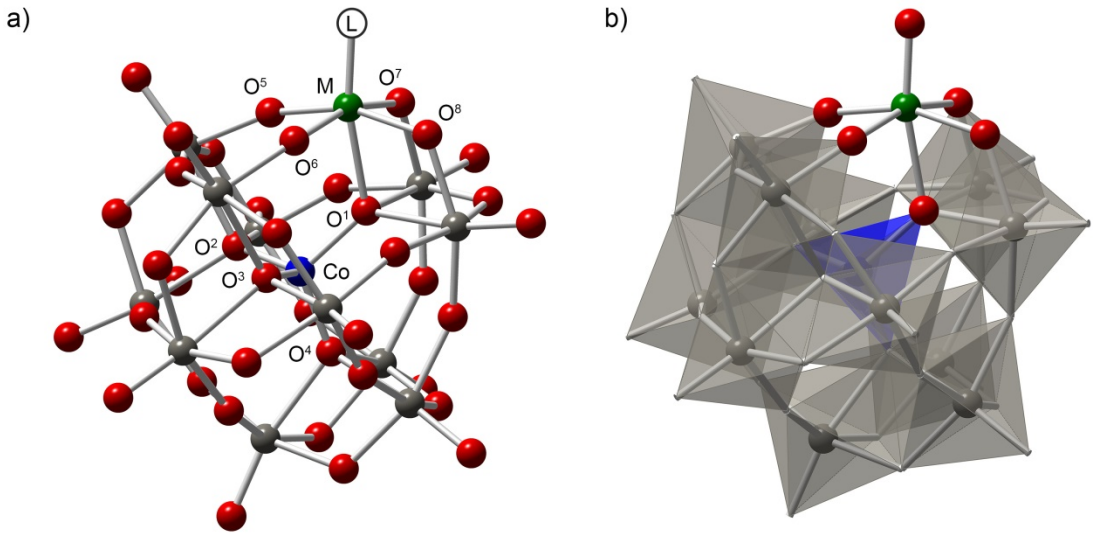

Figure 3.13. Representative structure of the TMSP derivatives and notation of the atoms in a) ball-and-stick, and b) mixed polyhedral notation. Color scheme: W, grey; O, red; Co, blue; M, green.

For this study, a range of 3d-transition metals (V^{4+} through Zn^{2+}) were incorporated into **3.3** to evaluate the effect they have on the photodynamics of the plenary complex, **3.1**. Binding of the transition metal to **3.3** maintained the trivalent nature of the heteroatom, so to access the desired Co^{II}-centered anions it was necessary to reduce the resulting Co^{III} complexes by one electron. In most cases this was achieved using sodium ascorbate; for **3.4** and **3.7**, excess vanadyl sulfate and Fe^{2+} were used as reducing agents, respectively, to similar effect on cobalt. An analogous series of TMSP complexes, $[Co^{III}(M^{x}OH_{y})W_{11}O_{39}]^{(11-x-y)-}$, is easily synthesized by omitting the reducing agent or

using a strong oxidizing agent; this is beyond the scope of the current study. Although single crystals of many of our compounds were obtained, we have limited our structural study to **3.8** and comparison with the literature structure of [$\mathbf{Co^{III}Co^{II}}$][61] and our DFT-calculated bond lengths (*vide infra*). This is because the high symmetry space groups result in twelve-fold disorder of the addendum heterometal and prevent extraction of accurate bond lengths. Satisfactory characterization of each complex has instead been accomplished by comparison to the lacunary complex **3.3** and its one-electron reduced parent **3.1** using infrared and UV-visible spectroscopy, cyclic voltammetry, and elemental analysis.

3.4.2 Calculated Ground State Geometries and Electronic Structures

Calculated important bond lengths (Table 3.3) and un-paired spin densities (Table 3.4) of selected atoms of the experimentally prepared TMSP anions [$\mathbf{CoM^x}$], as well as their one-electron oxidized forms [$\mathbf{CoM^x}$]$^+$, for $M^x = V^{IV}$, Cr^{III}, Mn^{II}, Fe^{III}, Co^{II}, Ni^{II}, Cu^{II}, Zn^{II}, are summarized below. A representative structure of the calculated systems with notation of atoms is given in Figure 3.13.

Table 3.3. Calculated important bond distances (in Å) for TMSP anions $[Co^{II}(M^{x}OH_{y})W_{11}O_{39}]^{(12-x-y)-}$, [**CoM^{x}**], and their one-electron oxidized forms [**CoM^{x}**]$^{+}$

Parameter		M-O^{1}	M-O^{5}	M-O^{6}	M-O^{7}	M-O^{8}
M = V^{IV}	[$Co^{II}V^{IV}$]	2.25	1.99	1.99	2.03	2.03
	[$Co^{II}V^{V}$]	2.28	1.98	1.98	1.84	1.84
M = Cr^{III}	[$Co^{II}Cr^{III}$]	1.87	1.96	1.96	2.00	2.00
	[$Co^{III}Cr^{III}$]	1.89	1.94	1.95	1.98	1.99
M = Mn^{II}	[$Co^{II}Mn^{II}$]	2.16	1.94	1.93	1.92	1.93
	[$Co^{II}Mn^{III}$]	2.07	1.93	1.91	1.96	1.96
M = Fe^{III}	[$Co^{III}Fe^{II}$]	2.09	2.06	2.01	2.17	2.19
	[$Co^{III}Fe^{III}$]	2.01	1.96	1.96	2.04	2.03
M = Co^{II}	[$Co^{II}Co^{II}$]	2.03	2.06	2.02	2.18	2.18
	[$Co^{III}Co^{II}$]	2.08	2.04	2.01	2.13	2.13
M = Ni^{II}	[$Co^{II}Ni^{II}$]	1.99	2.05	2.02	2.13	2.12
	[$Co^{III}Ni^{II}$]	2.02	2.04	2.00	2.11	2.09
M = Cu^{II}	[$Co^{II}Cu^{II}$]	2.19	2.02	1.98	2.06	2.10
	[$Co^{III}Cu^{II}$]	2.23	2.00	1.98	2.05	2.04
M = Zn^{II}	[$Co^{II}Zn^{II}$]	2.02	2.05	2.05	2.21	2.21
	[$Co^{III}Zn^{II}$]	2.07	2.05	2.05	2.15	2.15

Parameter		Co-O^{1}	Co-O^{2}	Co-O^{3}	Co-O^{4}
M = V^{IV}	[$Co^{II}V^{IV}$]	1.91	1.93	1.93	1.92
	[$Co^{II}V^{V}$]	1.90	1.92	1.92	1.92
M = Cr^{III}	[$Co^{II}Cr^{III}$]	1.94	1.91	1.91	1.90
	[$Co^{III}Cr^{III}$]	1.87	1.83	1.81	1.82
M = Mn^{II}	[$Co^{II}Mn^{II}$]	1.91	1.93	1.93	1.92
	[$Co^{II}Mn^{III}$]	1.92	1.92	1.92	1.91
M = Fe^{III}	[$Co^{III}Fe^{II}$]	1.85	1.85	1.85	1.85
	[$Co^{III}Fe^{III}$]	1.86	1.83	1.82	1.84
M = Co^{II}	[$Co^{II}Co^{II}$]	1.94	1.94	1.94	1.94
	[$Co^{III}Co^{II}$]	1.85	1.85	1.85	1.85
M = Ni^{II}	[$Co^{II}Ni^{II}$]	1.93	1.93	1.93	1.93
	[$Co^{III}Ni^{II}$]	1.85	1.84	1.85	1.84
M = Cu^{II}	[$Co^{II}Cu^{II}$]	1.92	1.93	1.93	1.93
	[$Co^{III}Cu^{II}$]	1.81	1.85	1.85	1.86
M = Zn^{II}	[$Co^{II}Zn^{II}$]	1.94	1.94	1.94	1.92
	[$Co^{III}Zn^{II}$]	1.84	1.85	1.85	1.84

Table 3.4. Calculated unpaired spin densities (in |e|) for TMSP anions $[Co^{II}(M^{x}OH_{y})W_{11}O_{39}]^{(12-x-y)-}$, [**CoM^{x}**], and their one-electron oxidized forms [**CoM^{x}**]$^{+}$

Parameter		M	Co	O^{1}	O^{2}	O^{3}	O^{4}
M = V^{IV}	$[Co^{II}V^{IV}]$	1.10	2.73	0.06	0.06	0.06	0.06
	$[Co^{II}V^{V}]$	0.00	2.73	0.06	0.06	0.06	0.06
M = Cr^{III}	$[Co^{II}Cr^{III}]$	3.01	2.72	0.01	0.06	0.06	0.06
	$[Co^{III}Cr^{III}]$	2.99	2.98	0.13	0.25	0.28	0.25
M = Mn^{II}	$[Co^{II}Mn^{II}]$	2.88	2.22	0.17	0.06	0.06	0.06
	$[Co^{II}Mn^{III}]$	3.80	2.73	0.19	0.06	0.06	0.06
M = Fe^{III}	$[Co^{III}Fe^{II}]$	3.78	2.99	0.30	0.23	0.23	0.22
	$[Co^{III}Fe^{III}]$	4.12	3.01	0.42	0.25	0.26	0.24
M = Co^{II}	$[Co^{II}Co^{II}]$	2.71	2.73	0.15	0.06	0.06	0.06
	$[Co^{III}Co^{II}]$	2.72	3.00	0.30	0.24	0.24	0.24
M = Ni^{II}	$[Co^{II}Ni^{II}]$	1.65	2.74	0.19	0.06	0.06	0.06
	$[Co^{III}Ni^{II}]$	1.67	3.00	0.33	0.24	0.24	0.24
M = Cu^{II}	$[Co^{II}Cu^{II}]$	0.65	2.73	0.06	0.06	0.06	0.06
	$[Co^{III}Cu^{II}]$	0.65	2.98	0.32	0.22	0.21	0.21
M = Zn^{II}	$[Co^{II}Zn^{II}]$	0.00	2.73	0.06	0.06	0.06	0.06
	$[Co^{III}Zn^{II}]$	0.00	2.99	0.25	0.23	0.23	0.23

Parameter		O^{5}	O^{6}	O^{7}	O^{8}	CoO_4	MO_4
M = V^{IV}	$[Co^{II}V^{IV}]$	-0.01	-0.01	0.00	0.00	2.97	1.08
	$[Co^{II}V^{V}]$	0.00	0.00	0.00	0.00	2.97	0.00
M = Cr^{III}	$[Co^{II}Cr^{III}]$	0.00	0.00	-0.01	-0.01	2.91	2.99
	$[Co^{III}Cr^{III}]$	0.00	0.00	0.00	0.00	3.89	2.99
M = Mn^{II}	$[Co^{II}Mn^{II}]$	0.01	0.01	0.00	0.00	2.57	2.90
	$[Co^{II}Mn^{III}]$	0.01	0.01	0.00	0.00	3.10	3.82
M = Fe^{III}	$[Co^{III}Fe^{II}]$	0.04	0.04	0.04	0.04	3.97	3.94
	$[Co^{III}Fe^{III}]$	0.15	0.16	0.15	0.16	4.17	4.74
M = Co^{II}	$[Co^{II}Co^{II}]$	0.04	0.04	0.04	0.04	3.06	2.87
	$[Co^{III}Co^{II}]$	0.04	0.04	0.04	0.04	4.02	2.88
M = Ni^{II}	$[Co^{II}Ni^{II}]$	0.04	0.04	0.06	0.06	3.11	1.85
	$[Co^{III}Ni^{II}]$	0.04	0.05	0.06	0.06	4.05	1.88
M = Cu^{II}	$[Co^{II}Cu^{II}]$	0.07	0.07	0.10	0.07	2.97	0.96
	$[Co^{III}Cu^{II}]$	0.07	0.07	0.10	0.10	3.94	0.99
M = Zn^{II}	$[Co^{II}Zn^{II}]$	0.00	0.00	0.00	0.00	2.97	0.00
	$[Co^{III}Zn^{II}]$	0.00	0.00	0.00	0.00	3.93	0.00

Previously we (and others) have shown,[41,62-64] through experimental and computational investigation, that the Co-O bond lengths around the central cobalt in **$Co^{II}W_{12}$** (i.e. Co-$O^{1,2,3,4}$ bond distances in Table 3.3, see also Figure 3.13) and total spin densities of the CoO_4-unit are indicative of the cobalt oxidation state. The Co-O bond lengths around the central cobalt are significantly longer for the $[Co^{II}O_4]$ fragment than for $[Co^{III}O_4]$. Similarly, here, we use both the DFT-calculated Co-O bond lengths around the central cobalt and amount of the unpaired spin densities in the MO_4- and CoO_4-units to determine the oxidation states of the M and Co-centers in anions $[CoM^x]$ and $[CoM^x]^+$. X-ray crystal structures of **$Co^{II}Co^{II}$** (see SI) and **$Co^{III}Co^{II}$** [61] indicate that our calculations replicate the geometric structures of these anions well. The central, tetrahedral Co in **$Co^{II}Co^{II}$** has a Co-O bond length of 1.914(7) Å (effectively an average of both Co-O-W and Co-O-Co due to disorder), while in **$Co^{III}Co^{II}$** this contracts to 1.82(2) Å. In our calculations, these distances are 1.94 and 1.85 Å respectively, and the small difference of *ca*. 0.03 Å is unsurprising when comparing solid state structures to those of calculated molecular systems.

Calculations show that the anion $[Co(VO)W_{11}O_{39}]^{8-}$ has energetically degenerate ferromagnetic ^5A and anti-ferromagnetic ^3A electronic states with Co(d^7) and V(d^1)-centers. In its ^3A electronic state the Co-center possesses three α-spins, while the V-center holds only one β-spin. Thus, this anion should be characterized as a $[Co^{II}(V^{IV}O)W_{11}O_{39}]^{8-}$ (**$Co^{II}V^{IV}$**) species. As seen in Table 3.3, the (VO) unit in this anion only weakly interacts with both the internal CoO_4 fragment (the calculated V-O^1 distance is 2.25 Å) and W-framework (calculated V-$O^{5,6,7,8}$ distances are 2.03-1.99 Å). One electron oxidation of **$Co^{II}V^{IV}$** is associated with the removal of an unpaired electron from

the V-center and leads to the formation of the $[Co^{II}(V^{V}O)W_{11}O_{39}]^{7-}$ anion (**$Co^{II}V^{V}$** in Table 3.3) with a d^0 vanadium center. The ground electronic state of this **$Co^{II}V^{V}$** anion is a high-spin S = 3/2 quartet state. Interestingly, the oxidation from **$Co^{II}V^{IV}$** to **$Co^{II}V^{V}$** results in a shortening of the V-$O^{5,6}$(W) bonds. Therefore, **$Co^{II}V^{V}$** is expected to be more stable (against dissociation of the vanadyl fragment) than its parent **$Co^{II}V^{IV}$**.

Anion $[CoCr(H_2O)W_{11}O_{39}]^{7-}$ is also found to have energetically degenerate ferromagnetic and anti-ferromagnetic coupled ^{7}A and ^{1}A-states with S = 3 total spin and Co(d^7) and Cr(d^3)-centers. Thus, it should be characterized as a $[Co^{II}Cr^{III}(H_2O)W_{11}O_{39}]^{7-}$ (**$Co^{II}Cr^{III}$**) species. The calculated Cr-O^1(Co) bond in **$Co^{II}Cr^{III}$** is significantly shorter than the V-O^1(Co) bond in **$Co^{II}V^{IV}$**. Calculated spin densities as well as Co-O bond distances in the CoO_4-core clearly show that one electron oxidation of **$Co^{II}Cr^{III}$** corresponds to removal of an electron from the Co-center, rather than from the Cr-center. Therefore, the one-electron oxidized form of **$Co^{II}Cr^{III}$** should be characterized as a $[Co^{III}Cr^{III}(H_2O)W_{11}O_{39}]^{6-}$ anion (**$Co^{III}Cr^{III}$**). Indeed, in the **$Co^{III}Cr^{III}$** anion the calculated Co-O bond distances are significantly shorter than those in the parent compound **$Co^{II}Cr^{III}$**. Furthermore, the calculated spin density on the CoO_4-unit of **$Co^{III}Cr^{III}$** is close to four, consistent with a tetrahedral Co(d^6)-center. It should be emphasized that oxidation of **$Co^{II}Cr^{III}$** to **$Co^{III}Cr^{III}$** leads to slight elongation of the Cr-O^1(Co) bond, likely because of strengthening of the competing Co-O^1(Cr) bond.

The Mn-atom of anion $[CoMn(H_2O)W_{11}O_{39}]^{8-}$ in its energetically lowest and degenerate ferromagnetically and anti-ferromagnetically coupled ^{7}A and ^{1}A-states with S = 3 total spin, and with Co(d^7) and Mn(d^5)-centers, is found to have only three unpaired spins. Its ^{9}A electronic state with S = 4 total spin and Mn(d^5)-center with five unpaired

α-spins lies only *ca.* 1 kcal/mol higher. Thus, anion $[CoMn(H_2O)W_{11}O_{39}]^{8-}$ could be characterized as a $[Co^{II}Mn^{II}(H_2O)W_{11}O_{39}]^{8-}$ (**$Co^{II}Mn^{II}$**). One electron oxidation of **$Co^{II}Mn^{II}$**, in contrast to **$Co^{II}Cr^{III}$**, leads to oxidation of the Mn-center, rather than the Co-center. As seen in Table 3.4, in $[CoMn(H_2O)W_{11}O_{39}]^{7-}$, the Mn-center possesses almost four unpaired spins in its energetically lowest ^{8}A and ^{2}A-states with S = 7/2 total spin. Thus, one electron oxidation of **$Co^{II}Mn^{II}$** leads to the $[Co^{II}Mn^{III}(H_2O)W_{11}O_{39}]^{7-}$ (**$Co^{II}Mn^{III}$**) anion. Once again, one-electron oxidation of **$Co^{II}Mn^{II}$** elongates the M-O^1(Co) bond distance.

Calculations show that for the second half of the transition metal series (M = Fe^{III} to Zn^{II}) all the anions are the $[Co^{II}M^{x}(H_2O)W_{11}O_{39}]^{(10-x)-}$ (**$Co^{II}M^{II}$** or **$Co^{II}M^{III}$**), species, and their one-electron oxidation associates with the removal of an electron from the CoO_4-fragment. Our calculations of the $[CoFe(H_2O)W_{11}O_{39}]^{7-}$ anion converged to its $[Co^{III}Fe^{II}]$ state with four α-spins on both Fe- and Co-centers, not the $[Co^{II}Fe^{III}]$ state expected based on experimental techniques. The $[Co^{II}Fe^{III}]$ state, which is expected to be only slightly (less than 1.0 kcal/mol) higher in energy, cannot be calculated at the DFT level. Therefore, in our estimation of the one-electron oxidation energy for the $[CoFe(H_2O)W_{11}O_{39}]^{7-}$ anion we used the energetically lowest $[Co^{III}Fe^{II}]$ state. As seen in Table 3.4, upon oxidation from [**$Co^{II}M^{II}$**] to [**$Co^{II}M^{II}$**]$^+$ (where M = Fe, Co, Ni, Cu and Zn) the number of unpaired spins in M-centers does not change, but it increases by one in the CoO_4-fragment. In addition, the Co-O bond distances in the CoO_4-unit significantly shorten upon this one-electron oxidation process.

In order to support the findings above we also calculated a one-electron oxidation potential for all reported anions, *i.e.* reactions **$Co^{II}V^{IV} \rightarrow Co^{II}V^{V}$**, **$Co^{II}Cr^{III} \rightarrow Co^{III}Cr^{III}$**,

$\mathbf{Co^{II}Mn^{II} \rightarrow Co^{II}Mn^{III}}$, $\mathbf{Co^{II}Fe^{III} \rightarrow Co^{III}Fe^{III}}$, and $\mathbf{Co^{II}M^{II} \rightarrow Co^{III}M^{II}}$, where M = Co, Ni, Cu and Zn (Table 3.5). In these calculations, we assumed that the electron dissociates directly to the water solution, while we did not include hydration energy of the electron into our final results. Therefore, absolute values of these calculated energies should be used with caution, while the relative changes of these values could be useful in determining the nature of the oxidation process. As seen in Table 3.5, the energy of these reactions is close for M = Cr, Fe, Co, Ni, Cu, and Zn, which suggests that the central Co^{II} heteroatom is oxidized in these systems. Deviation of the calculated values from that for the system with M = Co could be used to estimate the degree of electronic coupling between the Co- and M-centers, which varies as M = Cr >> Ni ≅ Cu > Zn > V > Fe. The calculated value for the system with M = Mn is very different from that for the other anions, indicative of oxidation occurring at the addendum heterometal.

Table 3.5. Calculated one-electron oxidation potentials (in kcal/mol) for TMSP anions $[Co^{II}(M^{x}OH_{y})W_{11}O_{39}]^{(12-x-y)-}$, $[\mathbf{CoM^{x}}]$, and their one-electron oxidized forms $[\mathbf{CoM^{x}}]^{+}$

Parameter		**ΔE_{ox}**
$M = V^{IV}$	$[Co^{II}V^{IV}]$	98.7
$M = Cr^{III}$	$[Co^{II}Cr^{III}]$	113.0
$M = Mn^{II}$	$[Co^{II}Mn^{II}]$	69.0
$M = Fe^{III}$	$[Co^{III}Fe^{II}]$	100.1
$M = Co^{II}$	$[Co^{II}Co^{II}]$	101.5
$M = Ni^{II}$	$[Co^{II}Ni^{II}]$	105.0
$M = Cu^{II}$	$[Co^{II}Cu^{II}]$	98.0
$M = Zn^{II}$	$[Co^{II}Zn^{II}]$	98.6

In summary, the computational data clearly show that the removal of an electron from $[Co^{II}(V^{IV}O)W_{11}O_{39}]^{8-}$ and $[Co^{II}Mn^{II}(H_2O)W_{11}O_{39}]^{8-}$ oxidizes vanadium and manganese centers, respectively. In contrast, the removal of an electron from $[Co^{II}M^{x}(H_2O)W_{11}O_{39}]^{(10-x)-}$ anions for M = Cr^{III}, Fe^{III}, Co^{II}, Ni^{II}, Cu^{II} and Zn^{II} oxidizes the Co-center of the CoO_4-unit, and leads to elongation of the M-O(Co) bond distance. Furthermore, all calculated TMSP anions are found to have energetically degenerate ferromagnetically and anti-ferromagnetically coupled ground electronic states with unpaired electrons on M- and Co-centers.

3.4.3 Static Infrared Spectroscopy

Successful incorporation of a transition metal within the pocket of a lacunary POM was verified by infrared spectroscopy. The IR spectrum for each TMSP complex and the precursor POM complexes **3.1 ($Co^{II}W_{12}$)**, **3.2 ($Co^{III}W_{12}$)**, and **3.3 ($Co^{III}W_{11}$)** are superimposed in Figure 3.14. The plenary complexes exhibit relatively few IR absorption bands due to their high symmetry. The reduction in symmetry upon formation of **3.3** leads to the observation of splitting of the W-O-W bands around 850 cm^{-1} and 750 cm^{-1}. This splitting is a general feature of lacunary POMs.[65,66] The incorporation of a transition metal into the lacunary POM leads to an increase in the symmetry of the complex, causing the characteristic W-O-W splitting to disappear for all TMSP complexes.

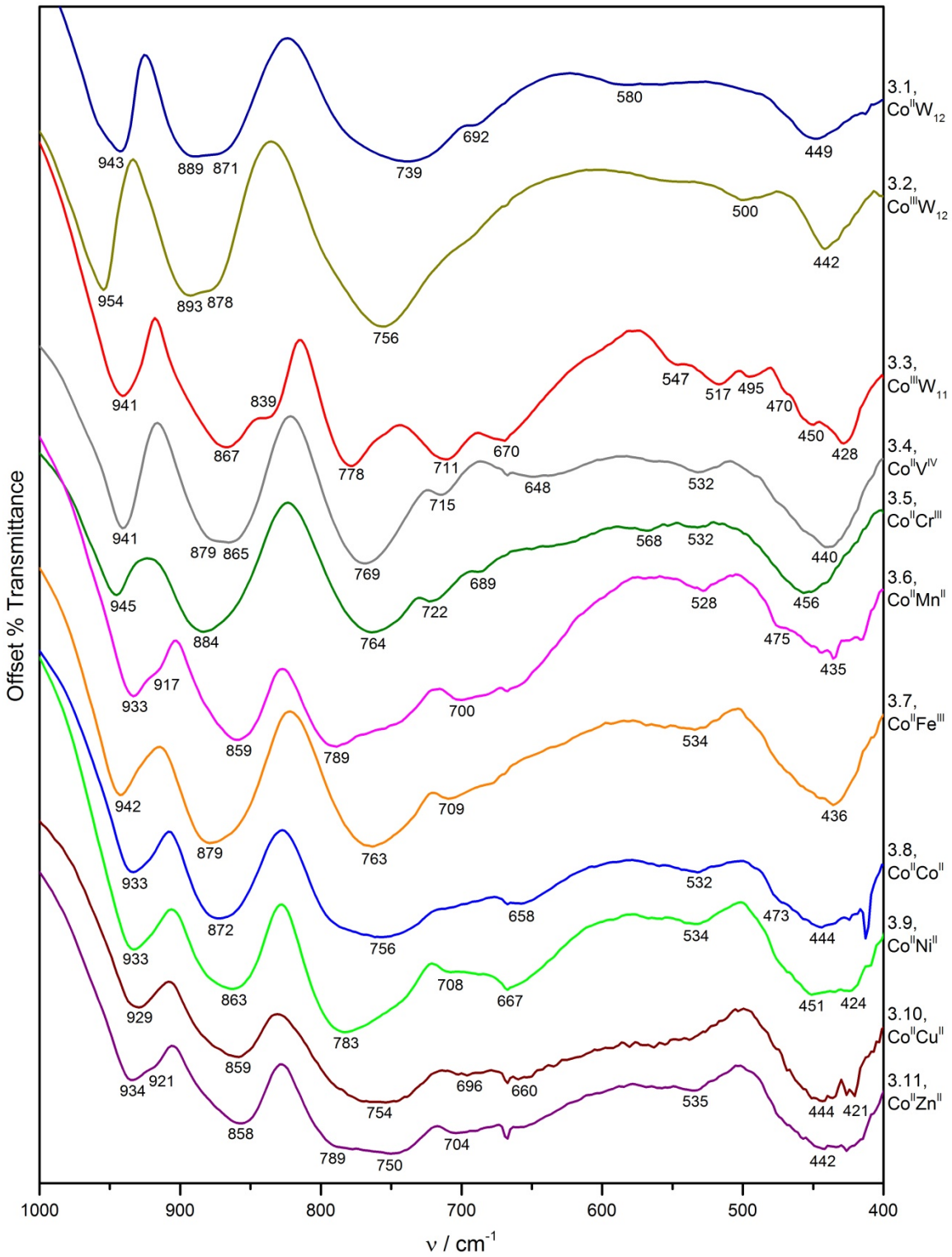

Figure 3.14. Offset infrared spectra (2% KBr pellet) for the plenary POMs **3.1** and **3.2**, the lacunary TMSP-precursor **3.3**, and eight TMSP derivatives **3.4-3.11**.

3.4.4 Static Electronic Absorption Spectroscopy

Comparison of the UV-visible absorption bands for each TMSP complex to the plenary complexes **3.1** and **3.2**, supported by the results of our calculations, allows for definitive assignment of the electronic transitions in this series. Comparison of the absorption bands to the plenary complex will also permit an investigation into the changes in electronic structure caused by substitution of a transition metal into the polytungstate framework.

The UV-visible absorption spectra for all complexes contain strong UV absorptions at 180 and 250 nm arising from $O_{2p} \rightarrow W_{5d}$ charge transfer transitions, a common feature in all polyoxotungstates. As previously reported,[41] the presence of a cobalt heteroatom introduces lower energy features consistent with MPCT and metal-centered electronic transitions. The UV-visible absorption spectra for this series (Figures 3.15 and 3.16) are consistent with previous assignments. Each complex exhibits a definitive feature centered at ~625 nm associated with the $^4A_2 \rightarrow {}^4T_1$ d-d transition of the tetrahedral Co^{II} heteroatom. The extinction coefficient at 625 nm is similar to that of the plenary complex, varying by less than 20% in all but two cases (Table 3.6). The most extreme deviation occurs for **3.4**, where the lower lying orbitals of V^{IV} result in the significant presence of $O_{2p} \rightarrow V_{3d}$ transitions tailing well into the visible spectrum, causing a marked increase in the extinction coefficients for this complex and the appearance that the cobalt $^4A_2 \rightarrow {}^4T_1$ transition is rising out of this structureless tail. Additional minor features present in each complex are the result of d-d transitions within the pseudo-octahedral substituted metals, most obviously seen in **3.4** and **3.7**. The shape and peak energy of the d-d manifold stays roughly the same throughout the TMSP series,

suggesting that any coupling to the substituted metal is weak or results in a uniform perturbation of the electronic structure of the Co^{II} heteroatom.

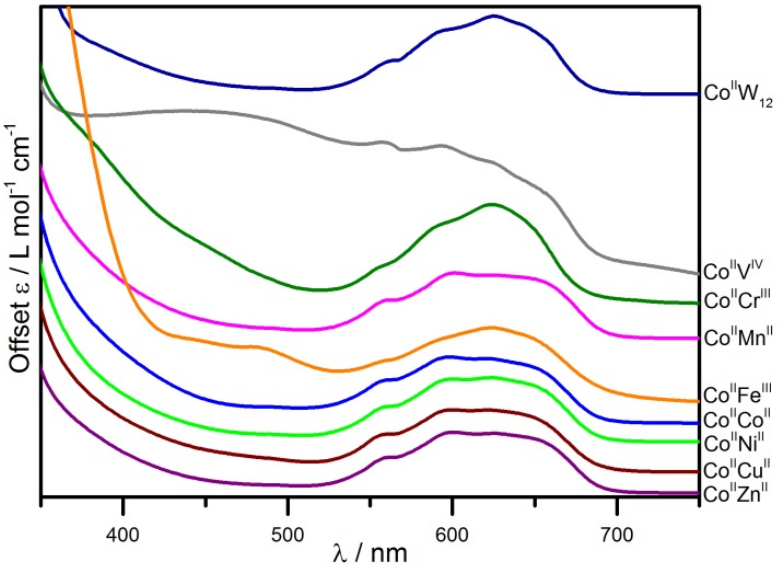

Figure 3.15. Offset visible electronic absorption spectra of the plenary Keggin POM **3.1** (**$Co^{II}W_{12}$**) and eight TMSP derivatives, **3.4**-**3.11**, in water. The spectra are offset to highlight the common feature at ~625 nm, assigned to the d-d transition of the tetrahedral Co^{II} heteroatom.

Table 3.6. Comparison of the electronic absorption spectra of TMSPs

Complex	ε_{400} / L mol^{-1} cm^{-1}	ε_{625} / L mol^{-1} cm^{-1}
$Co^{II}W_{12}$	108	223
$Co^{II}V^{IV}$	543	405
$Co^{II}Cr^{III}$	359	285
$Co^{II}Mn^{II}$	164	183
$Co^{II}Fe^{III}$	384	233
$Co^{II}Co^{II}$	205	184
$Co^{II}Ni^{II}$	144	191
$Co^{II}Cu^{II}$	175	198
$Co^{II}Zn^{II}$	128	182

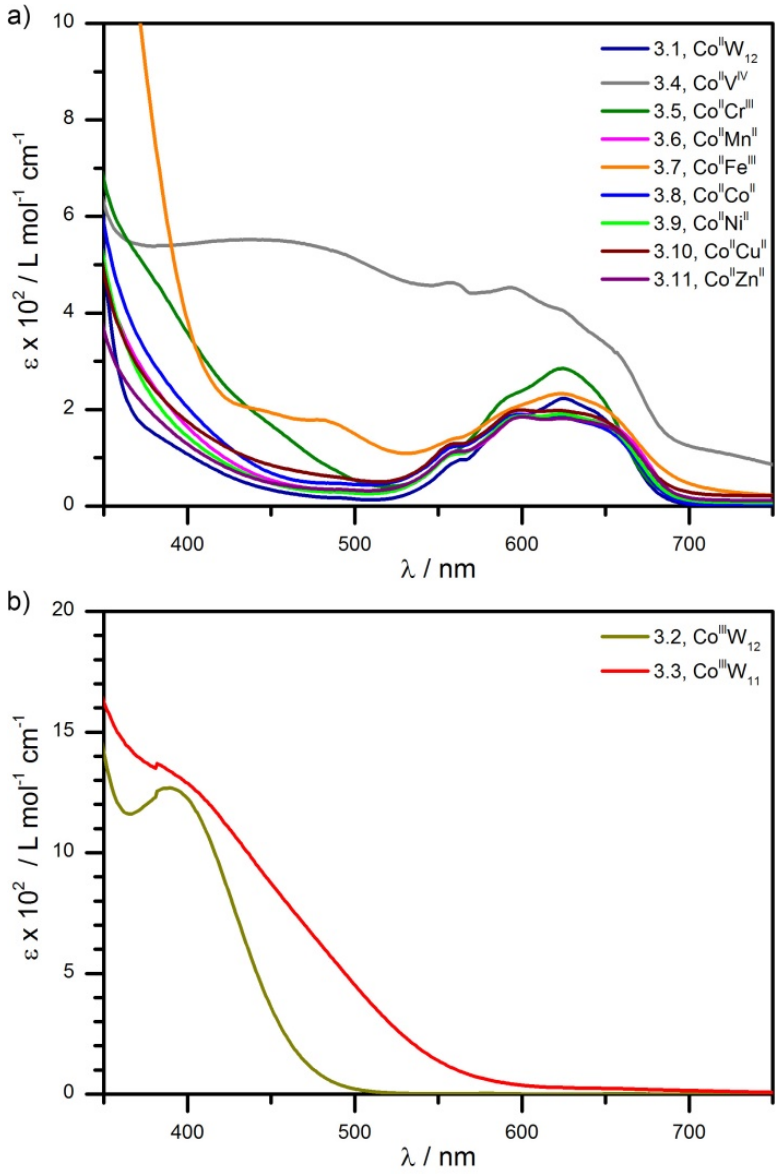

Figure 3.16. Visible electronic absorption spectra of a) **3.1** (**Co^{II}W$_{12}$**) and eight TMSP derivatives, **3.4**-**3.11**, in water, and b) **3.2** (**Co^{III}W$_{12}$**) and **3.3** (**Co^{III}W$_{11}$**). The spectra are overlaid for comparison of their extinction coefficients.

A broad tail extending from the UV is assigned to Co→W (MPCT) transitions in each complex. Here each TMSP complex has a higher extinction coefficient than the

plenary complex, with increases ranging from 18% to 500% at 400 nm (see Figure 3.16). This increase is most likely the result of O→M transitions introduced with the incorporated 3d transition metal, though enhancement of the MPCT transition cannot be discounted. Additional anisotropy induced by the asymmetric polytungstate framework with a 3d transition metal may result in a more intense MPCT band due to greater overlap between the ground and excited states, although interpretation of such broad absorption tails must be made with caution.

To explore the photodynamics of the MPCT excited state, it is important to consider whether the transition varies greatly upon substitution of the polytungstate framework such that another pump wavelength is necessary. The energy gap between the doubly-occupied oxygen orbitals and the empty tungsten orbitals upon substitution of the framework is relatively invariant.[67,68] Likewise, the heteroatom within Keggin POMs is considered to be largely electronically isolated from the framework itself.[64,69,70] Therefore, it is reasonable to assume, and is experimentally demonstrated (*vide infra*), that each TMSP complex possesses an MPCT transition within the absorption manifold at ~400 nm, the excitation wavelength used in our previous study.[41]

3.4.5 Electrochemistry

Cyclic voltammetry was performed on each TMSP complex, the plenary complex **3.1** (**$Co^{II}W_{12}$**), and the lacunary TMSP-precursor complex **3.3** (**$Co^{III}W_{11}$**) to evaluate the influence of the substituted transition metal on the redox behavior of the central cobalt heteroatom. Cyclic voltammograms for each complex were recorded in buffered solutions at pH 5, conditions under which all complexes are stable. Full cyclic

voltammograms, from oxidative (+1.2 V) to reductive (-1.0 V) potentials, were recorded, with all complexes exhibiting pH-dependent multi-electron tungsten reduction peaks consistent with Keggin POMs ($E_{1/2}$ starting at ≈ -500 mV).[71] In the case of **3.10**, applying a negative potential led to reduction of Cu^{II} to Cu^{0} and subsequent extraction from the POM and deposition on the glassy carbon electrode. Due to the similarities between all reported TMSPs at reductive potentials, only the oxidative processes are discussed further. Annotated oxidative and full cyclic voltammograms for each complex are shown in Figures 3.17-3.26.

The oxidative cyclic voltammogram for **3.8** will be considered representative of the entire series for the purposes of discussion, and is shown in Figure 3.23 (full electrochemical measurements are tabulated in Table 3.7; summary values for all complexes are provided in Table 3.8). Two pseudo-reversible redox processes are observed in **3.8** corresponding to the $Co^{II/III}$ couple for the central heteroatom ($E_{1/2}$ = 610 mV; ΔE = 110 mV) and the addendum pseudo-octahedral cobalt ($E_{1/2}$ = 840 mV; ΔE = 140 mV), consistent with the central cobalt being oxidized at a lower potential than the substituted metal (*vide supra*). For comparison, the single reversible redox process observed in **3.1** is at a more oxidizing potential ($E_{1/2}$ = 870 mV; ΔE = 70 mV), and is nearly the same as that observed in **3.3**. This shift in the redox potential of the central heteroatom is consistent with the greater negative charge on the TMSP.[71]

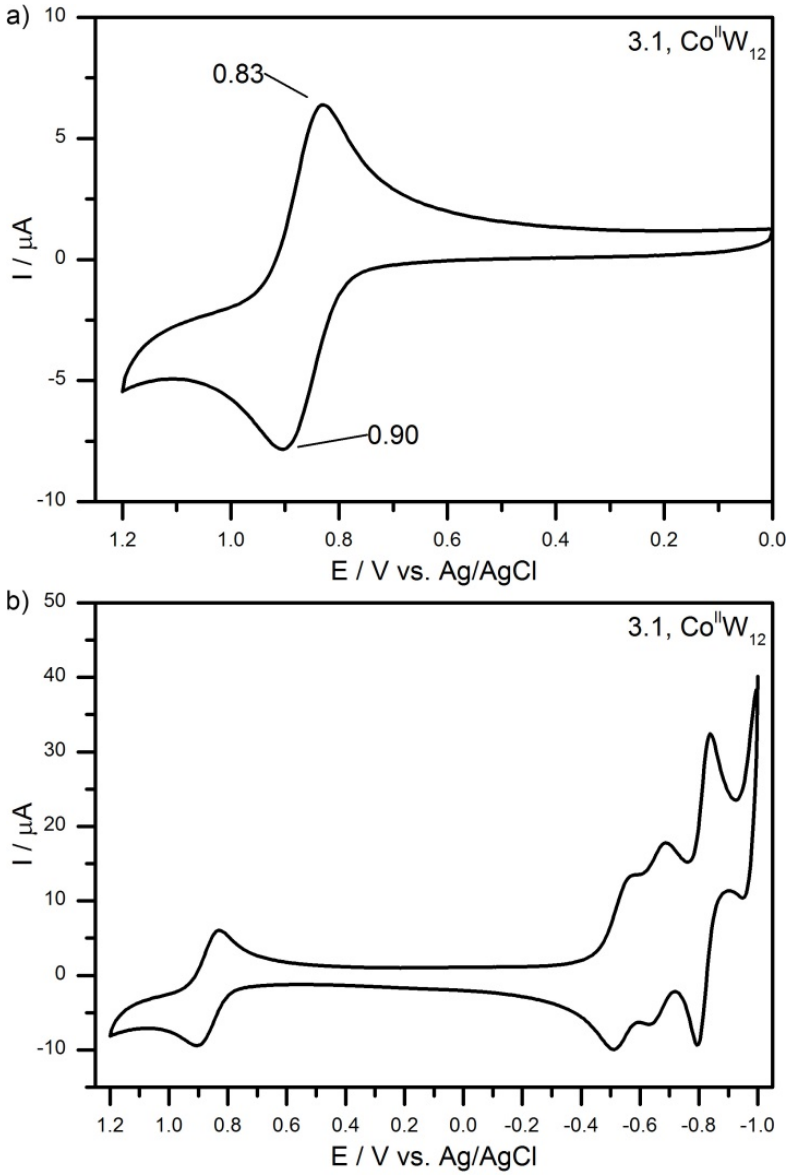

Figure 3.17. a) Oxidative and b) full cyclic voltammograms of ~1 mM **3.1** measured in 0.500 M potassium acetate buffer, pH 5, 50 mV/s scan rate. Resolved peaks in the oxidative voltammogram are annotated.

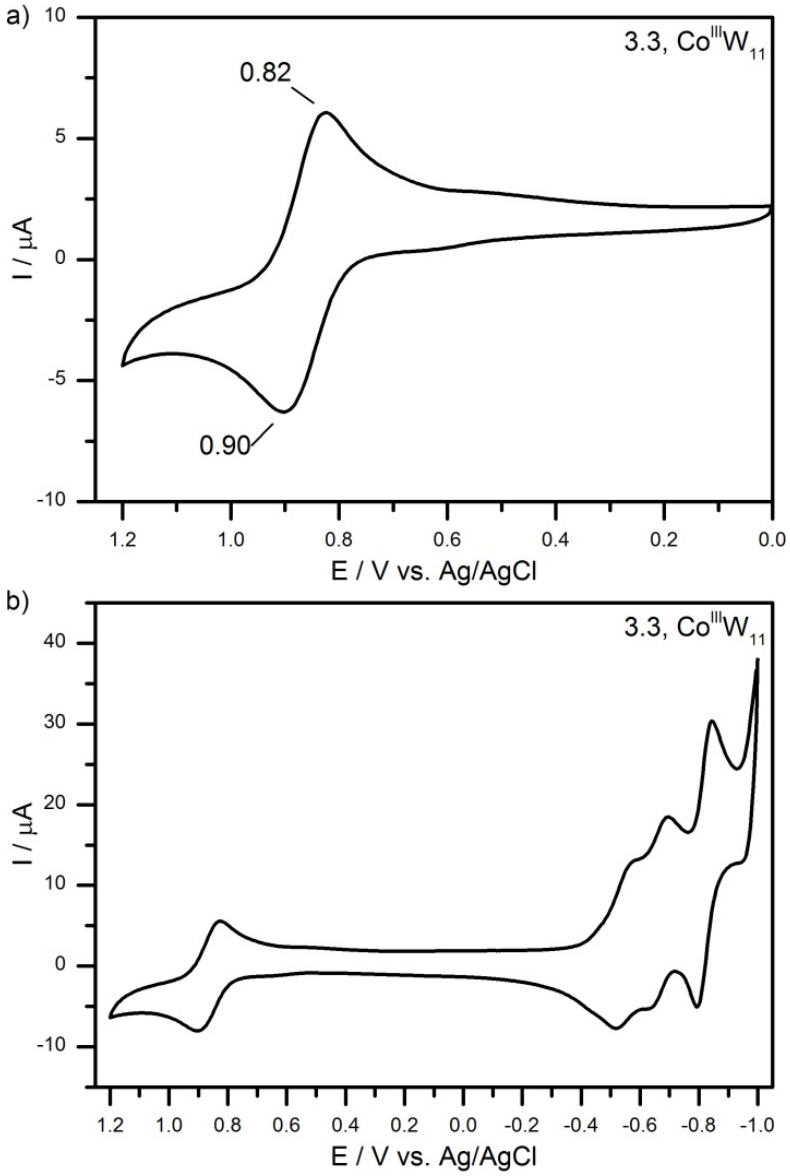

Figure 3.18. a) Oxidative and b) full cyclic voltammograms of ~1 mM **3.3** measured in 0.500 M potassium acetate buffer, pH 5, 50 mV/s scan rate. Resolved peaks in the oxidative voltammogram are annotated.

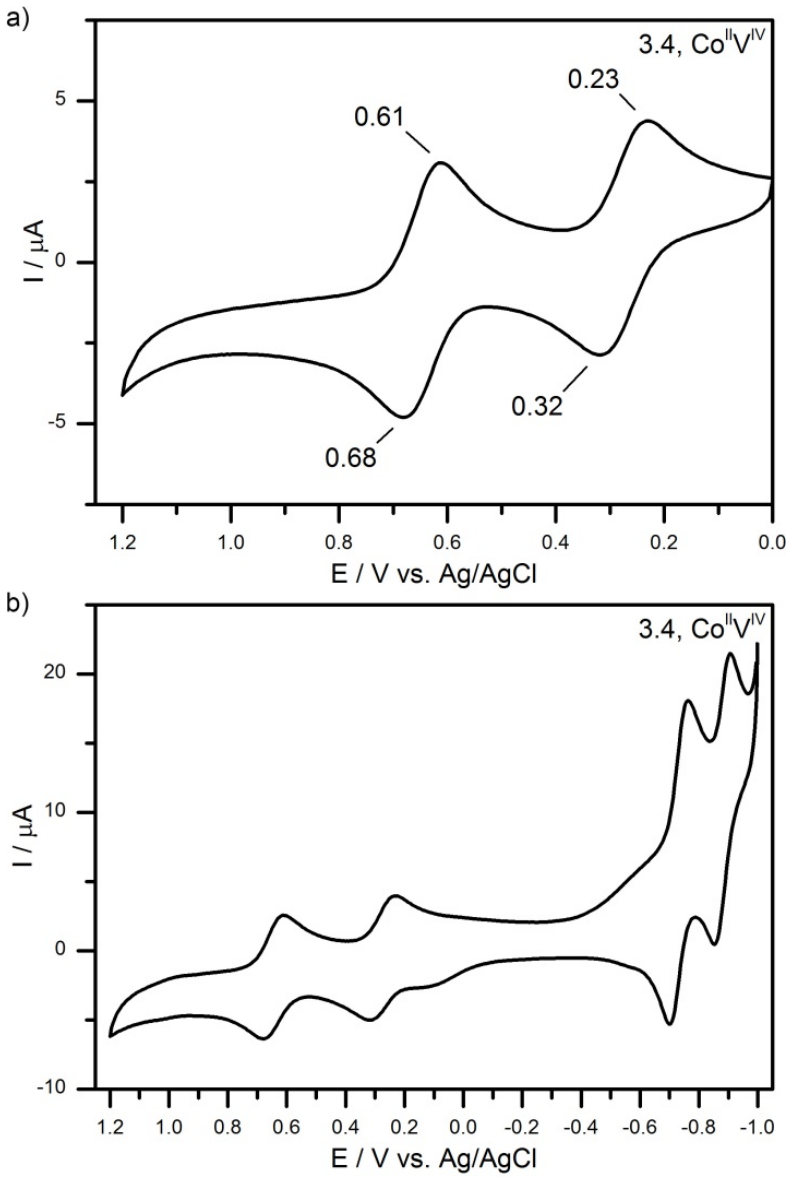

Figure 3.19. a) Oxidative and b) full cyclic voltammograms of ~1 mM **3.4** measured in 0.500 M potassium acetate buffer, pH 5, 50 mV/s scan rate. Resolved peaks in the oxidative voltammogram are annotated.

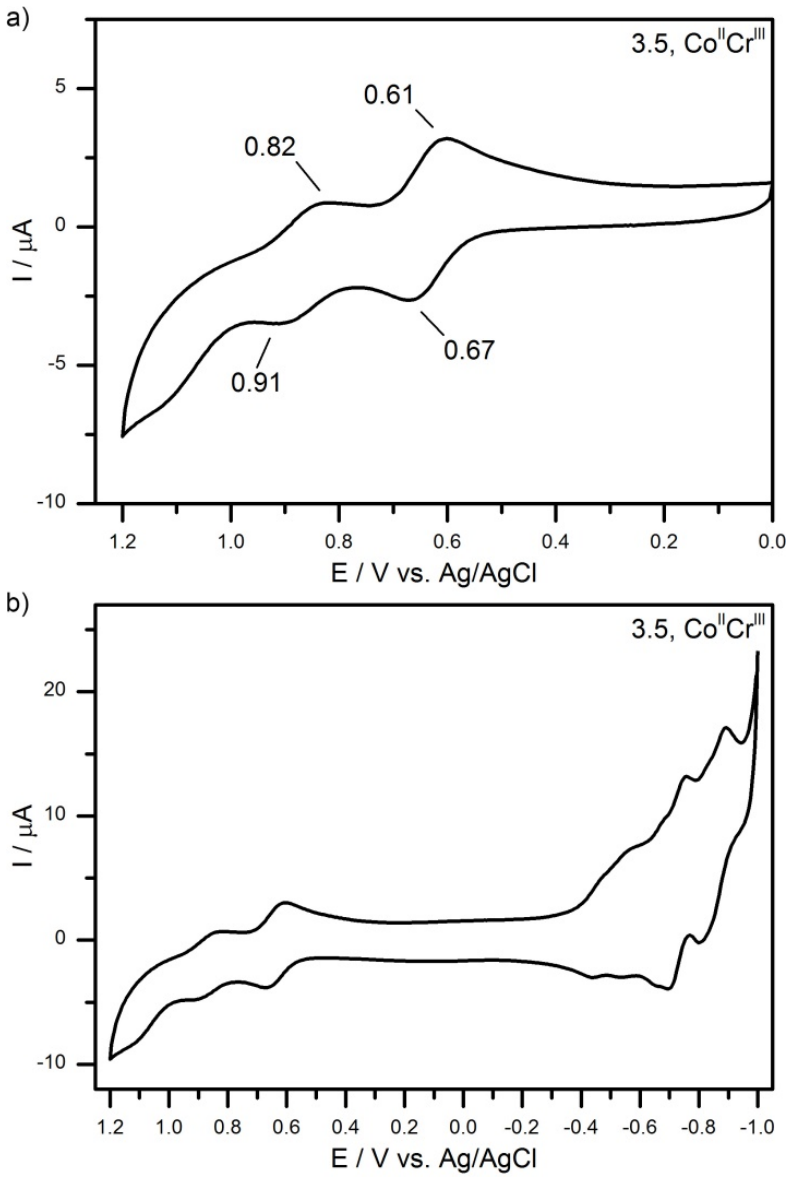

Figure 3.20. a) Oxidative and b) full cyclic voltammograms of ~1 mM **3.5** measured in 0.500 M potassium acetate buffer, pH 5, 50 mV/s scan rate. Resolved peaks in the oxidative voltammogram are annotated.

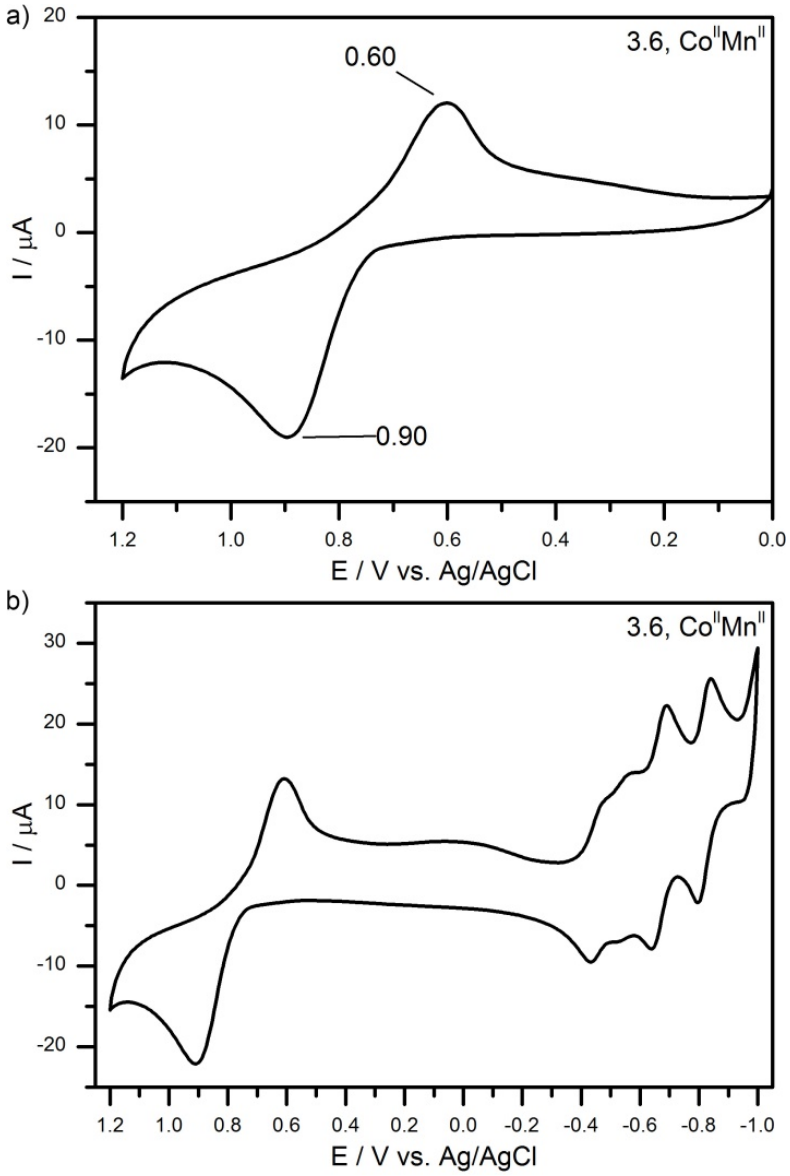

Figure 3.21. a) Oxidative and b) full cyclic voltammograms of ~1 mM **3.6** measured in 0.500 M potassium acetate buffer, pH 5, 50 mV/s scan rate. Resolved peaks in the oxidative voltammogram are annotated.

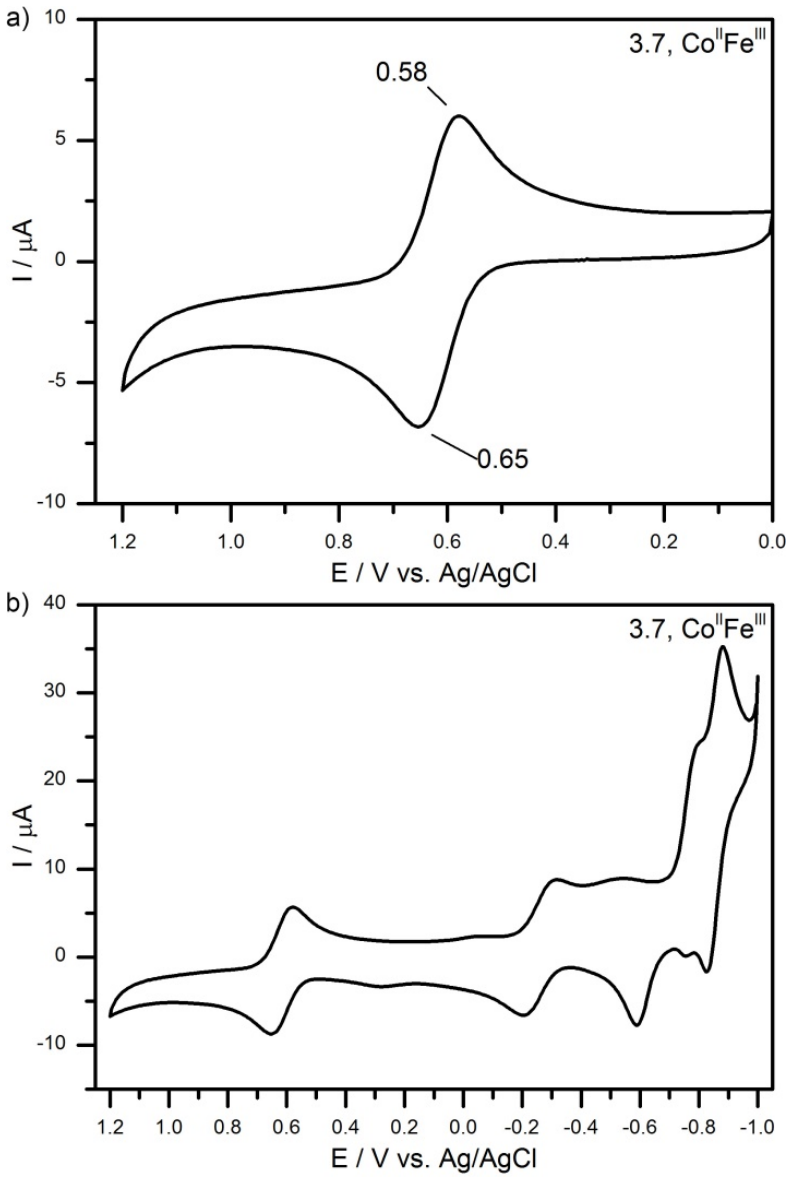

Figure 3.22. a) Oxidative and b) full cyclic voltammograms of ~1 mM **3.7** measured in 0.500 M potassium acetate buffer, pH 5, 50 mV/s scan rate. Resolved peaks in the oxidative voltammogram are annotated.

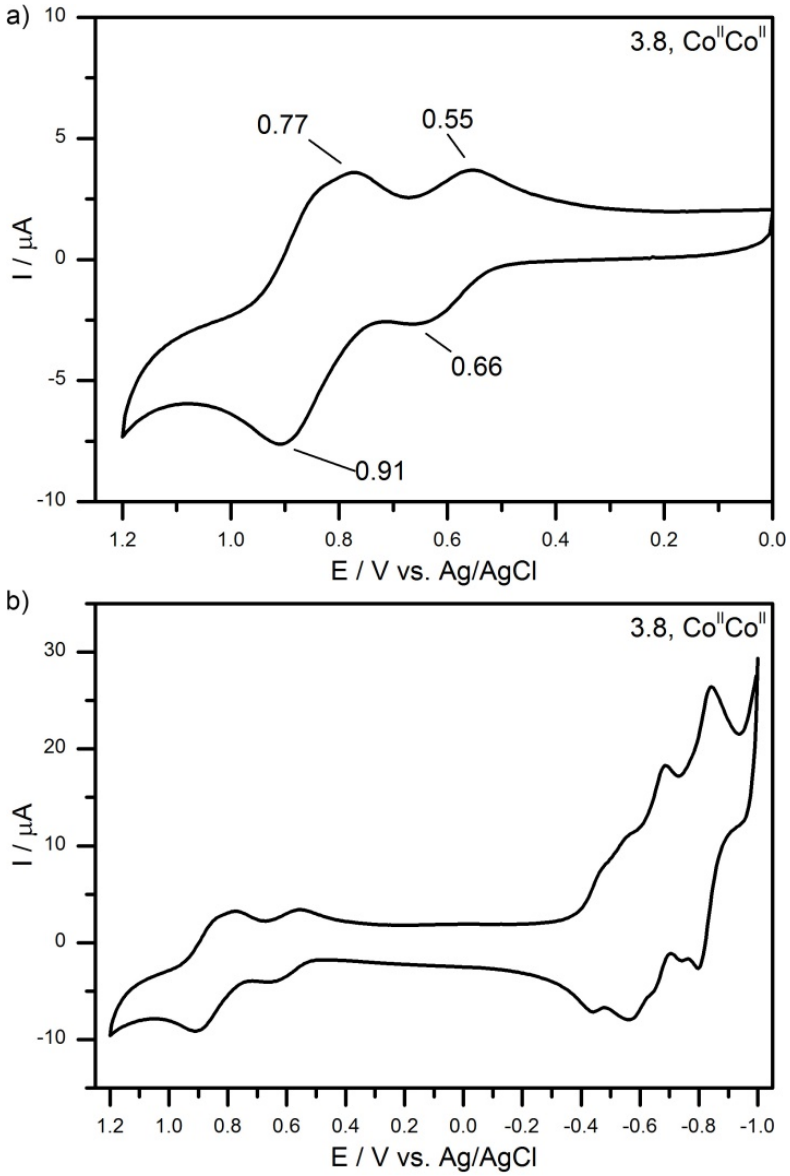

Figure 3.23. a) Oxidative and b) full cyclic voltammograms of ~1 mM **3.8** measured in 0.500 M potassium acetate buffer, pH 5, 50 mV/s scan rate. Resolved peaks in the oxidative voltammogram are annotated.

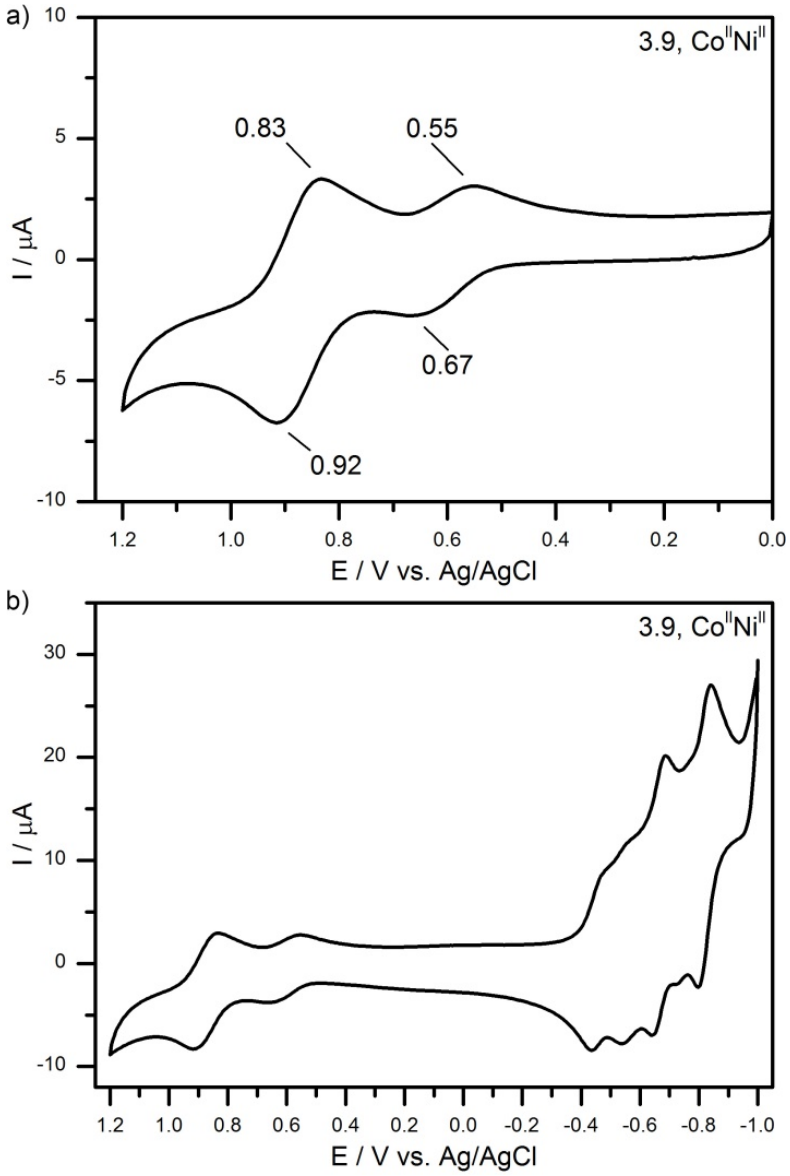

Figure 3.24. a) Oxidative and b) full cyclic voltammograms of ~1 mM **3.9** measured in 0.500 M potassium acetate buffer, pH 5, 50 mV/s scan rate. Resolved peaks in the oxidative voltammogram are annotated.

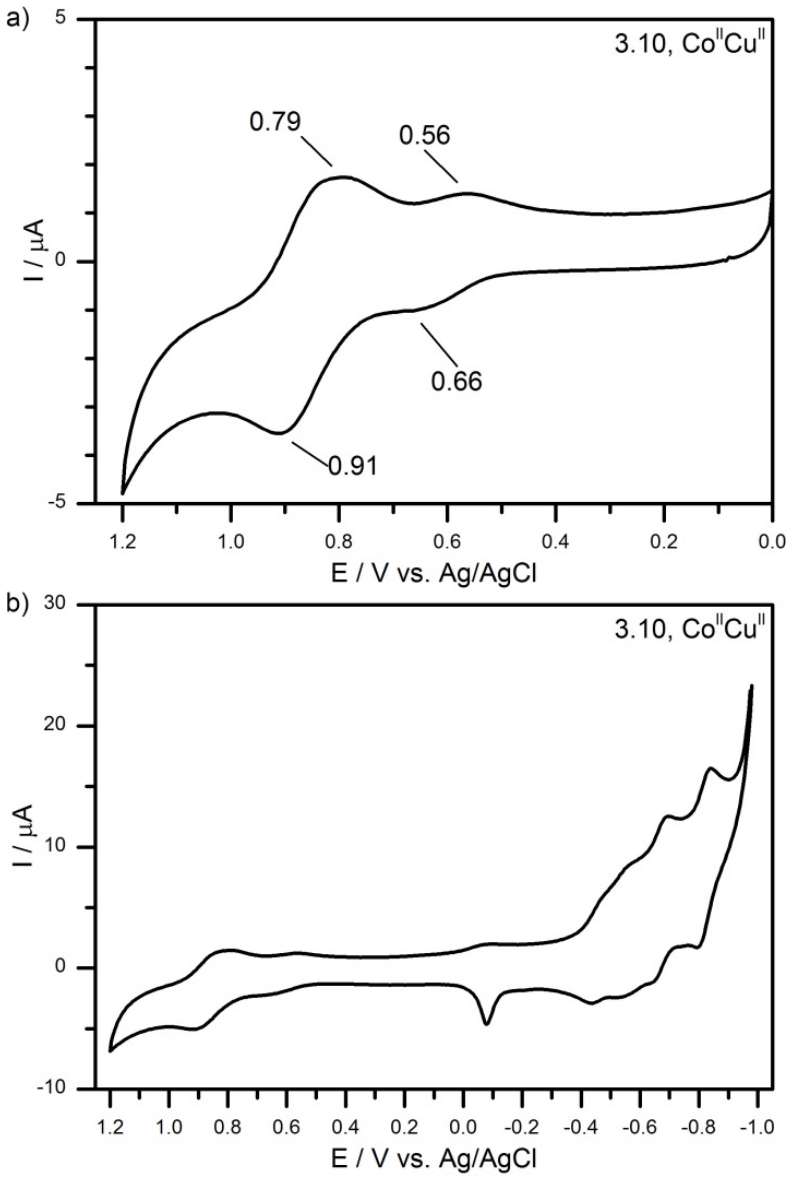

Figure 3.25. a) Oxidative and b) full cyclic voltammograms of ~1 mM **3.10** measured in 0.500 M potassium acetate buffer, pH 5, 50 mV/s scan rate. Resolved peaks in the oxidative voltammogram are annotated.

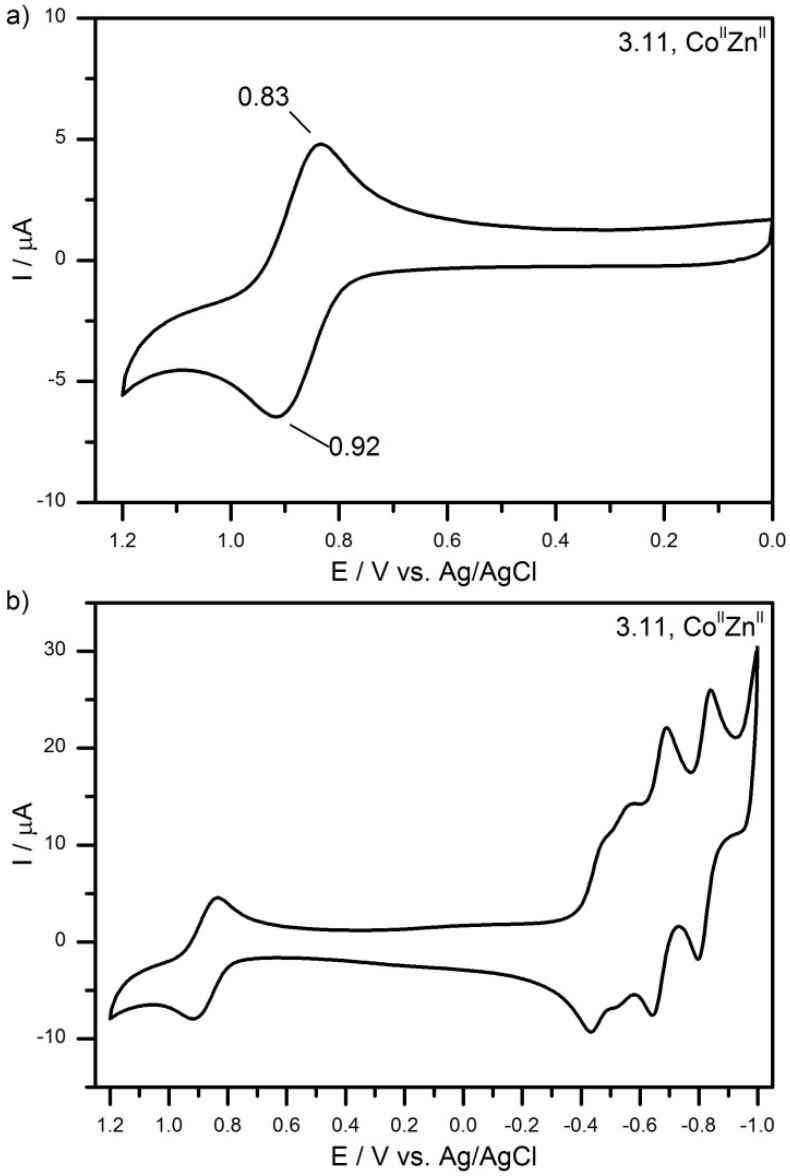

Figure 3.26. a) Oxidative and b) full cyclic voltammograms of ~1 mM **3.11** measured in 0.500 M potassium acetate buffer, pH 5, 50 mV/s scan rate. Resolved peaks in the oxidative voltammogram are annotated.

Table 3.7. Measured open circuit potentials (OCP, and OCP_{ox} for the isolated oxidized species where available) and resolved electrochemical potentials for **3.1**, **3.3**, and eight TMSP derivatives **3.4**-**3.11**[1]

Complex	**OCP**	**OCP_{ox}**	**$Co^{II/III}$**	**M**
	mV		$E_{1/2}$ (ΔE) / mV	
$Co^{II}W_{12}$	610	900	870 (70)	
$Co^{III}W_{11}$	n/a	910	860 (80)	
$Co^{II}V^{IV}$	200	700[2]	650 (70)	270 (90)
$Co^{II}Cr^{III}$	180	590	640 (70)	860 (90)
$Co^{II}Mn^{II}$	380	570	750 (300)	[3]
$Co^{II}Fe^{III}$	280	n/a	620 (70)	-260 (120)
$Co^{II}Co^{II}$	130	620[4]	610 (110)	840 (140)
$Co^{II}Ni^{II}$	300	760	610 (120)	880 (80)
$Co^{II}Cu^{II}$	360	810	610 (100)	850 (120)
$Co^{II}Zn^{II}$	600	820	880 (80)	

Complex	**W_1**	**W_2**	**W_3**	**W_4**
	$E_{1/2}$ (ΔE) / mV			
$Co^{II}W_{12}$	-540 (60)	-660 (60)	-820 (50)	
$Co^{III}W_{11}$	-540 (60)	-660 (60)	-820 (50)	
$Co^{II}V^{IV}$	-730 (60)	-880 (50)		
$Co^{II}Cr^{III}$	-530 (90)	-720 (80)	-850 (90)	
$Co^{II}Mn^{II}$	-450 (50)	-550 (40)	-670 (50)	-820 (40)
$Co^{II}Fe^{III}$	-570 (40)	-780 (40)	-850 (50)	
$Co^{II}Co^{II}$	-450 (20)	-560 (10)	-670 (40)	-810 (70)
$Co^{II}Ni^{II}$	-460 (40)	-550 (30)	-660 (45)	-800 (80)
$Co^{II}Cu^{II}$	-450 (40)	-550 (20)	-670 (50)	-820 (50)
$Co^{II}Zn^{II}$	-450 (40)	-550 (40)	-670 (50)	-820 (40)

[1] Peak separations, in mV, are in parentheses after the potential.

[2] The species measured is the two-electron oxidized species, $Co^{III}V^{V}$.

[3] Protonation and disproportionation reactions obscure the Mn redox couple.

[4] Static electronic spectroscopy, transient absorption spectroscopy, and electrochemistry indicate that the isolated one-electron oxidized species is incompletely oxidized, retaining some Co^{II}_{Td} in the sample.

Introduction of the addendum heterometal causes a significant shift (~250 mV) in the $Co^{II/III}$ redox couple throughout most of the TMSP series. In all but two cases, substitution leads to small differences in the position of the central $Co^{II/III}$ redox couple (all within a 40 mV range). In **3.6**, the observed peaks are separated by 300 mV and their shapes are consistent with chemical reactions occurring within the timeframe of the electrochemical experiment. This behavior is very similar to the pH-dependent behavior seen in $[SiMn^{II}(H_2O)W_{11}O_{39}]^{6-}$, an isostructural system, and is assigned to a combination of protonation and disproportionation reactions.[72] In **3.11**, the $Co^{II/III}$ redox couple is observed at the same potential as in the plenary complex ($E_{1/2}$ = 880 mV; ΔE = 80 mV). This result suggests that the influence of a redox-active substituted metal causes the redox couple of the central Co^{II} heteroatom to shift to lower potentials, irrespective of the negative charge on the complex. Therefore, these complexes narrow the difference in potential between the central heteroatom and the polytungstate framework, and the resulting red-shift in the MPCT transition is reflected in enhanced extinction coefficients at 400 nm. Thus, the peak absorption of the MPCT transition can be tuned (*vide infra*).

The TMSP derivatives containing substituted redox active metals also exhibit redox couples associated with the addenda heteroatom, with the exception of **3.6** noted above, where chemical reactions obscure the Mn redox couple. **3.4** ($E_{1/2}$ = 270 mV; ΔE = 90 mV) and **3.7** ($E_{1/2}$ = -260 mV; ΔE = 120 mV) both exhibit redox couples at more reducing potentials than the $Co^{II/III}$ couple and are consistent with literature reports.[45,71] Likewise, the addenda redox couple for **3.8** ($E_{1/2}$ = 840 mV; ΔE = 140 mV) is consistent with earlier reports.[42,43,73] **3.10** exhibits a $Cu^{II/III}$ redox couple ($E_{1/2}$ = 850 mV; ΔE = 120 mV) as well as a more negative couple ($E_{1/2}$ = -80 mV; ΔE = 60 mV) consistent with

anodic stripping of Cu^{II} to Cu^{0}.[74] Interestingly, both **3.5** ($E_{1/2}$ = 860 mV; ΔE = 90 mV) and **3.9** ($E_{1/2}$ = 880 mV; ΔE = 80 mV) exhibit redox couples associated with the substituted metal where an analogous TMSP series shows no electroactivity.[74]

Electrochemical measurements can be used to estimate the energy gap of the MPCT transition to consider whether a different pump wavelength is necessary, despite the transition being broad and obscured in the electronic absorption spectrum. The charge transfer transition of interest is between a filled Co_{Td} *e* orbital and an empty tungsten orbital, $Co_e \rightarrow W$. The total energy necessary to complete this transition is estimated as the sum of the energy gaps for $Co_e \rightarrow Co_{t2}$, the primary d-d transition, and $Co_{t2} \rightarrow W$, a lower energy MPCT approximated by the energy gap between the $Co^{II/III}$ and the lowest $W^{V/VI}$ redox couple (Table 3.7). The latter energy gap is ~1.14±0.08 eV for six of the substituted complexes, and increases to 1.38 eV and 1.33 eV for **3.4** and **3.11**, respectively. The six complexes with the smallest energy gaps therefore give an MPCT transition energy of 3.13±0.08 eV (398±10 nm), while **3.4** and **3.11**, with the largest energy gaps, will exhibit an MPCT transition energy of 3.38 eV (367 nm) and 3.31 eV (375 nm), respectively. In all cases, transition-metal substitution results in an estimated MPCT transition that is red-shifted relative to **3.1** (3.39 eV; 365 nm), affording MPCT transitions close to the 400 nm excitation wavelength used to investigate them at an ultrafast timescale. Substitution of the polytungstate framework effectively tunes the peak absorption of the MPCT transition to longer wavelengths, possibly contributing to the increased absorption at 400 nm observed in the TMSP series.

Table 3.8. Summary of TMSP electrochemistry and estimated transition energies based on electronic absorption spectra and electrochemistry data

Complex	**$Co^{II/III}$**	**M**	**W_1**
	$E_{1/2}$ / V vs. Ag/AgCl		
$Co^{II}W_{12}$	0.87	-	-0.54
$Co^{II}V^{IV}$	0.65	0.27	-0.73
$Co^{II}Cr^{III}$	0.64	0.86	-0.53
$Co^{II}Mn^{II}$	0.75	-	-0.45
$Co^{II}Fe^{III}$	0.62	-0.26	-0.57
$Co^{II}Co^{II}$	0.61	0.84	-0.45
$Co^{II}Ni^{II}$	0.61	0.88	-0.46
$Co^{II}Cu^{II}$	0.61	0.85	-0.45
$Co^{II}Zn^{II}$	0.88	-	-0.45

Complex	**Transition energies / eV**			**MPCT / nm**
	$Co_{t2}\rightarrow W$	$Co_e\rightarrow Co_{t2}$*	$Co_e\rightarrow W$	$Co_e\rightarrow W$
$Co^{II}W_{12}$	1.41	1.98	3.39	365
$Co^{II}V^{IV}$	1.38	2.00	3.38	367
$Co^{II}Cr^{III}$	1.17	1.99	3.16	392
$Co^{II}Mn^{II}$	1.21	1.99	3.20	388
$Co^{II}Fe^{III}$	1.18	1.99	3.17	391
$Co^{II}Co^{II}$	1.06	1.99	3.05	407
$Co^{II}Ni^{II}$	1.07	1.99	3.05	406
$Co^{II}Cu^{II}$	1.07	1.99	3.06	405
$Co^{II}Zn^{II}$	1.33	1.98	3.31	375

* The wavelength used for $Co_e\rightarrow Co_{t2}$ was typically the λ_{max} for each complex, except in cases where the λ_{max} did not represent the approximate center of the d-d manifold. In those cases a wavelength was selected among the visible multiplets.

3.4.6 Transient Absorption Spectra and Kinetics

Ultrafast measurements of each TMSP complex and the plenary **3.1** were recorded under identical conditions (0.250 M LiAc buffer, pH 5, pump power, probe power) for direct comparison of the photodynamics of the MPCT excited state. The transient absorption spectra and kinetics for **3.8**, representative of the entire series, are shown in Figure 3.27, while transient absorption spectra for all other complexes are shown in Figures 3.28-3.31. The transient spectra and kinetics for all complexes exhibit nearly identical features to those for **3.8** and are strongly reminiscent of the excited state dynamics of **3.1**.

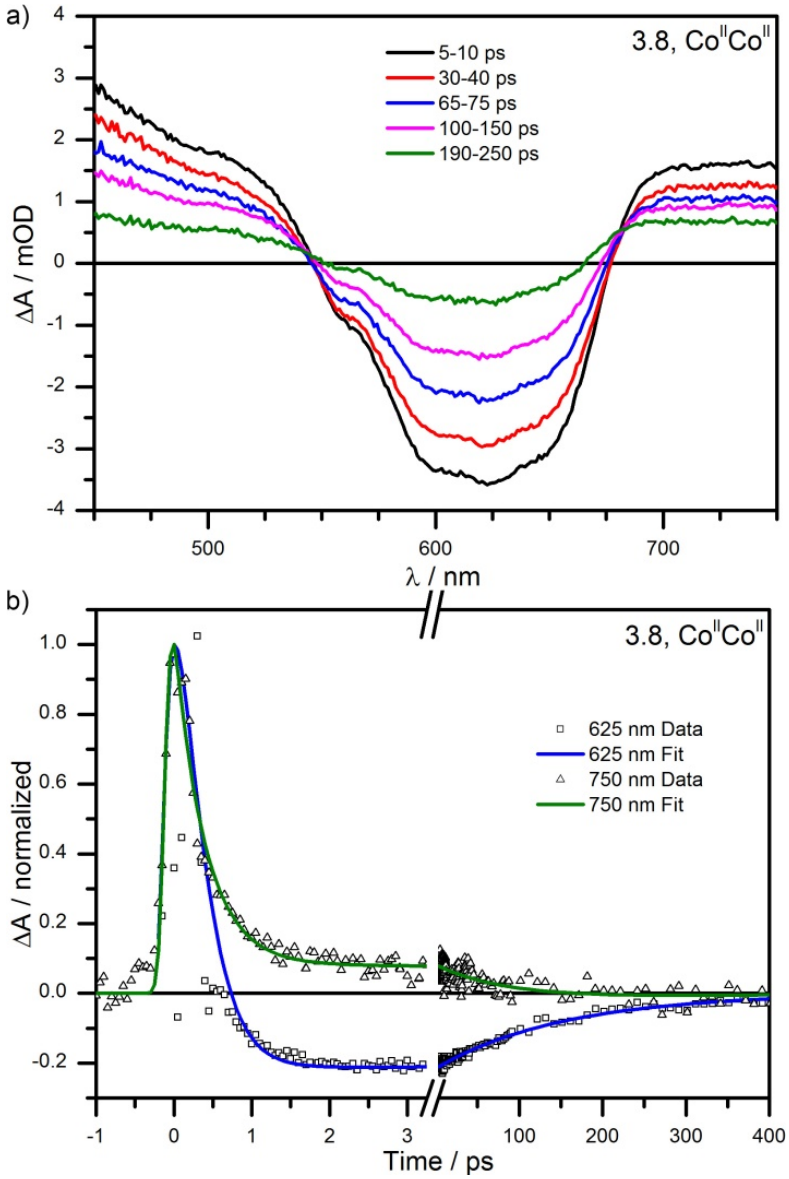

Figure 3.27. a) Transient absorption spectra and b) kinetics of **3.8** after excitation by an ultrafast pump pulse at 400 nm. Spectral traces are the average of multiple measurements within the noted time windows. Empirical measurements and multiexponential fits to the kinetics at two wavelengths are shown normalized to their respective peak fit values.

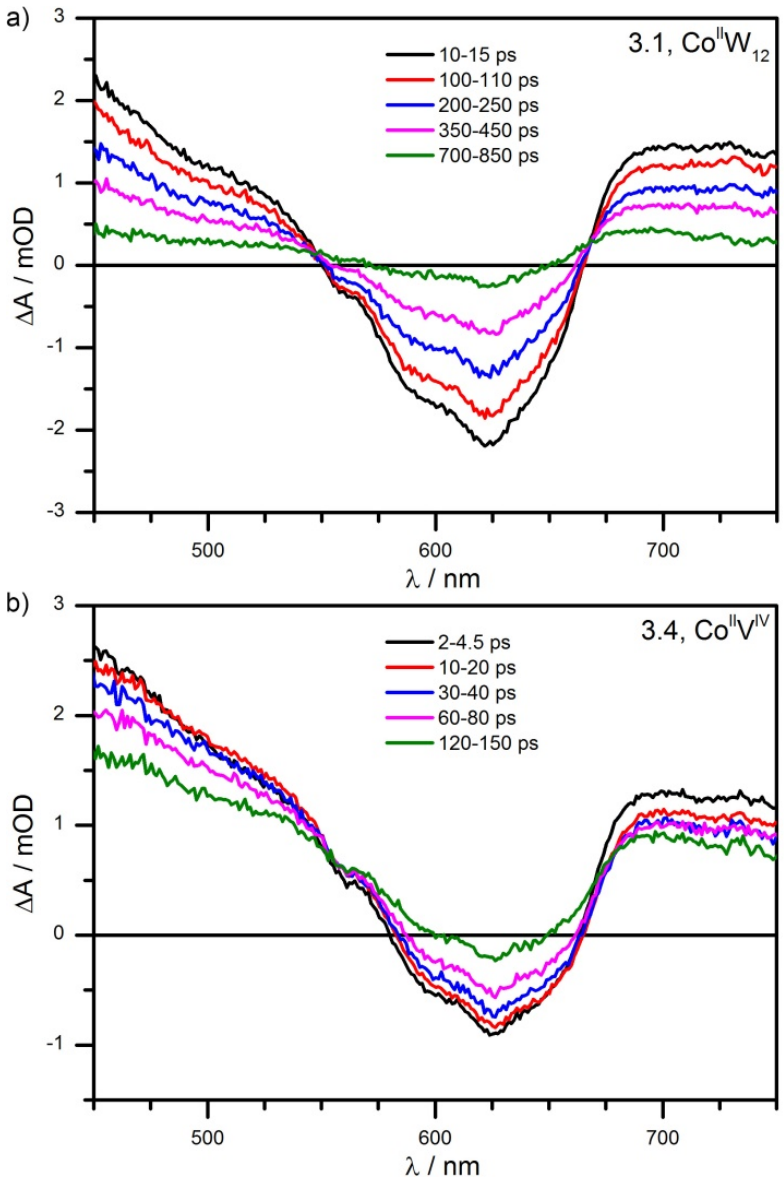

Figure 3.28. a) Transient absorption spectra of a) **3.1** and b) **3.4** after excitation by an ultrafast pump pulse at 400 nm. Spectral traces are the average of multiple measurements within the noted time windows.

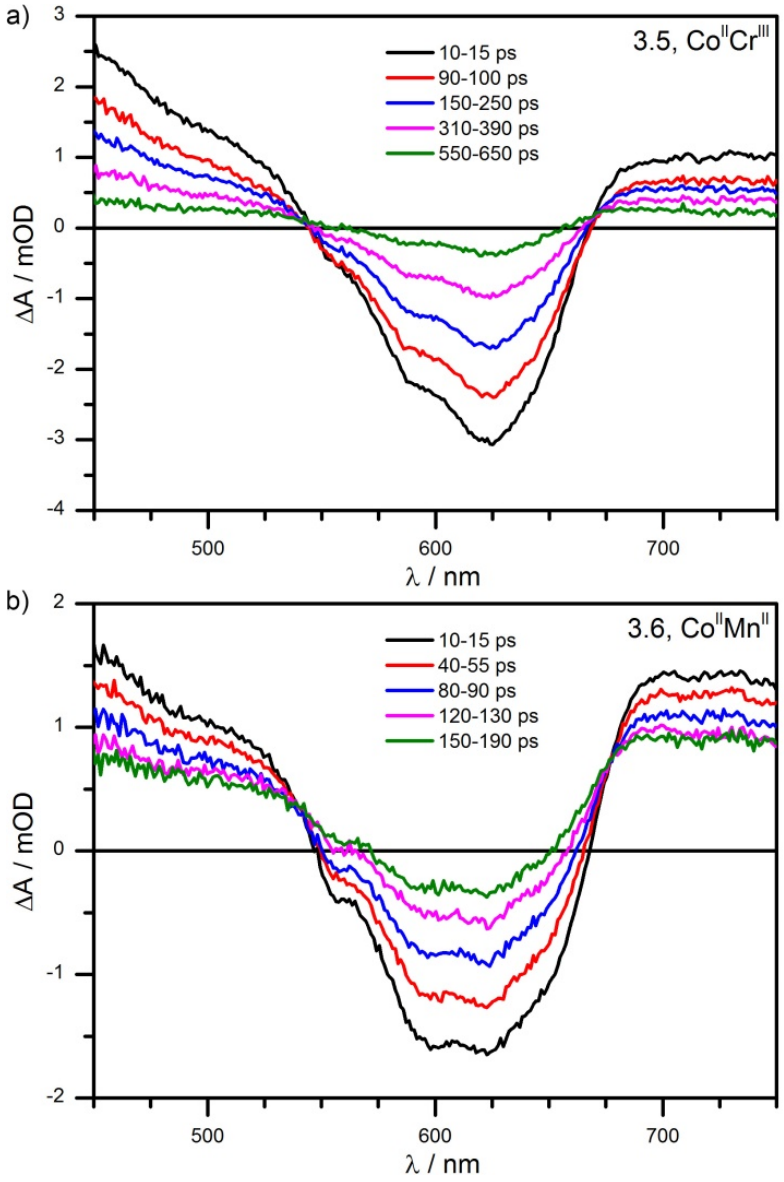

Figure 3.29. a) Transient absorption spectra of a) **3.5** and b) **3.6** after excitation by an ultrafast pump pulse at 400 nm. Spectral traces are the average of multiple measurements within the noted time windows.

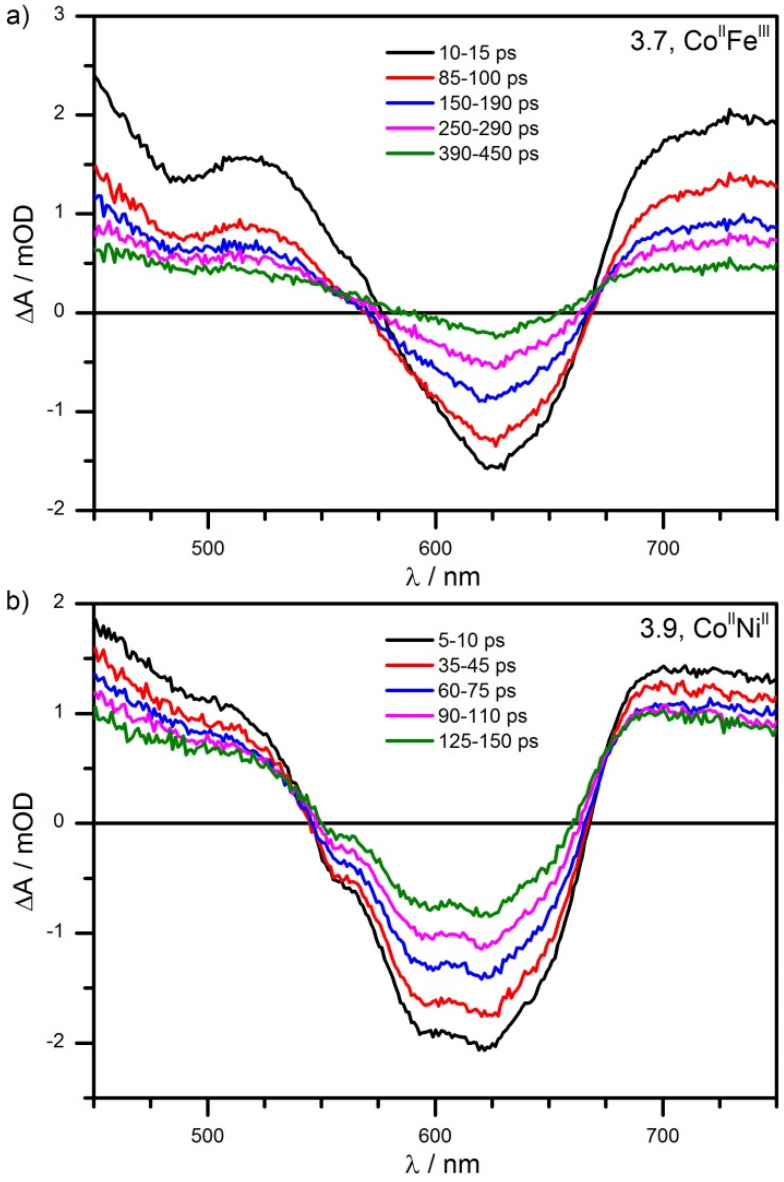

Figure 3.30. a) Transient absorption spectra of a) **3.7** and b) **3.9** after excitation by an ultrafast pump pulse at 400 nm. Spectral traces are the average of multiple measurements within the noted time windows.

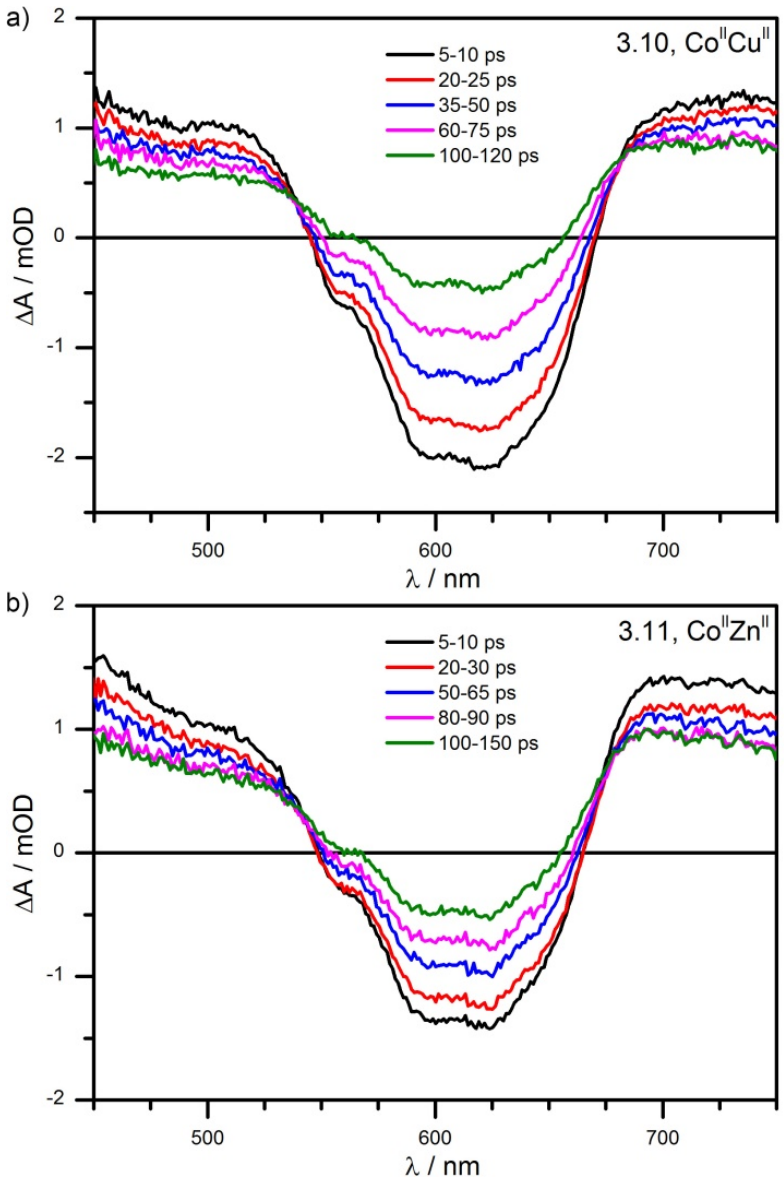

Figure 3.31. a) Transient absorption spectra of a) **3.10** and b) **3.11** after excitation by an ultrafast pump pulse at 400 nm. Spectral traces are the average of multiple measurements within the noted time windows.

The photodynamics of **3.1** are extensively discussed in our previous report;[41] a brief description of its features and comparison to the derivative TMSP series is given here. Following excitation at 400 nm, **3.8** produces a broad, intense absorption feature

consistent with a heteropoly blue excited state. The initial state decays rapidly to a second excited state with a ground state bleach centered at 625 nm and absorption bands at higher and lower energies. These features are indicative of an excited state in which an electron has been photoexcited from the tetrahedral Co^{II} heteroatom to empty orbital(s) located within the polytungstate framework, and are very similar to those of **3.1**. The transient absorption spectra for the other TMSP complexes reveal similar results. In each case, the initial excited state (τ_1) decays rapidly to the second excited state (τ_2) bearing features of the MPCT transition. Importantly, differences in the shape of the ground state bleach between the different compounds correspond to changes in the d-d manifold present in static electronic absorption spectra, confirming that the bleach always has the same origin.

Notably, however the lifetimes for both the initial (τ_1 = 440 ± 330 fs) and second excited states (τ_2 = 120 ± 44 ps) of **3.8** are considerably shorter than for **3.1**, with time constants that are 54% and 72% shorter, respectively. Indeed, in all eight TMSPs, both excited states decay at a faster rate than in the plenary complex (Figure 3.32 and Table 3.9), suggesting that substitution of $[W{=}O]^{4+}$ with $[M\text{-}OH_2]^{2+}$, $[M\text{-}OH_2]^{3+}$ or $[V{=}O]^{2+}$ introduces additional (or accelerates existing) deactivation pathways. While we are yet to find an unambiguous relationship between the excited state lifetimes of these species and any single aspect of the anion structures, we can identify several factors that likely influence τ_1 and τ_2. First, deactivation of the excited state will be strongly affected by the interaction of the anion with its environment (solvent and cations). In all of the TMSPs but **3.4**, the presence of a labile aqua ligand likely provides additional vibrational relaxation pathways to shorten both τ_1 and τ_2.[75-80] Moreover, the increased charge on the

anions *vs.* **3.1** (from 6- to 7-/8-) will give rise to increased ion pairing. This is known to stabilize CT excited states, and reduce excited state lifetimes in accord with the energy gap law:[81] note that in the case of **3.1** moving to a *less* polar medium was seen to dramatically increase τ_2.[41] Within the anions, the presence of orbitals at energies intermediate between the tetrahedral Co t_2 level and the W acceptor orbitals should also lead to shorter excited state lifetimes by the energy gap law[82-87] – electrochemical measurements and/or DFT calculations indicate that this situation is pertinent in **3.4**, **3.6,** and **3.7**. In the case of **3.6** and **3.4**, this intermediate energy level is occupied by an electron which could be transferred to Co^{III} upon formation of the MPCT excited state.

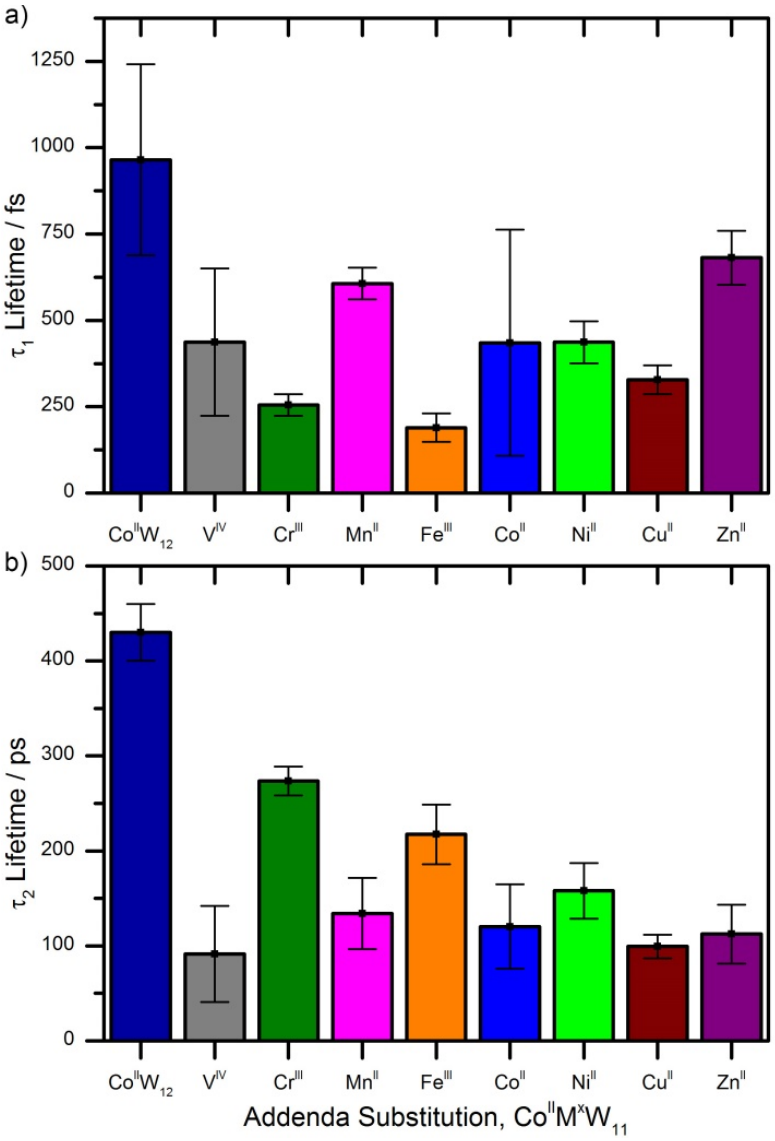

Figure 3.32. Comparison of the a) first and b) second excited state exponential lifetimes for the plenary POM complex $Co^{II}W_{12}$ and its eight TMSP derivatives upon excitation by an ultrafast pump pulse at 400 nm. Solvent conditions (0.250 M LiAc buffer, pH 5) and pump power were kept consistent between measurements. Error bars represent the 95% confidence interval for each lifetime, calculated by global fit analysis.

Table 3.9. Multi-exponential lifetimes of transient absorption spectra

Complex	**Lifetimes**	
	τ_1 / fs	τ_2 / ps
$Co^{II}W_{12}$	960 ± 280	430 ± 30
$Co^{II}V^{IV}$	440 ± 210	91 ± 50
$Co^{II}Cr^{III}$	260 ± 30	270 ± 15
$Co^{II}Mn^{II}$	610 ± 50	130 ± 37
$Co^{II}Fe^{III}$	190 ± 40	220 ± 31
$Co^{II}Co^{II}$	440 ± 330	120 ± 44
$Co^{II}Ni^{II}$	440 ± 60	160 ± 29
$Co^{II}Cu^{II}$	330 ± 40	99 ± 12
$Co^{II}Zn^{II}$	680 ± 80	110 ± 31

Bearing these factors in mind, it is interesting to note that the two longest-lived τ_2 excited states (270 ± 15 and 220 ± 31 ps respectively for **3.5** and **3.7**) are observed in the two least charged anions (both 7-), and the difference in lifetime between these two, albeit almost within experimental error, is consistent with the presence of the lower lying energy level (smaller energy gap) provided by $Fe^{III/II}$ in this system. Of the other six anions (all 8-), all but **3.9** have τ_2 of *ca.* 100 ps, and within the experimental error from one another, meaning that it is not possible to confidently discern an influence for either terminal ligand (oxo *vs* aqua) or intermediate energy levels (present in **3.6** and **3.4**) in this series. Furthermore, the slight increase in τ_2 seen for **3.9** does not correlate with the estimated extent of Co-M electronic coupling estimated from calculated one-electron oxidation potentials (*vide supra*), although it may relate to nickel's increased preference for square planar coordination. This would reduce the strength of interaction with the aqua ligand and the O^1 bridge to Co. Overall, from this study and our previous work,[41] it seems that the dominant influences on excited state lifetimes in these systems are the

location of the CT donor atom, and the strength of interaction between the anion and the medium.

3.5 Conclusions

A series of heterobimetallic TMSPs containing redox-active 3d-electrons, $[Co^{II}(M^xOH_y)W_{11}O_{39}]^{(12-x-y)-}$ (M^xOH_y = $V^{IV}O$, $Cr^{III}(OH_2)$, $Mn^{II}(OH_2)$, $Fe^{III}(OH_2)$, $Co^{II}(OH_2)$, $Ni^{II}(OH_2)$, $Cu^{II}(OH_2)$, $Zn^{II}(OH_2)$) have been synthesized and their photodynamics investigated. All complexes within the series have a demonstrated MPCT transition between the central cobalt heteroatom and the polytungstate framework, analogous to their plenary parent complex. Transition metal substitution of the polytungstate framework leads to significant changes in the electrochemical properties and red-shifting of the MPCT transition. In all cases, transition metal substitution leads to a decrease in the lifetimes of the MPCT excited state, but increases in absorption, with the Cr- and Fe-substituted systems apparently offering a reasonable compromise between significantly (3x or more) increased visible light absorption and excited state lifetimes >50% that of $[Co^{II}W_{12}O_{40}]^{6-}$. The decreased lifetimes are most likely due to nonradiative relaxation due to coordinating aqua ligands, and increased ion pairing (increased charge) that stabilizes CT excited states and reduces lifetimes by the energy gap law. Combined with our previous studies, this appears to indicate that the most promising avenue to increase MPCT lifetimes is to weaken the interaction of the POM framework with solvent and counter cations, while stronger visible absorption should be achieved through the use of 4^{th} and 5^{th} row elements as donor atoms.

3.6 References

(1) Urbani, M.; Grätzel, M.; Nazeeruddin, M. K.; Torres, T. s. *Chem. Rev.* **2014**, *114*, 12330.

(2) Yum, J.-H.; Baranoff, E.; Wenger, S.; Nazeeruddin, M. K.; Grätzel, M. *Energy Environ. Sci.* **2011**, *4*, 842.

(3) Hagfeldt, A.; Boschloo, G.; Sun, L.; Kloo, L.; Pettersson, H. *Chem. Rev.* **2010**, *110*, 6595.

(4) Kanan, M. W.; Nocera, D. G. *Science* **2008**, *321*, 1072.

(5) Youngblood, W. J.; Lee, S.-H. A.; Maeda, K.; Mallouk, T. E. *Acc. Chem. Res.* **2009**, *42*, 1966.

(6) Barnett, S. M.; Goldberg, K. I.; Mayer, J. M. *Nat. Chem.* **2012**, *4*, 498.

(7) Yin, Q.; Tan, J. M.; Besson, C.; Geletii, Y. V.; Musaev, D. G.; Kuznetsov, A. E.; Luo, Z.; Hardcastle, K. I.; Hill, C. L. *Science* **2010**, *328*, 342.

(8) Geletii, Y. V.; Botar, B.; Kögerler, P.; Hillesheim, D. A.; Musaev, D. G.; Hill, C. L. *Angew. Chem. Int. Ed.* **2008**, *47*, 3896.

(9) Lv, H.; Song, J.; Geletii, Y. V.; Vickers, J. W.; Sumliner, J. M.; Musaev, D. G.; Kögerler, P.; Zhuk, P. F.; Bacsa, J.; Zhu, G.; Hill, C. L. *J. Am. Chem. Soc.* **2014**, *136*, 9268.

(10) Helm, M. L.; Stewart, M. P.; Bullock, R. M.; DuBois, M. R.; DuBois, D. L. *Science* **2011**, *333*, 863.

(11) Du, P.; Schneider, J.; Jarosz, P.; Eisenberg, R. *J. Am. Chem. Soc.* **2006**, *128*, 7726.

(12) Morris, A. J.; McGibbon, R. T.; Bocarsly, A. B. *ChemSusChem* **2011**, *4*, 191.

(13) Kumar, B.; Smieja, J. M.; Kubiak, C. P. *J. Phys. Chem. C* **2010**, *114*, 14220.

(14) Ischay, M. A.; Anzovino, M. E.; Du, J.; Yoon, T. P. *J. Am. Chem. Soc.* **2008**, *130*, 12886.

(15) Meng, Q.-Y.; Zhong, J.-J.; Liu, Q.; Gao, X.-W.; Zhang, H.-H.; Lei, T.; Li, Z.-J.; Feng, K.; Chen, B.; Tung, C.-H.; Wu, L.-Z. *J. Am. Chem. Soc.* **2013**, *135*, 19052.

(16) Kuzyk, M. G. *J. Mater. Chem.* **2009**, *19*, 7444.

(17) Marder, S. R. *Chem. Commun.* **2006**, 131.

(18) Coe, B. J. *Acc. Chem. Res.* **2006**, *39*, 383.

(19) Chen, W.-C.; Lee, C.-S.; Tong, Q.-X. *J. Mater. Chem. C* **2015**, *3*, 10957.

(20) Yang, X.; Zhou, G.; Wong, W.-Y. *Chem. Soc. Rev.* **2015**, *44*, 8484.

(21) You, Y.; Nam, W. *Chem. Soc. Rev.* **2012**, *41*, 7061.

(22) Lo, K. K.-W. *Acc. Chem. Res.* **2015**, *48*, 2985.

(23) Langton, M. J.; Marques, I.; Robinson, S. W.; Félix, V.; D.Beer, P. *Chem. Eur. J.* **2016**, *22*, 185.

(24) Ghosh, P. K.; Brunschwig, B. S.; Chou, M.; Creutz, C.; Sutin, N. *J. Am. Chem. Soc.* **1984**, *106*, 4772.

(25) Lin, W.; Frei, H. *J. Am. Chem. Soc.* **2005**, *127*, 1610.

(26) Lin, W.; Frei, H. *J. Phys. Chem. B* **2005**, *109*, 4929.

(27) Han, H.; Frei, H. *J. Phys. Chem. C* **2008**, *112*, 16156.

(28) Han, H.; Frei, H. *J. Phys. Chem. C* **2008**, *112*, 8391.

(29) Wu, X.; Weare, W. W.; Frei, H. *Dalton Trans.* **2009**, 10114.

(30) Cuk, T.; Weare, W. W.; Frei, H. *J. Phys. Chem. C* **2010**, *114*, 9167.

(31) Takashima, T.; Yamaguchi, A.; Hashimoto, K.; Nakamura, R. *Chem. Commun.* **2012**, *48*, 2964.

(32) Takashima, T.; Nakamura, R.; Hashimoto, K. *J. Phys. Chem. C* **2009**, *113*, 17247.

(33) Choing, S. N.; Francis, A. J.; Clendenning, G.; Schuurman, M. S.; Sommer, R. D.; Tamblyn, I.; Weare, W. W.; Cuk, T. *J. Phys. Chem. C* **2015**, *119*, 17029.

(34) Weare, W. W.; Pushkar, Y.; Yachandra, V. K.; Frei, H. *J. Am. Chem. Soc.* **2008**, *130*, 13555.

(35) Wu, X.; Huang, T.; Lekich, T. T.; Sommer, R. D.; Weare, W. W. *Inorg. Chem.* **2015**, *54*, 5322.

(36) Zhao, C.; Huang, Z.; Rodríguez-Córdoba, W.; Kambara, C. S.; O'Halloran, K. P.; Hardcastle, K. I.; Musaev, D. G.; Lian, T.; Hill, C. L. *J. Am. Chem. Soc.* **2011**, *133*, 20134.

(37) Zhao, C.; Rodríguez-Córdoba, W.; Kaledin, A. L.; Yang, Y.; Geletii, Y. V.; Lian, T.; Musaev, D. G.; Hill, C. L. *Inorg. Chem.* **2013**, *52*, 13490.

(38) Zhao, C.; Kambara, C. S.; Yang, Y.; Kaledin, A. L.; Musaev, D. G.; Lian, T.; Hill, C. L. *Inorg. Chem.* **2013**, *52*, 671.

(39) Zhao, C.; Glass, E. N.; Sumliner, J. M.; Bacsa, J.; Kim, D. T.; Guo, W.; Hill, C. L. *Dalton Trans.* **2014**, *43*, 4040.

(40) Zhao, C.; Glass, E. N.; Chica, B.; Musaev, D. G.; Sumliner, J. M.; Dyer, R. B.; Lian, T.; Hill, C. L. *J. Am. Chem. Soc.* **2014**, *136*, 12085.

(41) Glass, E. N.; Fielden, J.; Kaledin, A. L.; Musaev, D. G.; Lian, T.; Hill, C. L. *Chem. Eur. J.* **2014**, *20*, 4297.

(42) Baker, L. C. W.; McCutcheon, T. P. *J. Am. Chem. Soc.* **1956**, *78*, 4503.

(43) Simmons, V. E. Ph.D. dissertation, Boston University, 1953.

(44) Nolan, A. L.; Burns, R. C.; Lawrance, G. A. *J. Chem. Soc., Dalton Trans.* **1998**, 3041.

(45) Bas-Serra, J.; Todorut, I.; Casañ-Pastor, N.; Server-Carrio, J.; Baker, L. C. W.; Acerete, R. *Synth. React. Inorg. Met.-Org. Chem.* **1995**, *25*, 869.

(46) Geletii, Y. V.; Bailey, A. J.; Boring, E.; Hill, C. L. *J. Chem. Soc., Chem. Commun.* **2001**, *2001*, 1484.

(47) APEXII (Version 2.0-1), SAINT (Version 7.23A) and SADABS (Version 2004/1), Bruker AXS, Inc., Madison, WI, USA 2005.

(48) Coppens, P.; Leiserowitz, L.; Rabinovich, D. *Acta Crystallogr.* **1965**, *18*, 1035.

(49) SHELXTL (v 6.1), Bruker AXS, Inc., Madison, WI, USA, 2000.

(50) Becke, A. D. *Phys. Rev. A* **1988**, *38*, 3098.

(51) Lee, C.; Yang, W.; Parr, R. G. *Phys. Rev. B* **1988**, *37*, 785.

(52) Becke, A. D. *J. Chem. Phys.* **1993**, *98*, 5648.

(53) Ditchfield, R.; Hehre, W. J.; Pople, J. A. *J. Chem. Phys.* **1971**, *54*, 724.

(54) Hehre, W. J.; Ditchfield, R.; Pople, J. A. *J. Chem. Phys.* **1972**, *56*, 2257.

(55) Hay, P. J.; Wadt, W. R. *J. Chem. Phys.* **1985**, *82*, 270.

(56) Wadt, W. R.; Hay, P. J. *J. Chem. Phys.* **1985**, *82*, 284.

(57) Hay, P. J.; Wadt, W. R. *J. Chem. Phys.* **1985**, *82*, 299.

(58) Rappe, A. K.; Casewit, C. J.; Colwell, K. S.; Goddard, W. A.; Skiff, W. M. *J. Am. Chem. Soc.* **1992**, *114*, 10024.

(59) Tomasi, J.; Mennucci, B.; Cammi, R. *Chem. Rev.* **2005**, *105*, 2999.

(60) Frisch, M. J.; Trucks, G. W.; Schlegel, H. B.; Scuseria, G. E.; Robb, M. A.; Cheeseman, J. R.; Scalmani, G.; Barone, V.; Mennucci, B.; Petersson, G. A.; Nakatsuji, H.; Caricato, M.; Li, X.; Hratchian, H. P.; Izmaylov, A. F.; Bloino, J.; Zheng, G.; Sonnenberg, J. L.; Hada, M.; Ehara, M.; Toyota, K.; Fukuda, R.; Hasegawa, J.; Ishida, M.; Nakajima, T.; Honda, Y.; Kitao, O.; Nakai, H.; Vreven, T.; J. A. Montgomery, J.; Peralta, J. E.; Ogliaro, F.; Bearpark, M.; Heyd, J. J.; Brothers, E.; Kudin, K. N.; Staroverov, V. N.; Kobayashi, R.; Normand, J.; Raghavachari, K.; Rendell, A.; Burant, J. C.; Iyengar, S. S.; Tomasi, J.; Cossi, M.; N. Rega, J. M. M.; Klene, M.; Knox, J. E.; Cross, J. B.; Bakken, V.; Adamo, C.; Jaramillo, J.; Gomperts, R.; Stratmann, R. E.; Yazyev, O.; Austin, A. J.; Cammi, R.; Pomelli, C.; Ochterski, J. W.; Martin, R. L.; K. Morokuma, V. G. Z.; Voth, G. A.; Salvador, P.; Dannenberg, J. J.; Dapprich, S.; Daniels, A. D.; Ö. Farkas, J. B. F.; Ortiz, J. V.; Cioslowski, J.; Fox, D. J. *Gaussian 09*, Revision C.01; Gaussian, Inc.: Wallingford, CT, 2009.

(61) Song, F.; Ding, Y.; Ma, B.; Wang, C.; Wang, Q.; Du, X.; Fu, S.; Song, J. *Energy Environ. Sci.* **2013**, *6*, 1170.

(62) Muncaster, G.; Sankar, G.; Catlow, C. R. A.; Thomas, J. M.; Coles, S. J.; Hursthouse, M. *Chem. Mater.* **2000**, 16.

(63) Nolan, A. L.; Allen, C. C.; Burns, R. C.; Craig, D. C.; Lawrance, G. A. *Aust. J. Chem.* **2000**, *53*, 59.

(64) Casan-Pastor, N.; Gomez-Romero, P.; Jameson, G. B.; Baker, L. C. W. *J. Am. Chem. Soc.* **1991**, *113*, 5658.

(65) Rocchiccioli-Deltcheff, C.; Thouvenot, R. *J. Chem. Res., Synop.* **1977**, *2*, 46.

(66) Rocchiccioli-Deltcheff, C.; Thouvenot, R.; Franck, R. *Spectrochim. Acta* **1976**, *32A*, 587.

(67) Maestre, J. M.; López, X.; Bo, C.; Daul, C.; Poblet, J.-M. *Inorg. Chem.* **2002**, *41*, 1883.

(68) Maestre, J. M.; López, X.; Bo, C.; Poblet, J.-M.; Casañ-Pastor, N. *J. Am. Chem. Soc.* **2001**, *123*, 3749.

(69) Varga, G. M.; Papaconstantinou, E.; Pope, M. T. *Inorg. Chem.* **1970**, *9*, 662.

(70) Weinstock, I. A. *Chem. Rev.* **1998**, *98*, 113.

(71) Sadakane, M.; Steckhan, E. *Chem. Rev.* **1998**, *98*, 219.

(72) Müller, A.; Dloczik, L.; Diemann, E.; Pope, M. T. *Inorg. Chim. Acta* **1997**, *257*, 231.

(73) Baker, L. C. W.; Simmons, V. E. *J. Am. Chem. Soc.* **1959**, *81*, 4744.

(74) Cheng, L.; Sun, H.; Liu, B.; Liu, J.; Dong, S. *J. Chem. Soc., Dalton Trans.* **1999**, 2619.

(75) Meshkova, S. B.; Topilova, Z. M.; Lozinskii, M. O.; Bol'shoi, D. V. *J. Appl. Spectrosc.* **1997**, *64*, 229.

(76) Moriyasu, M.; Yokoyama, Y.; Ikeda, S. *J. Inorg. Nucl. Chem.* **1977**, *39*, 2211.

(77) Bhaumik, M. L.; Nugent, L. J. *J. Chem. Phys.* **1965**, *43*, 1680.

(78) Hehlen, M. P.; Riesen, H.; Guedel, H. U. *Inorg. Chem.* **1991**, *30*, 2273.

(79) Dong, H.; Wheeler, R. A. *Chem. Phys. Lett.* **2005**, *413*, 176.

(80) Pavlovich, V. S. *ChemPhysChem* **2012**, *13*, 4081.

(81) Vining, W. J.; Caspar, J. V.; Meyer, T. J. *J. Phys. Chem.* **1985**, *89*, 1095.

(82) Englman, R.; Jortner, J. *Mol. Phys.* **1970**, *18*, 145.

(83) Freed, K. F.; Jortner, J. *J. Chem. Phys.* **1970**, *52*, 6272.

(84) Bixon, M.; Jortner, J. *J. Chem. Phys.* **1968**, *48*, 715.

(85) Caspar, J. V.; Kober, E. M.; Sullivan, B. P.; Meyer, T. J. *J. Am. Chem. Soc.* **1982**, *104*, 630.

(86) Robinson, G. W.; Frosch, R. P. *J. Chem. Phys.* **1963**, *38*, 1187.

(87) Bixon, M.; Jortner, J.; Cortes, J.; Heitele, H.; Michel-Beyerle, M. E. *J. Phys. Chem.* **1994**, *98*, 7289.

Charge Separation in Polyoxometalate-Based Systems for Solar Energy Production

Chapter 4

Charge Transfer in All-Inorganic Networks and a Tetramer Based on Tin(II)-Containing Polyoxometalates

with Chongchao Zhao, Bryant Chica, Djamaladdin G. Musaev, Jordan M. Sumliner, R. Brian Dyer, Tianquan Lian, and Craig L. Hill

Published partially in: Zhao, C.; Glass, E. N.; Chica, B.; Musaev, D. G.; Sumliner, J. M.; Dyer, R. B.; Lian, T.; Hill, C. L. "All-Inorganic Networks and Tetramer based on Tin(II)-Containing Polyoxometalates: Tuning Structural and Spectral Properties with Lone Pairs", *Journal of the American Chemical Society*, **2014**, *136(34)*, 12085-12091.

4.1 Abstract

Two MOF-like but all-inorganic polyoxometalate-based networks, $[Na_7X_2W_{18}Sn_9Cl_5O_{68}\cdot(H_2O)_m]_n$ (**4.1**, X = Si, *m* = 35; **4.2**, X = Ge, *m* = 41), and the molecular tetramer, $Na_6[\{Na(\mu\text{-}OH_2)(OH_2)_2\}_6\{Sn_6(B\text{-}SbW_9O_{33})_2\}_2]\cdot 50H_2O$ (**4.3**), have been prepared and characterized by X-ray diffraction and spectroscopic methods. All three compounds exhibit unique structural features, and networks **4.1** and **4.2** incorporate the highest nuclearity of Sn(II)-containing POMs to date. Tetramer **4.3** comprises bridging Sn(II) ions with $[B\text{-}SbW_9O_{33}]^{9-}$ units and exhibits two highly unusual features, a long-range Sb…Sb interaction and an intramolecular charge-transfer transition involving donation of the lone pair electron density on both Sb(III) and Sn(II) to the POM. The electronic structure and excited-state dynamics have been studied by transient spectroscopy, spectroelectrochemistry, DFT calculations and Resonance Raman spectroscopy. The synergistic effect of two types of stereoactive lone pairs on Sb(III) and Sn(II) is critical for the charge-transfer absorption feature in the visible.

4.2 Introduction

Polyoxometalates (POMs) have been widely studied in context with medicine, magnetism, materials science, and in particular, catalysis.[1-3] POMs cover a wide-range of sizes and archetypes, from molecular species to giant wheel/capsule-shaped molecules.[4-9] Recently, like nanoparticles,[10,11] POMs have been introduced into metal-organic framework (MOF) pores for enhanced catalytic and photochemical reactions, and in some cases, for MOF stabilization.[12-16] POMs have also been covalently bound to organic linkages to form hybrid molecular cages and frameworks.[17,18] However, purely inorganic

molecular metal-oxide networks, for which POMs are ideal candidates, are rare. Although there are a few crystal structures of conventional (d^0) Keggin POMs linked into chains and networks through alkali metal counterions,[19-22] they dissociate upon dissolution and do not exhibit unique photochemical or catalytic properties. Purely POM-based networks containing transition-metals are of greater interest because by tuning the electronic properties of the substituted 3d metals, these functional networks can integrate the versatile catalytic and photocatalytic activities of POMs within the structural features of MOFs.[23,24] Cronin *et al.* have pioneered some carbon-free POM-linked structures and recently reported a network comprising Mn(II)-linked $[P_8W_{48}O_{184}]^{40-}$ units which exhibits unique electrochemical behavior.[25,26]

Nonbonding valence electron pairs, lone pairs, as often observed in p-block elements, play a significant role in structural chemistry, catalysts, and semiconductors.[27-29] In POMs with pyramidal heteroanions, stereochemically active lone-pair electrons frequently influence the structural features, as seen in some Sb(III), Bi(III), and As(III) centered derivatives.[30-37] The lone-pair-bearing p-block metals, i.e. Sn(II), can exist as internal heteroatoms or external metal centers, and the latter offers the potential for further coordination to a secondary building unit (SBU) to form high dimensional structures. However, so far this behavior has not been observed in Sn(II)-containing POMs.[38-43] More recently, photochemical properties of a stannato(II)tungstate have been reported, but this study lacks insightful electronic delineation.[43] Inspired by above observations, we report here two all-inorganic MOF-like Sn(II)-substituted POMs: $[Na_7X_2W_{18}Sn_9Cl_5O_{68}\cdot(H_2O)_m]_n$ (**4.1**, X = Si, m = 35; **4.2**, X = Ge, m = 41), and a similar tetrameric compound, $Na_6[\{Na(\mu\text{-}OH_2)(OH_2)_2\}_6\{Sn_6(B\text{-}SbW_9O_{33})_2\}_2]\cdot 50H_2O$ (**4.3**).

Compound **4.3** contains two types of stereoactive lone pairs. Each of these compounds displays unique structural features; and a range of techniques identify the nature and excited state dynamics of the unusual intramolecular charge-transfer absorption in **4.3**.

4.3 Experimental

4.3.1 General Methods and Materials

All reagents were purchased as reagent grade or higher and used as received. The tri-vacant POM precursors $Na_{10}[\alpha\text{-}SiW_9O_{34}]\cdot nH_2O$, $Na_{10}[\alpha\text{-}GeW_9O_{34}]\cdot nH_2O$ and $Na_9[B\text{-}SbW_9O_{33}]\cdot nH_2O$, were prepared according to reported methods and their purities confirmed by infrared spectroscopy.[30,44,45] Electronic absorption spectra were acquired using an Agilent 8453 spectrophotometer equipped with a diode-array detector and an Agilent 89090A cell temperature controller unit. Infrared spectra (2% by weight in KBr) were measured on a Thermo Nicolet 6700 FT-IR spectrometer. Elemental analyses were performed by Galbraith Laboratories Inc., Knoxville, Tennessee. Thermogravimetric analyses were acquired on a Perkin Elmer STA 6000 analyzer.

4.3.2 Syntheses

$[Na_7Si_2W_{18}Sn_9Cl_5O_{68}\cdot(H_2O)_{35}]_n$ (4.1). $Na_{10}[\alpha\text{-}SiW_9O_{34}]\cdot 23H_2O$ (1.6 g, 0.6 mmol) was dissolved in 20 mL H_2O, followed by addition of 1.0 M HCl until the pH was ~6.7. $SnCl_2\cdot 2H_2O$ (285 mg, 1.25 mmol) was added to the above solution quickly. The solution immediately turned orange and some unidentified white precipitate formed, with the pH decreasing to 2.0. NaCl (400 mg) was then added. The mixtures were heated to 70 ºC for 30 min and then cooled to room temperature and filtered. Orange needle-shape

crystals were obtained after slow evaporation within a week. Yield: 430 mg (47% based on Sn). FTIR (1100-500 cm^{-1}; 2% KBr pellets), $\tilde{\nu}$, cm^{-1}: 996 (m), 948 (m), 890 (s), 786 (m), 687 (s), 646 (m), 532 (w). Anal. Calcd. for $H_{70}O_{103}Cl_5Na_7Si_2Sn_9W_{18}$: Cl, 2.7; Na, 2.5; Si, 0.86; Sn, 16.5; W, 51.0. Found: Cl, 2.5; Na, 2.4; Si, 0.84; Sn, 15.5; W, 49.6. TGA (Figure 4.1a): weight loss, 9.7% (30-500 ºC; "$35H_2O$") and 2.7% (500-700 ºC; "5Cl").

$[Na_7Ge_2W_{18}Sn_9Cl_5O_{68}\cdot(H_2O)_{41}]_n$ (4.2). This complex was prepared using a similar procedure to that for **4.1** above except that $Na_{10}[\alpha\text{-}GeW_9O_{34}]\cdot nH_2O$ (1.7 g, 0.6 mmol) was used. Yield: 370 mg (40% based on Sn). FTIR (1100-500 cm^{-1}; 2% KBr pellets), $\tilde{\nu}$, cm^{-1}: 945 (m), 880 (s), 797 (s), 683 (s), 639 (m), 526 (w). Anal. Calcd. for $H_{82}O_{109}Cl_5Na_7Ge_2Sn_9W_{18}$: Cl, 2.7; Na, 2.4; Ge, 2.2; Sn, 16.0; W, 49.5. Found: Cl, 2.3; Na, 2.2; Ge, 1.9; Sn, 15.1; W, 48.1. TGA (Figure 4.1b): weight loss, 11.0% (30-500 ºC; "$41H_2O$") and 2.7% (500-700 ºC; "5Cl").

$Na_6[\{Na(\mu\text{-}OH_2)(OH_2)_2\}_6\{Sn_6(B\text{-}SbW_9O_{33})_2\}_2]\cdot 50H_2O$ (4.3). To a 0.5 M NaCl solution, $Na_9[B\text{-}SbW_9O_{33}]\cdot nH_2O$ (1.6 g, 0.6 mmol) was dissolved, and the pH was adjusted to ~6.5 by adding 1.0 M HCl. $SnCl_2\cdot 2H_2O$ (285 mg, 1.25 mmol) was added and the mixture was heated at 70 ºC for 15 min. The solution was then filtered and allowed to slowly evaporate. Red crystals were obtained within two days. Yield: 370 mg (40% based on Sn). FTIR (1100-500 cm^{-1}; 2% KBr pellets), $\tilde{\nu}$, cm^{-1}: 943 (s), 905 (m), 857 (m), 789 (s), 718 (s), 667 (s). UV-vis (H_2O), λ, nm (ε, L mol^{-1} cm^{-1}): 400 (10500). Anal. Calcd. for $H_{136}O_{200}Na_{12}Sb_4Sn_{12}W_{36}$: Na, 2.3; Sb, 4.0; Sn, 11.7; W, 54.5. Found: Na, 2.2; Sb, 3.7; Sn, 11.2; W, 55.0. TGA (Figure 4.1c): weight loss, 7.3% (30-500 ºC; "$50H_2O$").

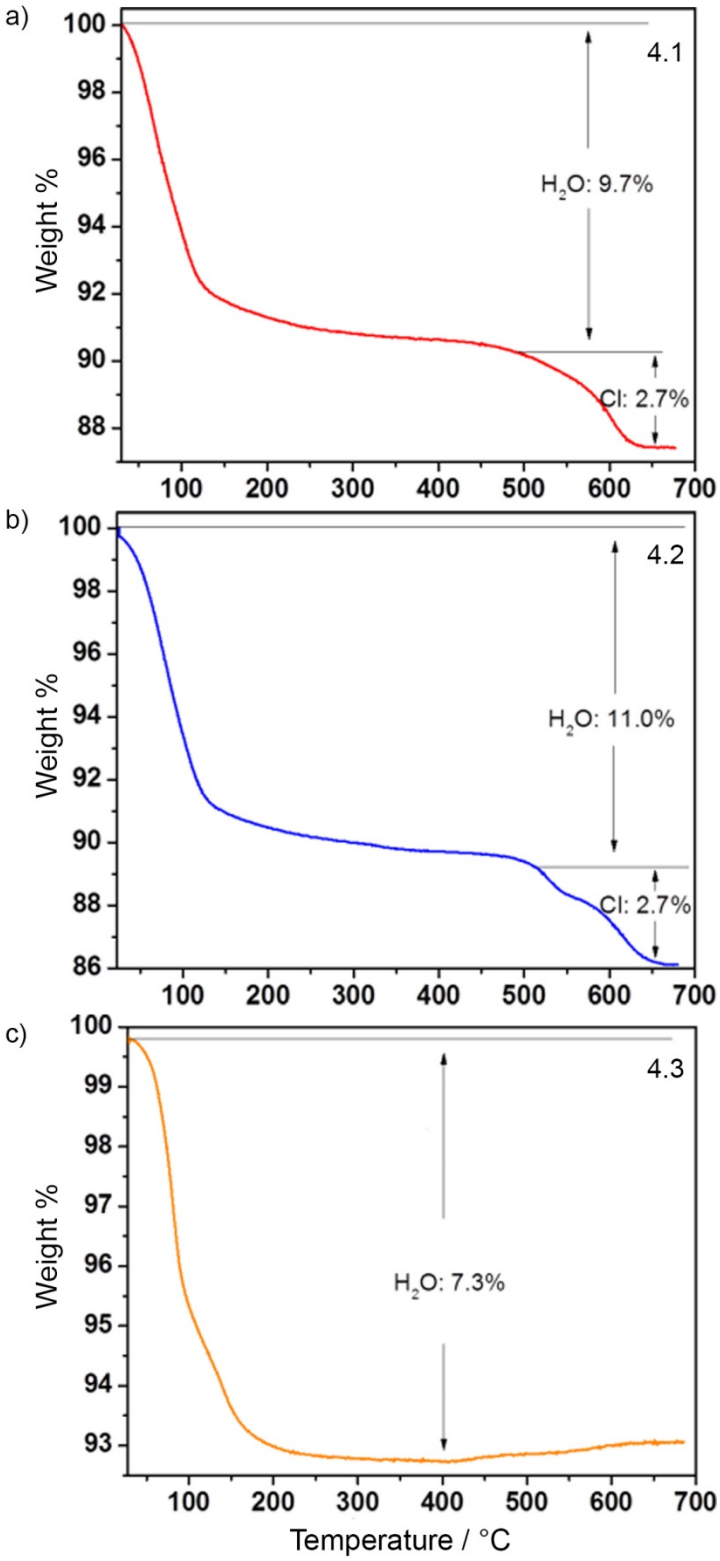

Figure 4.1. Thermogravimetric analyses of **4.1**, **4.2**, and **4.3**, with the sources of weight loss annotated.

4.3.3 Single Crystal X-ray Structural Determination

X-ray analysis was performed on a Bruker D8 SMART APEX CCD sealed tube diffractometer. Diffraction intensities were measured using graphite monochromated Mo K_α radiation (λ = 0.71073 Å) at 173(2) K. Data collection, indexing, and initial cell refinements were carried out by using SMART; frame integration and final cell refinements were accomplished by SAINT.[46] A multiple absorption correction including face-indexing was done by SADABS.[47] The molecular structures were determined by Direct Methods and Fourier techniques and refined by full-matrix least squares. Structure solution and refinement were accomplished using SHELXTL-97.[48] Crystallographic data are summarized in Table 4.1.

Table 4.1. Crystal structure data and statistics for compounds **4.1**, **4.2** and **4.3**

	4.1	**4.2**	**4.3**
Empirical formula	$H_{70}O_{103}Cl_5Na_7Si_2Sn_9W_{18}$	$H_{82}O_{109}Cl_5Na_7Ge_2Sn_9W_{18}$	$H_{136}O_{200}Na_{12}Sb_4Sn_{12}W_{36}$
***T* / K**	173(2)	173(2)	173(2)
***F_w* / g mol^{-1}**	6499.99	6695.94	12156.60
Crystal system	Tetragonal	Tetragonal	Trigonal
Space group	*P42/ncm*	*P42/ncm*	*R-3m*
***a* / Å**	21.438(4)	21.416(3)	17.778(5)
***b* / Å**	21.438(4)	21.416(3)	17.778(5)
***c* / Å**	23.126(4)	23.133(3)	45.221(13)
***V* / Å^3**	10629(3)	10610(2)	12378(6)
Z	4	4	6
ρ_{calcd} / g cm^{-3}	3.696	3.758	4.598
μ / mm^{-1}	21.697	22.268	27.546
Reflection collected	93868	58692	12880
Independent refl. (R_{int})	5454 (0.1042)	5861 (0.0895)	3350 (0.1171)
Goodness-of-fit	1.151	1.177	0.998
R_1 / I>2σ(I)	0.0685	0.0666	0.0680
wR_2	0.1550	0.1043	0.1204
Largest diff. peak and hole / eÅ^{-3}	3.729, -2.737	2.343, -1.950	5.875, -4.457

$R_1 = \Sigma \, ||F_0|-|F_c|| / \Sigma |F_0|$; $wR_2 = \{\Sigma[w(F_0^2-F_c^2)^2 / \Sigma w(F_0^2)^2]\}^{1/2}$

4.3.4 Raman Spectroscopy

Raman spectra were taken using excitation at the 514.5 nm line of an Ar^+ ion laser (Spectra Physics) and the 632.8 nm line from a He-Ne laser. Samples were held in NMR tubes and illuminated in a 135º geometry. Scattered light was collected by a 20X microscope objective (Olympus). Scattered excitation light was rejected by supernotch holographic filters (Kaiser Optical) and the Raman scattered light was focused on the entrance slit of a Holo-spec f/1.8 imaging spectrograph (Kaiser Optical) and dispersed on a Pixis 400 CCD camera (Princeton Instruments). Data acquisition was controlled by custom LabView software. Integration times were adjusted to utilize a reasonable amount of the CCD dynamic range (between 0.5-5 seconds). Photostability and lack of sample degradation were confirmed by noting a lack of change in the Raman spectra even under prolonged illumination conditions at increased laser power.

4.3.5 Transient Spectral and Kinetic Analysis

The femtosecond transient absorption spectrometer is based on a regeneratively amplified Ti:sapphire laser system (coherent Legend, 800 nm, 150 fs, 3 mJ/pulse and 1 kHz repetition rate) and the Helios spectrometer (Ultrafast Systems LLC). The instrument has been described in detail elsewhere.[49,50] Compounds **4.1** and **4.2** were dissolved in acidified dimethylformamide for transient measurements. Compound **4.3** was converted to the tetrabutylammonium salt and dissolved in acetonitrile for transient measurements. The kinetic traces at selected wavelengths were modeled as multi-exponential decay functions analytically convoluted with the instrument response function.

4.3.6 Electrochemistry and Spectroelectrochemistry

Cyclic voltammograms (CVs) of **4.3** were obtained at room temperature using a BAS CV-50W potentiostat with a standard three-electrode configuration. A glassy-carbon electrode was used as the working electrode. The reference and counter electrodes were Ag/AgCl (3 M NaCl) (BASi) and a platinum wire, respectively. All reported reduction potentials are relative to this reference electrode. CVs were performed in 20 mM sodium acetate buffer (pH = 4) with 0.4 M LiCl as a supporting electrolyte. Visible-light spectroelectrochemical experiments were performed with a BASi CV-50W potentiostat, in an ALS SEC-2F spectroelectrochemical flow cell (0.5 mm pathlength) equipped with an Ocean Optics USB2000+ spectrometer and an LS-1 tungsten lamp. The working electrode was an FTO-coated glass slide, the reference electrode was Ag/AgCl in 3M NaCl (BASi) and the auxiliary electrode was a stainless steel tube. Ocean Optics Spectrasuite software was used to record the visible spectra and collect absorbance vs. time measurements at applied potentials.

4.3.7 Computational Studies

Geometries of the polyanion **4.3** were optimized, both in gas phase and in implicit water solution, with no geometric constraints, at its ground singlet state. In these calculations, we used the DFT method (M06L functional)[51] in conjunction with the split-valence 6-31G(d) basis sets for oxygens and lanl2dz basis sets and associated ECPs for the W, Sb and Sn atoms,[52-54] which below are referred to as M06L/[lanl2dz + 6-31G(d,p)]. The solvent effects were approximated by the polarizable continuum model

(PCM)[55,56] employing the UFF radii[57] for all atoms. The above calculations were carried out with the Gaussian 09 software package.[58]

4.4 Results and Discussion

4.4.1 Structural Description

Compounds **4.1** and **4.2** both exhibit porous architectures reminiscent of MOFs. The repeating unit of **4.1** and the Sn(II) centers are shown in Figures 4.2a and 4.2b, respectively. Figure 4.2c shows the μ_4-Cl bridges that reside in tetrahedral positions with Sn-Cl-Sn angles (trans-) of 116.5º and 142.6º. Each repeating unit of **4.1** is perpendicular to its two neighbors forming a one-dimensional (1D) chain. To our knowledge, Cl-bridged 1D POM chains have not been reported previously. Each 1D chain is bound to the four identical proximal chains through $[Na(H_2O)_4]^+$ ions. The *P*42/ncm space group dictates that the symmetry-equivalent 1D chains assemble around the *4*-fold axis to generate an internal porous channel along the c-axis. The channel diameter is ~9.2 Å estimated from the boundary oxygen nuclei (Figure 4.3a). Another channel with a diameter of 6.1 Å, defined between the edge chloride atoms, is present along the [110] direction (Figure 4.3b). The accessible void space of the 3D channels is ~28.0% of the unit cell volume (PLATON/SOLV).[59]

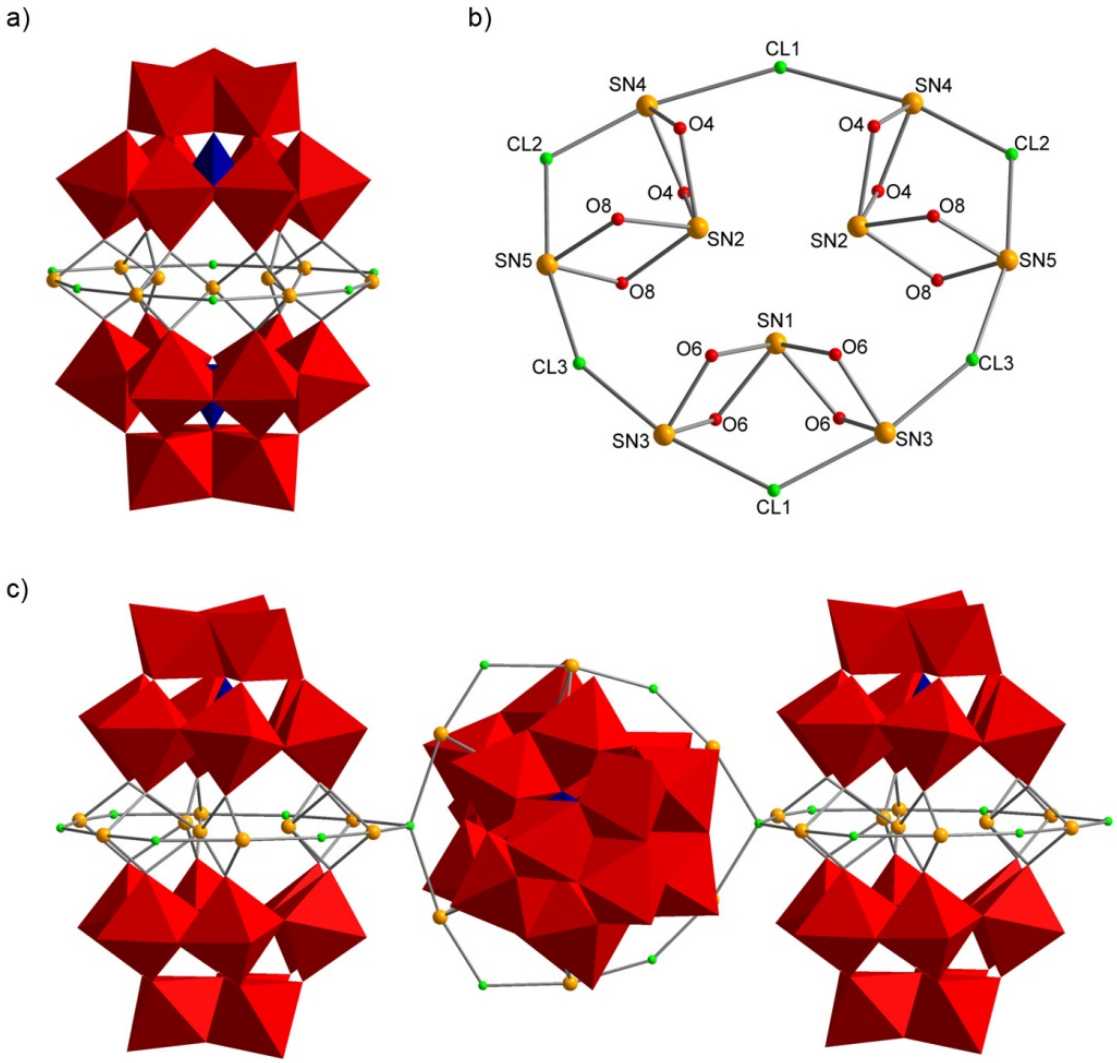

Figure 4.2. a) X-ray structure of a single polyanion unit of **4.1** in combined ball-and-stick and polyhedral notation. Color scheme: Cl, green; Sn, orange; SiO_4, blue; WO_6, red. b) Representation of the nine Sn(II) centers. c) 1D chain of **4.1** through μ_4-Cl centers.

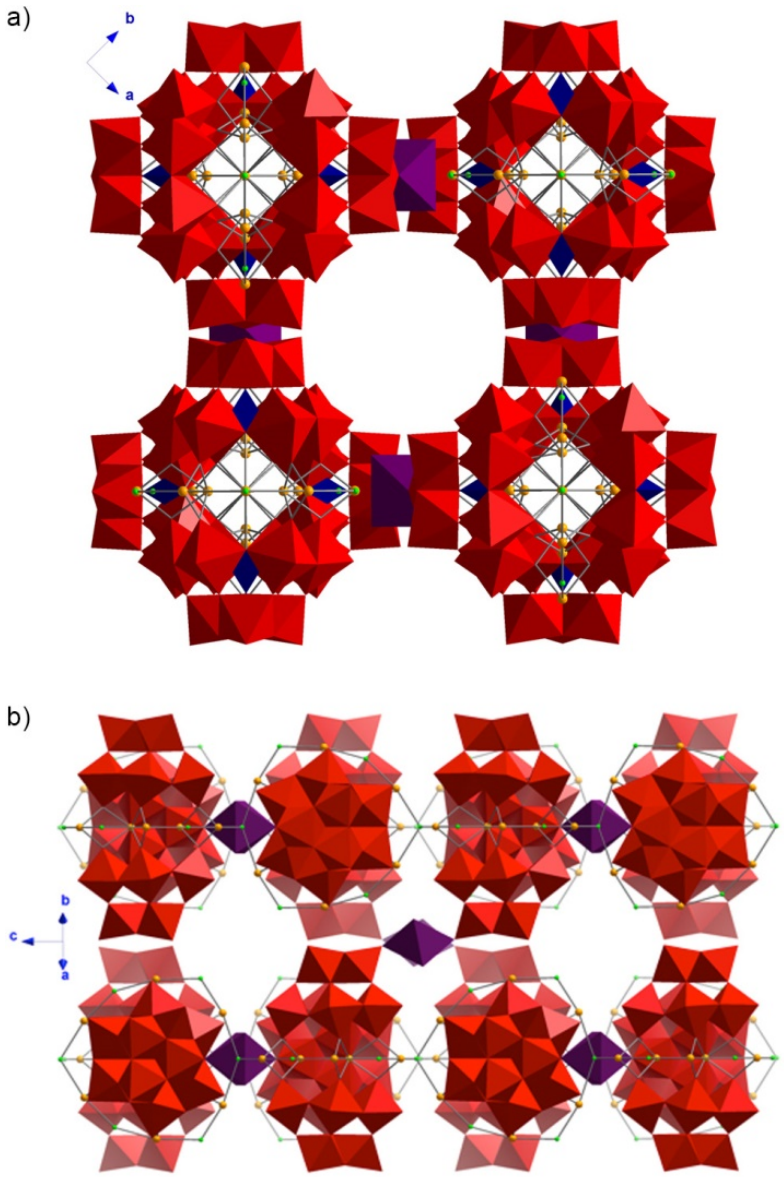

Figure 4.3. a) Porous channels along the *c*-axis in **4.1**. b) The secondary channels along the [110] direction in **4.1**. Color scheme: Cl, green; Sn, orange; SiO_4, blue; WO_6, red; Na, purple.

The polyanion unit of **4.1** (D_{3h} symmetry) consists of two $[\alpha\text{-}SiW_9O_{34}]^{10-}$ units linked by nine Sn(II) centers. Bond valence sum (BVS) calculations of all nine Sn(II) centers range from 1.75 to 1.98, indicating the low oxidation state (Table 4.2). The

structure can be viewed as a typical sandwich motif $\{Sn_3(XW_9)_2\}$, as seen in $[Sn_3(SiW_9O_{34})_2]^{14-}$,[38] surrounded by a 12-membered $\{Sn_6Cl_6\}$ ring in the belt position (Figure 4.2b). The inner Sn(II) ions display a SnO_4 seesaw molecular geometry with Sn-O distances from 2.25 to 2.29 Å, and O-Sn-O angles from 114.5º – 115.9º (O_{ax}-Sn-O_{ax}, O_{eq}-Sn-O_{eq}; ax = axial, eq = equatorial) and 69.6º – 77.4º (O_{ax}-Sn-O_{eq}), respectively. The lone-pairs on Sn(II) occupy the third equatorial position and point towards the central C_3 axis.

Table 4.2. Bond valence sum calculation results for Sn(II) centers in **4.1**, **4.2**, and **4.3**

	4.1	**4.2**	**4.3**
Sn1	1.97	1.82	1.87
Sn2	1.81	1.72	1.87
Sn3	1.92	1.87	
Sn4	1.75	1.79	
Sn5	1.91	1.89	

The $\{Sn_6Cl_6\}$ ring in the polyanion of **4.1** encircles $[Sn_3(SiW_9O_{34})_2]^{14-}$ through Sn-O-Sn bonds with angles of 106.2º – 107.3º. The external Sn(II) centers reside in SnO_2Cl_2 building blocks, which display a seesaw geometry with two chlorides in axial positions and two oxygens in equatorial positions, respectively. The external lone-pairs face away from C_3 axis. The Cl-Sn-Cl bond angles are 165.5º – 166.5º while O-Sn-O angles are 74.6º – 75.3º. The Sn-O bond distances are 2.12 – 2.15 Å, while Sn-Cl bonds show long distances ranging from 2.68 to 3.18 Å. The Sn-(μ_2-Cl)-Sn linkages are shorter than the Sn-(μ_4-Cl)-Sn linkages.[60,61]

$[\{Na(\mu\text{-}OH_2)(OH_2)_2\}_6\{Sn_6(B\text{-}SbW_9O_{33})_2\}_2]^{6-}$ (the polyanion of **4.3**) is a tetramer constructed of two $[Sn_6(B\text{-}SbW_9O_{33})_2]^{6-}$ units linked to each other through a polymeric

cation, $[Na_6(\mu\text{-}OH_2)_6(OH_2)_{12}]^{6+}$ (Figure 4.4). $[Sn_6(B\text{-}SbW_9O_{33})_2]^{6-}$ comprises two $[B\text{-}SbW_9O_{33}]^{9-}$ ligands joined by six Sn(II) centers, a structural motif similar to that in $[Sn_6(SnW_9O_{33})_2]^{8-}$.[42] Complex **4.3** (with a D_{3d} polyanion) crystallizes in the trigonal *R-3m* space group and has one $[B\text{-}SbW_9O_{33}]^{9-}$ unit rotated by 60º relative to the other. The Sn-O bonds range from 2.25 to 2.29 Å. Each Sn(II) is four-coordinated and in the +2 oxidation state (Table 4.2). The Sn-O-Sn bond angles are 107.8º – 109.5º, and the O-Sn-O angles are 118.1º – 118.7º (O_{ax}-Sn-O_{ax}, O_{eq}-Sn-O_{eq}) and 70.4º – 79.7º (O_{ax}-Sn-O_{eq}), respectively. Each Na^+ ion in $[Na_6(\mu\text{-}OH_2)_6(OH_2)_{12}]^{6+}$ resides in an octahedral environment with Na-O bond distances of 2.24 – 2.26 Å (terminal) and 2.43 – 2.49 Å (bridged), respectively. This nanosized cluster has a length of *ca.* 3 nm.

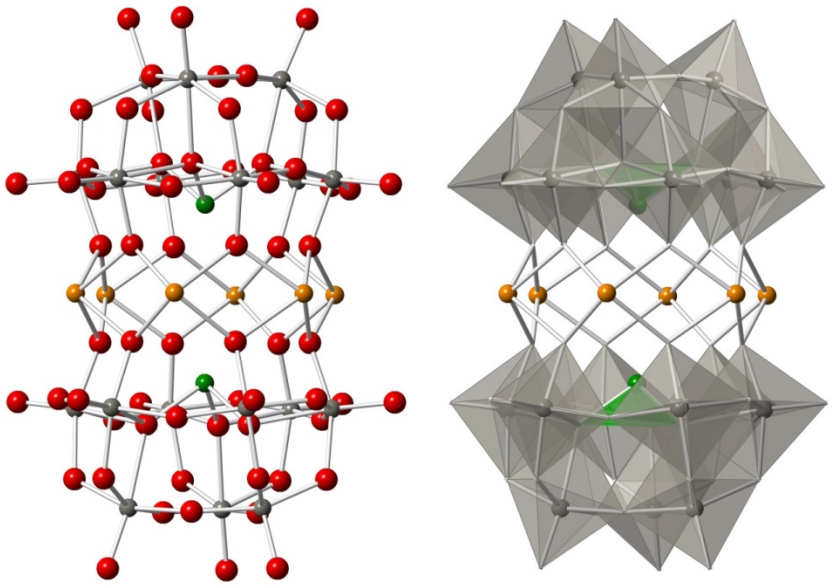

Figure 4.4. X-ray structure of $[Sn_6(B\text{-}SbW_9O_{33})_2]^{6-}$ (**4.3**) represented in ball-and-stick notation (left) and mixed polyhedral notation (right). Color scheme: Sb, green; Sn, orange; W, grey; O, red.

4.4.2 Electronic Absorption Spectra, Electrochemistry and Spectroelectrochemical Measurements

Network solids are generally not soluble, and that is the case with **4.1** and **4.2**. The compounds are colored (**4.1** and **4.2** are orange and **4.3** is red) in the solid state. As seen in Figures 4.5a and 4.5b, the UV-vis absorption spectrum of **4.3** shows a broad band in the visible region extending to about 650 nm ($\varepsilon_{400\ nm}$: 1.05×10^4 $M^{-1}\cdot cm^{-1}$). The $SnCl_2$ and POM ligand precursors, unlike **4.1**-**4.3**, are both colorless; consequently, this absorption feature is likely due to a transition involving lone-pair donors (could be located on Sn(II) and Sb(III) centers) and POM acceptors. Significantly, this p-block-element-to-POM electronic structure is distinct from the metal-to-polyoxometalate (MPCT) transitions in two recent reports because the latter involve donation of d electron density on the donor site, e.g. Re(I), to the delocalized POM multi-metal orbitals.[49,62,63] Particularly, the presence of lone pairs in **4.1**-**4.3** contributes to a large local dipole moment, which has been shown to facilitate electron-hole charge-separation.[64-66]

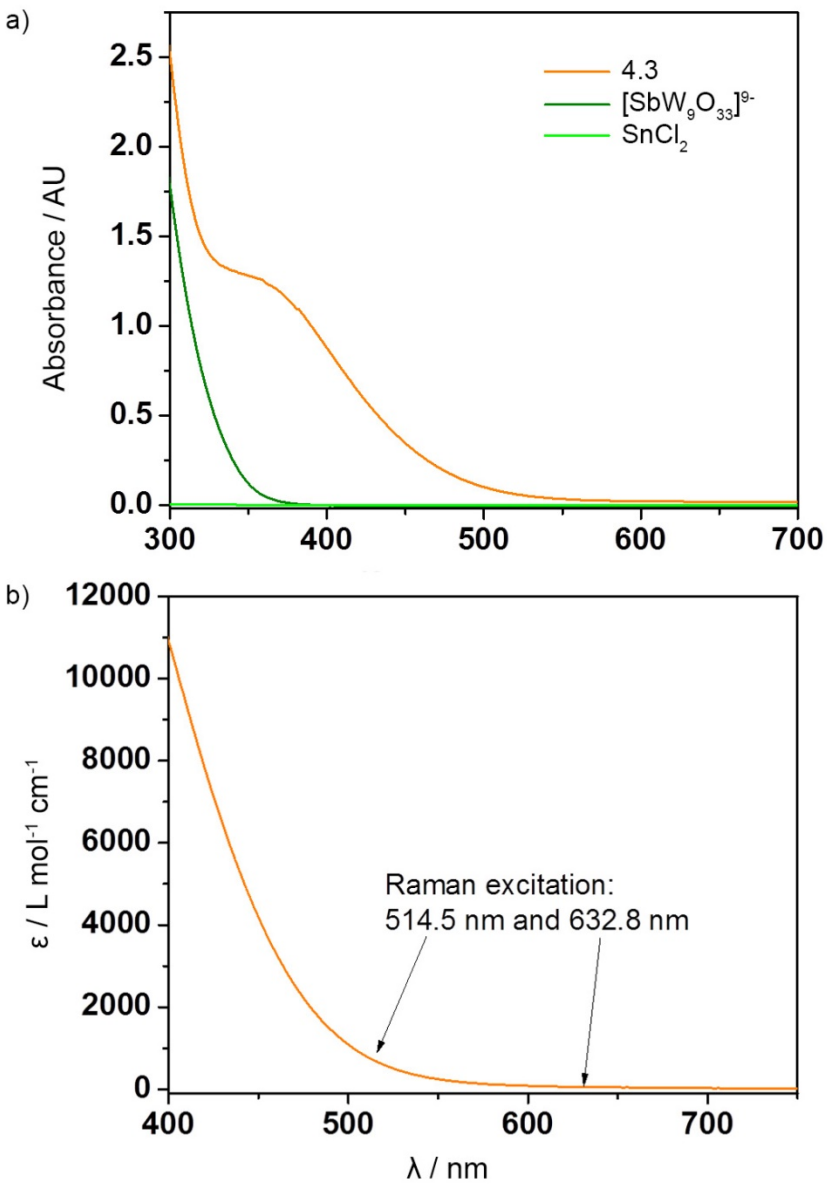

Figure 4.5. a) Electronic absorption spectra of **4.3**, $[B\text{-}SbW_9O_{33}]^{9-}$ (2 equivalents) and $SnCl_2$ (6 equivalents) in aqueous solution (pH 1). b) Electronic absorption spectrum of **4.3**, with arrows indicating the wavelengths used for Raman excitation.

As shown in Figure 4.6a, in the negative potential domain, the CVs of **4.3** display two quasi-reversible poorly resolved peaks with a nearly 1:1 current ratio, which is consistent with two one-electron transfer processes ($E_{1/2}$ at *ca*. -0.48V and -0.65V, respectively). These patterns are similar to those of $[B\text{-}SbW_9O_{33}]^{9-}$ derivatives.[67,68] The width of the CV peaks is consistent with slow electron transfer processes, likely due to high reorganization energies in **4.3**. The peaks in the negative domain are assigned to W(VI)/W(V) reductions. The peaks for the Sn(II)-centered redox processes do not show up in the CV scans. The spectroelectrochemical absorption spectra for reduced **4.3** in the ground state were recorded at an applied potential of -0.80V vs. Ag/AgCl. As seen in Figure 4.6b, a new absorption band from *ca*. 550 nm to the near-IR was observed, which is a characteristic feature of reduced POMs, the "heteropoly blues."[69] These new absorption features can be attributed to W(V) d-d and W(V)-W(VI) intervalence charge transfer (IVCT) transitions in reduced POMs.[70,71] Compound **4.3** shows good reversibility in spectroelectrochemical measurements, where bulk reduction and air-based reoxidation processes can be repeated sequentially. CVs were not collected for **4.1** or **4.2** due to poor solubility.

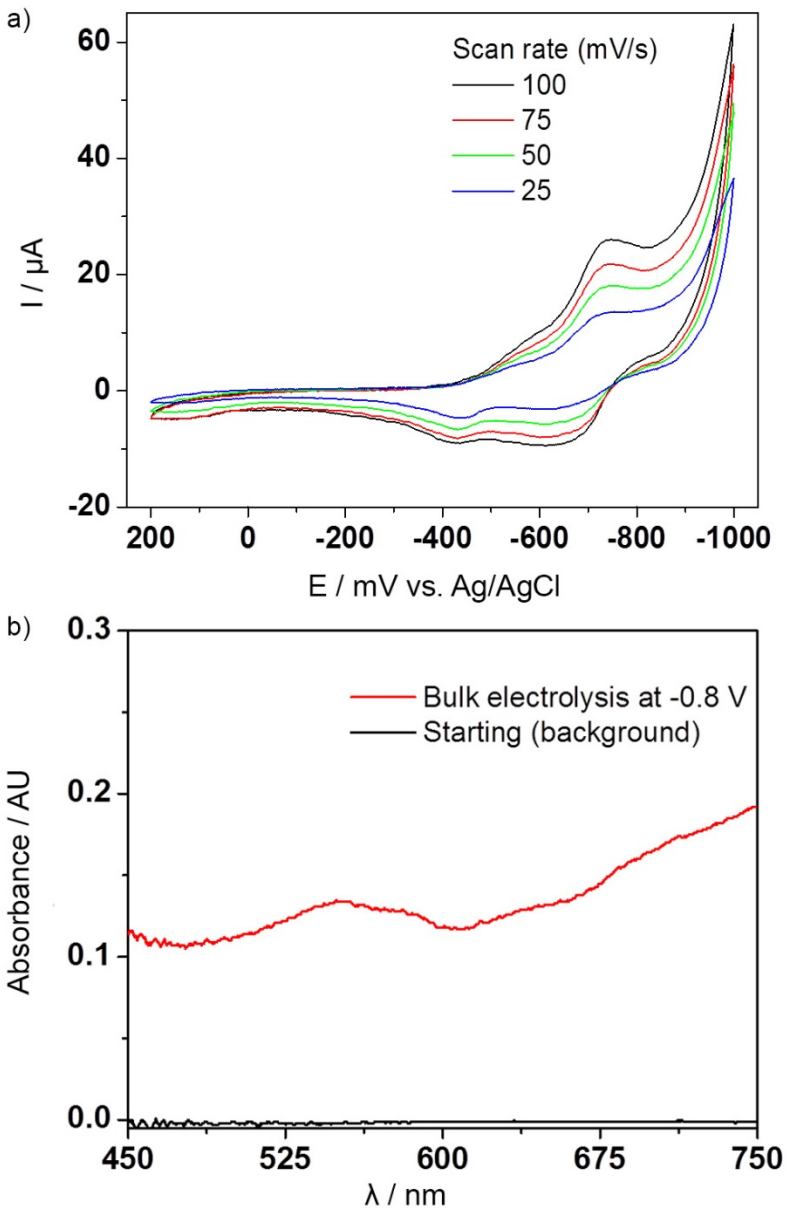

Figure 4.6. a) Cyclic voltammograms of **4.3** at multiple scan rates in the range of +200 to -1000 mV vs. Ag/AgCl, in 20 mM sodium acetate buffer (pH = 4) with 0.4 M LiCl as a supporting electrolyte. b) Ground state UV−vis absorption difference spectra of reduced **4.3** (generated at −0.8 V vs Ag/AgCl) relative to **4.3** as a starting background spectrum in sodium acetate buffer.

4.4.3 Computational Studies

Compound **4.3**, unlike **4.1** and **4.2**, contains Sb(III) lone pairs in addition to the Sn(II) lone-pair electrons and exhibits an extraordinarily high extinction coefficient in the visible region. In order to understand the origin of these intense transitions (absorptions), we investigated the geometrical and electronic structure of **4.3** using computational methods. The calculated Sn-O bond distances of the central hexanuclear Sn(II) "belt" range from 2.21 to 2.23 Å, the Sn-O-Sn bond angles are 107.1º – 107.8º, the W-O(Sn) bond distances are within 1.94 – 1.95 Å, and the Sb-O bond distances (symmetrically equivalent) are 2.01 Å. These geometric parameters are in excellent agreement with the experimental values.

Interestingly, the frontier orbital analyses of the singlet ground state indicate the existence of a weak Sb…Sb interaction in **4.3**: the calculated energy difference between the Sb-Sb bonding (HOMO-8) and Sb-Sb antibonding (HOMO-7) orbitals is only 0.33 eV (Figure 4.7). This is likely due to long-range lone-pair interaction.[72] The first six HOMOs of **4.3** are lone-pairs on the Sn centers, which are clustered within a 0.30 eV energy range. The next orbitals are primarily Sb-Sb and Sb-O in nature and doubly occupied. The leading LUMOs are mostly W-centered orbitals. The calculated HOMO-LUMO energy gap is 1.67 eV. Since single-electron transfer from HOMO to LUMO leads to a triplet state with a multi-determinant wavefunction, our calculations of the triplet state failed to converge; at this time we cannot report a reliable singlet-triplet energy splitting.

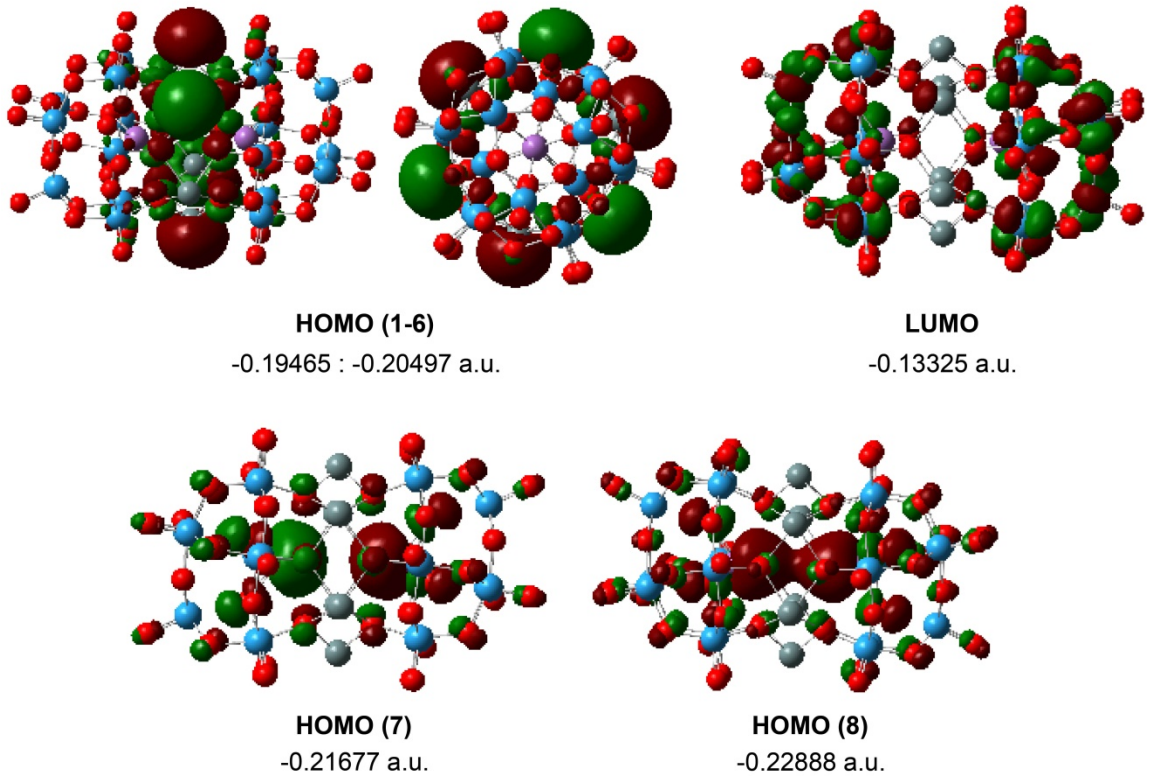

Figure 4.7. Several highest occupied (HOMO) and lowest unoccupied (LUMO) orbitals and their orbital energies (in Hartree) in complex **4.3**.

4.4.4 Resonance Raman Spectroscopy

Resonance Raman (RR) spectroscopy has also been used to characterize the putative lone-pair-to-POM charge-transfer transition in **4.3**. The RR spectra of **4.3** the colorless precursor $Na_9[B\text{-}SbW_9O_{33}]$, and $Na_9[\{Co(H_2O)\}_3\{Na(H_2O)_2\}_3(B\text{-}SbW_9O_{33})_2]$ (**4.4**),[73,74] a known complex with a $\{Co_3Na_3\}$ belt similar to $\{Sn_6\}$ in **4.3** were compared, and spectra were normalized to the intensity of the highest energy W-O stretch (~950-990 cm^{-1}). The rapid falloff of intensity at energies lower than ~200 cm^{-1} is due to the bandwidth of the holographic notch filter. Although detailed assignment of the vibrational spectra is beyond the scope of this work, conclusions can be drawn from the data. Two

Raman probe wavelengths were used, 514.5 nm and 632.8 nm, enabling a simple two-point excitation profile to be observed (Figure 4.5b). As shown in Figures 4.8a and 4.8b, upon changing the excitation wavelength from 632.8 nm (ε ~55 $M^{-1}cm^{-1}$ for **4.3**) to 514.5 nm (ε ~710 $M^{-1}cm^{-1}$ for **4.3**), there is a significant increase in relative intensity of several transitions in the low-frequency region (300 – 400 cm^{-1}), where mostly M-O stretching and O-M-O (M = Sb or Sn) bending modes are expected due to a large degree of coupling in the highly symmetric Sn cluster, and in the region ~800 cm^{-1} where W-O-M bending modes reside.[36,39,75-77] Specifically, the vibration at 487 cm^{-1} present in both **4.3** and $Na_9[B\text{-}SbW_9O_{33}]$ exhibits little perturbation upon complexation of the $\{Sn_6\}$ cluster, but gains great resonance enhancement upon excitation. This vibration can be assigned to a localized mode in the $[B\text{-}SbW_9O_{33}]^{9-}$ polyanion, which likely has both W-O and Sb-O character. Similarly the vibration at 627 cm^{-1} which can be observed as a weak mode in $Na_9[B\text{-}SbW_9O_{33}]$, gains comparable intensity to the nearby 690 cm^{-1} mode upon 514.5 nm excitation. Various other enhanced vibrations, such as the band at 825 cm^{-1}, likely a W-O-Sn stretching mode,[39] only arise after the formation of $\{Sn_6\}$ cluster, indicating either local Sn-O modes or coupling of POM modes to the $\{Sn_6\}$ core.

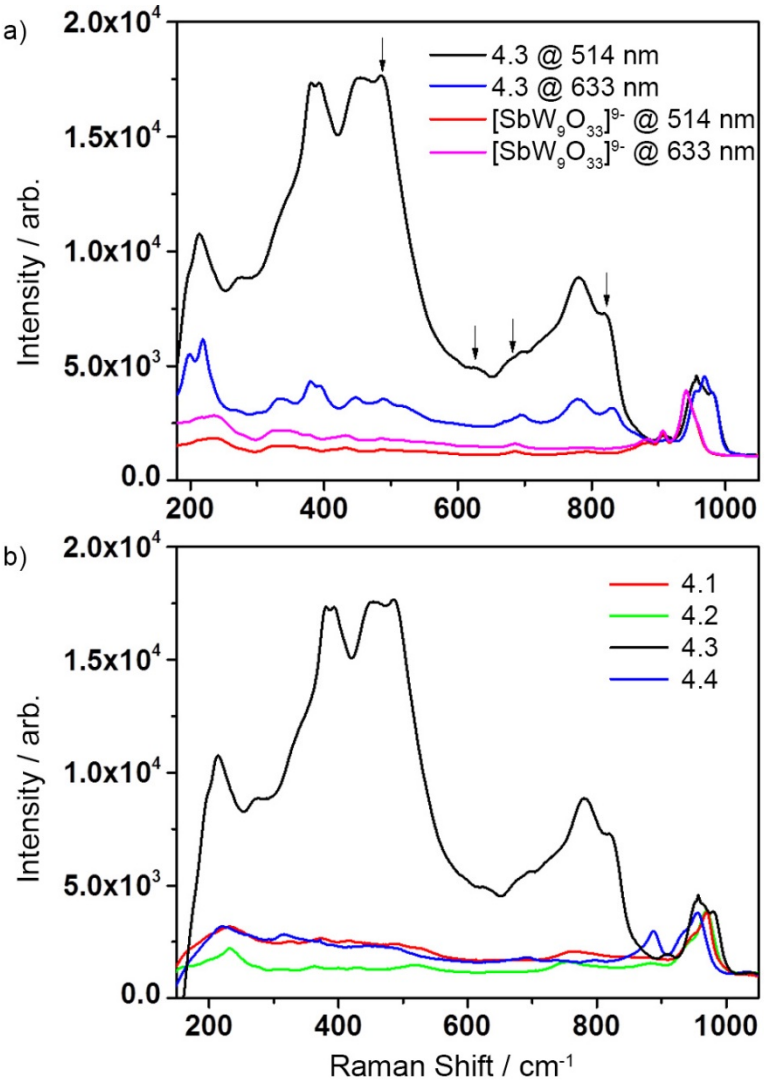

Figure 4.8. a) Resonance Raman spectra of **4.3** and $[B\text{-}SbW_9O_{33}]^{9-}$ acquired at two excitation wavelengths. Arrows indicate the representative modes discussed in the main text (487, 627, 690 and 825 cm^{-1}, respectively). b) Normalized Resonance Raman spectra of **4.1**-**4.4** at 514 nm excitation.

The observation of resonantly enhanced vibrations attributable to both local POM modes and modes coupled to the central $\{Sn_6\}$ cluster supports the assignment as a charge transfer transition. There is, however, no comparable enhancement trend for **4.1** or

4.2 (Figure 4.8b) despite a similar (although weaker) visible absorption. This observation supports the important role of Sb(III) and the unique structure of the central {Sn_6} cluster in the charge-transfer transition. There is also no enhancement of lower frequency bands for **4.4**, although it has a similar geometry to **4.3** and exhibits *d*-*d* bands in the visible region which principally involve five-coordinate Co(II) ions. This excludes the enhancement being a result of the geometric motif of the core atoms. Shifts in the redox potentials and energy levels of the POM LUMOs arising from different heteroatoms can account for some of the discrepancy of photoactivity for the three stannato(II)tungstates.[78-80] The collective results indicate that the synergistic effect of Sn(II) and Sb(III) lone-pairs account for the particular charge-transfer characteristics in **4.3**.

4.4.5 Transient Absorption Spectroscopy

Femtosecond visible pump-probe spectroscopy was used to study the kinetics of this lone-pair-to-POM transition. Upon photo-excitation (at 400 nm) the transient absorption spectra show a new species with a broad absorption from ~500 nm to near-IR (Figure 4.9a). The new absorption feature is reminiscent of the UV-vis absorption spectrum of an electrochemically-reduced **4.3** (Figure 4.6b), the result of the photoexcited electron residing in the delocalized POM acceptor orbitals. Differences between the two spectra are expected on the basis that the photoexcited species contains a transiently oxidized donor that cannot be replicated electrochemically. The kinetics are monitored at 520 and 720 nm, respectively, and fitted by multi-exponential functions. An instantaneous formation of the excited states and a bi-exponential decay was documented. There is a

long-lived component at 720 nm that persists with a time constant of 66 ps. This component has a shallow, broad absorbance that has a heteropoly-blue spectral signature (Figure 4.9b and Table 4.3).[81-83] These results, combined with the above HOMO/LUMO assignment, suggest a transition from lone-pair-donors to POM acceptors upon excitation; however, this does not exclude the possible contribution of LMCT (oxygen-to-tungsten) transitions in the transient spectra.

The excited state dynamics of **4.1** and **4.2** were also measured following photo-excitation at 400 nm. However, because **4.1** and **4.2** are network solids, harsh conditions (*ca.* 10% 1 M HCl in DMF) were necessary to force them to become soluble, which most likely disrupted their polymeric structures. The resulting dissociated sandwich-type POM species are structurally similar to **4.3**, while lacking the synergistic effect of Sn(II) and Sb(III) lone-pairs, but would still be expected to exhibit some charge transfer character.

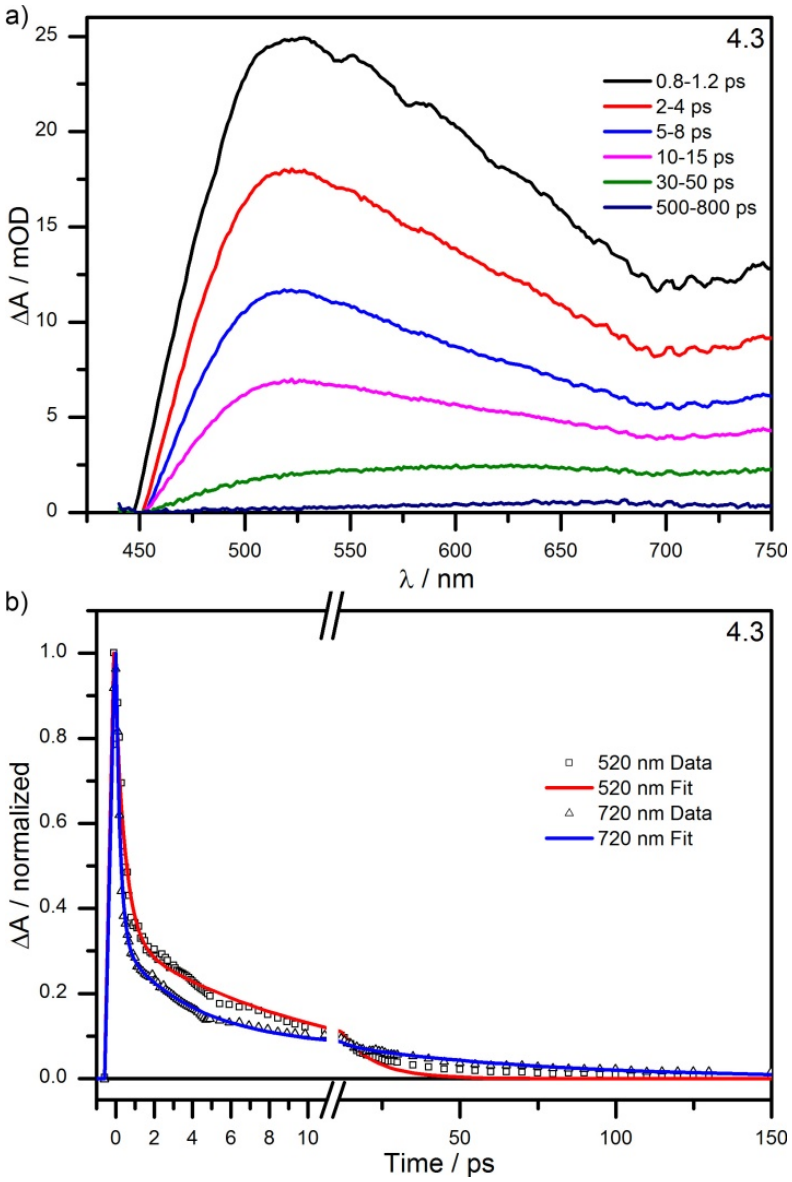

Figure 4.9. a) Transient absorption spectra and b) kinetics of **4.3-TBA** after excitation by an ultrafast pump pulse at 400 nm in MeCN. Spectral traces are the average of multiple measurements within the noted time windows. Empirical measurements and multi-exponential kinetic fits are shown normalized to peak fit values.

Table 4.3. Multi-exponential fitting parameters for the kinetic traces of **4.3-TBA** after 400 nm excitation

Wavelength	**Lifetimes**		**Norm. Coefficients**	
λ / nm	τ_1 / ps	τ_2 / ps	A_1	A_1
520	0.5 ± 0.1	10.8 ± 1.2	0.73	0.27
720	3.8 ± 0.5	66 ± 15	0.72	0.28

The transient absorption spectra for **4.1** and **4.2** are nearly identical, exhibiting a broad absorption from ~450 nm to beyond 750 nm (Figures 4.10 and 4.11). The only notable difference between the excited states of **4.1**/**4.2** and **4.3** is the lack of a transient peak at 520 nm in the former. Measurements were recorded at two different excitation pump power settings, relatively high pump power at 2.6 mW (2.6 μJ/pulse) and a lower pump power at 0.6 mW (0.6 μJ/pulse), to evaluate whether any nonlinear kinetic components or optical effects were present during measurement. The only effect variation in the pump power had was to improve the signal-to-noise ratio at higher pump power, and no sample degradation upon prolonged irradiation was observed at either power setting by UV-visible spectroscopy. Within the confidence intervals of the kinetic analysis, each compound shows identical excited state lifetimes (Figure 4.12 and Table 4.4).

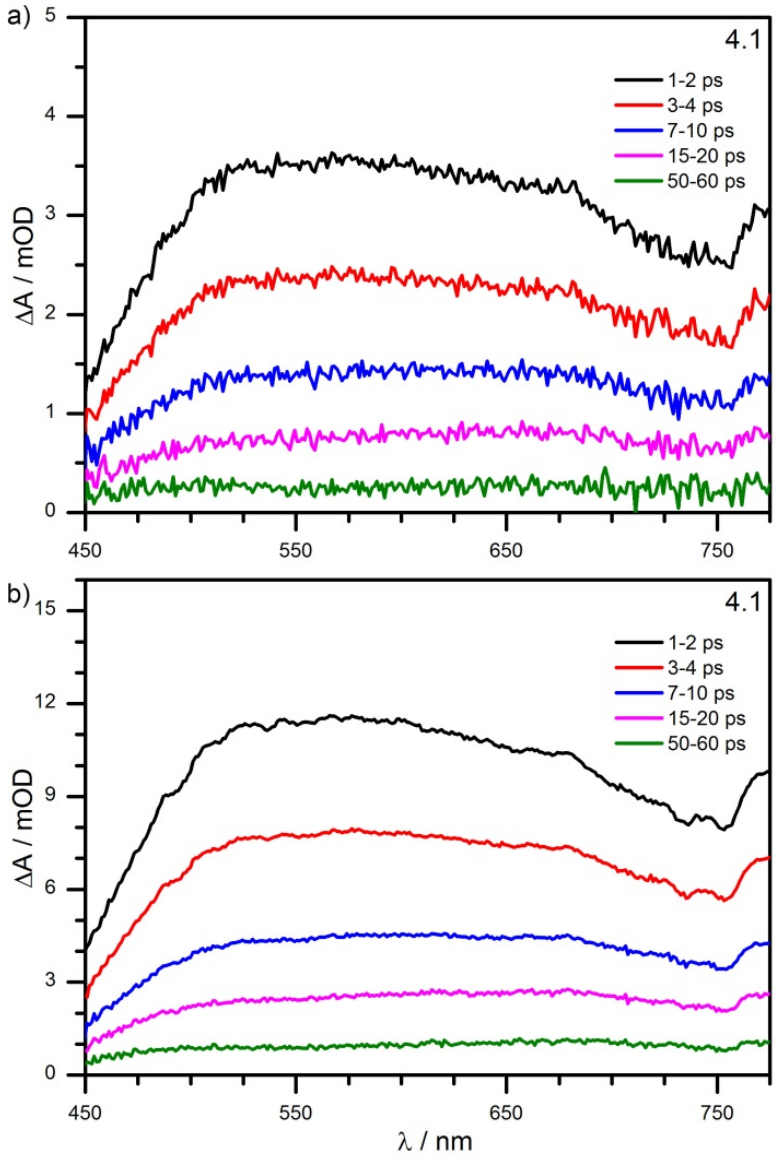

Figure 4.10. Transient absorption spectra of **4.1** in acidified DMF after excitation by a 400 nm ultrafast pump pulse at a) 0.6 μJ/pulse and b) 2.6 μJ/pulse. Spectral traces are the average of multiple measurements within the noted time windows.

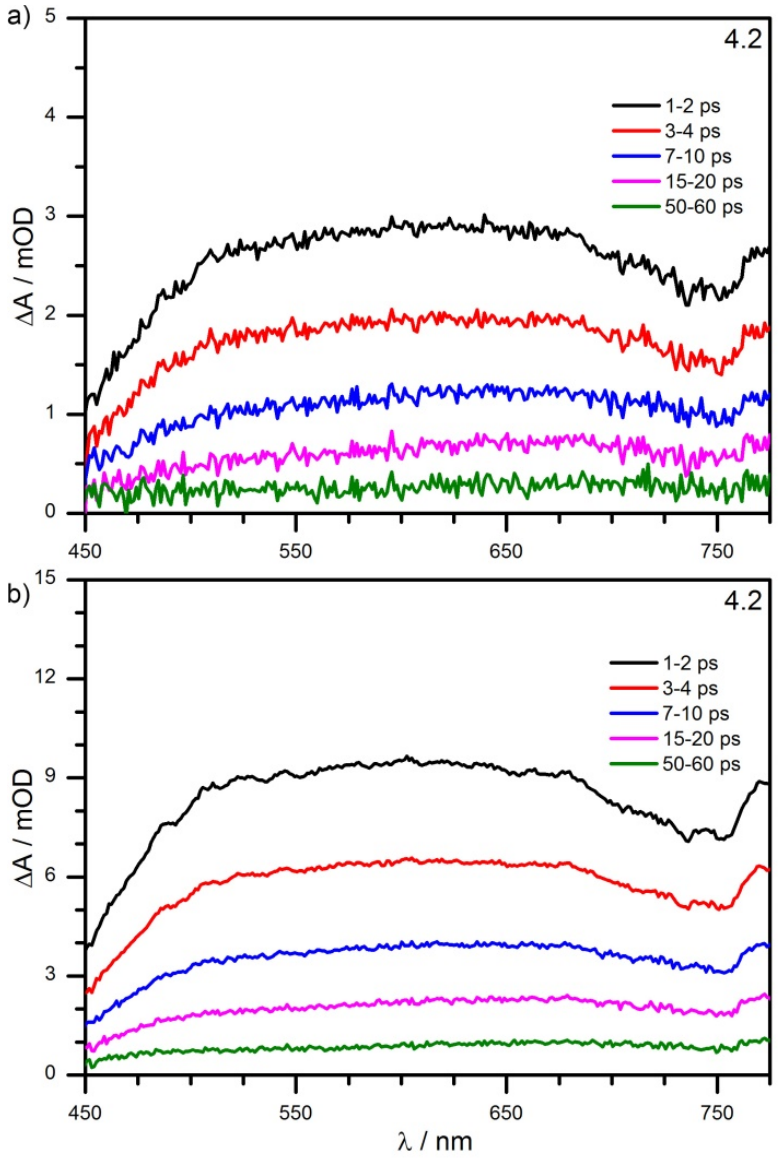

Figure 4.11. Transient absorption spectra of **4.2** in acidified DMF after excitation by a 400 nm ultrafast pump pulse at a) 0.6 μJ/pulse and b) 2.6 μJ/pulse. Spectral traces are the average of multiple measurements within the noted time windows.

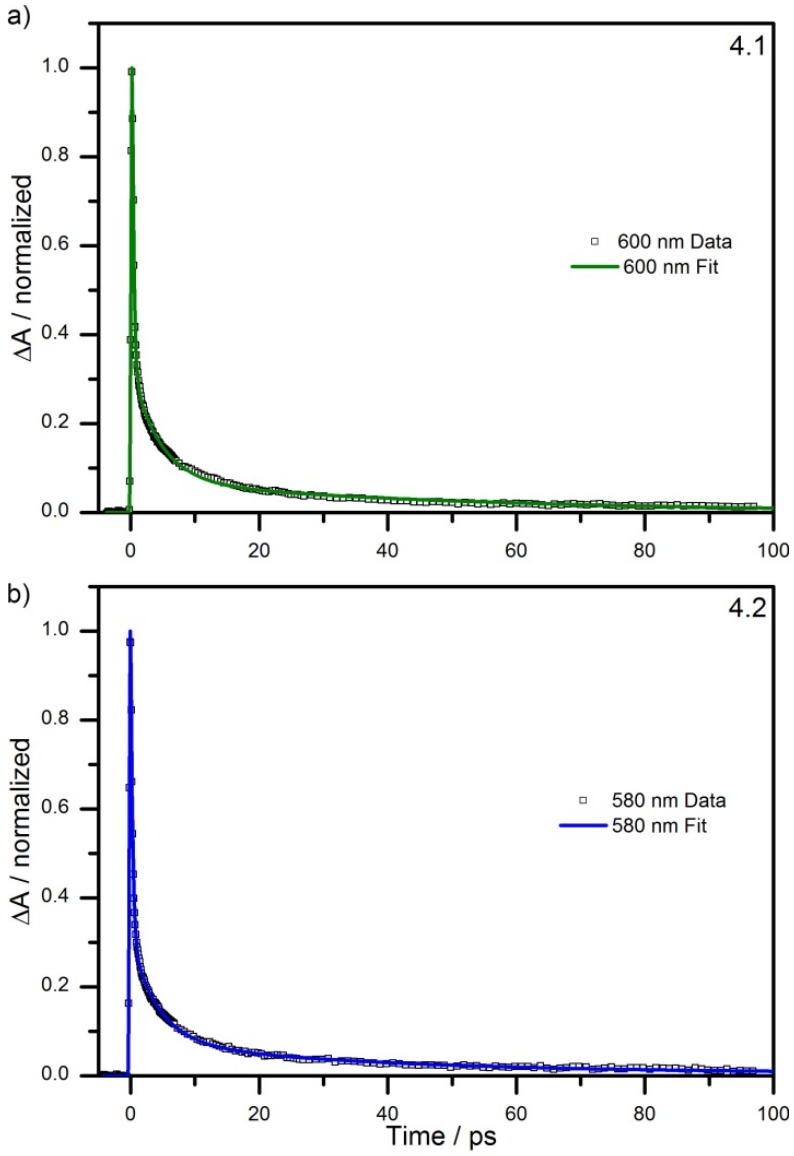

Figure 4.12. Transient kinetics of **4.1** and **4.2** in acidified DMF after excitation at 400 nm. Empirical measurements and multi-exponential kinetic fits are shown normalized to peak fit values.

Table 4.4. Multi-exponential fitting parameters for the kinetic traces of **4.1** and **4.2** after 400 nm excitation at high and low pump power

Compound	**Wavelength**	**Lifetimes**		**Norm. Coefficients**	
	λ / nm	τ_1 / ps	τ_2 / ps	A_1	A_1
4.1 (high)	600	4.4 ± 0.3	50 ± 5	0.79	0.21
4.1 (low)	600	4.2 ± 0.3	49 ± 6	0.78	0.22
4.2 (high)	580	4.3 ± 0.3	36 ± 4	0.79	0.21
4.2 (low)	580	4.7 ± 0.5	47 ± 7	0.76	0.24

4.5 Conclusion

Structural and spectral features of Sn(II)-containing POMs, networks **4.1** and **4.2**, and the molecular compound **4.3**, have been thoroughly investigated. The external lone pairs of Sn(II) in **4.1** and **4.2** direct the formation of high dimensional structures. The co-existence of Sb(III)/Sn(II) lone-pair electrons lead to a synergistic effect contributing to the charge-transfer absorption features of **4.3**. This study broadens the frontier of POM chemistry in the context of self-assembly and energy conversion, especially for the lesser-documented p-block element POM families.

4.6 References

(1) *Polyoxometalates: From Platonic Solids to Anti-retroviral Activity*; Pope, M. T.; Müller, A., Eds.; Kluwer Academic Publishers: Dordrecht, Netherlands, 1993.

(2) Miras, H. N.; Yan, J.; Long, D.-L.; Cronin, L. *Chem. Soc. Rev.* **2012**, *41*, 7403.

(3) Lv, H.; Geletii, Y. V.; Zhao, C.; Vickers, J. W.; Zhu, G.; Luo, Z.; Song, J.; Lian, T.; Musaev, D. G.; Hill, C. L. *Chem. Soc. Rev.* **2012**, *41*, 7572.

(4) Müller, A.; Shah, S. Q. N.; Bogge, H.; Schmidtmann, M. *Nature* **1999**, *397*, 48.

(5) Mal, S. S.; Kortz, U. *Angew. Chem. Int. Ed.* **2005**, *44*, 3777.

(6) Bassil, B. S.; Dickman, M. H.; Römer, I.; von der Kammer, B.; Kortz, U. *Angew. Chem. Int. Ed.* **2007**, *46*, 6192.

(7) Müller, A.; Serain, C. *Acc. Chem. Res.* **2000**, *33*, 2.

(8) Schäffer, C.; Merca, A.; Bögge, H.; Todea, A. M.; Kistler, M. L.; Liu, T.; Thouvenot, R.; Gouzerh, P.; Müller, A. *Angew. Chem. Int. Ed.* **2009**, *48*, 149.

(9) Botar, B.; Kögerler, P.; Hill, C. L. *J. Am. Chem. Soc.* **2006**, *128*, 5336.

(10) Lee, J. Y.; Farha, O. K.; Roberts, J.; Scheidt, K. A.; Nguyen, S. B. T.; Hupp, J. T. *Chem. Soc. Rev.* **2009**, *38*, 1450.

(11) Wang, C.; deKrafft, K. E.; Lin, W. *J. Am. Chem. Soc.* **2012**, *134*, 7211.

(12) Nohra, B.; El Moll, H.; Rodriguez-Albelo, L. M.; Mialane, P.; Marrot, J. é.; Mellot-Draznieks, C.; O'Keeffe, M.; Ngo Biboum, R.; Lemaire, J.; Keita, B.; Nadjo, L.; Dolbecq, A. *J. Am. Chem. Soc.* **2011**, *133*, 13363.

(13) Song, J.; Luo, Z.; Britt, D.; Furukawa, H.; Yaghi, O. M.; Hardcastle, K. I.; Hill, C. L. *J. Am. Chem. Soc.* **2011**, *133*, 16839.

(14) Zheng, S.-T.; Zhang, J.; Yang, G.-Y. *Angew. Chem. Int. Ed.* **2008**, *47*, 3909.

(15) Ma, F.-J.; Liu, S.-X.; Sun, C.-Y.; Liang, D.-D.; Ren, G.-J.; Wei, F.; Chen, Y.-G.; Su, Z.-M. *J. Am. Chem. Soc.* **2011**, *133*, 4178.

(16) Juan-Alcañiz, J.; Goesten, M. G.; Ramos-Fernandez, E. V.; Gascon, J.; Kapteijn, F. *New J. Chem.* **2012**, *36*, 977.

(17) Zheng, S.-T.; Zhang, J.; Li, X.-X.; Fang, W.-H.; Yang, G.-Y. *J. Am. Chem. Soc.* **2010**, *132*, 15102.

(18) Zhang, L.; Schmitt, W. *J. Am. Chem. Soc.* **2011**, *133*, 11240.

(19) Bonfim, R. d. P. F.; Moura, L. C. d.; Pizzala, H.; Caldarelli, S.; Paul, S.; Eon, J. G.; Mentré, O.; Capron, M.; Delevoye, L.; Payen, E. *Inorg. Chem.* **2007**, *46*, 7371.

(20) Han, X.-B.; Zhang, Z.-M.; Wang, Z.-S.; Zhang, H.; Duan, H.; Wang, E.-B. *Inorg. Chem. Commun.* **2012**, *18*, 47.

(21) Gao, S.; Cao, R.; Bi, W.; Li, X.; Lin, Z. *Microporous Mesoporous Mater.* **2005**, *80*, 139.

(22) Mothé-Esteves, P.; Pereira, M. M.; Arichi, J.; Louis, B. *Cryst. Growth Des.* **2009**, *10*, 371.

(23) Liu, D.; Lu, Y.; Tan, H.-Q.; Chen, W.-L.; Zhang, Z.-M.; Li, Y.-G.; Wang, E. *Chem. Commun.* **2013**, *49*, 3673.

(24) Li, F.; Meng, F.; Ma, L.; Xu, L.; Sun, Z.; Gao, Q. *Dalton Trans.* **2013**, *42*, 12079.

(25) Streb, C.; Ritchie, C.; Long, D.-L.; Kögerler, P.; Cronin, L. *Angew. Chem. Int. Ed.* **2007**, *46*, 7579.

(26) Mitchell, S. G.; Streb, C.; Miras, H. N.; Boyd, T.; Long, D.-L.; Cronin, L. *Nat. Chem.* **2010**, *2*, 308.

(27) Sato, J.; Kobayashi, H.; Inoue, Y. *J. Phys. Chem. B* **2003**, *107*, 7970.

(28) Walsh, A.; Payne, D. J.; Egdell, R. G.; Watson, G. W. *Chem. Soc. Rev.* **2011**, *40*, 4455.

(29) Brown, D. *J. Phys. Chem. A* **2011**, *115*, 12638.

(30) Bosing, M.; Loose, I.; Pohlmann, H.; Krebs, B. *Chem. Eur. J.* **1997**, *3*, 1232.

(31) Sazani, G.; Dickman, M. H.; Pope, M. T. *Inorg. Chem.* **2000**, *39*, 939.

(32) Bi, L.-H.; Al-Kadamany, G.; Chubarova, E. V.; Dickman, M. H.; Chen, L.; Gopala, D. S.; Richards, R. M.; Keita, B.; Nadjo, L.; Jaensch, H.; Mathys, G.; Kortz, U. *Inorg. Chem.* **2009**, *48*, 10068.

(33) Zhao, C.; Kambara, C. S.; Yang, Y.; Kaledin, A. L.; Musaev, D. G.; Lian, T.; Hill, C. L. *Inorg. Chem.* **2013**, *52*, 671.

(34) Corella-Ochoa, M. N.; Miras, H. N.; Kidd, A.; Long, D.-L.; Cronin, L. *Chem. Commun.* **2011**, *47*, 8799.

(35) Tsunashima, R.; Long, D.-L.; Endo, T.; Noro, S.-i.; Akutagawa, T.; Nakamura, T.; Cabrera, R. Q.; McMillan, P. F.; Kögerler, P.; Cronin, L. *Phys. Chem. Chem. Phys.* **2011**, *13*, 7295.

(36) Cabrera, R. Q.; Firth, S.; Blackman, C. S.; Long, D.-L.; Cronin, L.; McMillan, P. F. *J. Solid State Chem.* **2012**, *186*, 171.

(37) Long, D.-L.; Abbas, H.; Kögerler, P.; Cronin, L. *Angew. Chem. Int. Ed.* **2005**, *44*, 3415.

(38) Xin, F.; Pope, M. T. *J. Am. Chem. Soc.* **1996**, *118*, 7731.

(39) Botar, A.; Botar, B.; Gili, P.; Müller, A.; Meyer, J.; Bögge, H.; Schmidtmann, M. *Z. Anorg. Allg. Chem.* **1996**, *622*, 1435.

(40) Khoshnavazi, R.; Bahrami, L. *J. Coord. Chem.* **2009**, *62*, 2067.

(41) Krebs, B.; Droste, E.; Piepenbrink, M.; Vollmer, G. *C. R. Acad. Sci., Ser. IIc: Chim.* **2000**, *3*, 205.

(42) Sokolov, M. N.; Izarova, N. V.; Virovets, A. V.; Fedin, V. P.; Starikova, Z. A.; Antipin, M. Y. *Dalton Trans.* **2003**, 4389.

(43) Zhang, Z.; Lin, Q.; Zheng, S.-T.; Bu, X.; Feng, P. *Chem. Commun.* **2011**, *47*, 3918.

(44) Tézé, A.; Hervé, G. *J. Inorg. Nucl. Chem.* **1977**, *39*, 2151.

(45) Tézé, A.; Hervé, G. *J. Inorg. Nucl. Chem.* **1977**, *39*, 999.

(46) *SAINT*; Bruker AXS, Inc.: Madison, WI, 2009.

(47) *SADABS*; Bruker AXS, Inc.: Madison, WI, 2008.

(48) *SHELXTL-97*; Bruker AXS, Inc.: Madison, WI, 2003.

(49) Zhao, C.; Huang, Z.; Rodríguez-Córdoba, W.; Kambara, C. S.; O'Halloran, K. P.; Hardcastle, K. I.; Musaev, D. G.; Lian, T.; Hill, C. L. *J. Am. Chem. Soc.* **2011**, *133*, 20134.

(50) Glass, E. N.; Fielden, J.; Kaledin, A. L.; Musaev, D. G.; Lian, T.; Hill, C. L. *Chem. Eur. J.* **2014**, *20*, 4297.

(51) Zhao, Y.; Truhlar, D. G. *Theor. Chem. Acc.* **2008**, *120*, 215.

(52) Hay, P. J.; Wadt, W. R. *J. Chem. Phys.* **1985**, *82*, 270.

(53) Wadt, W. R.; Hay, P. J. *J. Chem. Phys.* **1985**, *82*, 284.

(54) Hay, P. J.; Wadt, W. R. *J. Chem. Phys.* **1985**, *82*, 299.

(55) Tomasi, J.; Persico, M. *Chem. Rev.* **1994**, 2027.

(56) Cammi, R.; Tomasi, J. *J. Comput. Chem.* **1995**, *16*, 1449.

(57) Rappe, A. K.; Casewit, C. J.; Colwell, K. S.; Goddard, W. A.; Skiff, W. M. *J. Am. Chem. Soc.* **1992**, *114*, 10024.

(58) Frisch, M. J.; Trucks, G. W.; Schlegel, H. B.; Scuseria, G. E.; Robb, M. A.; Cheeseman, J. R.; Scalmani, G.; Barone, V.; Mennucci, B.; Petersson, G. A.; Nakatsuji, H.; Caricato, M.; Li, X.; Hratchian, H. P.; Izmaylov, A. F.; Bloino, J.;

Zheng, G.; Sonnenberg, J. L.; Hada, M.; Ehara, M.; Toyota, K.; Fukuda, R.; Hasegawa, J.; Ishida, M.; Nakajima, T.; Honda, Y.; Kitao, O.; Nakai, H.; Vreven, T.; J. A. Montgomery, J.; Peralta, J. E.; Ogliaro, F.; Bearpark, M.; Heyd, J. J.; Brothers, E.; Kudin, K. N.; Staroverov, V. N.; Kobayashi, R.; Normand, J.; Raghavachari, K.; Rendell, A.; Burant, J. C.; Iyengar, S. S.; Tomasi, J.; Cossi, M.; N. Rega, J. M. M.; Klene, M.; Knox, J. E.; Cross, J. B.; Bakken, V.; Adamo, C.; Jaramillo, J.; Gomperts, R.; Stratmann, R. E.; Yazyev, O.; Austin, A. J.; Cammi, R.; Pomelli, C.; Ochterski, J. W.; Martin, R. L.; K. Morokuma, V. G. Z.; Voth, G. A.; Salvador, P.; Dannenberg, J. J.; Dapprich, S.; Daniels, A. D.; Ö. Farkas, J. B. F.; Ortiz, J. V.; Cioslowski, J.; Fox, D. J. *Gaussian 09*, Revision C.01; Gaussian, Inc.: Wallingford, CT, 2009.

(59) Spek, A. L. *J. Appl. Crystallogr.* **2003**, *36*, 7.

(60) Alcock, N. W.; Pennington, M.; Willey, G. R. *J. Chem. Soc., Dalton Trans.* **1985**, 2683.

(61) Veith, M.; Wolfanger, H.; Huch, V. *Z. Naturforsch., B: Chem. Sci.* **1995**, *50*, 1130.

(62) Zhao, C.; Rodríguez-Córdoba, W.; Kaledin, A. L.; Yang, Y.; Geletii, Y. V.; Lian, T.; Musaev, D. G.; Hill, C. L. *Inorg. Chem.* **2013**, *52*, 13490.

(63) Takashima, T.; Yamaguchi, A.; Hashimoto, K.; Nakamura, R. *Chem. Commun.* **2012**, *48*, 2964.

(64) Kudo, A.; Kato, H.; Nakagawa, S. *J. Phys. Chem. B* **2000**, *104*, 571.

(65) Miseki, Y.; Kudo, A. *ChemSusChem* **2011**, *4*, 245.

(66) Zhang, Z.; Lin, Q.; Kurunthu, D.; Wu, T.; Zuo, F.; Zheng, S.-T.; Bardeen, C. J.; Bu, X.; Feng, P. *J. Am. Chem. Soc.* **2011**, *133*, 6934.

(67) Kortz, U.; Savelieff, M. G.; Bassil, B. S.; Keita, B.; Nadjo, L. *Inorg. Chem.* **2002**, *41*, 783.

(68) Bi, L.-H.; Li, B.; Bi, S.; Wu, L.-X. *J. Solid State Chem.* **2009**, *182*, 1401.

(69) Pope, M. T.; Varga, G. M. *Inorg. Chem.* **1966**, *5*, 1249.

(70) Kozik, M.; Hammer, C. F.; Baker, L. C. W. *J. Am. Chem. Soc.* **1986**, *108*, 7627.

(71) Yamase, T. *Chem. Rev.* **1998**, *98*, 307.

(72) Long, D.-L.; Kögerler, P.; Cronin, L. *Angew. Chem. Int. Ed.* **2004**, *43*, 1817.

(73) Wang, J.-P.; Ma, P.-T.; Li, J.; Niu, H.-Y.; Niu, J.-Y. *Chem. Asian J.* **2008**, *3*, 822.

(74) Zhao, C. Ph.D. dissertation, Emory University, 2013.

(75) Nalin, M.; Messaddeq, Y.; Ribeiro, S. J. L.; Poulain, M.; Briois, V.; Brunklaus, G.; Rosenhahn, C.; Mosel, B. D.; Eckert, H. *J.Mater. Chem.* **2004**, *14*, 3398.

(76) Balula, S. S.; Granadeiro, C. M.; Barbosa, A. D. S.; Santos, I. C. M. S.; Cunha-Silva, L. *Catal. Today* **2013**, *210*, 142.

(77) Keyes, T. E.; Gicquel, E.; Guerin, L.; Forster, R. J.; Hultgren, V.; Bond, A. M.; Wedd, A. G. *Inorg. Chem.* **2003**, *42*, 7897.

(78) Stowe, A. C.; Nellutla, S.; Dalal, N. S.; Kortz, U. *Eur. J. Inorg. Chem.* **2004**, 3792.

(79) Mbomekalle, I.-M.; Lopez, X.; Poblet, J. M.; Secheresse, F.; Keita, B.; Nadjo, L. *Inorg. Chem.* **2010**, *49*, 7001.

(80) Kuznetsov, A. E.; Geletii, Y. V.; Hill, C. L.; Morokuma, K.; Musaev, D. G. *Theor. Chem. Acc.* **2011**, *130*, 197.

(81) Duncan, D. C.; Fox, M. A. *J. Phys. Chem. A* **1998**, *102*, 4559.

(82) Texier, I.; Delaire, J. A.; Giannotti, C. *Phys. Chem. Chem. Phys.* **2000**, *2*, 1205.

(83) Tanielian, C.; Seghrouchni, R.; Schweitzer, C. *J. Phys. Chem. A* **2003**, *107*, 1102.

Charge Separation in Polyoxometalate-Based Systems for Solar Energy Production

Chapter 5

Charge Transfer Lifetimes in Other Polyoxometalate Chromophores

with Chongchao Zhao, Jordan M. Sumliner, John Bacsa, Daniel Taehyun Kim, Weiwei Guo, and Craig L. Hill

Published partially in: Zhao, C.; Glass, E. N.; Sumliner, J. M.; Bacsa, J.; Kim, D. T.; Guo, W.; Hill, C. L. "Complexation of metal carbonyl units with $[\alpha\text{-}PW_{11}O_{39}]^{7-}$ and $[\alpha_2\text{-}P_2W_{17}O_{61}]^{10-}$: insights into the chiral "twisted-sandwich" dimeric structures", *Dalton Transactions*, **2014**, *43(10)*, 4040-4047.

5.1 Abstract

The oxidative stability of polyoxometalates has inspired the investigation of their applicability as stable photosensitizers in an artificial photosynthetic system. Two representative complexes, $[\{Ru^{IV}_4O_4(OH)_2(H_2O)_4\}(\gamma\text{-}SiW_{10}O_{36})_2]^{10-}$ (**5.1**) and $[P_2W_{23}O_{80}\{Re(CO)_3\}_2]^{10-}$ (**5.2**), were synthesized and their structure and photodynamics have been investigated by transient absorption spectroscopy. Both complexes exhibit short-lived transient excited states similar to other polyoxometalate-based chromophores.

5.2 Introduction

In the modern era, global energy consumption has increased by ~2% annually on average, a growth which will require the doubling of energy production capacity every 35 years.[1] Currently, greater than 80% of global energy production is derived from the combustion of fossil fuels, whose limited quantity and environmental side effects cannot satisfy future demand.[2] Energy derived from the sun is the most practical and available resource for sustained and renewable energy. While the growth of solar cell deployment in recent years has provided needed breadth to the renewable energy sector, the need to efficiently store the electricity derived from solar cells remains an issue.[3,4] In most applications, the solution to this problem lies in the conversion of energy into chemical bonds by mimicking photosynthesis, a process referred to as solar fuels or artificial photosynthesis.[5-7]

A principle challenge for solar fuel production is the efficient absorption of solar energy with subsequent capture of the charge-separated state. In one common scheme, the charge separated state is utilized by allowing the electron to participate in a proton

reduction process to evolve hydrogen, while multiple photo-generated holes are used to oxidize water.[8-11] In a typical photo-driven experiment, $[Ru(bpy)_3]^{2+}$ serves as the photosensitizer, in which the excited state is quenched by a sacrificial electron acceptor such as $S_2O_8^{2-}$, generating $[Ru(bpy)_3]^{3+}$, which oxidizes a water oxidation catalyst (WOC). While $[Ru(bpy)_3]^{2+}$ is a model photosensitizer, its decomposition under oxidizing conditions competes with water oxidation.[12] The design of a stable photosensitizer to pair with stable catalysts is a limiting challenge of a viable artificial photosynthetic system.

To address this problem, the oxidative stability of polyoxometalates (POMs) have been leveraged in the development of POM-based chromophores. In these systems, the excited state is characterized by an oxidized metal and a reduced polytungstate framework. This model is a direct analogue to $[Ru(bpy)_3]^{2+}$, where the excited state $[Ru(bpy)_3]^{2+*}$ can be described as an oxidized metal center and a reduced bpy ligand (either localized or delocalized across the three ligands, depending on the timescale).[13,14] Transient absorption spectroscopy, combined with other spectroscopic, electrochemical, and computational techniques have been used to characterize the excited state dynamics of these POM-based systems. The first POM-based chromophore of this class, $[P_4W_{35}O_{124}\{Re(CO)_3\}_2]^{16-}$, was found to have an average lifetime of only 1.4 ps upon excitation at 400 nm, too short for the bimolecular electron transfer reactions necessary for catalysis to occur.[15]

Other POM-based chromophores have been reported recently, both all-inorganic and organic-inorganic hybrid complexes.[15-19] All-inorganic POM chromophores possess the oxidative and thermal stability of POMs, though they lack the well-defined

spectroscopic handles available in organic hybrids. In this report, the excited state dynamics of two representative POM chromophores are presented: $[\{Ru^{IV}_4O_4(OH)_2(H_2O)_4\}(\gamma\text{-}SiW_{10}O_{36})_2]^{10-}$ (**5.1**), an all-inorganic chromophore and water oxidation catalyst, and $[P_2W_{23}O_{80}\{Re(CO)_3\}_2]^{10-}$ (**5.2**), a POM supporting a metal carbonyl complex.

5.3 Experimental

5.3.1 General Methods and Materials

All reagents were purchased as reagent grade or higher and used as received. $Rb_8K_2[\{Ru^{IV}_4O_4(OH)_2(H_2O)_4\}(\gamma\text{-}SiW_{10}O_{36})_2]\bullet 25H_2O$ (**5.1**) was synthesized according to a known literature procedure.[20] The Keggin and Dawson polyoxometalate precursors $Na_7[\alpha\text{-}PW_{11}O_{39}]$ and $K_{10}[\alpha_2\text{-}P_2W_{17}O_{61}]$ were prepared according to literature procedures.[21,22] The low-valent complexes $M(CO)_3(CH_3CN)_3(BF_4)$ (M = Re, Mn) were made following known methods but using $AgClO_4$ in place of $AgBF_4$.[23] The purities of these compounds were analyzed by ^1H NMR, ^{31}P NMR, FT-IR, and UV-visible spectroscopy as appropriate. Infrared spectra (2% by weight in KBr) were acquired on a Thermo Nicolet 6700 FT-IR spectrometer. UV-visible spectra were collected using an Agilent 8453 spectrophotometer equipped with a diode-array detector interfaced with an Agilent 89090A cell temperature controller unit. ^{31}P NMR spectra (162.13 MHz) in D_2O were measured on a Varian INOVA 400 spectrometer with 85% H_3PO_4 (0 ppm) as an internal standard. Elemental analyses were performed by Galbraith Laboratories Inc., Knoxville, Tennessee (K, Mn, Na, P, Re, W) and Atlantic Microlab Inc., Norcross, Georgia (C, H, N).

5.3.2 Syntheses

$Rb_8K_2[\{Ru^{IV}_4O_4(OH)_2(H_2O)_4\}(\gamma\text{-}SiW_{10}O_{36})_2]\bullet 25H_2O$ (5.1). The synthesis was adapted from the published method.[20] To 65 mL deionized water at room temperature was added $K_8[\gamma\text{-}SiW_{10}O_{36}]\bullet 12H_2O$ (4.00 g, 1.33 mmol), followed quickly by $RuCl_3\bullet H_2O$ (0.60 g, 2.67 mmol). The resulting solution is dark brown with a pH of ca. 2.6. The pH was further adjusted to 1.6 by the dropwise addition of 6M HCl. After further stirring for five minutes, a solution of RbCl (2.4 g, 20 mmol) dissolved in 10 mL H_2O was added to the solution in portions. The solution was filtered and allowed to develop crystals through slow evaporation at room temperature. Brown plate crystals were collected after four days. Yield: 1.1 g (24% based on W). FTIR (2% KBr pellet), $\tilde{\nu}$, cm^{-1}: 1616 (m), 999 (m), 947 (m-s), 914 (s), 874 (s), 802 (vs), 765 (vs), 690 (sh), 630 (sh), 572 (m-s), 542 (m-s). UV-vis (0.1 M HCl), λ_{max}, nm (ε, L mol^{-1} cm^{-1}): 445 (50000).

$K_7Na_3[P_2W_{23}O_{80}\{Re(CO)_3\}_2]\bullet 38H_2O$ (5.2). $Na_7[\alpha\text{-}PW_{11}O_{39}]$ (286 mg, 0.10 mmol) and $Re(CO)_3(CH_3CN)_3BF_4$ (48 mg, 0.10 mmol) were dissolved in 15 mL of hot deionized water. The mixtures were heated at ~70 ^{o}C for 30 minutes, during which time the solution slowly became orange-red. The solution was then cooled to room temperature and the pH was adjusted to ~2.5 by addition of 1.0 M HCl. The solution became dark red in color and was filtered. KCl (200 mg, 2.7 mmol) was added to the solution in small portions. Plate-shaped single crystals suitable for X-ray diffraction were collected after slow evaporation for *ca.* 3 weeks. Yield: 45 mg (13% based on P). FTIR (2500-400 cm^{-1}, 2% KBr pellet): 2013 (s), 1900 (s), 1879 (s), 1099 (s), 1046 (s), 956 (s), 903 (m), 838 (s), 785 (w), 743 (w), 708 (w), 653 (w), 598 (w), 513 (w). UV-vis (H_2O), λ, nm (ε, L mol^{-1} cm^{-1}): 400 (11000). ^{31}P NMR: -12.7 ppm. Anal. Calcd. for

$C_6H_{76}O_{124}K_7Na_3P_2Re_2W_{23}$: K, 3.8; Na, 0.97; P, 0.87; Re, 5.2; W, 59.2. Found: K, 3.8; Na, 1.1; P, 0.83; Re, 5.1; W, 59.5.

5.3.3 Single Crystal X-ray Structural Determination

X-ray analysis of **5.2** was performed on a Bruker D8 SMART APEXII CCD sealed tube diffractometer. Diffraction intensities were measured using graphite monochromated Mo K_α radiation (λ = 0.71073 Å) at 173(2) K. Structure solution, refinement, graphics were generated using SHELXTL-97 software.[24,25] The largest residual electron density for each structure was located close to the W atoms and was most likely due to imperfect absorption corrections frequently encountered in heavy-metal atom structures. Crystal data collection and refinement parameters are given in Table 5.1. Supplementary crystallographic data, CCDC- 917606 (**5.2**), can be obtained free of charge from The Cambridge Crystallographic Data Center via www.ccdc.cam.ac.uk/data_request/cif.

Table 5.1. Crystal structure data for compound **5.2**

Empirical formula	$C_6H_{76}O_{124}K_7Na_3P_2Re_2W_{23}$
***T* / K**	173(2)
F_w / g mol^{-1}	7137.93
Crystal system	Triclinic
Space group	$P\bar{1}$
***a* / Å**	13.0794(4)
***b* / Å**	19.8716(6)
***c* / Å**	21.3258(6)
α / °	76.506(2)
β / °	84.428(2)
γ / °	82.631(2)
***V* / Å^3**	5332.3(3)
Z	2
ρ_{calcd} / g cm^{-3}	4.224
μ / mm^{-1}	27.349
Reflection collected	179537
Independent refl. (R_{int})	24038 (0.0761)
Goodness-of-fit	1.064
R_1 / I>2σ(I)	0.0416
wR_2	0.1045
R_1 (all data)	0.0578
wR_2	0.1165
Largest diff. peak and hole / eÅ^{-3}	6.237, -4.372

$R_1 = \Sigma\ ||F_0|-|F_c||/\Sigma|F_0|$; w$R_2 = \{\Sigma[w(F_0^2-F_c^2)^2/\Sigma w(F_0^2)^2]\}^{1/2}$

5.3.4 Transient Absorption Spectroscopy

The femtosecond transient absorption spectrometer is based on a regeneratively amplified Ti:sapphire laser system (coherent Legend, 800 nm, 150 fs, 3 mJ/pulse and 1 kHz repetition rate) and the Helios spectrometer (Ultrafast Systems LLC), described in detail elsewhere.[15,19] Samples were measured in a 1 mm path length quartz cuvette to minimize the solvent response due to the optical Kerr effect. The solvent response in neat solvent was recorded immediately following sample measurement. The sample was

constantly stirred by a magnetic stirrer during measurement, and no evidence of sample degradation was seen based on comparisons of the electronic absorption spectra before and after measurement. Detailed analysis of the transient spectra and kinetics was performed using Ultrafast Systems Surface Xplorer Pro software. Both selected wavelength kinetic analysis and global fit analysis via singular value decomposition were performed. For global fit analysis the principal kinetic component was fit to a multi-exponential decay function convoluted with the Gaussian instrument response function (fwhm: ~150 fs).

5.4 Results and Discussion

5.4.1 Structure and Absorption Spectroscopy of an All-Inorganic Chromophore

The structure of $[\{Ru^{IV}_4O_4(OH)_2(H_2O)_4\}(\gamma\text{-}SiW_{10}O_{36})_2]^{10-}$ (**5.1**), a known WOC, is represented in Figure 5.1.[20] The center of the structure consists of a core $\{Ru^{IV}_4(\mu\text{-}O)_4(\mu\text{-}OH)_2(H_2O)_4\}^{6+}$ unit, in which four ruthenium(IV) (d^4) atoms are at corners of a distorted tetrahedron. The ruthenium atoms are bridged by hydroxo and oxo ligands (hydroxo ligands bridge two ruthenium atoms nearest the POM ligands, while oxo ligands bridge the center; determined by BVS). The core is ligated to two $[\gamma\text{-}SiW_{10}O_{36}]^{8-}$ POMs through out-of-pocket coordination, with each ruthenium bound by two Ru-O-W bonds to separate tungsten octahedra (corner-sharing). The two POM units are rotated relative to each other by 90°, yielding a D_{2d} symmetry to **5.1** overall.

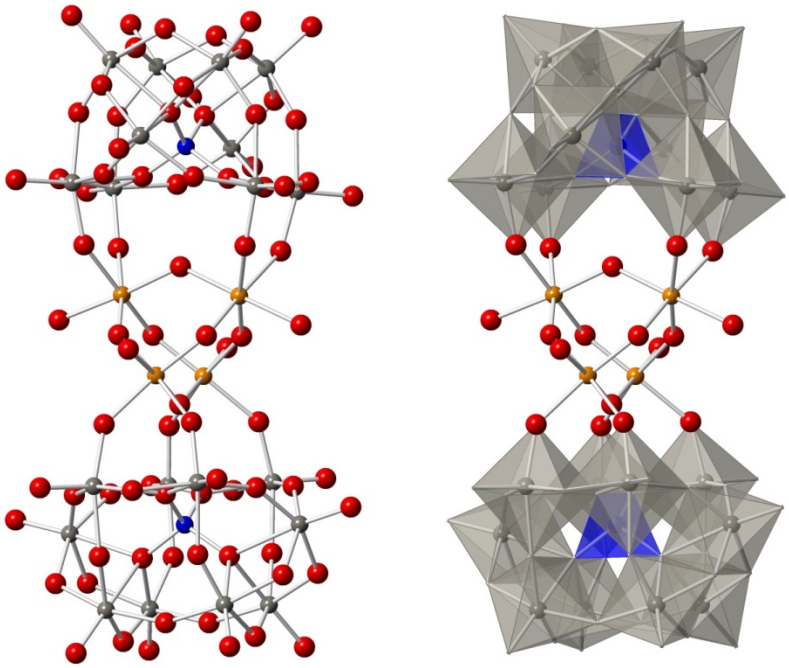

Figure 5.1. X-ray structure of $[\{Ru^{IV}_4O_4(OH)_2(H_2O)_4\}(\gamma\text{-}SiW_{10}O_{36})_2]^{10-}$ (**5.1**) represented in ball-and-stick notation (left) and mixed polyhedral notation (right), highlighting the tetra-ruthenium core. Color scheme: Si, blue; Ru, orange; W, grey; O, red.

The strong electronic absorption properties of **5.1** make it an appealing candidate for photosensitization. The electronic absorption spectrum (Figure 5.2) shows an intense absorption tailing from the UV, with shoulders at *ca.* 270 and 340 nm with extinction coefficients in excess of 70,000 and 30,000 L mol^{-1} cm^{-1}, respectively. The tail extends across the visible region, yielding an intense brown color in solution. These broad absorption features are consistent with vibronically-coupled O→W and O→Ru charge transfer (CT) bands. Of particular note, **5.1** possesses a strong pH-dependent absorption with a peak at 445 nm 30,000 L mol^{-1} cm^{-1}.[10,20,26] The assignment of this feature is still under investigation, but its pH-dependence and intensity suggests it is an LMCT band associated with protonation of the oxo ligands in the tetra-ruthenium core.

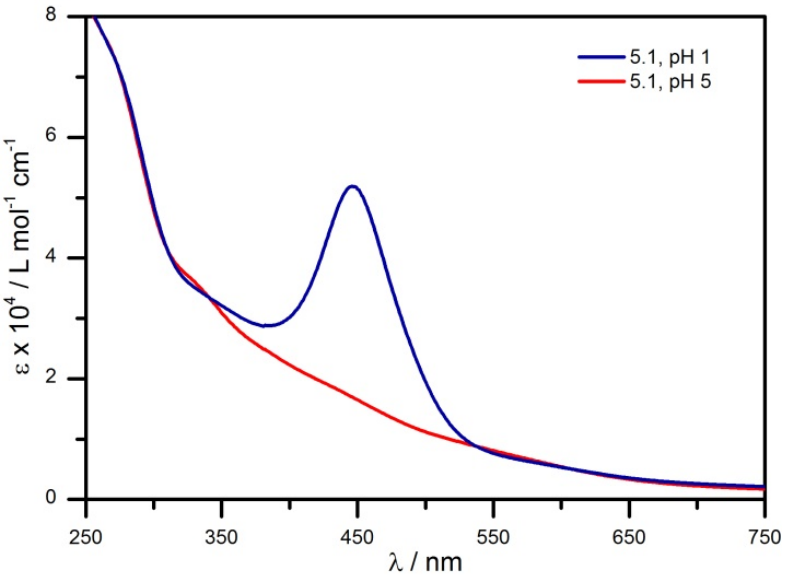

Figure 5.2. Electronic absorption spectrum of **5.1** in 0.1 M HCl (pH 1, blue) and 0.25 M lithium acetate buffer (pH 5, red).

5.4.2 Transient Absorption Spectroscopy of an All-Inorganic Chromophore

The excited state dynamics of **5.1** were evaluated by transient absorption spectroscopy in both 0.1 M HCl (pH 1) and 0.25 M lithium acetate buffer (pH 5). At pH 1, excitation at 400 nm pumps into the high-energy tail of the CT transition at 445 nm; at pH 5 the pH-dependent CT transition has disappeared, though an intense absorption remains from the underlying LMCT bands.

Upon excitation at 400 nm at pH 1, **5.1** exhibits a transient bleach at *ca.* 450 nm and a concomitant excited state absorption at lower energy with a peak near 550 nm (Figure 5.3a). As previously noted, the character of the excited state is more likely to be associated with an LMCT process than the MPCT processes investigated in other systems. The broad excited state absorption shares a similar spectral range to previously reported “heteropoly blue” excited states, but the transient feature has a maximum

intensity at shorter wavelengths (*ca.* 525-550 nm) and tails off at lower energy, rather than growing in intensity at longer wavelengths (*vide infra*). The kinetics of the excited state decay are shown in Figure 5.3b at two representative wavelengths. Global fit analysis fit the kinetics of **5.1** to an instantaneous formation of the excited state (within the temporal resolution of the instrument) and a bi-exponential decay function. The excited state is short-lived, with an average lifetime of only 1.8 ps and time constants of τ_1 = 680 ± 140 fs and τ_2 = 3.4 ± 0.7 ps. The ground state of **5.1** recovers completely within 15 ps.

At pH 5, **5.1** does not exhibit any detectable transient behavior in the visible spectrum (data not shown). This behavior lends further support to the CT band at pH 1 being the result of protonation of the tetra-ruthenium core, and not a Ru→W MPCT transition.

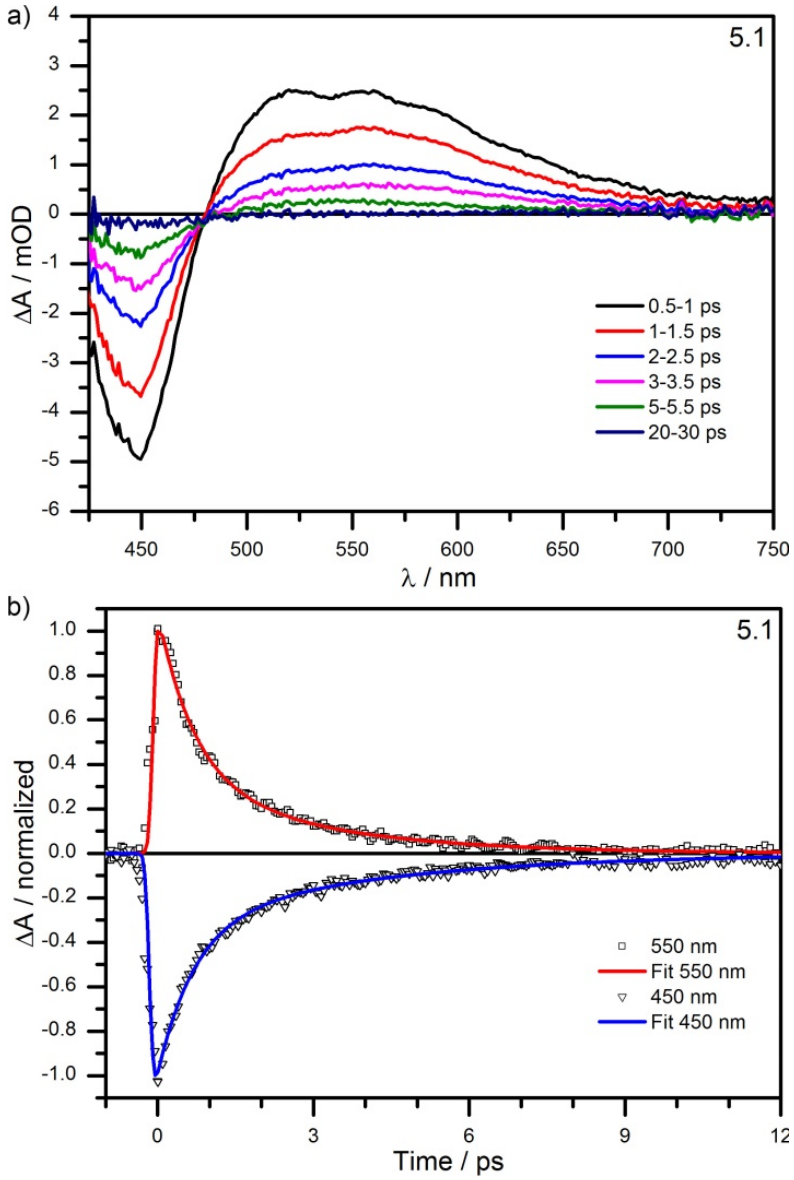

Figure 5.3. a) Transient absorption spectra and b) kinetics of **5.1** after excitation by an ultrafast pump pulse at 400 nm in 0.1 M HCl. Spectral traces are the average of multiple measurements within the noted time windows. Empirical measurements and multi-exponential kinetic fits are shown normalized to their respective peak fit values.

5.4.3 Structure of a Metal Carbonyl Hybrid Chromophore

The structure of **5.2**, shown in Figure 5.4, shows an ideal C_2 symmetry with only one ^{31}P NMR peak. The bond distances of Re-O and C-O are in the range of 1.88 to 1.91 Å and 1.16 to 1.20 Å respectively, which are consistent with other POM-supposed metal carbonyl complexes (Table 5.2).[15,18,27-42] The structure can be regarded as the dimerization of two $[\alpha\text{-}PW_{11}O_{39}]^{7-}$ polyanions with an extra $[WO_2]^{2+}$ unit as the rotating center. This structural feature is similar to that found in some organo-ruthenium-substituted POMs.[43,44] The central W atom resides in a distorted octahedral cage, and the four neighboring metals $\{ReW_3\}$ are almost in the same plane (±1º). The chirality of this complex derives from two $[\alpha\text{-}PW_{11}O_{39}]^{7-}$ units staggered relative to one another around the central W atom, resulting in a torsion angle of ±48.5º. However, unlike $[Hf(PW_{11}O_{39})_2]^{11-}$, which crystallizes in a chiral space group,[45-48] **5.2** crystallizes in the centrosymmetric space group $P\bar{1}$. Thus, **5.2** is racemic (Λ- and Δ- forms of two enantiomers in a 1:1 ratio) in the solid state.

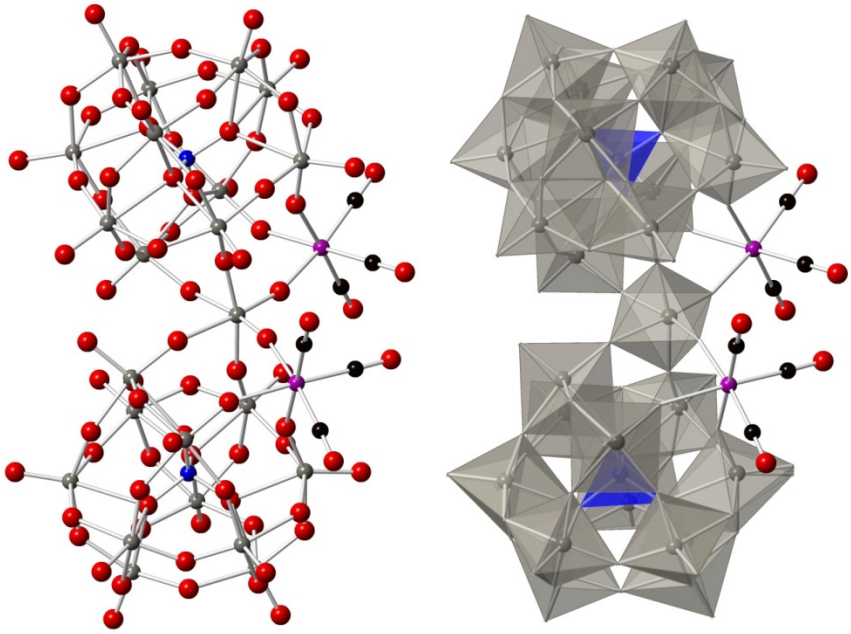

Figure 5.4. X-ray structure of $[P_2W_{23}O_{80}\{Re(CO)_3\}_2]^{10-}$ (**5.2**) represented in ball-and-stick notation (left) and mixed polyhedral notation (right). Color scheme: P, blue; Re, magenta; W, grey; C, black; O, red.

Table 5.2. Selected bond lengths, bond angles and CO stretching vibrations for **5.2**

Parameter	**Value**
P-O[a] / Å	1.52-1.56
Re-O[a] / Å	2.07-2.15
Re-C[b] / Å	1.88-1.91
C-O[b] / Å	1.16-1.20
Re-C-O[b] / °	176-180
C-O stretch / cm^{-1}	2013, 1900, 1879

[a] Oxygen from POMs.

[b] Carbon and oxygen from carbonyl groups.

5.4.4 Transient Absorption Spectroscopy of Metal Carbonyl Hybrid Chromophore

Compound **5.2** has a dark-red color in the solid state and a high absorptivity covering the entire UV-visible spectrum extended to ~650 nm in solution. The reddish color first appears upon reaction of $[\alpha\text{-}PW_{11}O_{39}]^{7-}$ with solvated $[Re(CO)_3]^+$, a characteristic feature indicating the formation of W-O-Re bonds.[15] The extinction coefficient for **5.2** ($\varepsilon_{400} \sim 1.1\times10^4$ L mol^{-1} cm^{-1}) is significantly higher than for the first POM-supported metal carbonyl complex reported, $[P_4W_{35}O_{124}\{Re(CO)_3\}_2]^{16-}$ ($\varepsilon_{400} \sim 6.2\times10^3$ L mol^{-1} cm^{-1}).[15] Similar to that complex, the high absorption in **5.2** is attributed to an MPCT transition from Re(I) centers to POM ligands.

Femtosecond visible transient absorption measurements were recorded on **5.2** to probe the excited-state dynamics upon photo-excitation at 400 nm. Transient spectra of **5.2** at selected time delays (Figure 5.5a) show a broad absorption feature extending across the visible spectrum from 500 nm into the near-IR region. These new absorption features are attributed to the well-documented photochemical characteristic of reduced POMs referred to as "heteropoly blues." The kinetics of the excited state are uniform across the region probed, from 500 nm to 780 nm, supporting the conclusion that the visible absorption is the result of a single absorptive species, represented at 650 nm in Figure 5.5b. Global analysis satisfactorily fit the kinetics arising from excitation at 400 nm using a triexponential function convoluted with the instrument response function. The formation time of the excited state has a time constant of $\tau_1 = 20 \pm 13$ fs, which is within the temporal resolution of the instrument and can be considered instantaneous. Following excitation, the excited state decays with two time constants. The faster time constant, $\tau_2 = 1.2 \pm 0.2$ ps, reflects rapid internal conversion within the polytungstate

framework. The slower dynamic process with a time constant of $\tau_3 = 4.7 \pm 0.7$ ps may be representative of vibrational cooling within the complex as previously established. The ground state recovers completely within 20 ps.

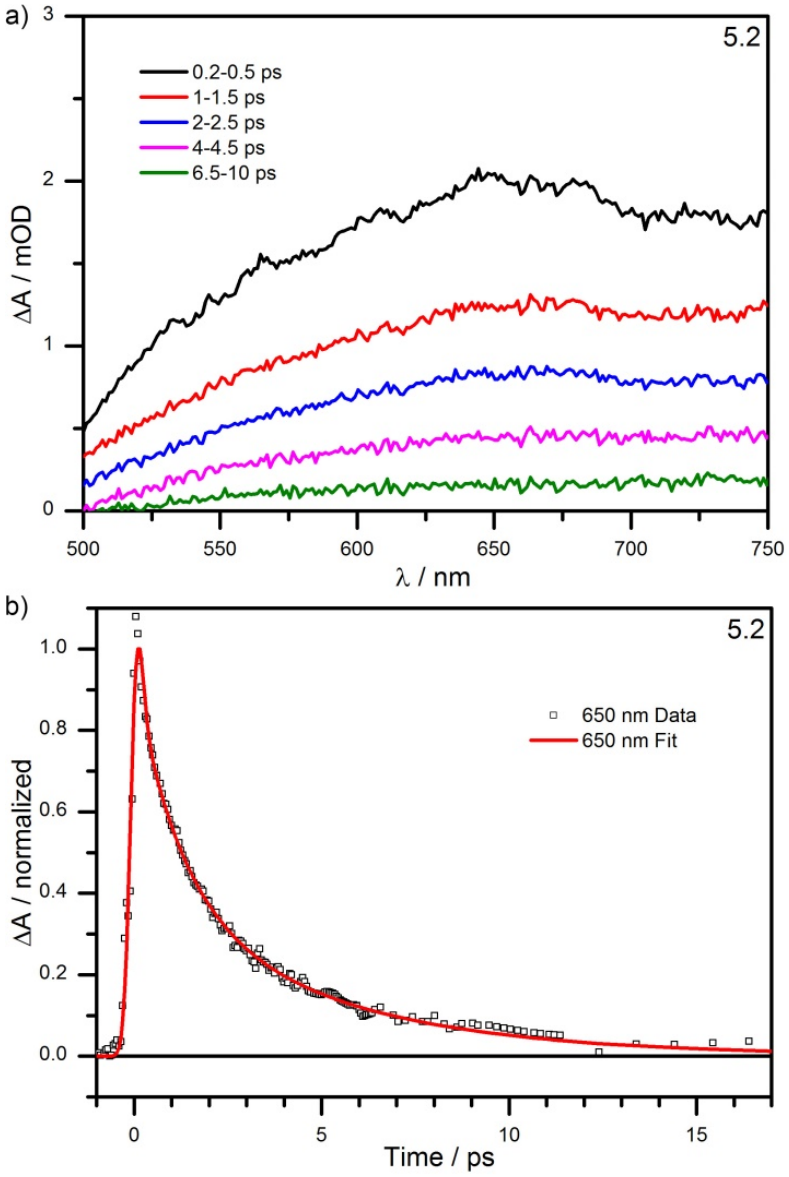

Figure 5.5. a) Transient absorption spectra and b) kinetics of **5.2** after excitation by an ultrafast pump pulse at 400 nm in H_2O. Spectral traces are the average of multiple measurements within the noted time windows. Empirical measurements and the multi-exponential kinetic fit are shown normalized to the peak fit value.

5.5 Conclusion

The polyoxometalate anions $[\{Ru^{IV}_4O_4(OH)_2(H_2O)_4\}(\gamma\text{-}SiW_{10}O_{36})_2]^{10-}$ (**5.1**) and $[P_2W_{23}O_{80}\{Re(CO)_3\}_2]^{10-}$ (**5.2**) have been synthesized and their photodynamics investigated. Both chromophoric complexes exhibit transient behavior arising from different electronic transitions, but their excited states are short-lived. These complexes, both an all-inorganic chromophore (**5.1**) and a POM-supporting metal carbonyl complex (**5.2**) illustrate the types of short-lived intramolecular charge transfer chromophores found in POMs.

5.6 References

(1) *BP Statistical Review of World Energy: June 2015*, British Petroleum, 2015.

(2) *Key World Energy Statistics*, International Energy Agency, 2015.

(3) Lewis, N. S.; Nocera, D. G. *Proc. Natl. Acad. Sci.* **2006**, *103(43)*, 15729.

(4) Cook, T. R.; Dogutan, D. K.; Reece, S. Y.; Surendranath, Y.; Teets, T. S.; Nocera, D. G. *Chem. Rev.* **2010**, *110*, 6474.

(5) Grätzel, M. *Nature* **2001**, *414*, 338.

(6) Meyer, T. *Acc. Chem. Res.* **1989**, *22*, 163.

(7) Rüttinger, W.; Dismukes, G. C. *Chem. Rev.* **1997**, *97*, 1.

(8) Young, K. J.; Martini, L. A.; Milot, R. L.; III, R. C. S.; Batista, V. S.; Schmuttenmaer, C. A.; Crabtree, R. H.; Brudvig, G. W. *Coord. Chem. Rev.* **2012**, *256*, 2503.

(9) Kaveevivitchai, N.; Chitta, R.; Zong, R.; Ojaimi, M. E.; Thummel, R. P. *J. Am. Chem. Soc.* **2012**, *134*, 10721.

(10) Geletii, Y. V.; Huang, Z.; Hou, Y.; Musaev, D. G.; Lian, T.; Hill, C. L. *J. Am. Chem. Soc.* **2009**, *131*, 7522.

(11) Lv, H.; Geletii, Y. V.; Zhao, C.; Vickers, J. W.; Zhu, G.; Luo, Z.; Song, J.; Lian, T.; Musaev, D. G.; Hill, C. L. *Chem. Soc. Rev.* **2012**, *41*, 7572.

(12) Ghosh, P. K.; Brunschwig, B. S.; Chou, M.; Creutz, C.; Sutin, N. *J. Am. Chem. Soc.* **1984**, *106*, 4772.

(13) Yeh, A. T.; Shank, C. V.; McCusker, J. K. *Science* **2000**, *289*, 935.

(14) Damrauer, N. H.; Cerullo, G.; Yeh, A.; Boussie, T. R.; Shank, C. V.; McCusker, J. K. *Science* **1997**, *275*, 54.

(15) Zhao, C.; Huang, Z.; Rodríguez-Córdoba, W.; Kambara, C. S.; O'Halloran, K. P.; Hardcastle, K. I.; Musaev, D. G.; Lian, T.; Hill, C. L. *J. Am. Chem. Soc.* **2011**, *133*, 20134.

(16) Zhao, C.; Glass, E. N.; Chica, B.; Musaev, D. G.; Sumliner, J. M.; Dyer, R. B.; Lian, T.; Hill, C. L. *J. Am. Chem. Soc.* **2014**, *136*, 12085.

(17) Zhao, C.; Rodríguez-Córdoba, W.; Kaledin, A. L.; Yang, Y.; Geletii, Y. V.; Lian, T.; Musaev, D. G.; Hill, C. L. *Inorg. Chem.* **2013**, *52*, 13490.

(18) Zhao, C.; Kambara, C. S.; Yang, Y.; Kaledin, A. L.; Musaev, D. G.; Lian, T.; Hill, C. L. *Inorg. Chem.* **2013**, *52*, 671.

(19) Glass, E. N.; Fielden, J.; Kaledin, A. L.; Musaev, D. G.; Lian, T.; Hill, C. L. *Chem. Eur. J.* **2014**, *20*, 4297.

(20) Geletii, Y. V.; Botar, B.; Kögerler, P.; Hillesheim, D. A.; Musaev, D. G.; Hill, C. L. *Angew. Chem. Int. Ed.* **2008**, *47*, 3896.

(21) Brevard, C.; Schimpf, R.; Tourné, G.; Tourné, C. M. *J. Am. Chem. Soc.* **1983**, *105*, 7059.

(22) Randall, W. J.; Droege, M. W.; Mizuno, N.; Nomiya, K.; Weakley, T. J. R.; Finke, R. G. In *Inorg. Synth.*; Cowley, A. H., Ed.; John Wiley & Sons, Inc.: New York, 1997; Vol. 31, p 167.

(23) Edwards, D. A.; Marshalsea, J. *J. Organomet. Chem.* **1977**, *131*, 73.

(24) *SHELXTL, ver. 6.14*; Bruker AXS, Inc.: Madison, WI, 2003.

(25) Sheldrick, G. M. *Acta Crystallogr., Sect. A* **1990**, *46*, 467.

(26) Geletii, Y. V.; Besson, C.; Hou, Y.; Yin, Q.; Musaev, D. G.; Quinonero, D.; Cao, R.; Hardcastle, K. I.; Proust, A.; Kögerler, P.; Hill, C. L. *J. Am. Chem. Soc.* **2009**, *131*, 17360.

(27) Knoth, W. H. *J. Am. Chem. Soc.* **1979**, *101*, 2211.

(28) Knoth, W. H.; Domaille, P. J. *Inorg. Chem.* **1983**, *22*, 818.

(29) Besecker, C. J.; Klemperer, W. G. *J. Am. Chem. Soc.* **1980**, *25*, 7598.

(30) Besecker, C. J.; Day, V. W.; Klemperer, W. G.; Thompson, M. R. *Inorg. Chem.* **1985**, *24*, 44.

(31) Klemperer, W. G.; Main, D. J. *Inorg. Chem.* **1990**, *29*, 2355.

(32) Day, V. W.; Fredrich, M. F.; Thompson, M. R.; Klemperer, W. G.; Liu, R. S.; Shum, W. *J. Am. Chem. Soc.* **1981**, *103*, 3597.

(33) Klemperer, W. G.; Zhong, B. X. *Inorg. Chem.* **1993**, *32*, 5821.

(34) Siedle, A. R.; Lyon, P. A.; Hodgson, K. O.; Roe, A. L. *Inorg. Chem.* **1987**, *26*, 219.

(35) Nagata, T.; Pohl, B. M.; Weiner, H.; Finke, R. G. *Inorg. Chem.* **1997**, *36*, 1366.

(36) Besserguenev, A. V.; Dickman, M. H.; Pope, M. T. *Inorg. Chem.* **2001**, *40*, 2582.

(37) Villanneau, R.; Delmont, R.; Proust, A.; Gouzerh, P. *Chem. Eur. J.* **2000**, *6*, 1184.

(38) Villanneau, R.; Proust, A.; Robert, F.; Gouzerh, P. *Chem. Eur. J.* **2003**, *9*, 1982.

(39) Sadakane, M.; Iimuro, Y.; Tsukuma, D.; Bassil, B. S.; Dickman, M. H.; Kortz, U.; Zhang, Y.; Ye, S.; Ueda, W. *Dalton Trans.* **2008**, 6692.

(40) Niu, J.; Yang, L.; Zhao, J.; Ma, P.; Wang, J. *Dalton Trans.* **2011**, *40*, 8298.

(41) Zhao, J.; Zhao, J.; Ma, P.; Wang, J.; Niu, J.; Wang, J. *J. Mol. Struct.* **2012**, *1019*, 61.

(42) Zhao, J.; Wang, J.; Zhao, J.; Ma, P.; Wang, J.; Niu, J. *Dalton Trans.* **2012**, *41*, 5832.

(43) Artero, V.; Laurencin, D.; Villanneau, R.; Thouvenot, R.; Herson, P.; Gouzerh, P.; Proust, A. *Inorg. Chem.* **2005**, *44*, 2826.

(44) Nomiya, K.; Hayashi, K.; Kasahara, Y.; Iida, T.; Nagaoka, Y.; Yamamoto, H.; Ueno, T.; Sakai, Y. *Bull. Chem. Soc. Jpn.* **2007**, *80*, 724.

(45) Hou, Y.; Fang, X.; Hill, C. L. *Chem. Eur. J.* **2007**, *13*, 9442.

(46) Hasenknopf, B.; Micoine, K.; Lacôte, E.; Thorimbert, S.; Malacria, M.; Thouvenot, R. *Eur. J. Inorg. Chem.* **2008**, 5001.

(47) Du, D.-Y.; Yan, L.-K.; Su, Z.-M.; Li, S.-L.; Lan, Y.-Q.; Wang, E.-B. *Coord. Chem. Rev.* **2013**, *257*, 702.

(48) Zhang, J.; Hao, J.; Wei, Y.; Xiao, F.; Yin, P.; Wang, L. *J. Am. Chem. Soc.* **2009**, *132*, 14.